Landslide susceptibility assessment in the Chiconquiaco Mountain Range area, Veracruz (Mexico)

Inaugural-Dissertation zur Erlangung der Doktorwürde der Philosophischen Fakultät

der

Julius-Maximilians-Universität Würzburg

vorgelegt von

Martina Wilde

aus

Karlsruhe

Würzburg 2021

Erstgutachterin: Prof. Dr. Birgit Terhorst

Zweitgutachter: Prof. Dr. Bernd Zimanowski

Drittgutachter: Prof. Dr. Alexander Fekete

Tag des Kolloquiums: 23. Februar 2022

Acknowledgments

First of all, I would like to express my sincere gratitude to my supervisor Prof. Dr. Birgit Terhorst for the constant support, encouragement, and the opportunity to write a PhD thesis. I would like to sincerely thank Prof. Dr. Roland Baumhauer for his consistent support as mentor and his insightful feedback throughout the years of my studies. Many thanks to Prof. Dr. Bernd Zimanowski for supporting me as mentor of this work and for patiently answering numerous questions.

Particular thanks goes to the German Academic Exchange Service (DAAD), who supported the present study as part of their scholarship program "Jahresstipendien für Doktoranden". Without this funding the field work and my stay in Mexico would not have been possible. The Faculty of Philosophy of the University of Würzburg also gratefully provided funding for this PhD thesis.

I am especially grateful to Dr. Elizabeth Solleiro Rebolledo for making it possible for me to stay at the Institute of Geology at the UNAM. Without all the help and assistance I received there, this project would not have been possible. I would also like to thank Dr. Sergey Sedov for his thoughts and ideas as well as the continuous support. In my time at the institute, on all the field trips, and the wonderful 'seminario' I felt part of the group, which is not taken for granted. Furthermore, my sincere thanks goes to Dr. Sergio Rodríguez Elizarrarás for his support, hospitability, and the enormous amount of time he generously invested in helping and supporting me. I would also like to thank Wendy Morales Barrera for her immense commitment and indispensable support. She always moved mountains to help and support me and I will always be grateful to her. Thank you Wendy for sharing your passion, enthusiasm, and especially for introducing me to this beautiful area of Mexico.

I am particularly grateful to Thomas Kreuzer for his expertise, assistance, discussions, helpful ideas, and always being extremely supportive. I owe Dr. Daniel Schwindt many thanks for making the effort to travel so far to contribute to the field work and I deeply appreciate all the support and encouragement. Special thanks goes to Dr. Matthias Bücker for supporting me in the field and beyond. He always ensured that we were perfectly staffed and technically equipped and thus made a significant contribution to the success of the field investigations. I would also like to thank Dr. Tobias Ullmann for his support and especially for sharing his experience on the field of photogrammetry with me. A special thanks goes to Prof. Dr. Herbert Voßmerbäumer for his constant motivation.

I am sincerely grateful for all the helping hands during fieldwork. Without the assistance, personnel and technical support provided by the Civil Protection of Veracruz and the consulting engineering company GEOTEM Ingeniería, especially Carlos Pita de la Paz and Emilio García García, the fieldwork would not have been possible. In this context I would also like to thank Johannes Bücker, Hugo Salgado, Tobias Sprafke, and Julian Krause for their support and assistance in the field. Many thanks are extended to Dr. Liseth Perez for gratefully taking care of shipping my samples from Mexico to Germany, which in the end was only possible because of her persistence.

Further thanks go to Martin Krech, Henriette Brand, and Katrin Hagen for the support with the laboratory work and also to Jorge René Alcalá Martínez, Jaime Diaz Ortega, and Teresa Pi Puig, who welcomed and greatly supported me in their laboratories at the UNAM. I would like to thank Anja Lenz for accompanying me in the field and her willingness to conduct her thesis in this project. We experienced many ups and downs during fieldwork and I am very thankful that we have been through this together. Many thanks to Miriam Füssl, for conducting her thesis in the frame of this work, and particularly for her patience to carry on with the laboratory work even when it seemed to be a never-ending story.

A special thanks goes to my Mexican friends and colleagues Gina, Jasmin, Berenice, Gabo, Oney, Eliuth, Ema, Aturo, Rafael, and Luisa for welcoming me so warmly and openly and for supporting me during my time in Mexico. I am grateful to my colleagues Simon Meyer-Heintze, Daniel Jäger, Marius Röder, Angela Tintrup gen. Suntrup, and Christian Büdel of the Institute of Geography and Geology in Würzburg for their help, discussions, and support. I would also like to thank Inka Wilhelm, Dorothee Ullrich and Günter Moritz for their administrative and organizational support. Julian Schwäble contributed excellent editorial comments to this draft, and I owe him many thanks for proofreading of the thesis. Finally, I would like to express my sincere gratitude to my family for their patience, understanding, and amazing support.

Abstract

In Mexico, numerous landslides occur each year and Veracruz represents the state with the third highest number of events (Díaz et al. 2020). Especially the Chiconquiaco Mountain Range, located in the central part of Veracruz, is highly affected by landslides and no detailed information on the spatial distribution of existing landslides or future occurrences is available. This leaves the local population exposed to an unknown threat and unable to react appropriately to this hazard or to consider the potential landslide occurrence in future planning processes.

Thus, the overall objective of the present study is to provide a comprehensive assessment of the landslide situation in the Chiconquiaco Mountain Range area. Here, the combination of a site-specific and a regional approach enables to investigate the causes, triggers, and process types (site-specific approach) as well as to model the landslide susceptibility for the entire study area (regional approach).

For the site-specific approach, the focus lies on characterizing the Capulín landslide, which represents one of the largest mass movements in the area. In this context, the task is to develop a multi-methodological concept, which concentrates on cost-effective, flexible and non-invasive methods. This approach shows that the applied methods complement each other very well and their combination allows for a detailed characterization of the landslide.

The analyses revealed that the Capulín landslide is a complex mass movement type. It comprises rotational movement in the upper parts and translational movement in the lower areas, as well as flow processes at the flank and foot area and therefore, is classified as a compound slide-flow according to Cruden and Varnes (1996). Furthermore, the investigations show that the Capulín landslide represents a reactivation of a former process. This is an important new information, especially with regard to the other landslides identified in the study area. Both the road reconstructed after the landslide, which runs through the landslide mass, and the stream causing erosion processes at the foot of the landslide severely affect the stability of the landslide, making it highly susceptible to future reactivation processes. This is particularly important as the landslide is located only few hundred meters from the village El Capulín and an extension of the landslide area could cause severe damage.

The next step in the landslide assessment consists of integrating the data obtained in the site-specific approach into the regional analysis. Here, the focus lies on transferring the generated data to the entire study area. The developed methodological concept yields applicable results, which is supported by different validation approaches.

The susceptibility modeling as well as the landslide inventory reveal that the highest probability of landslides occurrence is related to the areas with moderate slopes (< 35°) covered by slope deposits. These slope deposits comprise material from old mass movements and erosion processes and are highly susceptible to landslides. The results give new insights into the landslide situation in the Chiconquiaco Mountain Range area, since previously landslide occurrence was related to steep slopes of basalt and andesite.

The susceptibility map is a contribution to a better assessment of the landslide situation in the study area and simultaneously proves that it is crucial to include specific characteristics of the respective area into the modeling process, otherwise it is possible that the local conditions will not be represented correctly.

Kurzzusammenfassung

In Mexico ereignen sich jedes Jahr zahlreiche Rutschungen und Veracruz ist der Bundesstaat mit der dritthöchsten Anzahl von solchen Ereignissen (Díaz et al. 2020). Besonders das Chiconquiaco Gebirge, welches im zentralen Bereich von Veracruz liegt, ist stark von Rutschungen betroffen und trotzdem sind keine detaillierten Informationen zur räumlichen Verbreitung existierender Rutschungen oder zu deren erwarteten, zukünftigen Auftreten verfügbar. Dadurch ist die lokale Bevölkerung mit einer nicht einschätzbaren Bedrohungslage konfrontiert und kann weder auf diese angemessen reagieren noch das potentielle Auftreten von Rutschungen in künftigen Planungsprozessen berücksichtigen.

Das übergeordnete Ziel der vorliegenden Arbeit besteht daher darin, eine umfassende Beurteilung der Rutschungssituation im Chiconquiaco Gebirge zu erstellen. Hierbei ermöglicht die Kombination eines standortspezifischen und eines regionalen Ansatzes sowohl die Untersuchung der Ursachen, Auslöser und Prozesstypen (standortspezifischer Ansatz), als auch die Modellierung der Rutschanfälligkeit für das gesamte Untersuchungsgebiet (regionaler Ansatz).

Bei dem standortspezifischen Ansatz liegt der Schwerpunkt auf der Charakterisierung der Capulín Rutschung, bei der es sich um eine der größten Massenbewegungen in dieser Region handelt. In diesem Rahmen besteht die Aufgabe darin, ein multi-methodologisches Konzept zu entwickeln, welches sich hauptsächlich auf kostengünstige, flexible und nicht-invasive Methoden konzentriert. Dieser Ansatz zeigt, dass sich die verwendeten Methoden sehr gut ergänzen und ihre Kombination eine detaillierte Charakterisierung der Rutschung ermöglicht.

Die Ergebnisse legen dar, dass die Capulín Rutschung eine komplexe Massenbewegung ist. So umfasst sie Rotationsbewegungen im oberen und Translationsbewegungen im unteren Bereich, sowie Fließprozesse an der Flanke und im Fußbereich und kann daher nach Cruden und Varnes (1996) als Kombination aus Gleit- und Fließprozessen (compound slide-flow) klassifiziert werden. Des Weiteren zeigen die Ergebnisse, dass es sich bei der Capulín Rutschung um eine Reaktivierung einer älteren Rutschung handelt. Das ist eine wichtige neue Erkenntnis besonders im Hinblick auf die anderen Rutschungen, die im Untersuchungsgebiet festgestellt wurden. Sowohl die nach der Rutschung wieder aufgebaute Straße, die durch die Rutschmasse verläuft, als auch der

Fluss, der Erosionsprozesse am Fuß der Rutschung verursacht, beeinträchtigen die Stabilität der Capulín Rutschung maßgeblich, was sie sehr anfällig für zukünftige Reaktivierungsprozesse macht. Dies ist besonders wichtig, da die Rutschung nur wenige hundert Meter von dem Ort El Capulín entfernt ist und eine Erweiterung des Rutschgebietes erhebliche Schäden verursachen könnte.

Im Anschluss werden die durch den lokalen Ansatz erhaltenen Daten in die regionale Analyse integriert. Der Fokus bei diesem Vorgehen liegt dabei auf der Übertragung der generierten Daten auf das gesamte Untersuchungsgebiet. Das hier entwickelte methodische Konzept erzielt verwertbare Ergebnisse, was durch verschiedene Validierungsansätze bekräftigt werden kann.

Sowohl die Suszeptibilitätsmodellierung als auch das Rutschungsinventar zeigen, dass die höchste Wahrscheinlichkeit für das Auftreten von Rutschungen vor allem in den Gebieten mit moderater Hangneigung (< 35°) liegt, welche mit Hangschutt bedeckt sind. Diese Hangablagerungen bestehen aus Material von alten Massenbewegungen und Erosionsprozessen und zeigen eine hohe Anfälligkeit für Rutschungen. Die Ergebnisse liefern neue Erkenntnisse über die Rutschungssituation im Chiconquiaco Gebirge, da vorher das Auftreten von Rutschungen mit den steilen Hängen aus Basalt und Andesit in Verbindung gebracht wurde. Auf Grundlage der generierten Suszeptibilitätskarte ist eine bessere Bewertung der Rutschungssituation im Untersuchungsgebiet möglich. Weiterhin zeigt sie, dass es von entscheidender Bedeutung ist, spezifische Eigenschaften der jeweiligen Untersuchungsgebiete in die Modellierung miteinzubeziehen, da sonst die Gefahr besteht, dass die örtlichen Gegebenheiten fehlerhaft eingeschätzt werden.

Table of Contents

Acknowledgments ..... **I**

Abstract ..... **III**

Kurzzusammenfassung ..... **V**

Table of Contents ..... **VII**

1. Introduction **1**

2. Study area **11**

3. Methods and data **25**

3.1 Geomorphological analyses 25

3.1.1 Digital elevation model generation 25

3.1.2 Landslide mapping 33

3.1.3 DEM of Difference 35

3.1.4 Slip surface determination 37

3.1.5 Landslide volume calculation 40

3.2 Sediment analyses 43

3.2.1 Field survey 44

3.2.2 Laboratory analysis 44

3.3 Slope stability assessment 46

3.3.1 Step I – Input data generation 48

3.3.2 Step II – Validation process 51

3.3.2.1 Method of slices – Bishop's Simplified Method 52

3.3.2.2 Calculations in Slope/W 54

3.3.2.3 FoS comparison 56

3.3.3 Step III (A) - Slope stability modeling – infinite slope method 56

3.3.4 Step III (B) – Slope stability modeling – Bishop's simplified method (3D) 60

3.3.5 Step IV – Evaluation process 62

4. Results of the geomorphological analyses **63**

4.1 Geomorphological characterization of the Capulín landslide 63

4.2 Digital elevation models 66

4.2.1 Analysis of the DEM 2016 66

4.2.2 Analysis of the DEM 2013 71
4.3 Analysis of the landslides in the Chiconquiaco Mountain Range 75
4.4 DEMs of Difference (DoDs) 78
4.4.1 Analysis of the DoD 2013 78
4.4.2 Analysis of the DoD 2016 81
4.4.3 DoD of the post-event DEMs 84
4.4.4 Comparison of the DoD 2013 and DoD 2016 85
4.5 Slip surface determination for the Capulín landslide 86
4.6 The volume of the Capulín landslide 91

5. Results of the sediment analyses 95
5.1 Sediments in the Capulín landslide area 96
5.1.1 Scarp area 96
5.1.2 Eastern flank 102
5.1.3 Western flank 106
5.1.4 Slide mass 111
5.2 Sediments in the surrounding areas 116
5.3 Sediments in the Escalanar landslide area 124

6. Results of the slope stability modeling 131
6.1 Step I – Input parameter generation 131
6.2 Step II – Validation process of the input parameters 132
6.3 Step III (A) - Slope stability modeling based on infinite slope method 135
6.3.1 Input parameters for SAFETYFACTOR 135
6.3.2 Slope stability modeling with SAFETYFACTOR (infinite slope method) 139
6.4 Step III (B) - Slope stability modeling based on Bishop's simplified method 143
6.4.1 Input parameters for Scoops3D 143
6.4.2 Slope stability modeling with Scoops3D (method of slices) 145
6.5 Step IV – Comparison of the slope stability approaches 147
6.5.1 Simple SAFETYFACTOR map vs. filtered SAFETYFACTOR map 147
6.5.2 Filtered SAFETYFACTOR map vs. classified slope map 150
6.5.3 Filtered SAFETYFACTOR map vs. literature-value SAFETYFACTOR map 153
6.5.4 Scoops3D map vs. filtered SAFETYFACTOR 157

7. Discussion ... **161**
7.1 Site-specific approach ... 161
7.1.1 Classification and characterization of the Capulín landslide ... 161
7.1.1.1 Precondition and preparatory factors ... 161
7.1.1.2 Trigger ... 169
7.1.1.3 Landslide characterization and type classification ... 171
7.1.2 Methodological approaches ... 183
7.1.2.1 Digital elevation model generation ... 184
7.1.2.2 Applicability of DEMs of Difference ... 188
7.1.2.3 Slip surface determination ... 189
7.1.2.4 Landslide volume calculations ... 191
7.2 Regional landslide susceptibility assessment ... 193
7.2.1 Input data generation ... 193
7.2.2 Landslide susceptibility assessment ... 195

8. Conclusion ... **207**

References ... **211**

List of Figures ... **243**

List of Tables ... **247**

Appendix ... **249**
Appendix A ... 249
Appendix B ... 252
Appendix C ... 253
Appendix D ... 254
Appendix E ... 256
Appendix F ... 260
Appendix G ... 265
Appendix H ... 266
Appendix I ... 271
Appendix J ... 272
Appendix K ... 273

1. Introduction

Landslides are down-slope movements of material, such as rock and soil, under the influence of gravity (e.g., Varnes 1978, Cruden and Varnes 1996, Highland and Bobrowsky 2008). They are complex phenomena, which pose a global natural hazard causing thousands of fatalities each year and resulting in billions of dollars of economic losses (Kjestadt and Highland 2009, Petely 2012, Klose et al. 2014, Froude and Petely 2018, Emberson et al. 2020). However, global landslide research efforts are generally small in relation to the costs caused by landslide damage (Keefer and Larsen 2009). The processes leading to the occurrence of landslides are highly variable and are distinguished in 'causes' and 'triggers' (e.g. Varnes 1978, Wieczorek 1996, Lu and Godt 2013). 'Causes' or 'disposition factors' comprise precondition (e.g. steep inclined slopes) and preparatory factors (e.g. weathering or deforestation), while 'triggers' usually are represented by single events, such as intensive rainfall, volcanic eruption or earthquakes leading to the initiation of motion (e.g. Wieczorek 1996, Prinz and Strauß 2011, Lu and Godt 2013). Landslides record a wide spectrum of velocities, ranging from extremely rapid (> 5 m/sec) to extremely slow (< 16 mm/year) (Cruden and Varnes 1996). Furthermore, they are differentiated regarding their activity state. The distinction is made between 'active' (where the landslide is presently moving), 'suspended' (meaning the landslide has moved in the last 12 month but is not currently active), reactivated (describing a landslide, which is active after an inactive phase), and inactive processes. Whereas latter can comprise dormant (where the causes remain and a reactivation could be possible), stabilized (describing landslide situations, where the causes have been changed, e.g. through artificial measures), abandoned (where the original causes do no longer affect the inactive landslide), and relict (development of the landslides occurred under different environmental conditions) states (Varnes 1978, WP/WLI 1993, Cruden and Varnes 1996).

In general, the term landslide includes all types of gravitational mass movements, which can be distinguished in different process types, such as falls, topples, spreads, flows, and slides (for further details on landslide classification see e.g. Cruden and Varnes 1996, Hungr et al. 2014). The combined occurrence of two or more types is indicated by using several types combined, e.g. rotational slide-flow (Varnes 1978, Cruden and Varnes 1996, Hungr et al. 2014). An overview of the sliding properties is given in the following as the

focus of this study lies on sliding processes in particular and, furthermore, the terms 'landslide' and 'slide' ('sliding processes') will be used synonymously in this thesis.

The main features of a landslide are divided into areas of erosion or depletion and accumulation, and consist of main scarp, flanks, main body, rupture surface (here also referred to as slip surface), landslide foot, and toe (Figure 1-1). Based on the slip surface sliding processes can further be divided into rotational and translational slides (e.g. Varnes 1978, WP/WLI 1990, Cruden and Varnes 1996, Hungr et al. 2014).

A concavely curved slip surface and an approximately rotational movement about an axis parallel to the slope characterize rotational landslides (Figure 1-1). Usually, the slip surface has a depth (max. thickness of slide) to length (max. length of rupture surface) ratio between 0.15 and 0.33 (Skempton and Hutchinson 1969, Varnes 1978, Cruden and Varnes 1996, Highland and Bobrowsky 2008). Most commonly, they occur in relatively homogenous materials. The upper part of the displaced material typically is tilted backwards toward the scarp and occasionally small ponds can develop in this area. Reactivation processes are not uncommon, especially in cases where the drainage system of the slope is substantially disrupted. In case of a relatively constant motion, the slide mass can move as a coherent mass with small internal deformation. Movement rates range between few centimeters per year and several meters per week (Varnes 1978, Cruden and Varnes 1996, Highland and Bobrowsky 2008).

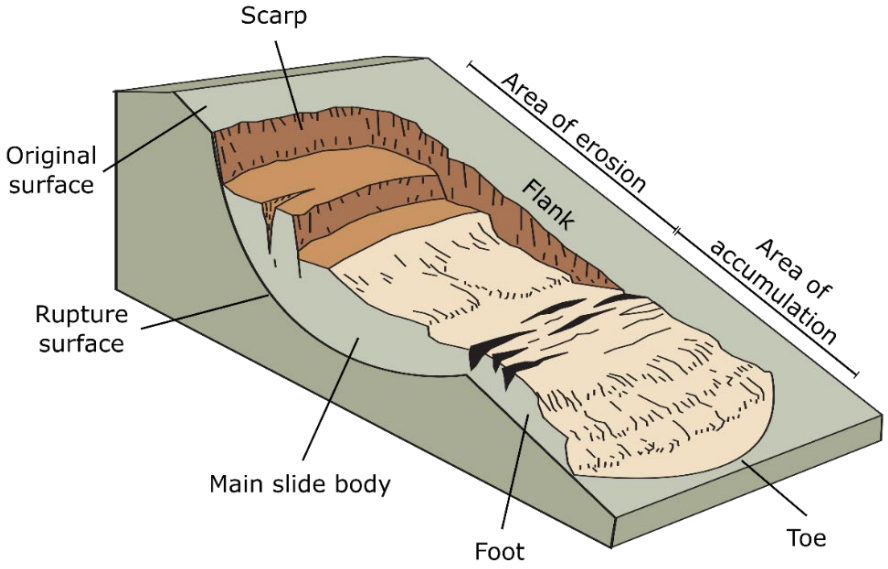

Figure 1-1. Schematic of a rotational slide showing the main features of a landslide. Source: Modified after Cruden and Varnes (1996), Highland and Bobrowsky (2008).

Translational landslides move along a fairly planar surface, with a slip surface nearly parallel to the slope (Figure 1-2, Skempton and Hutchinson 1969, Highland and Bobrowsky 2008). Generally, these slides occur along discontinuities, such as faults, bedding surfaces or the contact between bedrock and overlying debris. The depth to length ratio of the slip surface is normally under 0.1 and the slide mass usually exhibits relatively small deformations (Skempton and Hutchinson 1969, Varnes 1978, Cruden and Varnes 1996). Globally, translation movements represent the most common landslide type and their magnitude ranges from very small local slides to regional distribution with width of several kilometers. Movement rates can vary widely ranging between few centimeters per year and several meters per day (Highland and Bobrowsky 2008). They can further be distinguished into block- and slab slides, where block slides mainly occur in relatively hard in-situ material, while slab slides typically occur in weathered or colluvial material moving as one single unit (Skempton and Hutchinson 1969, Varnes 1978, Cruden and Varnes 1996). Stabilization of translation processes is very difficult and reactivation processes or repeated occurrences are highly likely (Highland and Bobrowsky 2008). Landslides recording both, translational- and rotational characteristics, thus are formed by a combination of planar and curved elements, are defined as compound slides (Skempton and Hutchinson 1969, Cruden and Varnes 1996). The primary triggering factors for both sliding processes are intense rainfall, increase in ground water levels due to e.g. snowmelt, flooding, or filling of reservoirs as well as earthquakes (Highland and Bobrowsky 2008).

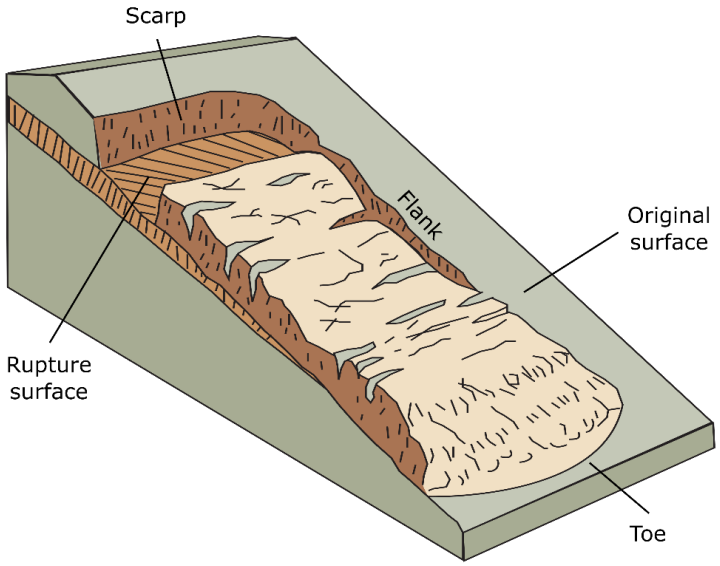

Figure 1-2. Schematic of a translational slide showing the main features. Source: Modified after Cruden and Varnes (1996), Highland and Bobrowsky (2008).

The creation of susceptibility maps allows for the determination of landslide occurrence by dividing a region into zones with differing probabilities of landslide occurrence (e.g. Brabb 1991, Guzzetti et al. 1999, Corominas et al. 2014, Shano et al. 2020). Landslide susceptibility can be assed by qualitative (knowledge-driven and inventory based methods) or quantitative methods (such as physically based slope stability approaches and data-driven methods), whereas physically based approaches express landslide susceptibility as the probability of slope failure or as Factor of Safety (e.g. Soeters and Van Westen 1996, Aleotti and Chowdhury 1999, Corominas et al. 2014). It is important to note that susceptibility maps, unlike hazard maps, do not provide any information on temporal occurrence of landslides (Soeters and Van Westen 1996, Aleotti and Chowdhury 1999, Corominas et al. 2014).

The diversity of disposition factors and triggers as well as the wide range of processes makes landslide investigations a challenging task and in order to address these multiple factors a variety of different analysis methods is required. Consequently, the current focus in landslide research is on the application of multiple methods from different scientific disciplines such as engineering, geography, and geology. To enhance the understanding of landslides it is crucial to characterize the surface and subsurface conditions of such processes. On this matter, the combination of digital elevation models (DEMs) and geophysical analyses has proven to be very effective (e.g. Bichler et al. 2004, Ausilio and Zimmaro 2017, Mreyen et al. 2018, Bentivenga et al. 2019). Geophysical methods together with sediment- and geomorphological analyses enable to determine landslide features such as volume or slip surface location and can be used to construct three-dimensional models of landslides (e.g. Bichler et al. 2004, Brückl et al. 2006, de Bari et al. 2011, Soto et al. 2017). To characterize landslide materials, borehole analyses can further complement geophysical and geomorphological surveys and DEMs from different time periods additionally allow for the identification of areas of erosion and accumulation (e.g. de Bari et al. 2011, Tomás et al. 2018, Buša et al. 2020, Samodra et al. 2020, Perrone et al. 2021). Moreover, in order to monitor active landslides these methods can be extended by inclinometer measurements (e.g. Ling et al. 2016, Nikolakopoulos et al. 2017).

Besides characterizing and monitoring landslide features, the application of multiple methods builds the base for susceptibility assessment as well. Field- and laboratory analyses have proven to be crucial for slope stability modeling and are further supported by geophysical analyses (e.g. Fall et al. 2006, Federici et al. 2007, Thiery et al. 2017).

Currently, the goal is to take one step beyond susceptibility modeling towards early warning systems for landslides. One promising approach is the combination of susceptibility models with investigations on rainfall thresholds (Formetta et al. 2014, Weidner et al. 2019). However, the key here are detailed and reliable susceptibility maps and detailed threshold information, which in most cases are still unavailable.

Landslide situation in Mexico: Mexico is highly affected by various natural hazards, due to its unique composition of topographic, geological, and climatic factors (Domínguez Morales et al. 2016). The occurring hazards comprise e.g. volcanic and seismic activity, storm events, floods, and landslides. Latter phenomena caused over 3,400 deaths between 1935 and 2017 (Alcántara-Ayala 2008, Díaz et al. 2020). During this time period, almost 3,000 gravitational mass movements were registered, from which 1,967 were sliding processes. In the year of 2019 alone, landslides affected over 1,400,000 people. The main triggers are related to hydro-meteorological factors like storms and rainfalls, whereas earthquakes play a minor role (Alcántara-Ayala 2004, Díaz et al. 2020). Overall, the expectation is that these triggers will even increase due to climate change (e.g. Schroth et al. 2009, Gariano and Guzzetti 2016). The states with the most landslide events are Chiapas (726), Oaxaca (353), Veracruz (260), Michoacán (194), and Puebla (173). The landslides are mainly located in the mountainous areas of Mexico, whereas a concentration can be observed along the Trans-Mexican-Volcanic Belt (Figure 1-3, Díaz et al. 2020).

One of the most devastating events was the landslide in La Paz (Baja California) in 1976, which caused 1,000 casualties (Alcántara-Ayala 2008). The landslide at San Juan Grijalva (Chiapas) from 2007 represents another devastating event, which different research groups analyzed (e.g. Hernández-Madrigal et al. 2011, Hinojosa-Corona et al. 2011).

Investigations on landslides in Chiapas were carried out by e.g. Mendoza-Rosas and De la Cruz-Reyna (2010) and Sánchez-Núñez et al. (2012) focusing on hazard analyses. Capra et al. (2003, 2007), Alcántara-Ayala (2004) and Borja-Baeza et al. (2006) conducted further hazard assessments in the state of Puebla. Flores and Alcántara-Ayala (2012) investigated susceptibility regarding shallow landslides in the state of Mexico.

As the interference in landslide-prone areas increases, further research focuses on the progression of demographic pressure and land use change (Alcántara-Ayala et al. 2006, Restrepo and Alvarez 2006, Alcántara-Ayala and Dykes 2010). Moreover, enhanced

research activity can be observed related to the volcano Pico de Orizaba, which was subject of numerous investigations focusing on landslide mapping and hazard analyses (Concha-Dimas et al. 2005, Hubbard et al. 2007, Legorreta Paulín and Lugo Hubp 2013, Legorreta Paulín et al. 2014a, 2015).

Guzmán Lagunes and Morales Barrera (2014), who investigated numerous landslides that occurred in 2013, carried out landslide research in the state of Veracruz. In their work, they focused on analyzing the triggers and on documenting the major events, including the related damages. Another important study in Veracruz was conducted by Rodríguez Elizarrarás and Morales Barrera (2011), who analyzed the geological hazards in Veracruz, and prepared a hazard map for the entire state (at a scale of 1 : 700,000).

Although, numerous investigations on landslides in Mexico exist, the authorities mainly focus on reactive measures rather than investing in preventive approaches. One example for measures that takes place after an event occurred is the relocation of the affected population. In Veracruz, twelve communities were relocated, whereas only two of them were permanent, leaving the remaining communities still at risk (Díaz et al. 2020).

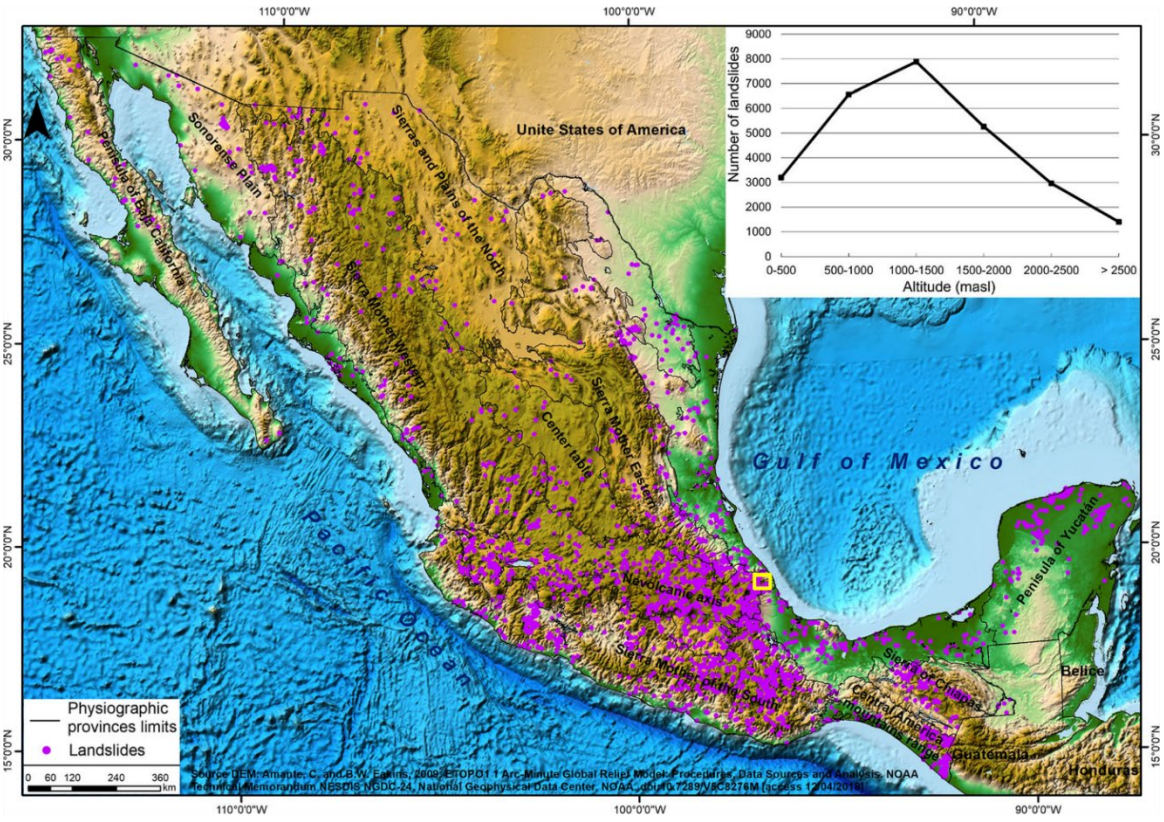

Figure 1-3: Landslide distribution in Mexico. Study area marked in yellow. Source: Modified after Díaz et al. (2020).

This shows that preventive measures are crucial in order to address the landslide hazard in Mexico and therefore, the overall objective of this study is to assess the landslide susceptibility for a region in the Chiconquiaco Mountain Range, located in the center of the state of Veracruz (regional approach). This region records a high landslide activity and was strongly affected in the year of 2013, when numerous landslides occurred due to extreme precipitation events, causing enormous damages and resulting in the need for evacuation measures (Guzmán Lagunes and Morales Barrera 2014).

The detailed understanding of landslide susceptibility demands for in-depth knowledge of disposition factors and processes, which thus, functions as base for slope stability modeling. In this study, the landslide susceptibility analysis is conducted by combining a detailed local study (goal I) with a broader regional approach (goal II and III). In order to achieve this overall objective the following (sub) objectives are defined (Figure 1-4):

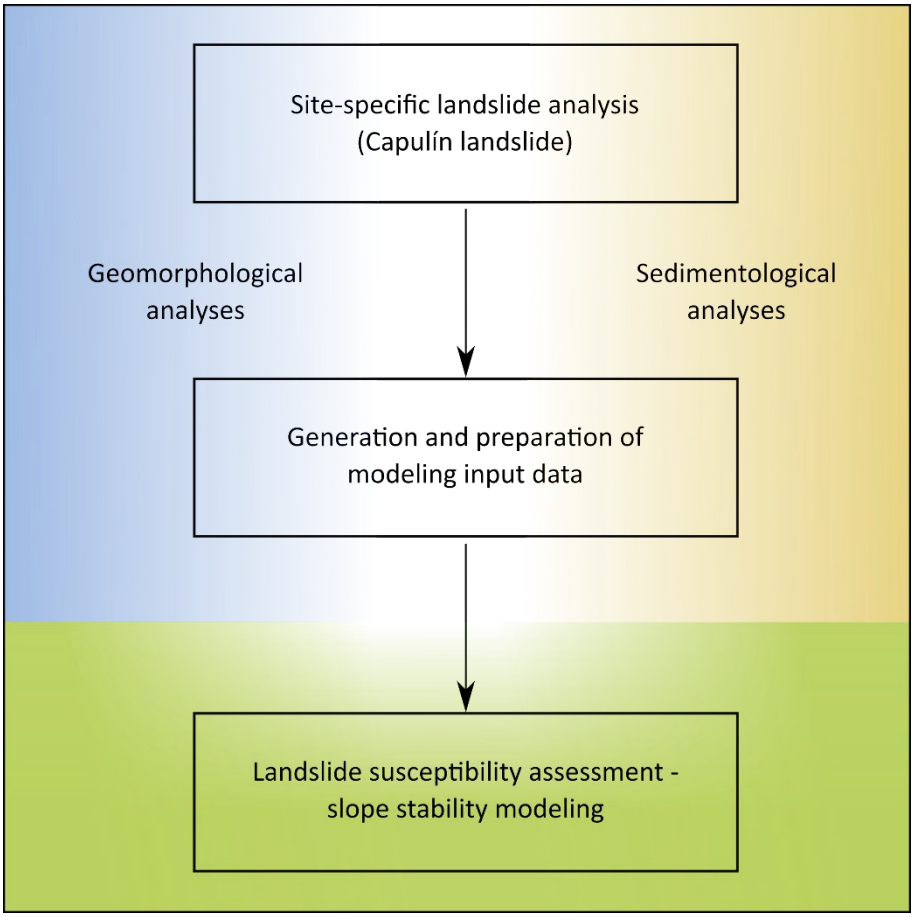

Figure 1-4: Summary of the goals and working steps of this study. Source: Own illustration.

(I) Site-specific landslide analysis: The first goal is to obtain profound knowledge of the disposition and preparatory factors as well as landslide processes and therefore, a case study is established, which forms the base for a variety of geomorphological and sedimentological analyses. The objective in this site-specific approach further is to identify the potential of these different methods to acquire input parameters for slope stability modeling. For the geomorphological analyses of the landslide, post-event digital elevation models (DEMs) are generated and compared to a pre-event DEM, by establishing DEM of Differences (DoD). Moreover, the goal is to evaluate the potential of these generated DEMs and the DoDs to improve the understanding of the landslide characteristics. The investigations on the slip surface further aim to contribute to the process understanding of the landslide. For further characterization of the landslide, the volume is calculated. Here, the goal is to evaluate the strength and weaknesses of different calculation approaches. An additional objective is to characterize the landslides situation in the study area. For that reason, a landslide inventory is composed, which simultaneously forms the basis for the validation of the upcoming susceptibility maps.

Furthermore, sediment analyses contribute to a better understanding of the landslide as they can provide valuable information on sediment provenance and their characteristics. It is the goal to evaluate how the sedimentological investigations in combination with the geomorphological analyses can improve the process understanding. In addition, the sediment data ought to be applied in the susceptibility modeling approach.

For this site-specific analysis, the Capulín landslide is selected. It represents the largest landslide event of the recent years (year of occurrence 2013) in this area. Additionally this landslide destroyed an important connecting road and caused major damages on numerous houses. As a consequence, over ten houses were no longer habitable and had to be permanently relocated. A reactivation and extension of the Capulín landslide could cause even more damage as it is located close to the El Capulín village and thus, would affected houses and infrastructure of the village. Moreover, the road, connecting the villages El Capulín and La Sombra was rebuild cutting through the landslides mass, which makes it highly vulnerable towards even small movements within the landslide area.

(II) Integrated approach to generate input data for slope stability modeling: In general, high data coverage for larger regions is not commonly available as comprehensive data acquisition

involves considerable time and expenses. However, oftentimes some spatially limited data or case studies are more frequently available. In order to reduce the dependence on comprehensive data sets, the focus of this study is to develop and evaluate the potential of a slope stability modeling approach, which requires only few input data and calculates the majority of the input data. Here, the goal is to incorporate the results of the case study, on the one hand, as input parameters (with the focus on the geomorphological data) and, on the other hand, for validation (mostly using the sedimentological data). In a next step, the objective is to evaluate this procedure. Hence, a slope stability model with a different theoretical background is integrated to validate the input parameter calculation results.

(III) Landslide susceptibility assessment: The main objective of this regional approach is to conduct slope stability analyses in order to assess the landslide susceptibility in the Chiconquiaco Mountain Range area. Therefore, the goal is to prepare the generated input data in such a way that allows for transferring the local case study to a larger area and to simultaneously investigate the potential of this approach. Furthermore, two models with different theoretical backgrounds are selected for calculating the slope stability in the study area. Each model contains its limitations and thus, the goal is to evaluate their strengths and possible shortcomings, especially with regard to the study area. For this purpose, the mapped landslides are used to review the resulting susceptibility maps and a comparison of the resulting maps is aspired.

2. Study area

The study area comprises 23 km² and is located in the municipality of Chiconquiaco, in the central part of the state of Veracruz, Mexico, approx. 250 km east of Mexico City. The Capulín landslide is situated within the study area close to the villages of El Escalanar and El Capulín approx. 30 km to the Gulf of Mexico (Figure 2-1).

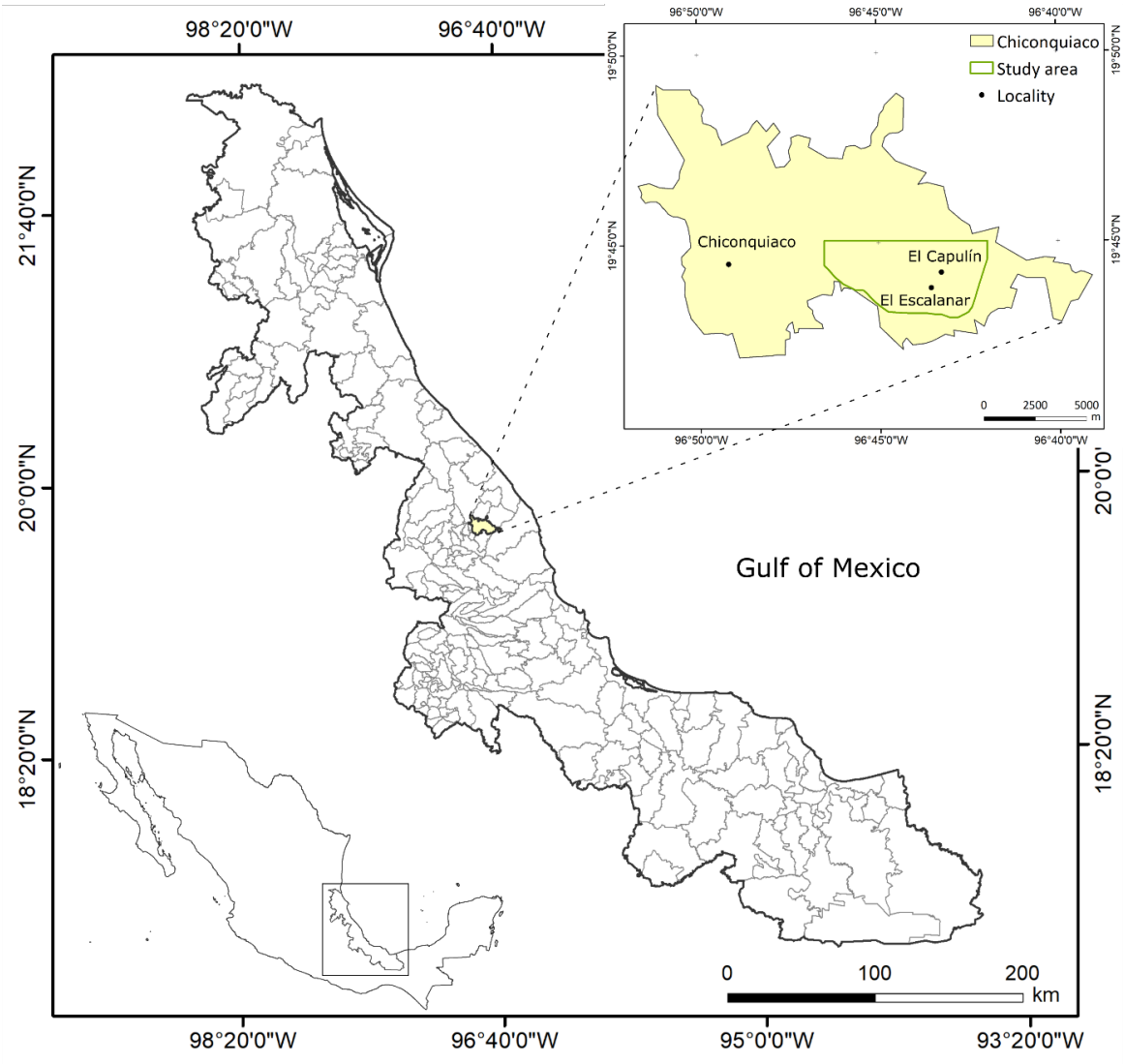

Figure 2-1. Position of the study area (marked in green) within the municipality of Chiconquiaco, Veracruz (Mexico). Source: INEGI (2020a).

Geology: One of the most decisive factors for the natural characterization of the study area is it distinctive geology. In this regard, Mexico is located at one of the world´s most complex plate tectonic situations, where four major lithospheric plates (North America, Pacific, Cocos, and Caribbean plate) interact (Clayton et al. 2004).

Due to the complex plate tectonic situation, Mexico can be subdivided into 17 tectonostratigraphic terranes (Sedlock et al. 1993). One of these is the Trans-Mexican-Volcanic Belt (TMVB), where the study area is located in. The TMVB is an approx. 1000 km long volcanic arc, which crosses the Mexican mainland from Puerto Vallarta in the east, over Guadalajara and Mexico City to Xalapa in the west (Ferrari et al. 2012). The TMVB itself is the product of subduction along the Middle American trench and therefore, strongly influenced by shallow seismic activities, which occur at about the same time as the volcanic activities within the belt (Suter et al. 2001). The oldest rocks related to the phase of effusive volcanism date about 22 My ago (Ferrari et al. 2012). The high magmatic variability in the TMVB is the product of a variety of different factors, which interfere with each other. Most of those originate from the fact that two different oceanic plates with different compositional and geophysical characteristics are subduced here.

The local continental crust reveals a number of different ages, thicknesses and compositions and thus has very different influences on the magmatic differentiation of the ascending melts (Gómez-Tuena et al. 2007). Despite the high volcano-density in this belt these magmas tend to develop stratovolcanoes when they reach the (near-) surface crustal zone. Since this time, post-volcanic gravitational processes shape the landscape in a substantial way (Varley 2019). Consequently, a fine interweaving of volcanic rocks, volcanoclastic deposits, and the background sedimentation characterizes the local geology.

The study area is located in the easternmost part of the TMVB 20 km northeast of Xalapa (Figure 2-2). The local geology is dominated by carbonaceous clastic sediments of Paleocene to Quaternary age as well as basaltic to andesitic rocks. These volcanic rocks can be subdivided into a subduction related calc-alkaline suite and alkaline volcanic rocks. The calc-alkaline suite is the driving force behind cinder cones and shield volcanos, whereas alkaline volcanic rocks are associated to 1-10 m thick basalt plateaus (Figure 2-3; Gómez-Tuena et al. 2003). Around the study area the latter show a close spatial association to a Cretaceous NW-SE-orientated thrust fault, which is covered by above-mentioned sediments of the Veracruz Basin (Lopez-Infanzon 1991). The youngest geological deposits consist of talus sediments (also referred to as slope deposits), which cover most of the study area. A common characteristic feature is their poorly sorted grain size with boulders up to 10 m in diameter (Figure 2-4). Their likewise poor grain roundness testifies for the short transport distance and the close spatial association to the source rock. Outcrops of

sandstone and shale, which belong to the Tertiary terrigenous sequence, can be observed in the study area as well (Wilde et al. 2017a). The volcanic rocks surround the study area causing a north-opened U-shaped mountain range, which concentrates the sedimentary material in the center of the study area.

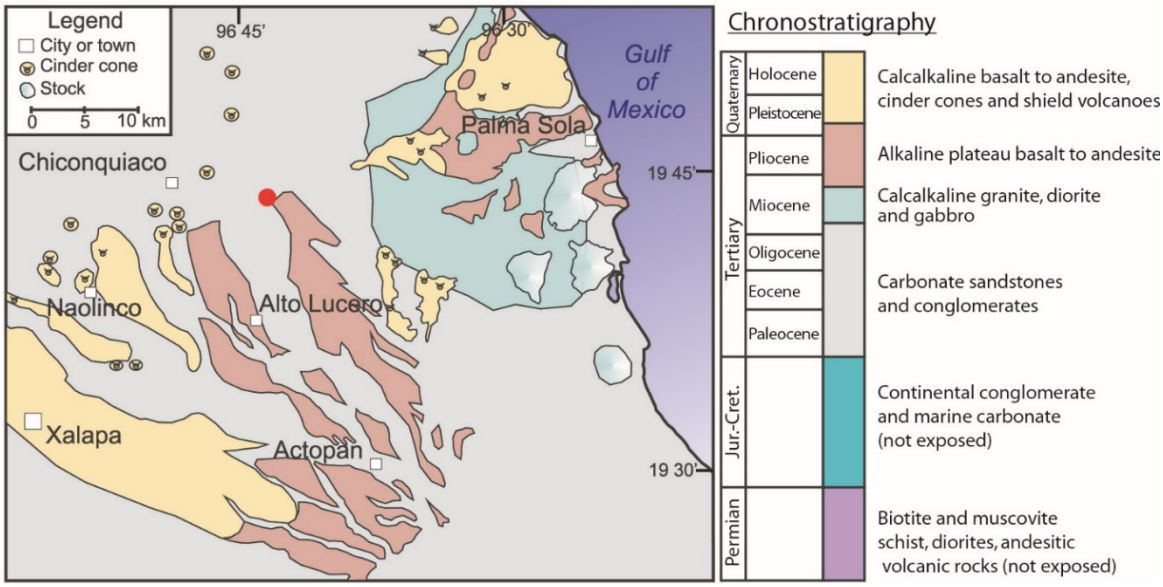

Figure 2-2. Litho- and chronostratigraphic map of the easternmost Trans-Mexican Volcanic Belt. Study area marked in red. Source: Modified after Gómez-Tuena et al. (2003).

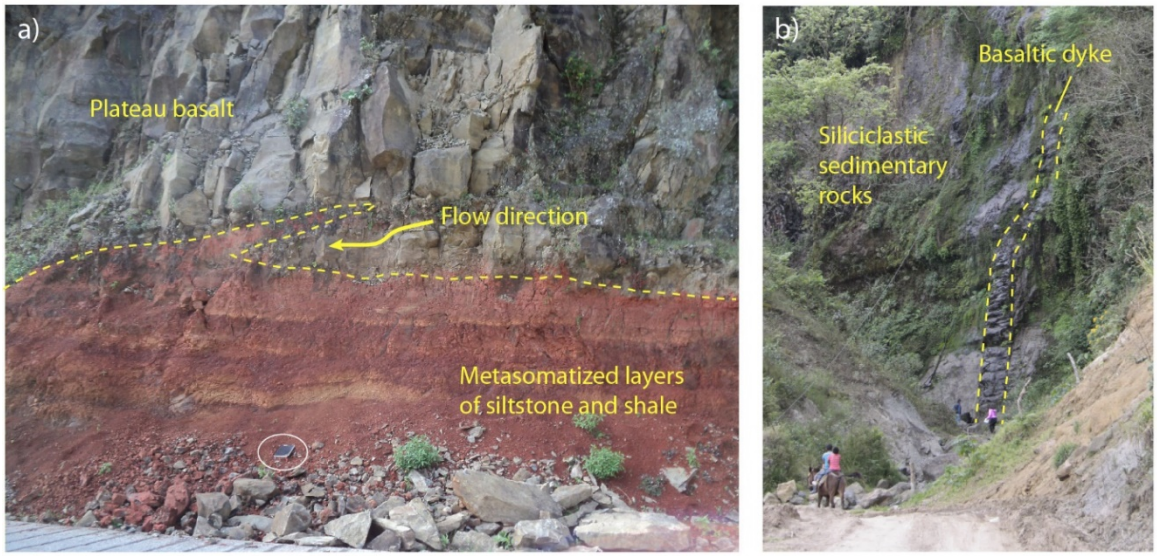

Figure 2-3. Characteristic occurrences of mafic volcanic rocks in the study area. a) Footwall of a plateau basalt approx. 500 m west of El Capulín. In the center of the picture, there is a basaltic lava flow intruding into the layered sedimentary rocks. b) Basaltic dyke cutting though sedimentary rocks in the east of El Capulín. Source: Own photographs.

Figure 2-4. Basaltic dominated talus below a plateau basalt outcrop in the east of El Capulín. Source: Own photograph.

Climate: Together with the spatial distribution of geological units, the atmospheric influences represent the first-order natural factors affecting the study area. In general, the climate of Mexico can be divided in two major parts. Characteristic for the North are its aridic conditions in combination with generally low latitudes. Thus, wide areas, especially at the border to the United States of America are classified according to Köppen as desert (arid) or steppe (semiarid) (Bruster-Flores et al. 2019). Different temperature conditions between the Western Sierra Madre with its up to 3000 m heights and the coastal lowlands, including the Sonora and Chihuahua desert cause a further climatic subdivision between hot and cold deserts and steppes, respectively. The South of Mexico, below approx. 22° north, is characterized by tropical climates. Most of the western and eastern coastlines are dominated by tropical savannahs with cold winters. Only towards the Central Mexican Plateau with its high elevations, there is a transition to mild temperate, humid climate conditions (Pineda-Martinez and Carbajal 2017, Bruster-Flores et al. 2019).

The region around Veracruz at the Gulf of México is one of the most complex climatic regions in Mexico due to its close association with the coastline and the high elevation differences. Characteristic for the area are the strong trades and tropical cyclones in summer and fall (Giddings et al. 2005).

The meteorological station closest to the study area is Acatlán approx. 10 km in the southwest of El Capulín (Figure 2-10). Here the annual mean temperature is 15.3 °C. The

month with the lowest mean temperature is January with 12.2 °C, whereas May is the warmest month with 17.7 °C. Compared to those only minor temperature differences, the precipitation rates are highly variable. With 252 mm the mean precipitation value for the wettest month, September, is nearly ten times higher than that of the driest month March (36 mm) (Figure 2-5; SMN 2020a).

Beyond that, Mexico's climate is heavily influenced by hurricanes. While most adjacent countries have one coastline to the Atlantic or Pacific Ocean with high hurricane risk, Mexico has two. Therefore, hurricanes and tropical storms provide a significant amount of Mexico's moisture by precipitation. The orographic lifting by the Sierra Madre and the TMVB further intensify the rainfalls in those areas and cause a strong concentration of precipitation on the coastal areas (Jáuregui 2003). From a large-area perspective, the year 2013 was the most calm hurricane year since 1994. Not a single hurricane and only one tropical storm made landfall in the USA, which is well below average. Nevertheless, Mexico was hit hard by several tropical storms and hurricanes (e.g. Barry, Fernand, Ingrid; Figure 2-6), which caused very high precipitation followed by devastating floods with more than 50 casualties (Blake 2014).

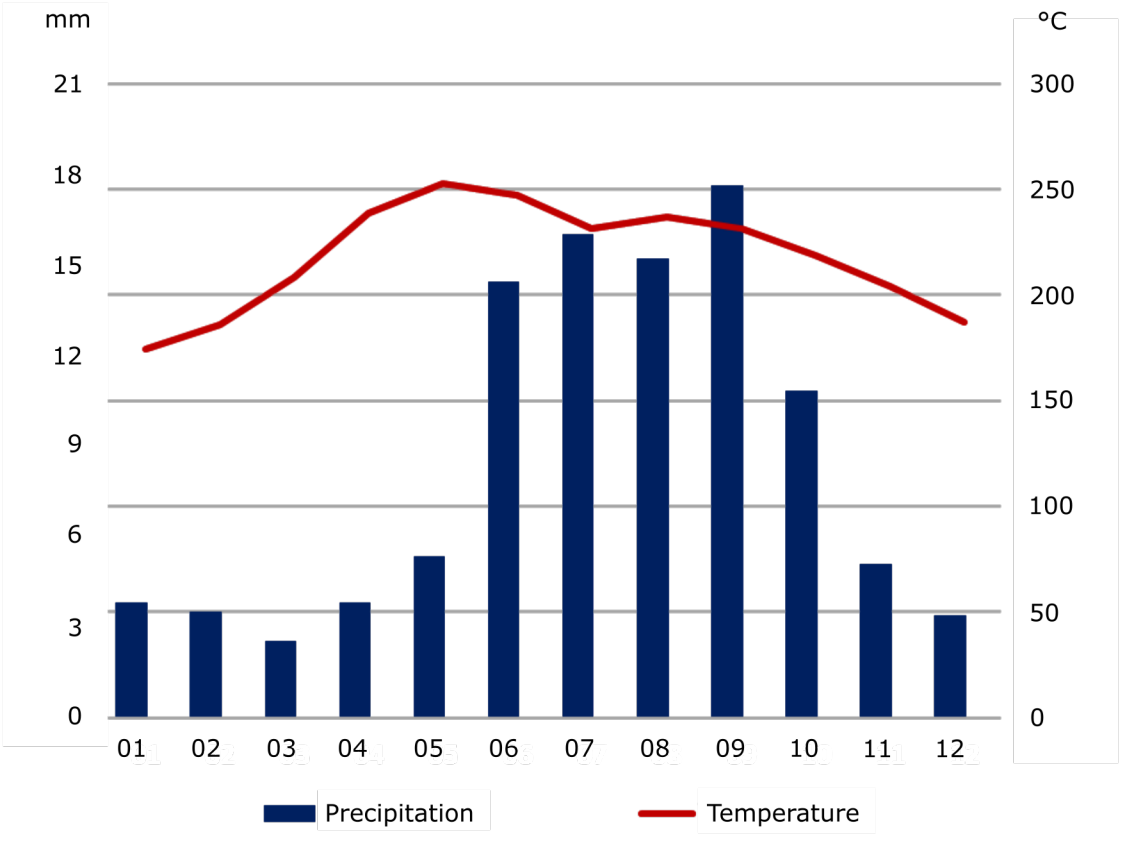

Figure 2-5. Mean monthly temperature and precipitation at Acatlán. Source: SMN (2020a).

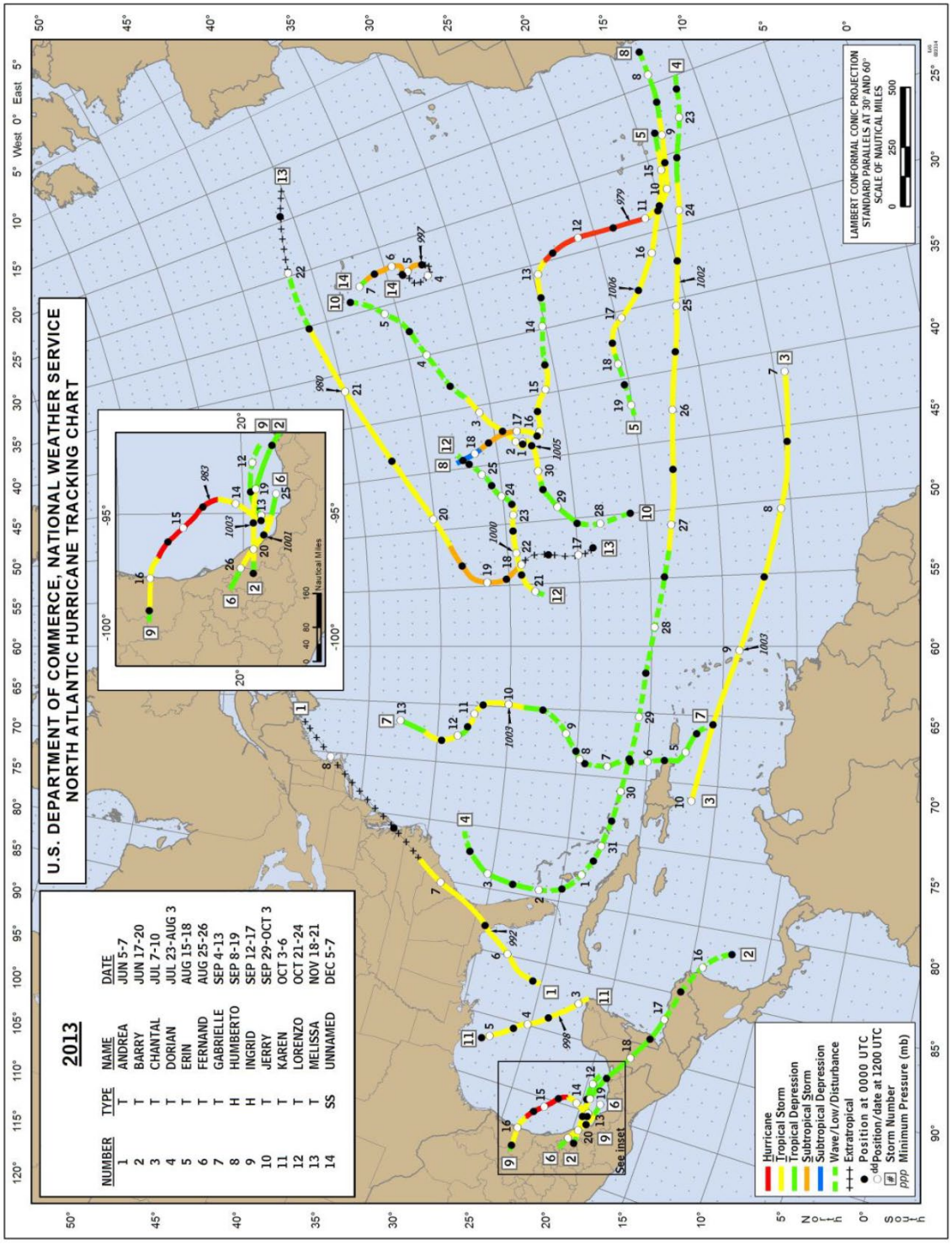

Figure 2-6. Tracks of hurricanes, tropical and subtropical storms during the 2013 Atlantic Ocean hurricane season. Source: Blake (2014).

The spatial distribution of precipitation in September 2013 (Figure 2-7a) reflects this concentration of tropical storms approaching from the Atlantic Ocean. The comparison with the mean precipitation from the September months 1971-2000 (Figure 2-7b, c) shows

that even for an area, which is regularly affected by tropical storms, the values in 2013 were extraordinarily high. The state of Veracruz is amongst the most affected areas. Here especially the hurricane Ingrid had a high local impact because of its unusual track. Affected by a mid/upper-level trough over northeastern Mexico it made a cyclonic loop approx. 160 km east of Veracruz on September 13th. For the next two days, the cyclone further increased its strength bringing the highest precipitations to Veracruz, Tabasco and Tamaulipas. Tuxpan (Veracruz) reported more than 560 mm precipitation from the 11th to 20th of September 2013 (Blake 2014). These high-moisture conditions caused a high number of floods and landslides. Among the latter, there was the Capulín landslide. This is of particular importance because more recent climatological studies in fact projected lower numbers of tropical cyclones, but an increase in their maximum intensity and in the cyclone-related rainfall (Walsh et al. 2019).

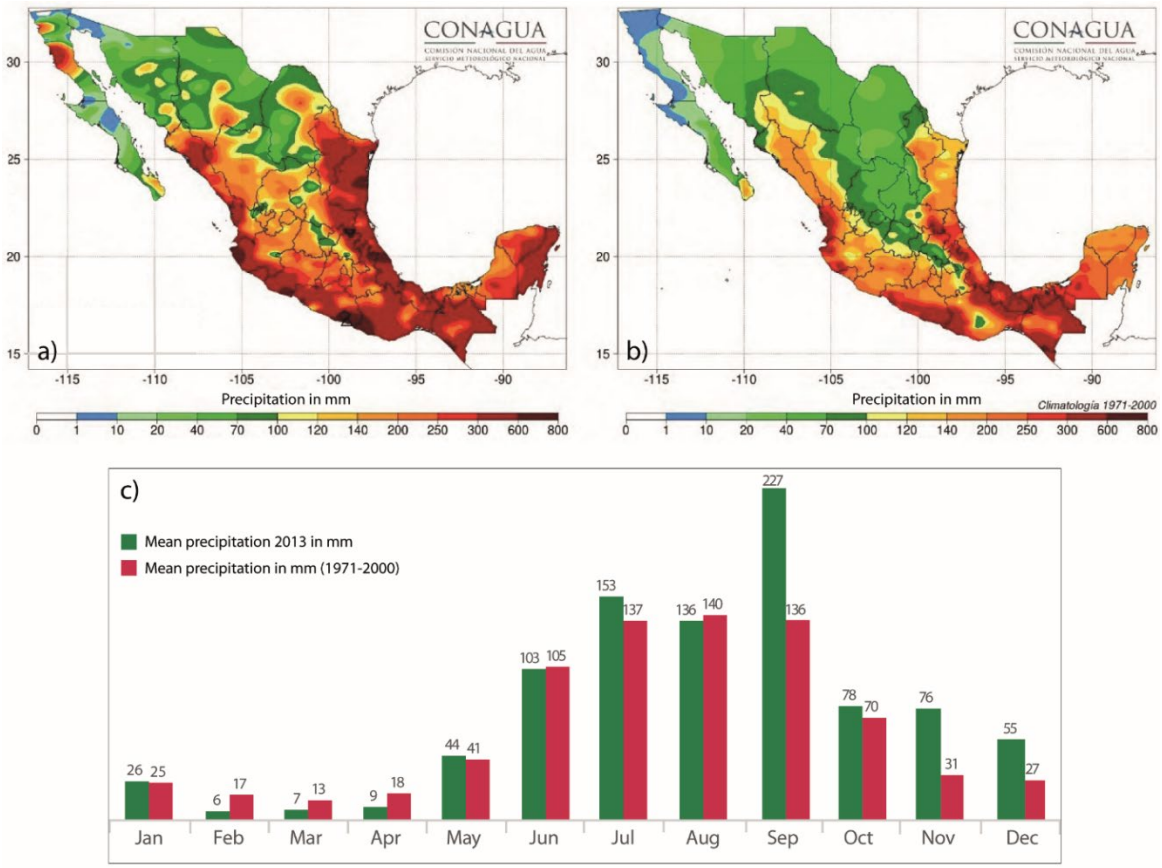

Figure 2-7. a) Mean precipitation in September 2013 in Mexico. Source: Modified after Ramírez (2013). b) Mean precipitation of all Septembers from 1971 to 2000. Source: Modified after Ramírez (2013). c) Direct comparison between the monthly precipitations in Mexico. Source: Del Carmen Velázquez Simental (2014).

Soils: The chemical and physical interaction of atmosphere, lithosphere and hydrosphere causes the development of soil. In general, the most important factors for is development and all its characteristics are moisture, temperature and biological activity (Díaz et al. 2019). While the latter is strongly depending on the first two factors, those are completely independent from each other. For Mexico, this means that because of its large variety of topographic and climatic factors it has a very high diversity in soils (Krasilnikov et al. 2013).

On the basis of calculated evapotranspiration and insolation hours per day Díaz et al. (2019) determined soil moisture regimes for all of Mexico. Those regimes show a dominance of aridic soil regimes in Northern Mexico, whereas the South records moisture regimes that are predominantly associated with subhumid climates (Díaz et al. 2019).

Even though the temperatures vary from subtropic in the North to tropic in the South, the latitudinal temperature gradient is only of minor importance for the soil development (Krasilnikov et al. 2013). In contrast, the altitude causes a vertical zonality from hot and wet at the coasts to cool and dry in the higher altitude inland areas (Figure 2-8; Krasilnikov et al. 2013).

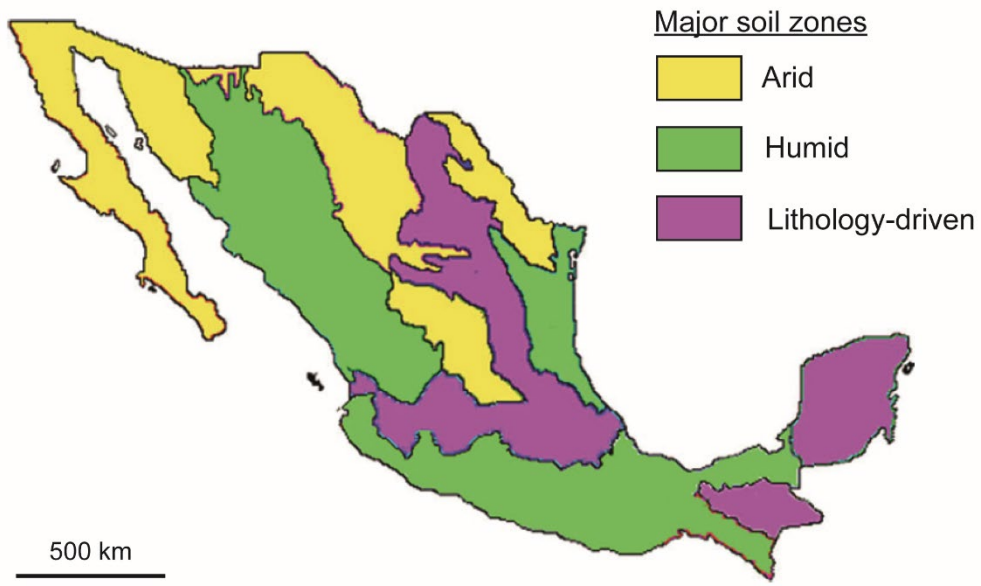

Figure 2-8. The three major soil zones of Mexico. Source: Modified after Krasilnikov et al. (2013).

In general, soil formation, which is driven by the mentioned factors transforms (near-) surface materials of any kind (minerals, plants etc.) into materials, which are in equilibrium with their (near-) surface environmental conditions (Dixon 2015). Therefore, the lithological variability is another crucial factor, which influences the spatial

distribution of soil types, especially in Mexico. For most clastic sedimentary rocks, the transformation of the non-soluble parts is not associated with major mineralogical changes. In contrast, the young volcanic rocks of the TMVB reveal a much higher mineralogical diversity with a high portion of minerals, which are unstable under (near-) surface environmental conditions. The weathering of these rock types and magmatogenic minerals provide different chemical and physical conditions, which prepare the ground for very diverse soil developments. Other lithology-driven areas are the Sierra Madre Occidental and Yucatan, where extensive limestone occurrence provides specific parent material, which affects pedogenesis more than the climate does (Figure 2-8; Krasilnikov et al. 2013).

The study area is located within the easternmost part of the TMVB, which means soil development is predominantly taking place on basalt and carbonaceous sedimentary rocks. Soil, on the basis of the latter lithology is predominately luvisol, which is characterized by its lessivation, which causes clay-enrichment in the Bt horizon. Yet, its appearance is spatially related to the coastal plain approx. 5 km in the northwest of the study area. Soil formation on basaltic and andesitic rocks, which dominate the study area itself, primarily involves the formation of clay minerals at the expense of the volcanic mineral paragenesis (Heidari and Raheb 2020). The driving force behind this process is the leaching of the cations (Ca^{2+}, Mg^{2+} and Na^{2+}), which go into pore-water solution and are easily drained. The neo-formed minerals reveal a poor crystallinity and an enrichment in Si^{4+}, Al^{3+} and Fe^{3+} (Rasmussen et al. 2010). Depending on the small-scale manifestation of the previously mentioned factors different soil types can develop. On volcanic material, the high nutrition supply accompanied by fast growing vegetation causes an initial accumulation of organic matter in the topsoil, which in turn leads to the formation of phaeozems. In narrow valleys, the combination of less insolation, high moisture levels and high amounts of volcanic glass supports the crystallization of montmorillonite and the formation of vertisols (Krasilnikov et al. 2013). Most of the study area is characterized by moist and warm conditions, and high biogenic activity. In the soil development, these factors cause an additional desilication, which reduces silicon abundance within the soil. The hydrolysis-driven decomposition of primary minerals and glasses causes the crystallization of paracrystalline allophan, imogolite, hisingerite, which is the characteristic feature of andosols (Figure 2-9; Zech and Hintermaier-Erhard 2002). Other soil types like Podzol host those minerals as well, but to a much lesser extent (Nanzyo et al. 2007).

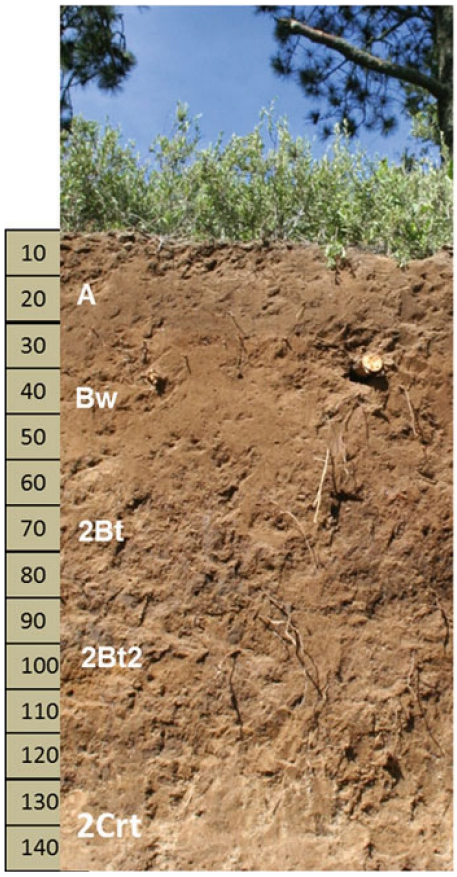

Figure 2-9. Andosol from Tlaxcala state. Source: Krasilnikov et al. (2013).

The most valuable characteristic feature of andosol is its ability to retain water for weeks and month after rainfall, which makes it a valuable resource. Andosol dominates large areas of Veracruz and especially near El Capulín and is agriculturally used for the cultivation of coffee and sugarcane (Krasilnikov et al. 2013).

Geomorphology: The geomorphology of the study area and its vicinity is strongly interacting with all other natural factors such as vegetation, hydrology, and soil development. In Veracruz, even more than in other places, the magnitude of relief determines the ecological characteristics and defines the way for further morphological developments (Renschler et al. 2007, García-Aguirre et al. 2010).

As a consequence of its position at the fluent transition between the coastal zone in the east and the volcanic province of the TMVB in the west the Chiconquiaco Mountain Range (Lascurain-Rangel et al. 2017), which hosts the study area, reveals a high diversity of geomorphological features (Lugo Hubp and Córdova 1991). The main driving forces for the development of relief are the various erosion and denudation processes in

combination with differences in the weathering resistance of the underlying lithologies. For the study area, the young Neogene age of the TMVB (Ferrari et al. 2012) causes relative steep slopes compared to all other lithologies. This is mainly because of the high weathering resistance of its volcanic rocks (e.g. basalt, andesite and tuff), which stand out amongst the lithologies with lower weathering resistance like the Tertiary carbonate-rich sandstones and conglomerates. Even though the TMVB can be regarded a relative young geomorphological feature in Mexico the mafic volcanic rocks in the vicinity of the study area reveal the highest ages within the TMVB (Miocene age of 16 - 11 Ma; Mori et al. 2007). As a consequence, there is also a high number of less steep slopes. Nevertheless, most of the slopes within the study area can be characterized as steep (20 - 45°) or abrupt (> 45°) (Figure 2-10; Lascurain-Rangel et al. 2017). Furthermore, the altitudes range between 1,900 and 1,100 m a.s.l. (INEGI 2019). To the east, this high elevation level decreases towards the coastal area with low altitudes. The geomorphology there is dominated by low mountains, which stand isolated or moderately dissected and reach 500 - 800 m a.s.l., and low to very low undulating fluvial plains (Hernández-Santana et al. 2016).

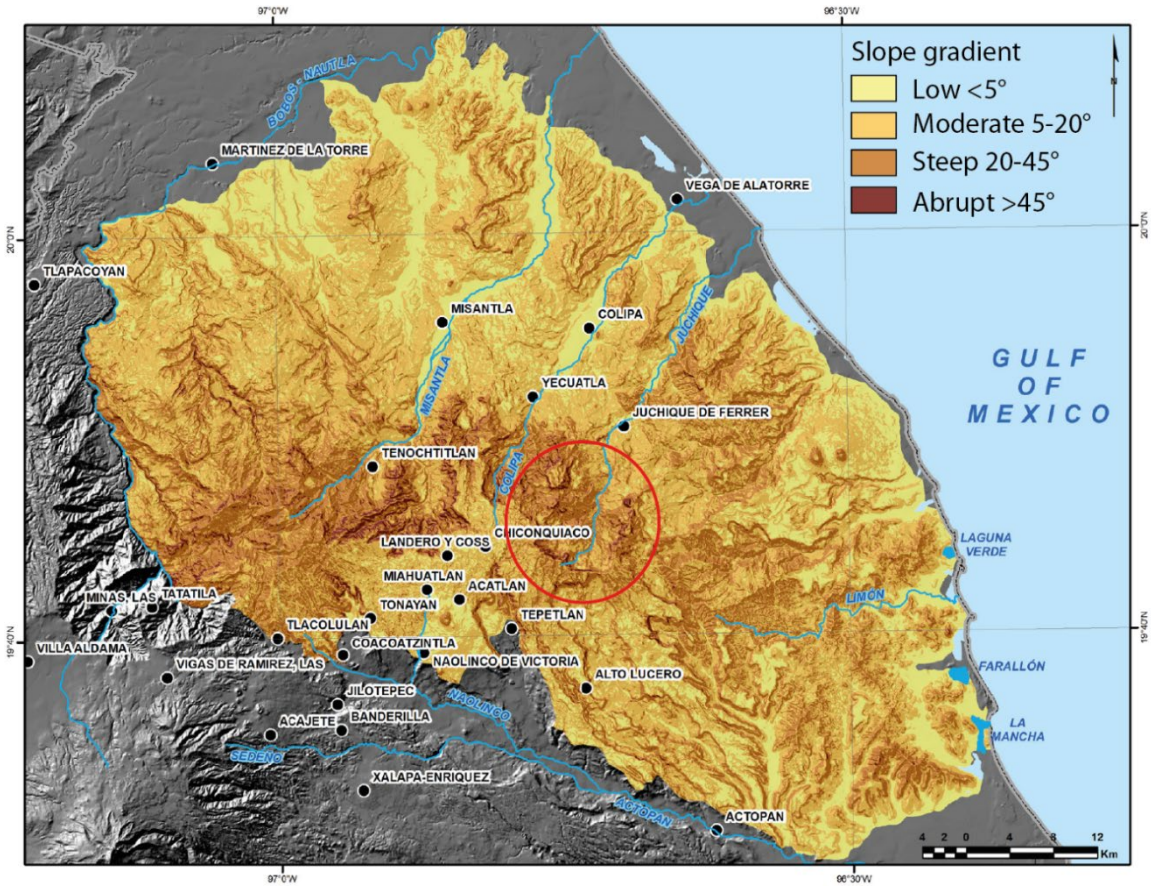

Figure 2-10. Slope gradient in the Chiconquiaco Mountain Range. Source: Modified after Lascurain-Rangel et al. (2017).

Even though the TMVB was subject to periglacial processes within the Pleistocene and the 'Little Ice Age', the relatively low altitude within this easternmost part prevented any geocryogenic influences within the study area (Heine 1994). Therefore, the dominating geomorphological processes, which shaped the morphology of the study area, are gravitational mass movements proximal to the elevated areas with steep slopes and fluvial erosion and sedimentation by the ephemeral rivers in the source area.

Hydrology: These topographic differences between the geomorphological zones are highly effective in regards of local precipitation. Isotopic studies at the transect between Veracruz (city) and Perote, few kilometers in the south of Xalapa, demonstrated the effectiveness of this transition. At 1,400 m a.s.l., an enrichment in $\delta^{18}O$ and δD could be recognized in the precipitation. This anomalous isotopic signature can be explained by the orographic-driven precipitation at the easternmost TMVB (Quezadas et al. 2015).

In the Chiconquiaco Mountain Range, four rivers hold a major share of the surface runoff: Minsantla, Colipa, Juchique and Limon (Lascurain-Rangel et al. 2017). This is a characteristic feature of the Mexican surface hydrology, where only 51 major rivers receive 87 % of the whole countries surface runoff (National Water Commission 2016). The entire study area, which is surrounded by steep basalt slopes in the east, the south and the west, represents the draining basin for the Juchique river, which flows into the Gulf of Mexico (Figure 2-11). This 50 km long river passes approx. 1,100 m of altitude from the study area to the ocean. The cross section of this drainage system represents a typical example of a river profile with a steep sloped upper course and a flat flood-zone near the coast (Grotzinger and Jordan 2017). The characteristic feature of the upper course is a generally strong imbalance between erosion and sedimentation favoring the erosion. The opposite is true for the coastal flood zones. At the transition of the mountains with high relief into areas with moderate slopes, the transporting rivers lose a lot of their transport capacity. The consequence is a proximal accumulation of sediments close to the source area with a generally low maturity (Nichols 2009). Because of a lack of large natural or artificial water reservoirs like lakes, ponds, or wetlands within or close to the study area, there is no sediment-buffer between the source areas and the Gulf of Mexico within the Juchique watershed.

The south of Veracruz has 22 lithological units classified as aquifers, which represent the major part of the local ground water. The intrusion of salt water into those aquifers, which

is a common phenomenon in other regions of Mexico (e.g. Baja California, Yucatan), is not regarded a problem in Veracruz, which is due to the high share of volcanic rocks in the underlying geology. Therefore, the aquifers in the vicinity of the study area are well charged and mostly of excellent quality (National Water Commission 2016).

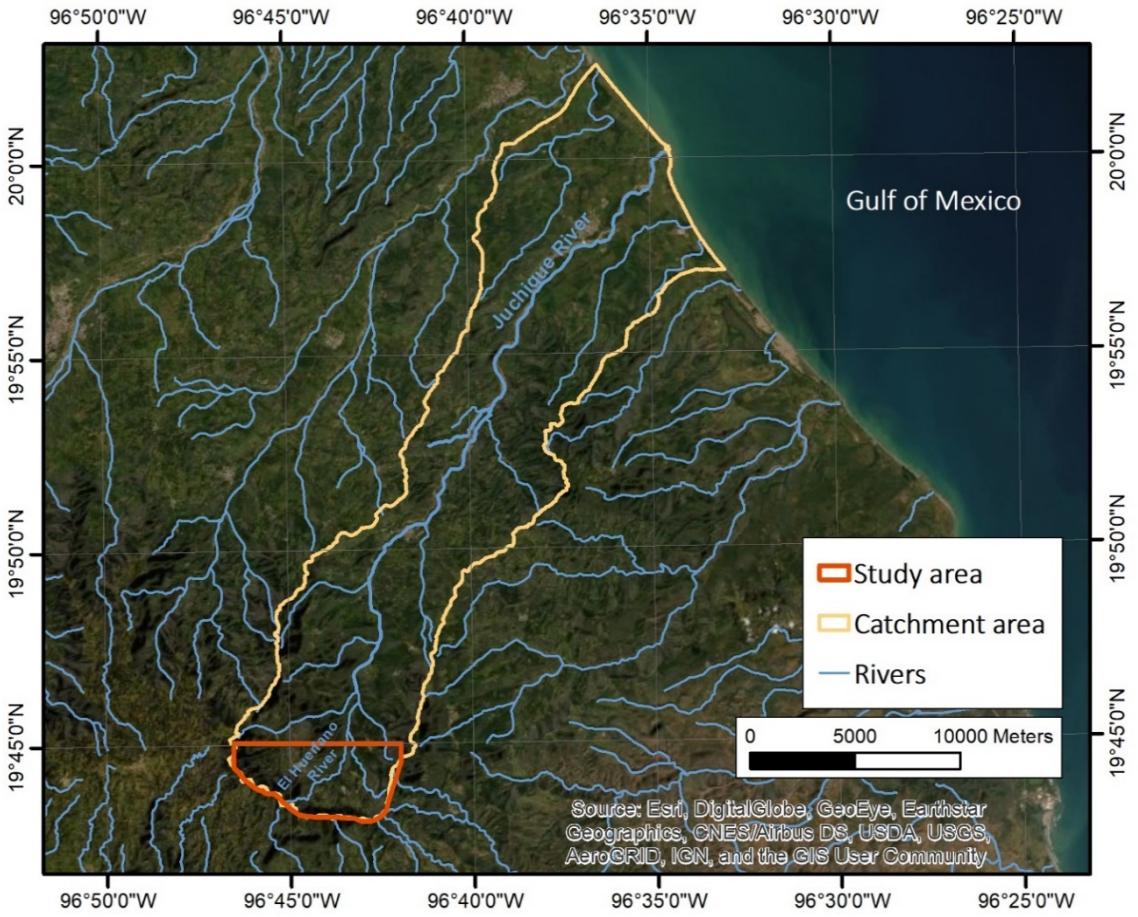

Figure 2-11. The study area as part of the hydrological drainage basin for the Juchique River. Source: Esri World Imagery (2019), INEGI (2020b).

Vegetation: Due to its wide latitudinal extension between 32 and 14°N and the above-mentioned large mountain systems, Mexico reveals a very high biogeographic diversity. The complexity of the various geographic factors favors the development of a very high number of biological habitats. Therefore, Mexico is ranked number three behind Brazil and Columbia in total number of species of plants and animals (Krasilnikov et al. 2013). The major vegetation types of Mexico are shrubs with 27.6 %, oak-pine forests with 16.9 %, agricultural land with 16.8 %, and grassland with 16.1 % surface cover. Tropical dry forests and tropical rainforest only have 10.4 % and 5.4 % share at the land use. Only 1.2 % of Mexico is covered by sand desert and human settlement only makes up 0.8 % (Figure 2-12;

Díaz et al. 2019). These current vegetation and land use forms are nearly exclusively a product of human interventions. While the impact of the native indigenous people only caused minor changes, the arrival of the Spanish induced a drastic decrease in forests, which at that time covered about two-thirds of Mexico (Krasilnikov et al. 2013).

In contrast, the current state of Veracruz has a high share of agriculture and grassland. Therefore, livestock breeding (47 %) and cultivation of coffee, sugarcane, and other crops typical for this region (28 %) occupy wide areas of the state (Gerez-Fernández and del Rosario Pineda-López 2011). Within the Chiconquiaco Mountain Range, in the close surrounding of the study area, steep slopes make the land less attractive for agriculture (23 %) but favorable for livestock breeding (51 %) and forestry (Lascurain-Rangel et al. 2017). The primary forest-dominated vegetation is reduced to few percents here. Because of the various changes the eco-system experienced since the Spanish arrived, even the potential for forest vegetation is reduced drastically and will be further reduced by the expected climate changes (Estrada-Contreras et al. 2015, Gómez-Díaz et al. 2018). Nevertheless, currently Veracruz is among the states with the highest diversity of endemic plants with 30 species of moss (Musci), 271 species belonging to the aster family (Asteraceae) and 38 grasses (Poaceae) (Delgadillo et al. 2003).

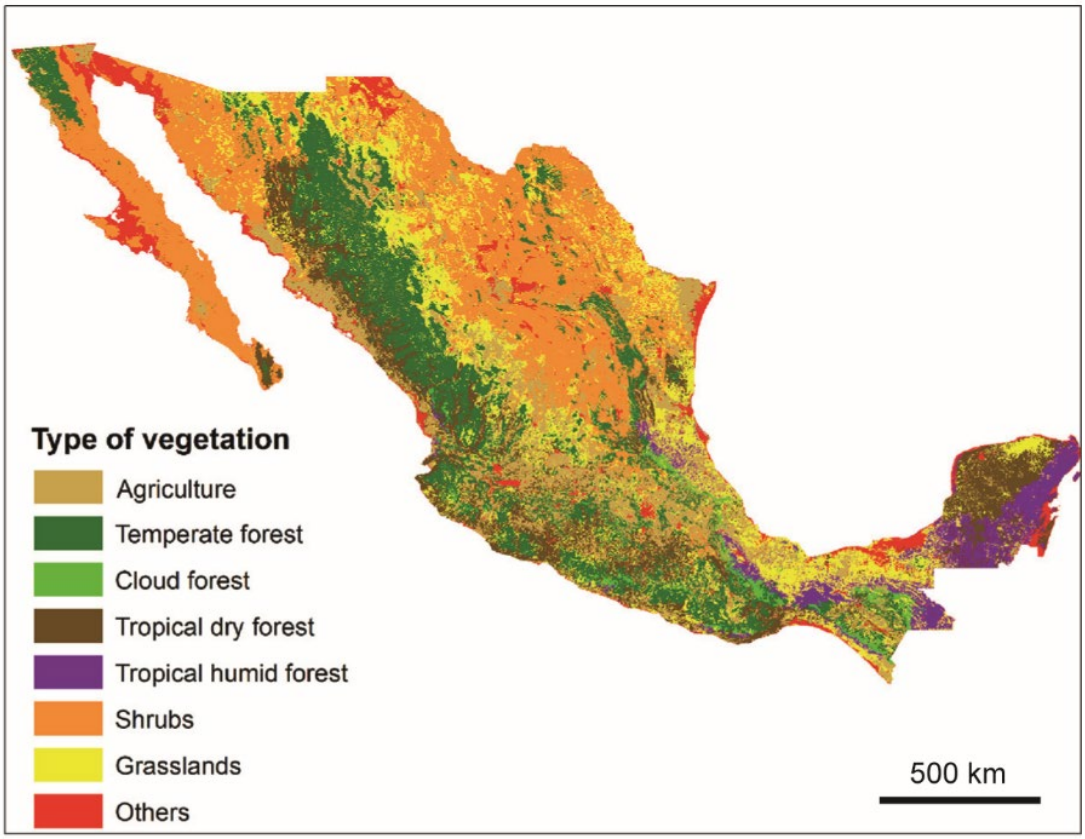

Figure 2-12. Current vegetation types and land use in Mexico. Source: Díaz et al. (2019).

3. Methods and data

3.1 Geomorphological analyses

Geomorphological analyses, such as localization of ancient mass movements, volume estimation, or slip surface identification, are crucial to gain a comprehensive understanding of process types, preparatory and disposition factors as well as to provide essential data for slope stability assessments. The following studies present information on availability, generation, and analyses of Digital Elevation Models (DEMs; chapter 3.1.1). Based on these DEMs landslides are mapped, and DEM time series are used to detect surface changes such as erosional and depositional areas (see chapters 3.1.2 and 3.1.3). The resulting DEMs of Difference allow for identification of slip surfaces and for calculations of landslide volumes (see chapters 3.1.4 and 3.1.5).

3.1.1 Digital elevation model generation

In the last 30 years, DEM related methods and data sources improved, further enabling the generation of high resolution DEMs (Wilson 2012). At present, they are indispensable for the analysis of land surfaces and applied in many different environmental disciplines (Wilson 2012). Furthermore, DEMs provide an opportunity to visualize and analyze surface morphology in great detail and thus, evolved to a key instrument in geomorphology. They are an important information source for landslide investigations and are widely used to detect and map these processes (Guzzetti et al. 2012).

Various sources, such as ground survey techniques, topographic maps, or remote sensing, provide data to generate DEMs. Latter include, among others, airborne or satellite radar as well as airborne laser systems (Nelson et al. 2009, Wilson 2012). Terrestrial laser scanning is also widely applied (Micheletti et al. 2015). The mentioned methods are cost-intensive, since they require expensive equipment (Westoby et al. 2012). High resolution imagery can be collected by using unmanned aerial vehicles (UAVs), which represent a more cost-effective and highly flexible alternative. For these reasons, UAVs became popular and techniques have been continuously improved during the last years (Hackney and Clayton 2015, Clapuyt et al. 2016). The imagery obtained from the UAVs builds the base to generate high resolution DEMs by applying Structure from Motion (SfM) algorithms (Hackney and Clayton 2015, James et al. 2017a). The SfM techniques enable to

generated three-dimensional (3D) models (point clouds) based on two-dimensional (2D) images from different perspectives (e.g. Eltner et al. 2017). This has become an effective, economical, and widely used method to acquire detailed surface information for geomorphological purposes (Westoby et al. 2012, Micheletti et al. 2015, Eltner et al. 2017). Image collection via UAVs and the resulting DEMs play an important role in landslide research as well, since they provide the opportunity to map and analyze mass movement processes (Niethammer et al. 2012, Lucieer et al. 2014a, Turner et al. 2015, Casagli et al. 2017, Rossi et al. 2018, Cignetti et al. 2019).

James et al. (2019) published guidelines for the usage of the SfM approach related to geomorphological research to ensure a uniform, constant, and comparable methodological application. In the present study, the workflow description of the DEM generation process is structured according to the guidelines of James et al. (2019) with some modifications. For the study area, a LiDAR DEM (Light Detection and Ranging Technique) of the year 2011, provided by the National Institute of Statistics and Geography (INEGI 2019) with a 5 x 5 m resolution, forms the base for the slope stability analyses. Further DEMs are not available, however, the landslide of interest in this study (Capulín landslide) occurred in 2013. Thus, an important objective is to generate DEMs representing the surface conditions after the landslide event in order to carry out detailed investigations. For this purpose, two datasets are applied, one data set comprises photographs from 2016, and the other set consists of photographs from 2013, forming the base for the compilation of DEMs.

DEM 2016: During a field campaign in 2016, a camera-equipped unmanned aerial vehicle (UAV) collected image data covering the Capulín landslide area.

Equipment: A DJI Phantom 3 Professional quadrocopter[1] (Figure 3-1b) equipped with a Sony EXMOR camera was used (see Table 3-1).

Survey design: The software Pix4Dcapture (2019) allows for the definition of the most important settings in advance and for the design and implementation of the survey.

[1] The UAV as well as technical and personnel support were provided by the consulting engineering company GEOTEM Ingeniería S.A. de C.V.: Contact information:
Alhelí Mz.7 Lt.13-A
Col. Ejidos San Pedro Martir
C.P. 14640, Tlalpan, Ciudad de México

Table 3-1. Technical details of the DJI Phantom 3 Professional and the camera (DJI 2019).

Technical specifications	Properties
Weight (including battery and propellers)	1,280 g
Maximum flight time	Approx. 23 minutes
Global navigation satellite system (GNSS)	GPS/GLONASS
Camera	Sony EXMOR 1/2.3", total pixels: 12.76 MP
Lens	FOV 94° 20 mm (equivalent 35 mm format) f/2.8 focus at ∞
Maximum image size	4,000 × 3,000
Format	JPEG, DNG (RAW)

Here, '3D-Grid Mission' mode was selected and the flight routes were planned. In order to cover the entire landslide area as well as the adjacent areas, the survey consisted of six flights, covering approx. 0.58 km², at an altitude of 100 m. The ground sampling distance (GSD), describing the pixel size (in cm/pixel), depends on the height of the camera above the ground (Vollgger and Cruden 2016, Cook 2017). At 100 m, the camera resolution (Table 3-1) results in approx. 4 cm/pixel. The image overlap was set to 80 % (instead of 90 %) with the objective to achieve an appropriate accuracy for the point cloud, and to have sufficient time for each flight. Uncontrollable factors, such as weather conditions, can interfere with the execution of the survey schedule (James et al. 2019). This was the case for flight number six, where strong winds interrupted the flight process, which required a repetition the following day.

Control measurements: Ground control points (GCPs) ensure precise georeferencing for the survey result (James et al. 2019). Therefore, removable spray paint was applied to mark GCPs with a maximum extent of 2 x 2 m (Figure 3-1c). A total of 21 GCPs were installed (Figure 3-1a), 11 of them located in the stable, external landslide areas, and 10 located in the landslide area. The GCPs were adapted to the specific requirements of the terrain, such as difficult access or high vegetation, and hence, could not be uniformly distributed (Figure 3-1a). All GCPs were measured with a ProMark 500 GPS (accuracy 1-5 cm).

Photogrammetric processing: Figure 3-2 depicts the photogrammetric procedure applied in this study. For image processing the software Agisoft Photoscan Professional version 1.2.6.2834 (Agisoft PhotoScan 2016) is used (on a Windows system; 32 GB RAM, Intel Core i7-7700 processor), which is a common software to apply the SfM-Multi View Stereo (MVS) technique (see Smith et al. 2016, Eltner et al. 2017). In general, prior to the import of photographs, a **visual pre-selection** takes place in order to reject low quality pictures.

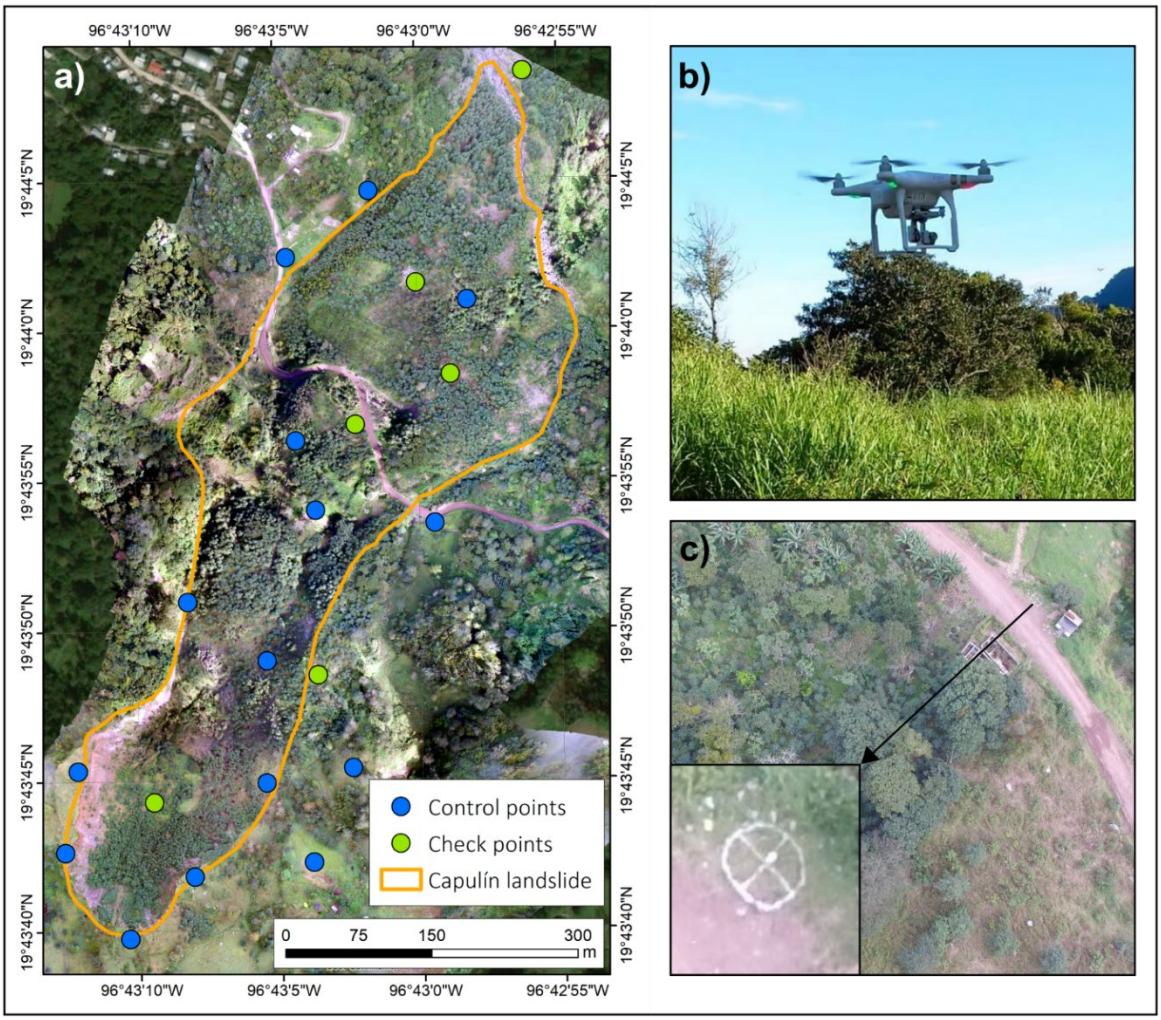

Figure 3-1. a) Distribution of the ground control points in the Capulín landslide. Control points marked in blue and check points marked in green. Source of background map: Esri World Imagery 2019. b) Photographs of the DJI Phantom 3 Professional. c) UAV photograph including a close-up of a ground control point. Source: Own illustration.

In this study, a total of 521 photographs provide a number of 279 high quality photos, which are sufficient for further processing. The relevant **photos are imported** into Agisoft Photoscan and the first step consists of the image brightness adjustment, followed by the photograph alignment. During this process, the program identifies and matches features (key points) in all photographs (Smith et al. 2016). Key points are image points, which are clearly identifiable in the photographs while tie points represent the most accurate and reliable key points. Tie points are instrumental in determining camera position and direction as well as in determining the 3D coordinates of tie points from the photographs (James and Robson 2012, Vollgger and Cruden 2016). Table 3-2 shows the alignment settings used for this study. The result corresponds to a **sparse cloud**, which represents the 3D coordinates of the key points. Subsequently, by deleting evident outliers, the quality of the sparse cloud is improved.

Table 3-2. Properties of the alignment setting. The setting 'reference' for the pair preselection means that the selection of the overlapping photographs is based on the measured camera locations (Agisoft PhotoScan 2016).

Parameter	Settings
Accuracy	Highest
Pair preselection	Reference
Key point limit	40,000 points
Tie point limit	10,000 points

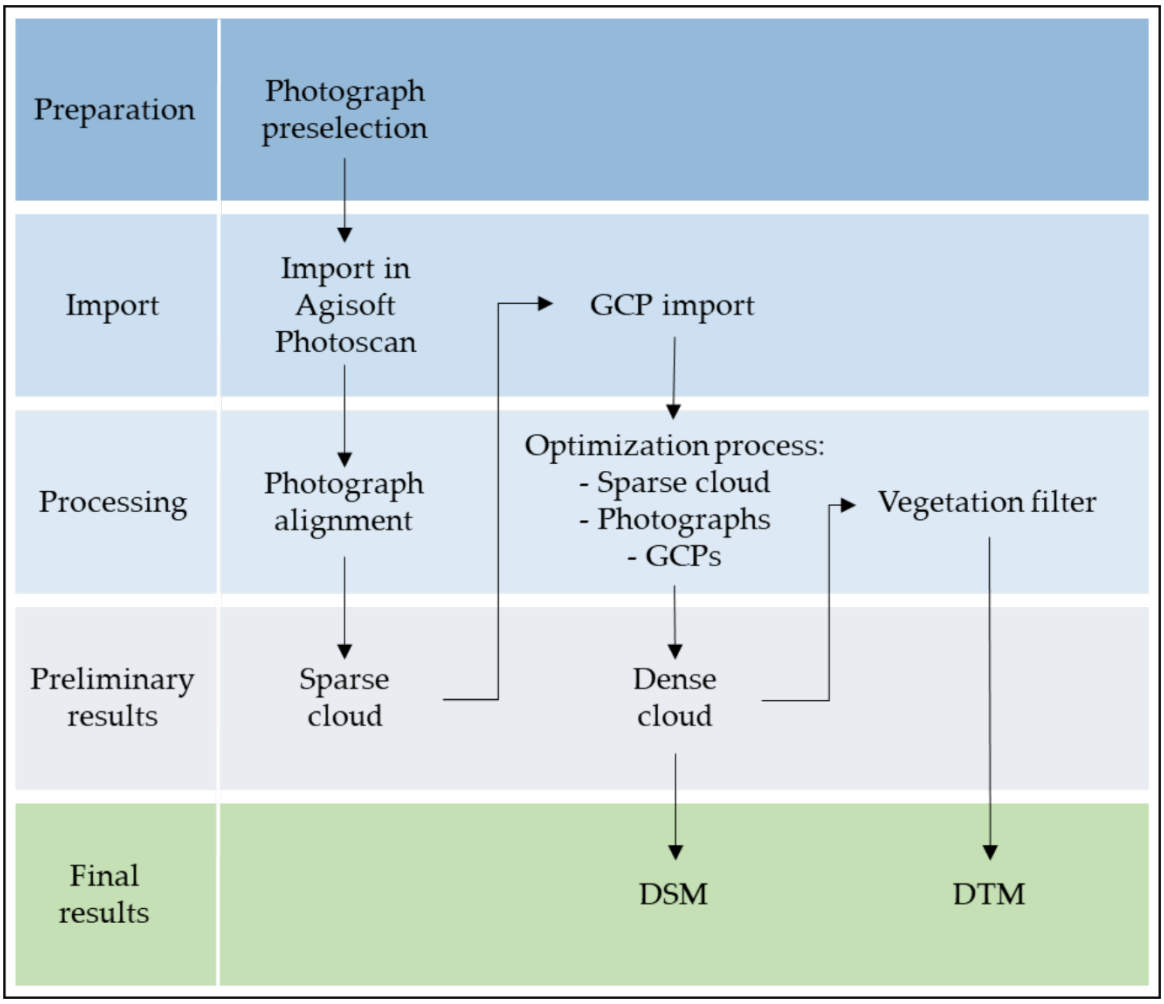

Figure 3-2. Photogrammetric processing workflow in Agisoft Photoscan Professional for the present study. Source: Own illustration.

GCPs are further imported in order to achieve the external orientation and thus, the internal coordinate system of the point cloud is transformed into an absolute (real world) coordinate system (Westoby et al. 2012). In advance, altitude values of six GCPs (GCP nos. 3, 5, 8, 17, 20, 21) required adjustment to the DEM 2011, in order to avoid discrepancy

between measured GCPs and the LiDAR DEM of 2011. Finally, the GCPs are identified, manually placed in the photographs, and then divided in control and check points (Figure 3-1a).

The next phase consists of an **optimization process in Agisoft** (Figure 3-2). The first step represents the optimization of the sparse cloud (result from alignment process) by adjusting reprojection error, reconstruction uncertainty, and projection accuracy. The reprojection error was very low, therefore, it is set to a threshold value of 0.25. The reconstruction uncertainty is set to the value 50 and the projection accuracy to 3.0. The conduction of the optimization process results in reducing the tie points of the sparse cloud from 258,457 to 99,717 points. The second step of the optimization process comprises the adjustment of the photographs and GCPs.

Posterior to the optimization process a **dense cloud** calculation with two configurations follows. First, the quality is set to 'high', since 'ultra high' quality results into too long calculation time. The high-quality setting is ideal for the creation of digital elevation models as the highest quality ('ultra high') has the disadvantage that despite the increase of the quality the noise increases as well (Anders et al. 2019). Secondly, 'moderate' depth filtering is selected, since 'aggressive' filtering can cause a severe loss of information. Subsequently, based on the resulting dense cloud a DEM is generated. Without further dense cloud filtering, the resulting DEM represents the surface and therefore, can be defined as a **digital surface model (DSM)**.

DTM generation: In order to calculate a **digital terrain model (DTM),** where all surface elements, e.g. vegetation and urban structures, are eliminated, a **filtering process** has to be applied. There are different possibilities to classify a dense cloud (Anders et al. 2019). Agisoft Photoscan provides various possibilities to filter ground points from dense clouds (Agisoft LLC 2016). The option 'classify ground points' allows for various parameter settings such as maximum angle, maximum distance, and cell size. Another valuable method is the selection of points by color, enabling runs with different colors (Agisoft LLC 2016).

A more elaborate, albeit time-consuming approach can be used to facilitate color classification. In this process the Normalized Difference Vegetation Index (NDVI) is calculated (raster calculator in Agisoft Photoscan), consequently changing the color of the

photographs. The modified photographs build the base for the calculation of the dense cloud. This yields the advantage that the color contrast (especially for vegetated and bare areas) appears clearer and it is therefore possible to perform the color classification with greater accuracy.

Recent versions of Agisoft (version 1.5.3 of Agisoft Metashape Professional was used) incorporate a new classification tool ('classify points') where multiple classes can be identified simultaneously (Agisoft LLC 2019). The most accurate classification results can be achieved by combining this new 'classify points' tool with the preliminary NDVI preparation of the dense cloud and subsequently, adjust inadequate classification (e.g. steep slopes classified incorrectly as 'buildings'), where necessary, with the remaining tools (e.g. 'select points by color'). The described classification enables the export of a DTM and an orthomosaic.

Accuracy assessment: Quality evaluation of the DEM requires an accuracy assessment starting with the evaluation of the GCP error. For this purpose, the 'Root Mean Squared Error' (RMSE) of the difference between measured GCPs locations and corresponding coordinates of the generated DEM is calculated (James et al. 2017a).

The next procedure consists of assessing the surface model error, which compares stable zones of two different DEMs, evaluating the relative elevation accuracy (Lucieer et al. 2014a, James et al. 2019). Smith et al. (2016) stated that only LiDAR and Terrestrial Laser Scanning (TLS) provide topographical data, which is suitable for comparison. Consequently, the youngest DEM has to be adjusted to the LiDAR DEM of 2011. The adjustment was executed for correcting the mismatch in elevation (Turner et al. 2015) and to enable the subtraction process for the DEM of Difference (DoD) (see chapter 3.1.3). In this case, it is important to address the offset of the DEMs rather than the accurate absolute location as the focus of this study lies mainly on the comparison of different DEMs. Thus, in order to determine the difference between both DEMs, it is necessary to compare those zones, which presumably did not experience any changes (referred to as stable areas). For this purpose, a specific mask delineates the stable areas (approx. 0.10 km²), and the DEMs (2011 and 2016) are extracted to the extent of this mask. Simultaneously, this mask builds the base to create approx. 5,000 points, which represent a random distribution within the extent of the mask. These points support the extraction of the values from both DEMs for each point. Consequently, each of the 5,000 points contains two elevation values from both DEMs. Subsequently, these values are integrated in the linear regression as well as for

'Root Mean Squared Error' (RMSE) calculations (Turner et al. 2015). Besides the calculation of the RMSE, it is necessary to address the mean error (ME) and the standard deviation (STD). The ME stands for the measurement of accuracy as it indicates the difference between the true value and the average of the measured values (James et al. 2019). The STD supports the evaluation of the precision best, however, STD can only be used, when the values are normally distributed (James et al. 2019). In cases where there is no normal distribution, RSME can be applied, although systematic and random errors cannot be clearly separated (James et al. 2019).

General errors in the georeferencing of the 3D-model can cause bias between both DEMs. For example, residuals of the vegetation filtering process can represent one error source. Related to this, it is highly relevant to consider these errors as more intensive filtering leads to high information loss.

DEM 2013: In a second approach, the photogrammetric processing is also applied to a data set from the year 2013 in order to generate a DEM depicting the situation directly after the landslide event (DEM 2013). 176 photographs were taken from a helicopter with a camera[2], however, lacking any GPS information. 88 of them provide high quality and are suitable for further processing. In a next step, it was necessary to mark the GCPS from 2016 in the photographs for the external orientation. During this procedure, it was possible to identify seven GCP locations, which function as control and check points. The parameter setting for the **alignment** is given in Table 3-3.

Table 3-3. Properties of the alignment setting. The setting 'generic' for the pair preselection means that the selection of the overlapping photographs is based on a prior matching process for which a lower accuracy is used (Agisoft PhotoScan 2016).

Parameter	**Settings**
Accuracy	High
Pair preselection	Generic
Key point limit	60,000 points
Tie point limit	10,000 points

[2] Photographs taken and provided by Dr. S. Rodríguez Elizarrarás, researcher at the Institute of Geology of the National Autonomous University of Mexico.

The determined setting for the reprojection error is 0.25, the one for the reconstruction uncertainty is 40, and 5.0 for the projection accuracy. The optimization process of the sparse cloud results in 49,052 tie points from originally 101,355 points. The simple ground filter (max. angle 20°, max. distance 3 m, cell size 50 m) is sufficient in this case (see Figure 3-3) as only minor parts of the landslide body were covered by vegetation and urban structures (small houses and cabins).

The classified dense cloud forms the base for the generation of the DEM 2013. The error assessment follows the same procedure as described for the DEM 2016. Furthermore, the RMSE of the GCPs was calculated, by adjusting the younger DEM 2013 to the LiDAR DEM (DEM 2011) and in a next step, RMSE, ME and STD were calculated. For offset calculation, the difference of both DEMs could only be measured over an area of 0.07 km² as the DEM 2013 records only small areas outside the landslide.

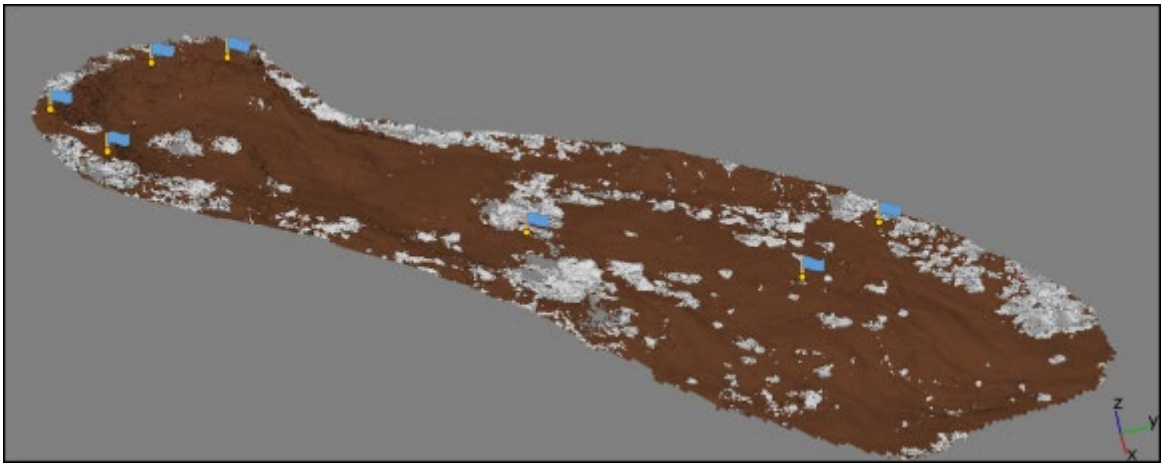

Figure 3-3. Ground point classification of the dense cloud based on the 2013 data. Brown color represents ground points and gray color unclassified vegetation. Flags show the locations of the ground control points. Source: Own illustration, derived from Agisoft PhotoScan 2016.

3.1.2 Landslide mapping

Landslide inventory maps are essential for the understanding of disposition and triggering factors. Moreover, they are crucial to assess landslide susceptibility, hazard, and risk (Highland and Bobrowsky 2008, Guzzetti et al. 2012, Bunn et al. 2019). Mass movements are commonly mapped based on the assumption that under consistent environmental conditions, the spatial distribution of recent and past landslides can provide valuable information on the occurrence of future slope failures (Carrara et al. 1995,

Highland and Bobrowsky 2008, Temme et al. 2020). Various possibilities exist to structure landslide inventory maps. In general, they concentrate on one type of movement process or they combine various processes. Further classifications consider e.g. age, size, and activity state (Guzzetti et al. 2012). Moreover, different methods are available to generate inventory maps. Information can be derived inter alia, from textual sources, maps, field investigations, aerial photograph interpretation, DEMs or satellite images (Guzzetti et al. 2012, Kreuzer and Damm 2020). The analysis of LiDAR derived DEMs is now a common and essential approach in landslide research (Guzzetti et al. 2012, Van Den Eeckhaut et al. 2012). The main advantages of LiDAR DEMs are its high resolution as well as the ability to depict the ground surface, allowing for the identification of landslide features under forested areas (e.g. Tseng et al. 2013, Van den Eeckhaut et al. 2007b). In recent years, different methods for automated and semi-automated landslide mapping have been developed, however, visual image analysis currently remains the most widely applied method (Guzzetti et al. 2012, Otto and Smith 2013, Santangelo et al. 2015, Hölbling et al. 2017, Bunn et al. 2019, Pánek et al. 2019).

For the study area, a landslide inventory map is created by visual analysis in order to locate and identify landslide forms. Contour lines with intervals of 5 and 10 m, slope and shaded relief maps (hillshades) are generated from the LiDAR DEM 2011 (5 m resolution), which build the base for landslide mapping. Hillshades are produced with a sun angle of 45° and varying azimuth angles (Figure 3-4), i.e. 45° (north-east), 90° (east), 135° (south-east), 180° (south), 225° (south-west), 270° (west), 315° (north-west), and 360° (north). Changing azimuth angles are useful for landslide mapping as different light sources provide variable results and complement each other (e.g. Haneberg et al. 2009). Furthermore, visual analyses involve orthophotos (INEGI 2020c) and Google Earth Pro (version 7.3.3.7786). Individual landslides are located and identified, and geomorphological characteristics are mapped as polygons (using ArcGIS). Due to extensive erosion processes, scarp and slide mass are marked as one polygon instead of characterizing them separately. In cases where the slide mass is not identifiable anymore, a line signature marks the scarp.

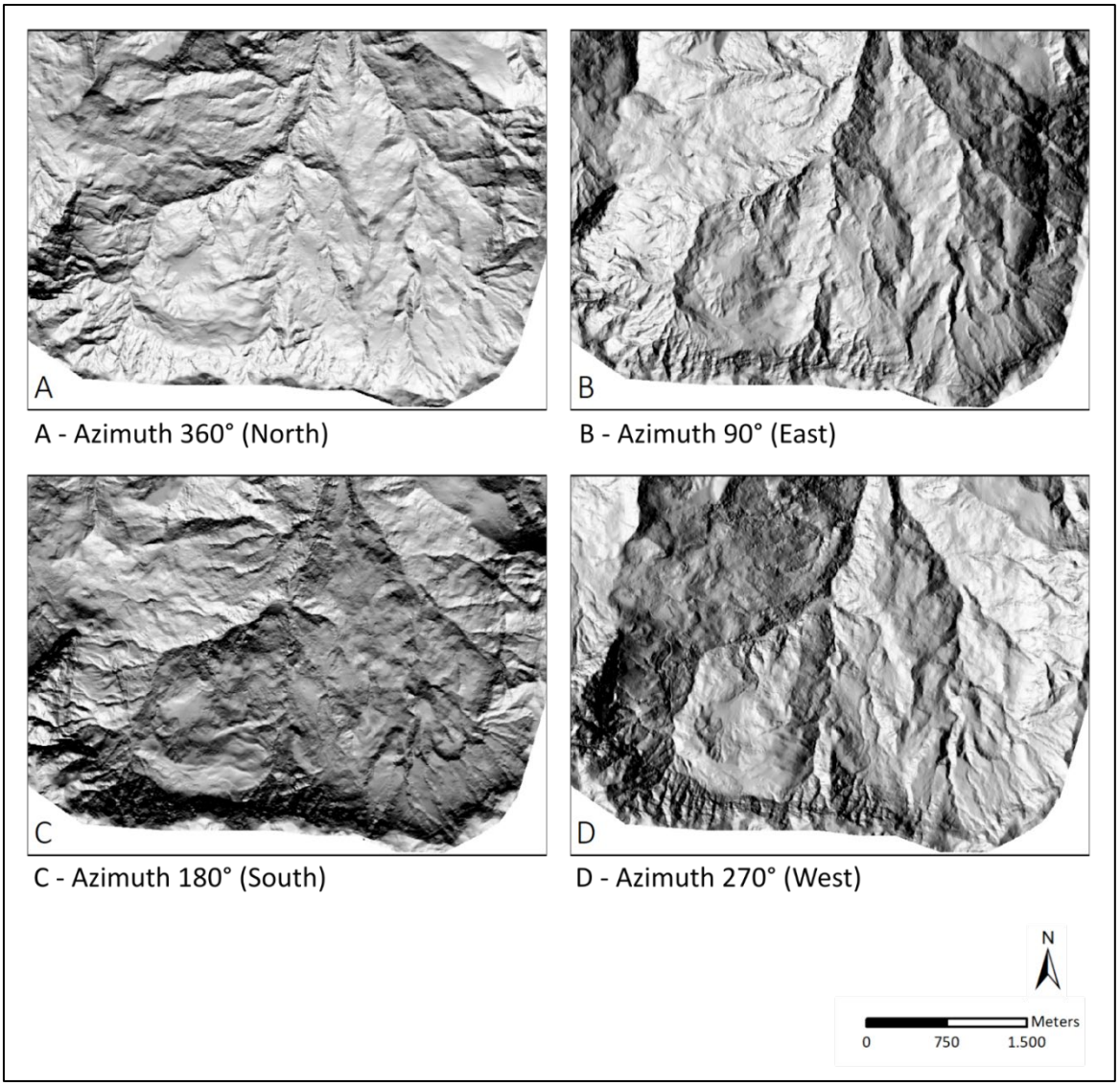

Figure 3-4. Hillshades of the study area with different azimuth angles, derived from the DEM 2011. Source: Own illustration. Hillshades: INEGI (2019).

3.1.3 DEM of Difference

DEMs of difference (DoD) describe the differences between two DEMs from successive time periods and they are widely used in geomorphological research (Williams 2012, Heckmann and Vericat 2018). They are applied for documentation and monitoring of landslides (e.g. Lindner et al. 2016, Eker et al. 2018, Seier et al. 2018) and they are further used in order to detect and trace topographic changes like areas of erosion and accumulation (e.g. Lague et al. 2015, Heckmann and Vericat 2018). Characterization of landslides, for example with the determination of the landslide volume, can be achieved by DoDs as well (e.g. Williams 2012, Jaboyedoff et al. 2020). Williams (2012), among others describes the calculation of DoDs by subtracting two subsequent DEMs that represent

different time periods. This is usually carried out in a GIS environment (e.g. de Bari et al. 2011, Hsieh et al. 2016, Seier et al. 2018).

This study applies DEMs derived via LiDAR (INEGI 2019), representing the pre-event conditions, and the generated DEM representing the post-event conditions for DoD analysis. For the generation of the DoD a simple subtraction of the two DEMs would not be sufficient, since it would not consider any errors transferred from the DEMs. However, error determination is important in order to ensure that detected changes are related to erosion and accumulation processes and not to errors inherited from the DEMs (Lane et al. 2003, Wheaton et al. 2010, Williams 2012). To achieve this goal, the error of each DEM has to be determined in order to calculate the error for the resulting DoD (Williams 2012, Bangen et al. 2014). In general, the DoD error (δ_{DoD}) is calculated as:

$$\delta_{DoD} = \sqrt{\left(\delta z_{post}\right)^2 + \left(\delta z_{pre}\right)^2} \tag{3.1}$$

where δz_{pre} is the individual error of the DEM that was surveyed before the landslide, and δz_{post} is the individual error of the DEM generated afterwards (Wheaton et al. 2010, Bangen et al. 2014). The LiDAR DEM error is expected to be in the range of centimeters, however, the real value is unknown and hence, the above described Equation 3.1 is not suitable for this approach. Consequently, the deviation of the DEMs is calculated to determine the DoD error.

Higher point precision is provided by the LiDAR derived DEM, and thus it forms the base to evaluate the new DEM. The results of the mean error (ME) as well as the standard deviation (STD) of the DEMs determine the DoD error δ_{DoD} (Bangen et al. 2014). The minimum level of detection (LoD_{min}), which distinguishes vertical changes from noise, was specified by utilizing the value of δ_{DoD} as a constant threshold for the DoD (Wheaton et al. 2010, Williams 2012, Vericat et al. 2017). This threshold is integrated to the DoD calculation process in order to address the uncertainties of the DoD. For this purpose, the Geomorphic Change Detection (GCD) software (see http://gcd.riverscapes.xyz/) is applied, which is an Add-in for ArcGIS (e.g. Wheaton et al. 2010, Vericat et al. 2017). The GCD subtracts the DEMs from each other and simultaneously includes the specified threshold. Thus, changes below the indicated threshold are not included in the calculation. The result correspond to a thresholded DoD where negative values indicate areas of erosion and positive values areas of accumulation (Wheaton et al. 2010, Williams 2012).

3.1.4 Slip surface determination

The slip surfaces depth, shape, and its orientation determine the subsurface geometry of a landslide. Information on slip surfaces are crucial, especially for slope stability analysis as they represent zones of critical shear strength or groundwater pressures (Carter and Bentley 1985). Based on the slip surface's shape, sliding types (e.g. translational or rotational) can be determined and volumes of slide bodies are calculated (e.g. James et al. 2019). Various approaches aiming at the identification of slip surfaces exist so far. Generally, applied and well known approaches are the half ellipsoid method or the balanced cross section method. These calculations locate and determine the depth of the potential slip surface (WP/WLI 1990, Cruden and Varnes 1996, Bishop 1999, Jaboyedoff et al. 2020).

Ground-truth data like drillings and exposures are essential to gain information on the slip surface (Carter and Bentley 1985, Highland and Bobrowsky 2008). Drilling procedures are commonly associated with further methods as for instance, oriented core samples, combined with laboratory analyses as well as with geophysical measurements were used by Furuya and Jiang (2015) for slip surface detection.

In the last years, non-invasive geophysical methods are in the focus of landslide research (e.g. Jongmans and Garambois 2007, Jongmans et al. 2009, Hibert et al. 2012). Variable and high flexible methods, such as electrical tomography (ERT), seismic refraction (SRT), seismic reflection, and ground penetrating radar enable the detection of slip surfaces. The essential objective of these methods is to differentiate the slide mass from the surrounding materials (e.g. Hack 2000, Jongmans and Garambois 2007, Pazzi et al. 2017). Geophysical techniques extend their value when combined with additional methods, like geomorphological and geological surveys as well as photogrammetric analysis (Naudet et al. 2008, de Bari et al. 2011).

In this study, the slip surface of the Capulín landslide is determined by combining data derived from geophysical surveys with geomorphological information from pre- and post-event DEMs. First of all, information on the depth and location of the potential slip surface is derived from geophysical surveys (I. **Data description**). The data obtained from the former step are further interpolated by applying different interpolation methods (II. **Interpolation**). In order to select the best fitting method, visual evaluation and the calculation of the RMSE are applied (**III. Evaluation**).

I. Data description: Primarily, the goal to detect depth and location of the slip surface requires information on surface and subsurface conditions. In this case, the surface data was measured in the field and further derived from the DEM 2016 (chapter 3.1.1). Geophysical analyses (ERT, SRT) provide subsurface information, obtained during various field campaigns at the Capulín landslide in cooperation with Dr. Daniel Schwindt[3] and Dr. Matthias Bücker[4]. The results and related subsurface models are published in Wilde et al. (2017a, b). Latter models (Appendix C) form the base for interpolation procedures in this work.

In order to obtain information on the thickness of the slide mass and the potential location of the slip surface, ERT and SRT are combined as they complement each other ideally (Perrone et al. 2014, Wilde et al. 2017a). The geophysical survey comprises five transects, four of them are located in the internal part and one in the external area of the landslide (cf. Figure 3-5). Transect 1 and 6 cover the lower parts of the slide mass as well as the foot area. Transect 2 and 5 represent the central part. Due to difficult field conditions in the scarp area, Transect 4 is located outside the landslide, on top of the scarp (Figure 3-5).

The resulting subsurface models (cf. Appendix C) allow for a differentiation between the recent slide mass and its underlying material, which is described as 'old land surface' in Wilde et al. (2017a, b) and this former surface can be located in all geophysical transects. Remarkably, it is possible to distinguish between a relict slide mass and an old land surface outside the landslide as well (cf. Appendix C, Wilde et al. 2017a). In this work, the assumption is made that the identified 'old land surface' (Wilde et al. 2017a, b) corresponds to the slip surface of the Capulín landslide. Therefore, depth information on the slip surface is derived from the subsurface models (cf. Appendix C) by creating points in a distance of 10 meters along the 'old land surface'. 10 m steps are selected as this tight spacing enables to capture the majority of significant elevation changes. For each point, the depth of the potential slip surface is measured in the subsurface model and further subtracted from the surface elevation (DEM 2016). As a result, each point contains the elevation information of the slip surface. Three additional points were added, which were located at the boundary of the landslide and identified at outcrops during field investigations. All points are divided into interpolation and validation points.

[3] Dr. Daniel Schwindt, Department Physical Geography, University of Göttingen
[4] Dr. Matthias Bücker, Institute for Geophysics and Extraterrestrial Physics, Technical University of Braunschweig

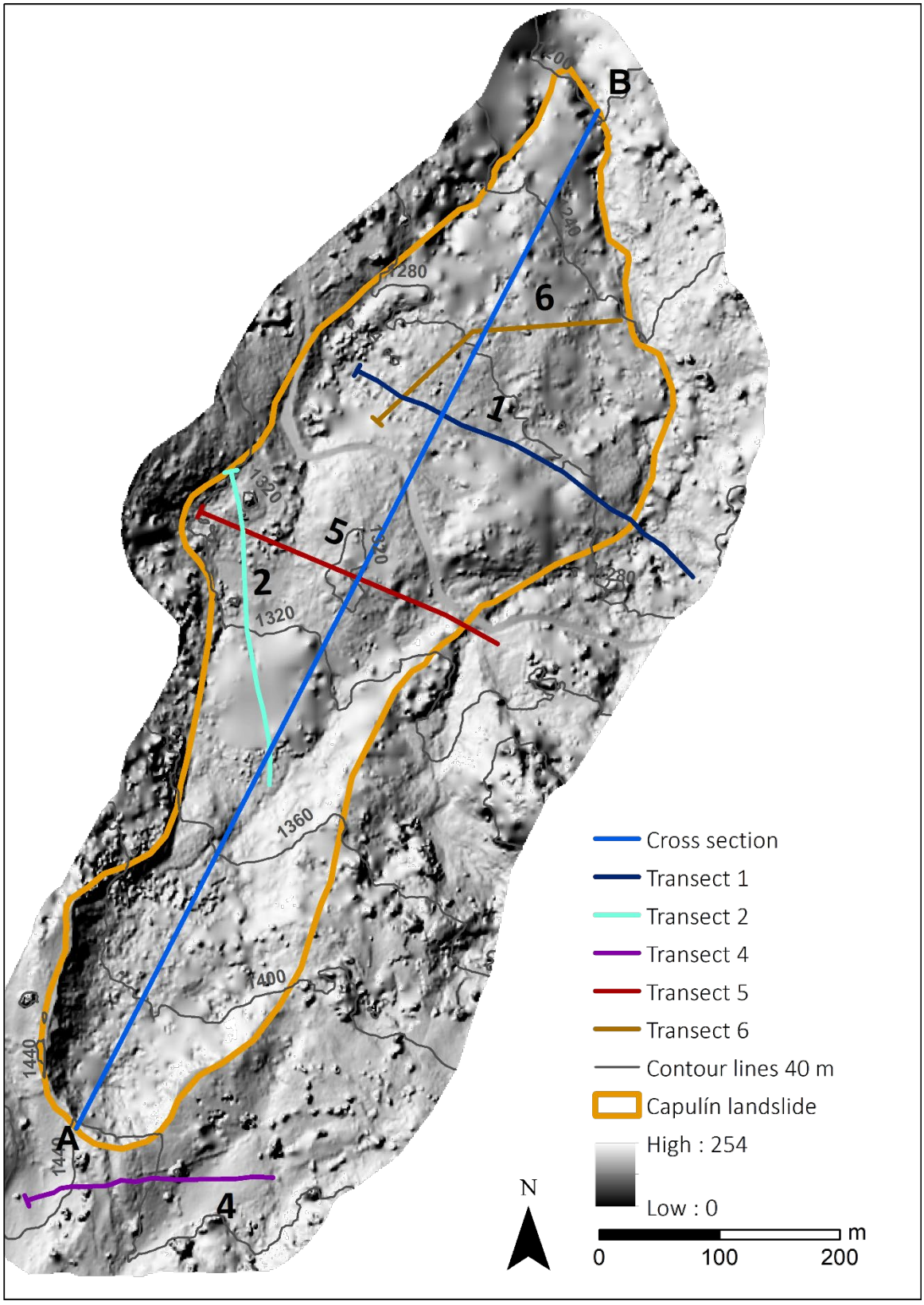

Figure 3-5. Location of the geophysical transects. Hillshade of 2016 forms the underlying map. A perpendicular line marks the beginning of each transect. Source: Modified after Wilde et al. (2017a, b). Source: Own illustration.

II. Interpolation: In the next step, the elevation values (from the interpolation group) are interpolated in order to obtain a depth map of the slip surface. At present, various interpolation techniques exist, reflecting different geometries due to diverse characteristics of the input data (e.g. Kalenchuk et al. 2009). It is common practice to compare different interpolation methods in order to choose the most suitable technique (Kalenchuk et al. 2009). In this context, Naudet et al. (2008) applied the ordinary kriging interpolation and Kalenchuk et al. (2009) tested various techniques. The method selection for this study comprises natural neighbor method, deterministic spline (type tension) method, and ordinary kriging technique (e.g. Lam 1983, Cressie 1990, Voltz and Webster 1990, Weber and Englund 1994, Albrecht 2007). Furthermore, a homogenous grid spacing of 5 meters forms the base for all interpolations.

III. Evaluation: The selection of the most suitable interpolation technique for this data set requires an evaluation of the resulting depth maps. Therefore, the validation points are used to calculate the RMSE and further visualization techniques are applied (e.g. Voltz and Webster 1990, Wood and Fisher 1993, Brus et al. 1996, Carrara et al. 1997, Desmet 1997, Aguilar et al. 2005). For the RMSE calculation, it is important to mention that the sample point locations are distributed inhomogenously and in some regions, validation points are not available. Thus, and additional interpretation of the interpolation results is necessary to evaluate the reliability of the spatial predictions (Kalenchuk et al. 2009). For this purpose, the three resulting depth maps are visualized in 2D and 3D, which allows for the identification of errors, such as e.g. unrealistic shifts, and structures that cannot be explained by geological or geomorphological properties.

3.1.5 Landslide volume calculation

Volume data can provide information on volume-frequency relationships (Dai and Lee 2001, Brardinoni and Church 2004, Malamud et al. 2004). Thus, the determination of landslide volume, combined with size and number of events, forms an essential base for landslide susceptibility and hazard assessment as well as for the evaluation of secondary processes (Malamud et al. 2004, Guzzetti et al. 2009, Marchesini et al. 2009).

Different methods exist for landslide volumes estimation. Field measurements like geomorphological, geophysical, geotechnical surveys, and drilling methods are used for detection of landslides boundaries and slip surfaces (e.g. Bichler et al. 2004, Pazzi et al.

2017). Furthermore, the application of statistical methods is common, which requires data, such as length, width, and slope angle (Guzzetti et al. 2009, Larsen et al. 2010). In recent years, landslide volumes are determined by subtracting pre- and post-event DEMs (e.g. Bichler et al. 2004, Guthrie et al. 2012, Chen et al. 2019, Koca and Koca 2019). Jaboyedoff et al. (2020) provides a comprehensive overview of the existing methods for volume estimation. In this context, it has to be mentioned that each method is characterized by advantages and disadvantages. Therefore, comparing different methods enables to cross-check and evaluate the obtained results. Against this background five volume calculations are compared to each other (Jaboyedoff et al. 2020). On the one hand, the objective is to find the most suitable method for this study. On the other hand, the comparison of different methods allows to asses data accuracy required to compute reliable results.

Primarily, the half ellipsoid approach (Approach I) described by Cruden and Varnes (1996) is applied, to calculate the volume of the displaced material (V_d) with following formula (WP/WLI 1990):

$$V_d = \frac{1}{6}\pi\, L_d W_d D_d \tag{3.2}$$

where D_d represents the maximum thickness of displaced material, W_d is the maximum width and L_d is the length of the slide mass (WP/WLI 1990, Cruden and Varnes 1996). The ellipsoid is fitted to the landslide extent according to Taylor et al. (2018). The thickness of the displaced material is derived from geophysical subsurface models (see previous chapter and Appendix C). These models show the post-event (DEM 2016) as well as the potential slip surface and their elevation difference, representing the thickness of the slide mass, can be measured.

The second approach (Approach II) consists of the volume calculation of eroded (V_e) and accumulated areas (V_a), derived from the DoD (see chapter 3.1.3). Eroded areas, represented by negative values, are separated from the accumulated areas, represented by the positive values. The volume for each area is calculated by multiplying the total area with the average thickness (de Bari et al. 2011). The total volume of difference (V_{DoD}) is then calculated by summarizing the absolute values of both volumes (Vericat et al. 2017). The result corresponds to the volume of displaced material compared to the pre-event surface. Both approaches (I and II) have difficulties as the first approach disregards elevation changes and the second one underestimates the volume (Bichler et al. 2004, de

Bari et al. 2011). Thus, an additional approach is carried out in order to address these problems.

The third approach (Approach III) requires the generation of a DoD for the post-event surface (DEM 2016) as well as the slip surface, where the resulting volume represents the volume of the displaced material (Vpost).

Approach IV combines the results of Approach I and II in order to calculate the volume of the material prior to the landslide event (Figure 3-6). V_{total} is calculated, by modifying the procedure described by de Bari et al. (2011) as:

$$V_{total} = V_d + |V_e| - |V_a| \tag{3.3}$$

where V_e (cf. Figure 3-6) represents the volume of the eroded and V_a of the accumulated material (derived from Approach II). V_d correspond to the volume from the half ellipsoid approach (Approach I; WP/WLI 1990, Cruden and Varnes 1996).

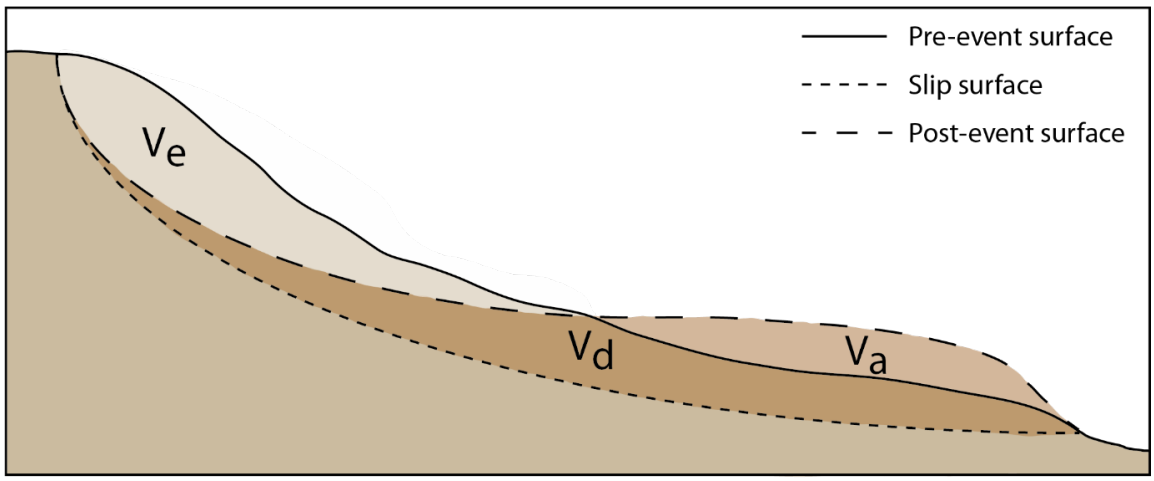

Figure 3-6. Schematic illustration of the components for the calculation of V_{total} (Approach IV). V_d is the volume of the half ellipsoid approach, V_e represents the volume of eroded material, and V_a of accumulated material. Source: Modified after de Bari et al. (2011).

In the approach from de Bari et al. (2011), the half ellipsoid volume (V_d) is modified from the original approach (Equation 3.2). In this context the authors assume that in their case the maximum thickness of displaced material (D_d) is equal to the maximum depth of the rupture surface from the original ground surface (D_r) (de Bari et al. 2011). Consequently,

they calculate V_{total} by adding their modified volume from the half ellipsoid approach to V_e and V_a. The result is equivalent to the post-event volume. Thus, in order to obtain the pre-event volume, the approach had to be modified (cf. Equation 3.3).

The last approach (V) represents the second approach for the calculation of the pre-event volume. It consists of a difference model (DoD) subtracting the slip surface from the pre-event surface (DEM 2011). Here, the volume of a potential slide mass, prior to the landslide event, is the final output (V_{pre}).

3.2 Sediment analyses

Sediment characteristics play an important role in landslide research and represent another essential predisposing factor, besides the above mentioned geomorphological characteristics. The determination of geotechnical properties of the slope sediments, especially the physical and mechanical parameters, is crucial for conducting slope stability assessments. In addition, pedological analyses allow for further characterization of the sediments and can provide important information on their provenance. The characterization of the sediments is based on the approach of combining field and laboratory analysis. The applied methods were chosen in order to receive a profound characterization of selected materials, however, with regard to fulfill the requirements for further slope stability modeling. The laboratory tests were performed largely following the recommendations of the German National Standards Institute. Moreover, exploratory work shows that, besides materials with sedimentological and volcanic origin, weathered sediments as well as soils are present in the study area. On this basis the decision was made, to use the pedological mapping guidelines (Ad-hoc-AG Boden 2005) for field description as with these instructions pedological characteristics as well as soil mechanical properties can be recorded. The terminology for soil used in this work refers to the conception used in soil science (Amelung et al. 2018) rather than to the engineering point of view (Prinz and Strauß 2011). The applied methods mostly involve standardized procedures, and therefore, will be described briefly with indication of the utilized references.

The following work integrates at some points raw- or analysis data from the theses of A. Lenz (Lenz 2019) and M. Füssl (Füssl 2020).

3.2.1 Field survey

Sampling took place in the Capulín landslide and close surroundings for further analyses between the years 2016 and 2018 and in total over 40 sites were sampled. Thereby, profiles and outcrops were sampled as individual sampling sites. The scarp area of landslides as well as the flanks can provide valuable information on the material properties. Thus, it was essential to place the sampling sites at the flanks and scarp of the Capulín landslide in order to gain a deeper insight of the way the material was affected by the slide process. Furthermore, the slide mass was sampled aiming to obtain detailed information on its composition, which can indicate the movement processes. In order to obtain reference material, which is crucial, among others, for investigating material provenance, the sampling design included the surrounding areas as well. Furthermore, the Escalanar landslide was sampled, including three sites and 25 samples.

The field description is based on the mapping guidelines according to Ad-hoc-AG Boden (2005), with the focus on soil texture, degree of consolidation, fabric, bulk density, voids, hydromorphological characteristics, carbonate content, soil moisture, soil color (Munsell Color company 2010), and humus content. Bulk samples as well as (replicate) core samples (volume of 100 m^3) were collected for further laboratory analyses. Coordinates and elevation a.s.l. were recorded for each sampling site (with a GPS), followed by a detailed description of the characteristics of the location.

3.2.2 Laboratory analysis

The *grain size distribution* plays an essential role in landslide investigations. On the one hand, it is important for the classification of the material and thus, provides valuable information on (e.g.) hydrological conditions. On the other hand, it is crucial for the calculation of various parameters, like hydraulic conductivity or friction angle, which represent important input parameters for slope stability modeling (Murthy 2003).

For the determination of the grain size distribution, a combination of the sieving and sedimentation method was applied according to DIN 18123-1 (1996a) and DIN ISO 11277 (2002). In general, the dry sieving method for the analysis of particles greater than 2 mm can be error-prone, especially for clay-dominated samples, therefore, the wet sieving method was used instead. Here, sieves with 2 mm (very fine gravel), 4 mm (fine gravel), and 8 mm (medium gravel) diameter were used. The sand fraction was divided in coarse

(2000-630 μm), medium (630-200 μm), and fine sand (200-63 μm) and in this case, the method of dry sieving was applied (as the silt and clay contents were already removed). The silt fraction, which was differentiated in coarse (63-20 μm), medium (20-6.3 μm), and fine silt (6.3-2 μm), as well as the clay fraction, defined as less than 2 μm, where determined with the sedimentation method based on the Stokes' law (DIN ISO 11277 2002, Prinz and Strauß 2011). For this purpose, the Köhn pipette analyses (Müller et al. 2009, Blume et al. 2011) was applied following the time steps according to Blume et al. (2011). As the samples in this study have their main differences in the smaller grain size fractions (< 2mm; cf. Appendix I), and in order to ensure consistency between the soil and sediment descriptions, the WRB (IUSS Working Group 2014) classification is used in the result chapters. However, for comparison a sediment-based classification according to Blott and Pye (2012) was used as well and is given in Appendix H - K.

The *limits of consistency* or Atterberg limits describe the plastic properties of cohesive material and thereby provide a measure for its sensitivity to water content changes (DIN 18122-1 1997). They can influence the shearing strength as it can vary at the plastic limit especially for different types of clays. They are also required for the derivation of cohesion and friction angle (DIN 1055 1976, Murthy 2003). The liquid limit (w_L), determined by the use of a Casa Grande liquid limit device as well as the plastic limit (w_P) were analyzed according to DIN 18122-1 (1997). The liquid limit represents the state of transition from the liquid state to the plastic state, whereas the plastic limit defines the limit between plastic and solid state (Murthy 2003, Dachroth 2017). The plasticity index (I_P), calculated by the subtraction of the liquid- and plastic limit, characterizes the plastic behavior of the material (Murthy 2003). Besides the consistency index (I_C) and the liquidity index (I_L), the activity index (I_A) was calculated in order to gain information on the different types of clay minerals (Prinz and Strauß 2011).

The *unit weight*, besides the *cohesion* and the *angle of friction*, represents an input parameter for the characterization of the material properties, which is required for stability modeling. The unit weight γ (kN/m³) or specific weight is calculated according to Murthy (2003) and Dachroth (2017) as the product of the bulk density and the acceleration due to gravity (9.81 m/sec²). The *dry bulk density* was calculated in accordance with DIN ISO 11272 (2001) by core samples with a volume of 100 cm³. Geomechanical parameters were obtained according to DIN 1055 (1976), which combines different laboratory data, like grain size

distribution and limits of consistency, in order to derivate geomechanical parameters like cohesion and friction angle. Non-cohesive soils were determined by using the soil texture classification (DIN 18196 2011) and bulk density. Cohesive soils were determined by the combination of soil texture classification and the consistency index (DIN 1055 1976).

The hydraulic conductivity of selected samples is analyzed in order to determine their behavior under hydraulic stress (Prinz and Strauß 2011). Therefore, *saturated hydraulic conductivity* was measured with the constant- and falling-head method according to DIN 18130-1 (1998a) and DIN 19683-9 (1998b). The material for saturated hydraulic conductivity analyses was collected during different field campaigns in the years 2016 and 2018.

On the one hand, pedological analysis allows for identification and characterization of soils and soil sediments. On the other hand, pedological parameters like organic matter or carbonate content can affect soil mechanical properties and therefore, it is an indispensable prerequisite to determine such parameters.

The *total carbon content (TC)* was determined by combustion analysis according to DIN ISO 10694 (1996c), using the analyzer Elementar vario ELcube.

The *pH* analyses is based on DIN ISO 10390 (2005) and each sample was measured with deionized water and $CaCl_2$. The pH values were classified in accordance with Ad-hoc-AG Boden (2005).

The determination of the *carbonate content* followed the recommendations of DIN 18129 (1996b) by volumetric method and can be classified according to Ad-hoc-AG Boden (2005).

3.3 Slope stability assessment

Slope stability can be assessed once the sediment characteristics and geomorphological conditions are determined (Abramson et al. 2002). Thus, physically based slope stability models are applied to incorporate the results from geomorphological and sedimentological analyses (cf. chapters 3.1 and 3.2). However, in the context of landslide susceptibility, these models demand detailed geometrical data and further, a comprehensive set of geotechnical input parameters. Geotechnical data require expensive and time-consuming analyses (i.e. field surveys and laboratory analyses). This fact usually leads to the situation that only few samples are available and therefore, most of the times

spatial data coverage is very low. As sampling and laboratory procedures are error-prone, data reliability can vary. Considering the described problematics, the present study aims to find balance between a restricted number of input data and the requirement to generate reliable slope stability maps. The related scientific approach is described below (Figure 3-7).

In order to maintain reliability and reproducibility it is crucial to use precise data that at the same time is easily accessible. Therefore, the input data is based on DEMs and geomorphological analyses. DEMs are available for many different regions of the world. Besides the DEMs, the slip surface location is required. Latter is more difficult to obtain, however, there are different methods for slip surface determination (Aryal et al. 2015).

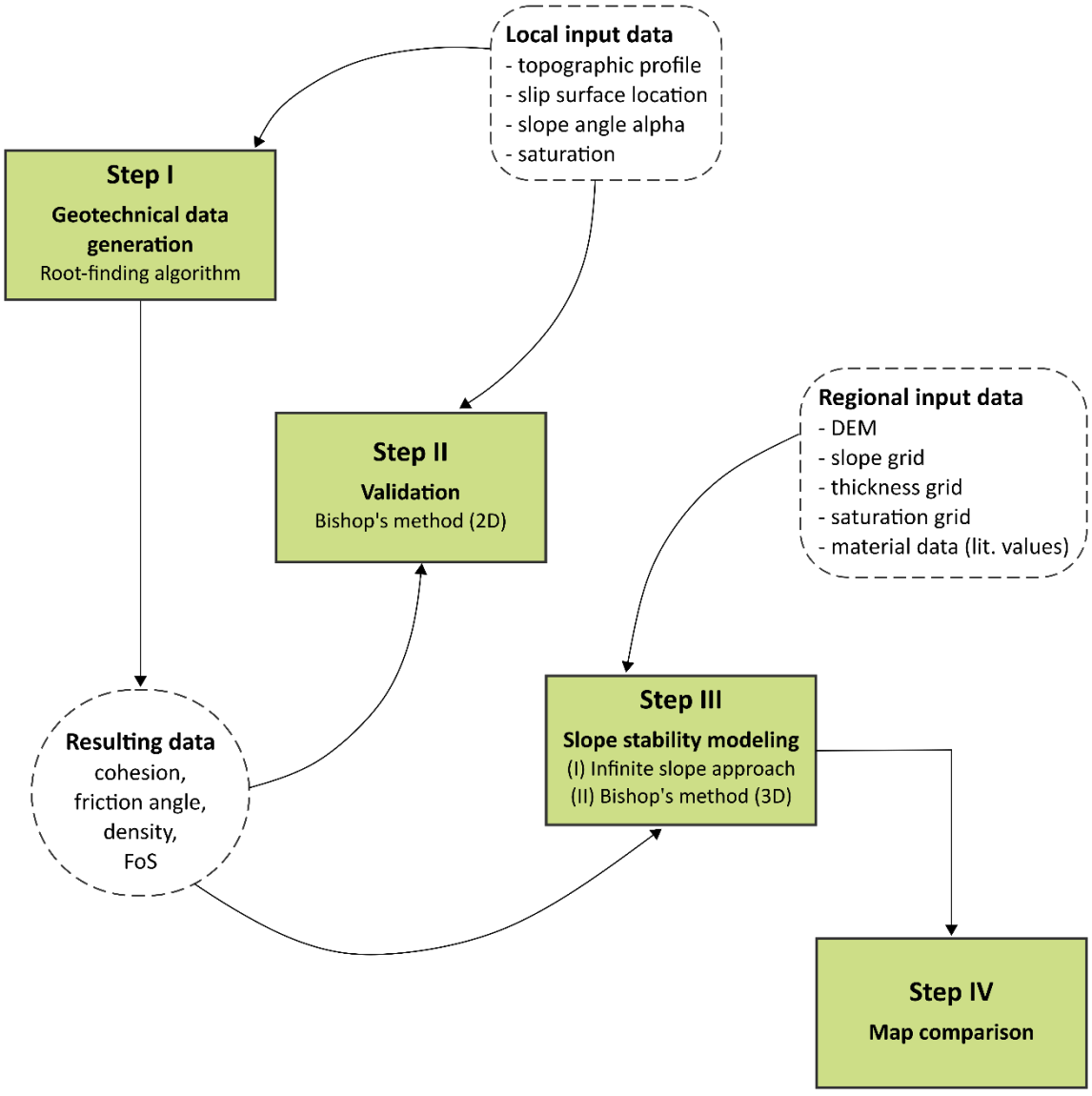

Figure 3-7. Process description of the developed slope stability approach. Source: Own illustration.

In this study, the determination of the slip surface is based on the chapters 3.1.4 and 4.4 and further used in this approach. After the geometrical input data is specified, the material properties are determined in Step I. In the present study cohesion, friction angle, and density are calculated on the base of geomorphological data (Step I). In order to assess the validity of the previous step the calculated parameters and derivation method are evaluated (Step II). In Step III, the results from the preceding steps are integrated in the slope stability modeling. Different approaches like finite element methods (FEM) or limiting equilibrium methods (LEM) exist to calculate slope stability (Duncan et al. 2014). However, they are based on mathematical models, each with its specific restrictions, which can lead to incompleteness of the susceptibility model. Hence, in this work two slope stability models with different theoretical backgrounds are applied and compared, in order to illustrate their strengths and weaknesses. This evaluation corresponds to the final Step IV (cf. Figure 3-7). In the following, each step is described in detail.

3.3.1 Step I – Input data generation

In the first step input data needs to be determined (Figure 3-7). Three main parameter groups are required for modeling slope stability, consisting of slope geometry, material properties, and hydrological conditions (e.g. Abramson et al. 2002). Material properties demonstrate a high susceptibility to error, and simultaneously are difficult to obtain for larger areas. In order to avoid the described errors, the material properties are calculated. Consequently, the remaining two groups have to be determined prior to the calculation (see detailed description below).

In order to generate the geotechnical parameters based on geometrical and hydrological data a suitable slope stability model has to be selected. Related to this, the infinite slope approach, a limit equilibrium method, is applied to calculate the Factor of Safety (FoS) (Duncan et al. 2014).

In general, limit equilibrium methods are essential for slope stability modeling, and the major part of them is used for two-dimensional and a smaller part for three-dimensional analyses (Abramson et al. 2002). These methods address slope stability by computing a FoS (Duncan et al. 2014). The FoS is defined as the ratio of resisting forces (shear strength) to driving forces (shear stress). The resisting forces represent the shear strength of the material, which is a function of friction angle and cohesion, and act in opposite direction

of the motion. Whereas the driving forces, with gravity as major force, act in the direction of the motion, facilitating downward movement (Pradhan et al. 2019). This means that FoS is the factor by which the shear strength has to be divided in order to achieve an equilibrium between shear strength and shear stress (Duncan et al. 2014). It is important to keep in mind that this factor only satisfies static equations and does not consider deformation or strain behavior (Krahn 2003).

In order to use a static equilibrium equation to calculate the FoS, data on the slip surface are required (Duncan et al. 2014). The FoS can be calculated either for a single body on top of a slip surface, or by separating the slide mass into slices. An example for the single body approach is the infinite slope method, which considers the equilibrium for a single mass, assuming a slope of infinite extent and a slip surface parallel to the slope surface (Abramson et al. 2002, Duncan et al. 2014).

In this approach, in order to calculate the FoS, the following equation according to Selby (1982) is applied:

$$FoS = \frac{c' + (\gamma - m\,\gamma_w)\, z\, cos^2\beta\, tan\phi'}{\gamma\, z\, sin\beta\, cos\beta} \tag{3.5}$$

c' corresponds to the effective cohesion (kN/m²), γ is the unit weight of soil (kN/m³), and γ_w denotes the unit weight of water (9.81 kN/m³). ϕ' represents the friction angle (°), z the depth of the slip surface (m), and β the inclination angle of the slope and slip surface (°). Variable m represents the vertical height of the water table related to the slip surface. If m is 0, the water table is below the slip surface, and if m is 1, it above the slip surface, reaching the ground surface (Selby 1982).

Usually slope stability is assessed by determing the Factor of Safety (FoS) of a certain slope or area by Equation 3.5. However, in this study, it is essential to mention, that this equation was further used to calculate geotechnical parameters. Therefore, the infinite slope equation had to be solved for the parameters cohesion (c'), unit weight (γ), and friction angle (ϕ').

Due to the fact that an analytical solution for the inverted Equation 3.5 does not exist, the Newton-Raphson method, which is a root-finding algorithm, can be applied, which allows for numerical solution of nonlinear equations. For a multidimensional problem, the Newton-Raphson method is modified (Press et al. 2006) to:

$$\boldsymbol{x}_{i+1} = \boldsymbol{x}_{\boldsymbol{i}} - \frac{\nabla f(\boldsymbol{x}_{\boldsymbol{i}}) * f(\boldsymbol{x}_{\boldsymbol{i}})}{\|\nabla \mathrm{f}(x_i)\|_2^2} \tag{3.6}$$

In this approach:

$$\boldsymbol{x} = \begin{pmatrix} x_{\phi} \\ x_{\rho} \\ x_c \end{pmatrix} \tag{3.7}$$

where x_ϕ represents the friction angle and x_ϱ the density. x_c is the cohesion and f is a fixed point function:

$$f(\boldsymbol{x}) \; = \; FoS(\boldsymbol{x}) - F_0 \tag{3.8}$$

where FoS(x) corresponds to Equation 3.5 and F_0 is a defined value. Technically, f(x) should represent the FoS Equation (f(x) = FoS(x)). However, this means that the FoS equals 0 as this is the condition for root-finding algorithms to solve an equation. Thus, Equation 3.8 enables that the FoS value can vary. It follows that the derivation of the geotechnical parameters can only be achieved by determing a FoS. For example, F_0 is defined to be 1.5 and the calculation of the FoS (FoS(x)) results in the same value. In this case, f(x) becomes 0 and the root-finding algorithm can be applied, i.e. x_{i+1} could be solved.

In summary, to solve the infinite slope equation (3.5) slope angle, slip surface depth, saturation, and FoS have to be known. However, further specifications are required. The Newton-Raphson method utilizes, as most root-finding algorithms do, iterations to find the roots (zeros). In order to limit this process, a number of iterations needs to be specified (Press et al. 2006). In this approach, it was set to 10,000. The second requirement is to start from one or more initial estimations to improve the solution (Press et al. 2006). This means that for cohesion, density, and friction angle a range needs to be specified as initial values. Here, the results from the laboratory analyses are applied (cf. chapter 3.2). The described information are prerequisites to solve the infinite slope equation. The script for the root-finding calculation is listed in Appendix A.

Input parameters: Required input data are geometrical and hydrological values. For slope geometry, the inclination angle of the slope and slip surface (β) as well as the slip surface depth (z) have to be specified. For the calculation of the parameter z, the slip surface is

subtracted (DoD) from the pre-event DEM 2011. The average depth of the erosional areas is calculated from this DoD and corresponds to z. The inclination angle β is determined by measuring the angle from the scarp to the outcrop of the slip surface (Figure 3-8). To address the hydrological conditions (m) the assumption is made that the landslide occurred while the saturation of the material was at an advanced stage, since no detailed information on the actual circumstances is available. In a last step, the FoS has to be determined. Usually, factor of safety values are between 1.0 and 1.3 (Selby 1982). In engineering designs, a more conservative range of 1.5 to 2.5 is estimated (Selby 1982). Abramson et al. (2002) indicate a FoS range between 1.25 and 1.5 for slope designs. In this study, the exact saturation remains unknown, and to address this uncertainty, the initial factor of safety value is set to 1.5.

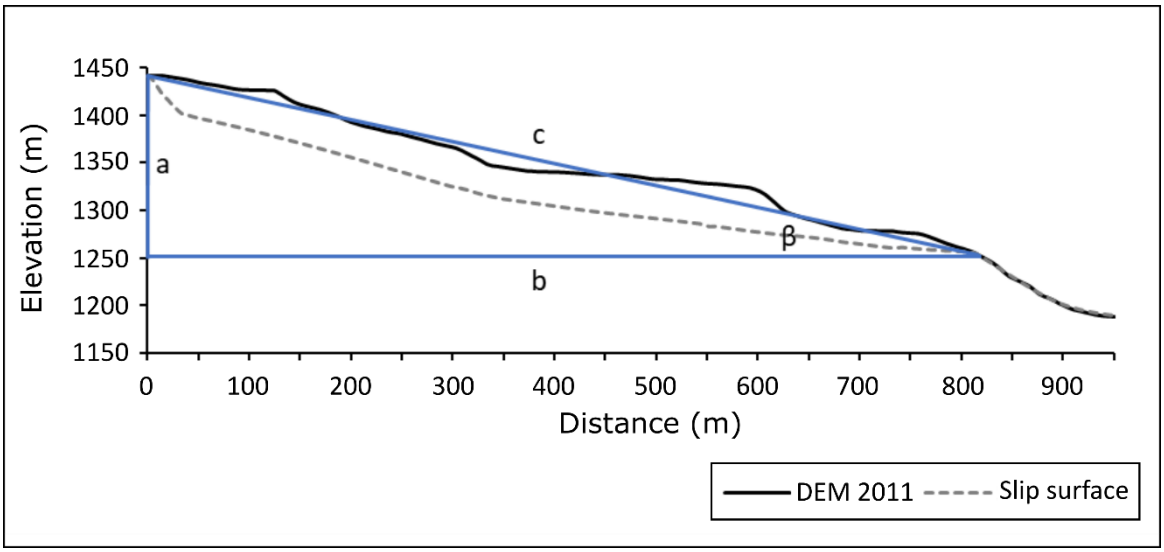

Figure 3-8. Cross section of the pre-event surface and the potential slip surface of the Capulín landslide. Blue lines indicate measurements for the inclination angle β. Source: Own illustration.

3.3.2 Step II – Validation process

Before the generated data from Step I can be used for slope stability modeling, the applicability of the developed approach needs to be validated. This validation is necessary as each model has its restrictions that can compromise the result. The mathematical model (infinite slope method) represents a very simplified limit equilibrium approach. Therefore, in a second approach, a more complex model, the method of slices, is used to validate Step I.

3.3.2.1 Method of slices – Bishop's Simplified Method

The method of slices corresponds to the limit equilibrium approach and divides the landslide body into vertical slices and solves the equation for each slice (Duncan et al. 2014). Latter approach has been widely used especially in the field of geotechnical engineering and was first presented in the early 20th century (Krahn 2003). Over the years, many modifications were made in order to improve the accuracy and to extend its scope of application (Chowdhury et al. 2010). The main difference between these methods is related to the question, which static equilibrium conditions they can satisfy. The equilibrium conditions are (I) equilibrium of horizontal forces, (II) equilibrium of vertical forces, and (III) equilibrium of moments (Abramson et al. 2002, Duncan et al. 2014). For instance, the Janbus simplified method only satisfies force but not moment equilibrium, whereas the Ordinary method of slices only considers moment equilibrium (Abramson et al. 2002, Duncan et al. 2014). Bishop's simplified method satisfies an overall moment equilibrium and vertical force equilibrium (Bishop 1955, Duncan et al. 2014). In the Spencer's method as well as in the Morgenstern and Price method, all three equilibrium conditions are considered and therefore, these methods represent rigorous approaches (Morgenstern and Price 1965, Krahn 2003, Chowdhury et al. 2010). In Step II, Bishop's simplified method was applied in a two-dimensional analysis to validate the suitability of the approach and the results from Step I.

Firstly, Bishop's simplified approach assumes a circular slip surface, and discretizes the slide mass into individual slices for calculating the FoS (Bishop 1955, Abramson et al. 2002, Chowdhury et al. 2010, Duncan et al. 2014). For the determination of the normal forces acting on the base of the slice, the equilibrium of forces in vertical direction is calculated. Here, the shear strength and normal force are resolved in direction of the weight (Abramson et al. 2002, Chowdhury et al. 2010, Reid et al. 2015). The resulting normal stress is further incorporated in the equation for equilibrium of moments in order to calculate the FoS (Duncan et al. 2014).

This method is illustrated in Figure 3-9a, where a_n represents the horizontal distance between the center of a slice and the center of the circle (with radius r) as well as α_n the inclination angle of the slices base (Duncan et al. 2014). W_n is the weight of the nth slice (Figure 3-9b), S_n represents the shear force on the base of the nth slice, and N the normal force acting on the base of the slice (Duncan et al. 2014). Furthermore, Bishop's simplified method satisfies the equilibrium of moments about the center of the circular surface as

well as the equilibrium of forces in the vertical direction (Abramson et al. 2002, Duncan et al. 2014). In Figure 3-9b, it can be observed that this method considers the lateral forces of the slices (E_n and E_{n+1}) to be horizontal. At the same time, it does not regard interslice shear stresses. The horizontal forces are not specifically included in the calculation method as only vertical forces are considered (Chowdhury et al. 2010, Duncan et al. 2014). Hence, it can be concluded, that Bishop's simplified method does not satisfy all requirements for static equilibrium, since it does not include equilibrium of horizontal forces (Abramson et al. 2002, Chowdhury et al. 2010, Duncan et al. 2014).

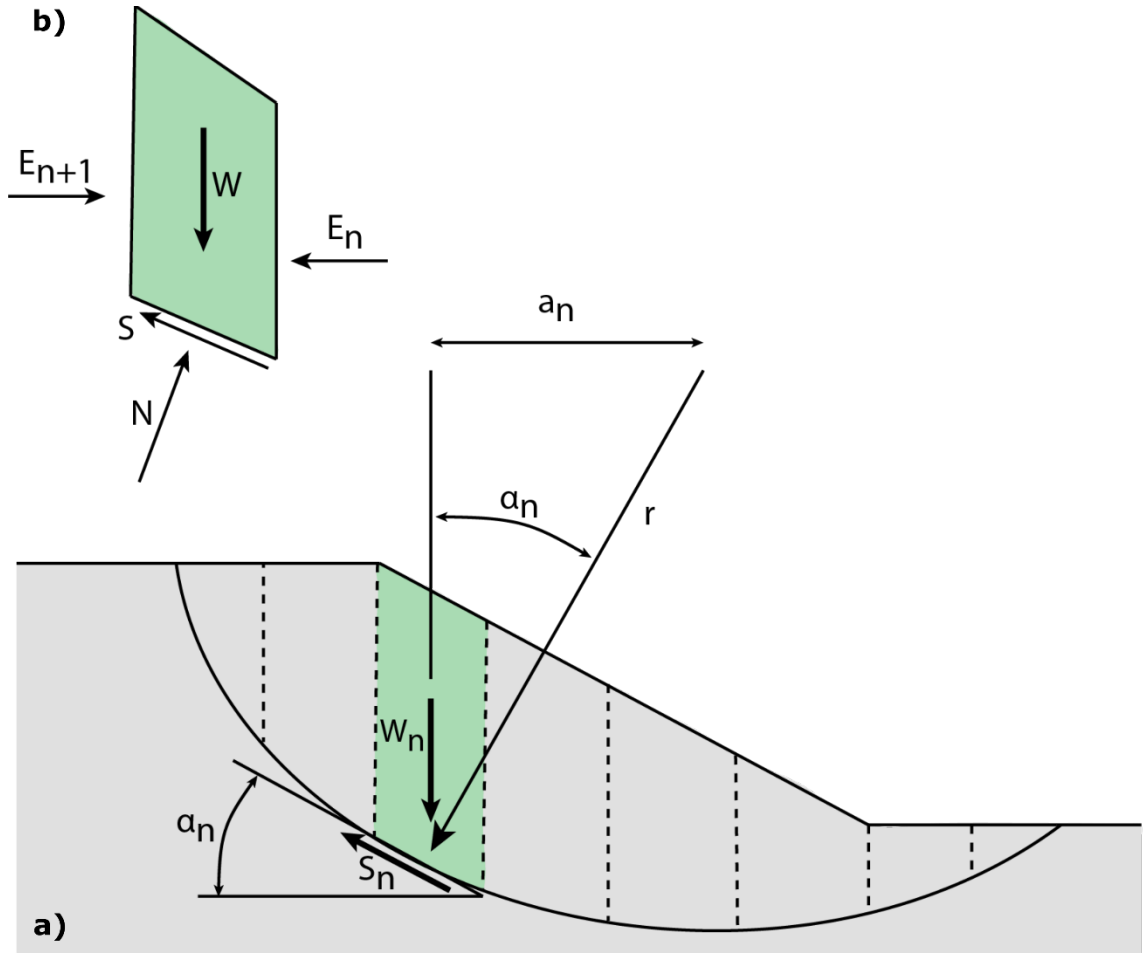

Figure 3-9. a) Schematic representation of a sliding mass with circular slip surface, divided into vertical slices and forces acting on a slice. b) Single slice with forces. Source: Modified after Duncan et al. (2014).

3.3.2.2 Calculations in Slope/W

The software 'Slope/W' is used to perform the limit equilibrium analysis. Slope/W is a commercial software product by GEO-SLOPE International Ltd., which uses limit equilibrium approaches to compute the Factor of Safety (Geo-Slope International 2018). In this work, version 'GeoStudio 2019' was employed. The user can choose from different approaches such as Janbu's, Spencer's and Morgenstern-Price method, or Bishop's simplified method (only to name a few examples) and the FoS can be calculated for different slips surface shapes (Geo-Slope International 2018).

Input data - The general requirements to evaluate slope stability comprise information on slope geometry, material properties, pore pressure, and loading (if applicable). These data also represent the main parameters that are required to calculate the FoS with the Software Slope/W (Geo-Slope International 2018).

The main components of **slope geometry** are slope surface topography and information on the slip surface. Related to the surface information, a representative cross section (A-B) of the Capulín landslide is derived from the pre-event DEM of 2011 (cf. Figure 3-10a, b). Slope/W provides various possibilities to determine the slip surface. One option is to specify entry and exit points of the slip plane. A further option consists of the grid and radius method, where a grid, specifying the coordinates of the radius and center of this circle, is specified. Latter method can be used in the case of a circular slip surface (Geo-Slope International 2018). It is further possible to fully specify the slip surface, in case the location is known (Geo-Slope International 2018). As this was the case here, the slip surface, determined in chapter 4.5, is fully specified (cf. Figure 3-10b). The **material properties** in Slope/W are addressed by applying a material strength model. Different options can be selected like e.g. anisotropic strength model, bilinear models, or the Mohr-Coulomb strength envelope (Geo-Slope International 2018). Latter approach describes the material strength, combining shear and normal stresses and represents a common approach in slope stability analyses (Abramson et al. 2002, Chowdhury et al. 2010). The Mohr-Coulomb model requires the specification of cohesion, friction angle, and unit weight of the materials in order to compute shear strength properties of the materials. The goal in Step II was to validate the derived parameters from Step I, and thus, the Mohr-Coulomb envelop is selected as it includes all calculated parameters. In order to ensure comparability, the material is defined as one layer as it was the case in Step I (Geo-Slope International 2018).

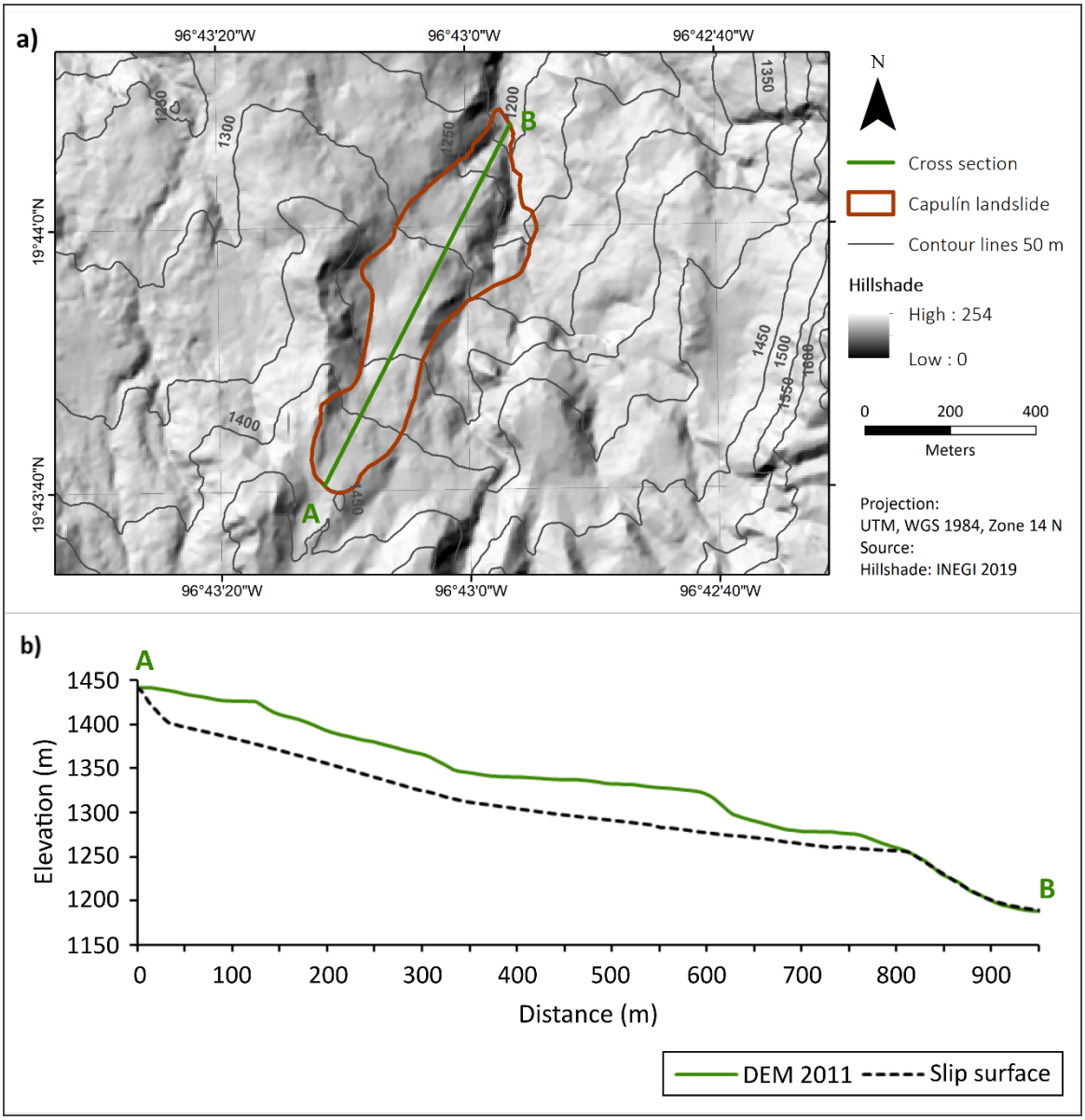

Figure 3-10. a) Polygon of the Capulín landslide, including the location of the cross section (A-B). b) Cross section (A-B) of the Capulín landslide, representing the topography before the event (in green), and the slip surface (in black, dashed line). Source: Own illustration. Source of background map: Esri World Imagery (2019).

Besides the specification of the shear strength parameters, the indication of **pore water pressures** is essential to determine the shear strength of slope material (Duncan et al. 2014, Geo-Slope International 2018). In Slope/W, this can be done with different configurations, such as indicating the spatial distribution of actual pressure conditions (definition of pore water pressures heads combined with a spatial function), or defining a piezometric line (Geo-Slope International 2018). As no detailed information on the hydrological conditions are available for the studied landslide, the option to define a piezometric surface is

applied. Single or multiple lines can represent the piezometric surface. In order to calculate the pore water pressure the depth below the indicated piezometric line is multiplied by the unit weight of water (Duncan et al. 2014). In the case of Slope/W, the pore water pressure of the slice base is calculated by multiplying the vertical distance between the piezometric line and the center of the slice base with the unit weight of water (Duncan et al. 2014, Geo-Slope International 2018). With this last step, the modeling process can start.

3.3.2.3 FoS comparison

For the validation process, the computed FoS_{Bishop} based on the Bishop's simplified method (Slope/W) can be compared to the $FoS_{infinite}$ calculated with the infinite slope approach (Step I). Primarily, different FoS values are integrated into the root-finding algorithm (Newton-Raphson method, cf. chapter 3.3.1), resulting in various geotechnical parameters. For example, the FoS of 2.0 is specified in the root-finding algorithm, which produces a certain set of values for the parameters cohesion, friction angle, and unit weight. The latter form the material input data for Slope/W and thus, the FoS_{Bishop} can be computed. Based on the same geotechnical input data Equation 3.5 determines the $FoS_{infinite}$. By consequence, a comparability is established. Since the two approaches are based on different mathematical theories, an exact accordance of the factors cannot be expected.

3.3.3 Step III (A) - Slope stability modeling – infinite slope method

The generation of geotechnical input data in Step I and its validation in Step II enable the calculation of the infinite slope approach for a larger area. The freely available program 'SAFETY FACTOR' (tool author: A. Günther), a tool provided by SAGA GIS (System for Automated Geoscientific Analyses, version 6.2.0, Conrad et al. 2015) is used in order to apply the infinite slope model in a GIS environment. SAFETY FACTOR is based on the Equation 3.5 (chapter 3.3.1), which is suitable for landslides with a comparable low length to depth relation of the landslide and a parallel slip surfaces (Selby 1982, Duncan et al. 2014). It computes a slope stability raster, representing the ratio of the resisting and driving forces acting on a potential slip surface. Slope stability is calculated for each pixel separately. The raster represents a continuous FoS, which can further be classified into FoS-classes ('highly unstable', 'unstable', 'moderate', 'stable', 'highly stable').

The program requires following input parameters:

- inclination angle of the slope (**slope**)
- depth of the slip surface (**thickness**)
- water saturation of the slope (**saturation**)
- cohesion, friction angle, unit weight (**geotechnical parameters**)

The program provides the option to indicate all input values globally, i.e., minimum and maximum values of each parameter for the whole area. Furthermore, a spatial distribution can be achieved, by the formation of process regions, comprising specific values. The determination of such regions is essential as it offers the possibility to divide the study area into zones. Thus, areas with the same geotechnical properties are identified and summarized into process regions.

In the present study, the **process regions** (Figure 3-11) are determined based on the geological map (1:500,000) and the slope grid (in degrees) derived from the DEM 2011 (INEGI 2019). The slope grid is classified into steep and flat areas and these classes are combined with the geological units resulting in three main process regions (cf. Figure 3-11).

Region 1 is classified as 'basalt' according to the geological map, mainly consisting of steep slopes (> 40°) and is primarily located at the margins of the study area (INEGI 2019). As the smallest of the three regions, Region 2 is characterized by tuff and slope deposit and exhibits steep slopes (> 40°) as well. Region 3 accounts for the majority of the study area and represents the same geological and sedimentological units as Region 2, however, differs in the elevation range as it consists of moderate to flat slopes (> 40°).

The **geotechnical parameters** cohesion, friction angle, and density are assigned to the three process regions. For each parameter one raster, containing the minimum and one containing the maximum values is created. Accordingly, each raster (e.g., cohesion raster) contains different values depending on the process region. The main geological unit of Region 1 is basalt with geotechnical values according to Selby (1982). The parameters for tuff according to Asniar et al. (2019) build the base for Region 2. Instead of literature values, Region 3 involves input data from Step I of the described workflow. Minimum and maximum values are assigned to process Region 1 and 2. Whereas for Region 3 minimum and maximum values were not necessary, since the derived values were determined specifically for this region.

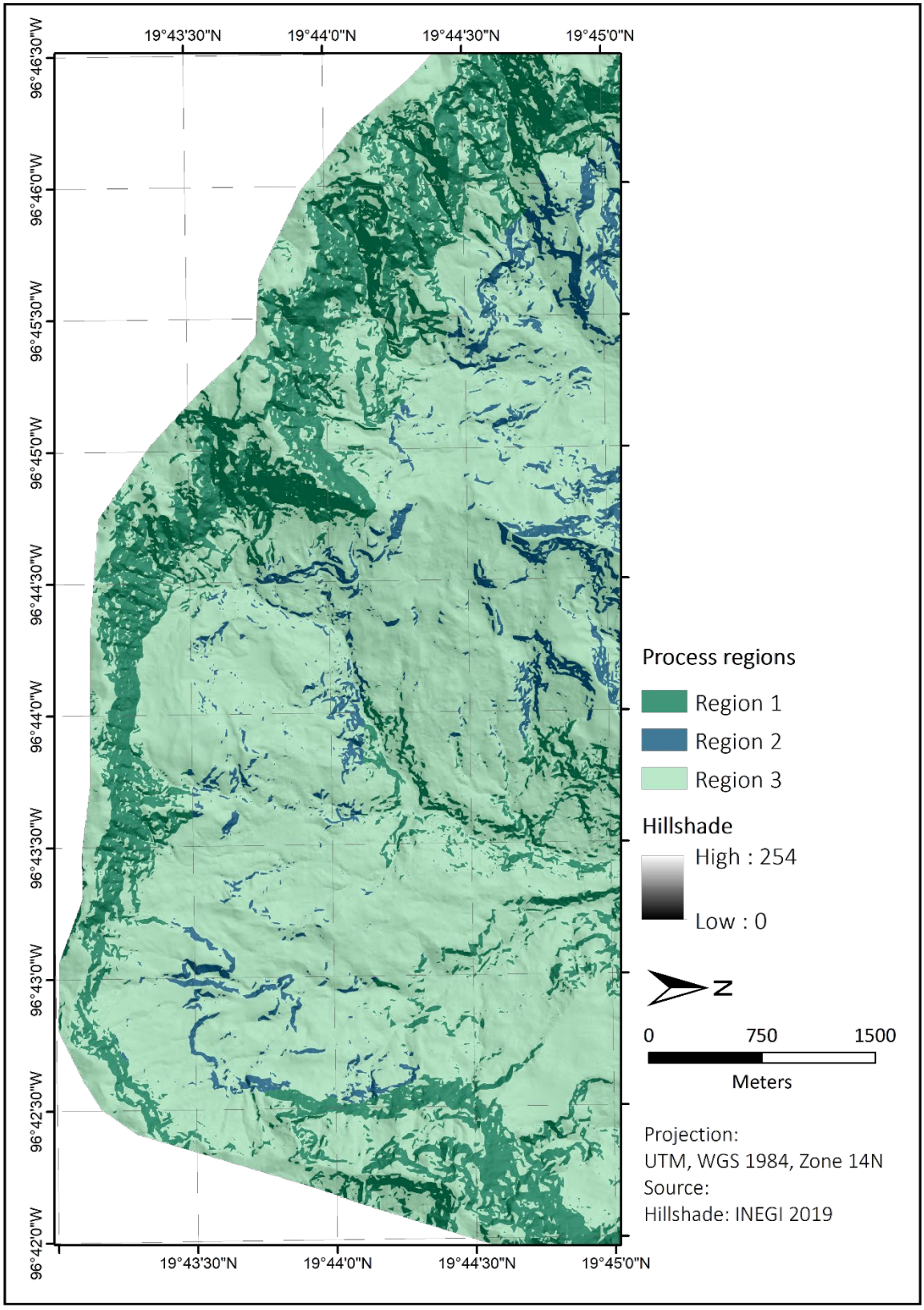

Figure 3-11. Process regions of the study area. Region 1, with the geological unit basalt and slopes greater than 40°. Region 2, with slopes greater than 40°, located in the geological unit of tuff and slope deposits. Region 3, representing moderate to flat slopes (< 40°) with tuff and slope deposits. Source: Own illustration. Source of background map: Esri World Imagery (2019).

The DEM 2011 provides the topographic parameters. **Slope inclination** is calculated in radians for the complete area. As second topographic information the SAFETYFACTOR tool requires the depth of the slip surface (**thickness** or **layer thickness),** which corresponds to the depth measured from the surface to the potential slip surface (Selby 1982).

For the entire study area, the thickness is determined by considering the relationship between layer thickness and slope and can be calculated by the following equation as:

$$T = d * (slope_{max} - grid_{slope}) \tag{3.9}$$

where *T* is the thickness grid, with each cell containing a value representing thickness from the surface to the potential slip surface at a certain slope degree, and s*lope*$_{max}$ represents the maximum value of the slope raster. G*rid*$_{slope}$ represents the entire slope raster, and d is a parameter to be determined with:

$$d = \frac{t}{(slope_{max} - s1)} \tag{3.10}$$

where *s1* represents a certain slope degree and *t* is the thickness at this slope degree (s1).

In order to calculate *d* it is a necessary requirement to use an exemplary case study where the thickness at a specified slope is known.

The last parameter for SAFETYFACTOR is the **saturation.** These values are determined by calculating a flow map in GIS (SAGA) using the flow accumulation recursive tool. This tool processes recursively all cells that are connected upwards and continues the process until each DEM cell is processed (Tarboton 1997). The calculation is carried out based on the DEM 2011 and the output is a flow accumulation raster. This raster has a wide value range and needs to be adjusted as the slope stability analysis requires values that range from 0 (no saturation) to 1 (fully saturated). For the required modification, a logarithmic normalization is selected in order to consider the large value range. This can be observed in the following equation:

$$sat = 1 - \ln(\frac{\mathrm{e1}}{sat_{max}}) / \ln(\frac{sat_{min}}{sat_{max}}) \tag{3.11}$$

where *e1* is the raster cell value of the flow accumulation grid, *sat*$_{max}$ is the maximum value and *sat*$_{min}$ the minimum value of the flow accumulation raster. *Sat* is the resulting raster that represents the saturation for the area of interest.

3.3.4 Step III (B) – Slope stability modeling – Bishop's simplified method (3D)

In Step II Bishop's simplified method has been applied in a two-dimensional analysis for the single slope of the Capulín landslide. In Step III-B, slope stability is computed for the entire study area by employing Bishop's simplified method in a three-dimensional approach. The software Scoops3D analyzes slope stability based on DEM data (Reid et al. 2015). Scoops3D implements the limit equilibrium method and extends it from a two- to a three-dimensional approach applying the method of columns (Reid and Brien 2006, Reid et al. 2015). This methods differs from the 2D approach as it extends the vertical slices, in which the slide mass is normally divided in, into vertical columns. Thus, a three-dimensional slope stability analysis of various potential landslides is computed, while simultaneously it takes three-dimensional characteristics into account (Reid et al. 2015). Scoops3D first identifies areas with potential landslides within the DEM using spheres as in general spherical slip surfaces are assumed, to cut the terrain model (DEM). This process generates intersections, which are defined as trial surfaces (Reid and Brien 2006, Reid et al. 2015). The program analyzes the entire DEM and can compute a large number of intersections. The software design allows for defining search parameters, such as search lattice extend, limit of the material volume, and resolution of the search (Reid et al. 2015).

In a second step, the stability of these trial surfaces is analyzed with the limit equilibrium method. Scoops3D offers the option to choose between the Ordinary method and Bishop's simplified method (Reid and Brien 2006, Reid et al. 2015). For comparative purpose, latter approach was selected in this work. The result of the limit equilibrium analysis is a uniform FoS for each trial surface, meaning that each pixel of an intersection represents the same FoS value (Reid et al. 2015). During this procedure, each pixel can be analyzed by various different trial surfaces and therefore, the smallest FoS has to be selected for each pixel. In this process, each cell of the DEM can be included into various different intersections and therefore, the trial surface representing the lowest FoS is specified as the potential slip surface for this particular cell (Reid and Brien 2006, Reid et al. 2015, Weidner et al. 2019). As final result, the slope stability calculation in Scoops3D produces a raster representing the minimum FoS values, which were calculated on the potential slip surfaces for each pixel of the DEM (Reid et al. 2015).

Input data: Scoops3D offers a wide range of configuration options that allow for the integration of specific characteristics. The main parameters required for the slope stability analysis, besides a DEM (**topography**), are thickness of an arbitrary number of **layers**, and

definition of the **hydrological conditions**. Latter can be defined by pore-pressure ratio, indicated as a piezometric surface, or can remain undetermined (Reid et al. 2015). For each indicated layer, the specification of **material properties** is required as well. For the present study, these properties are defined as follows:

- **Topography:** For the specification of the topography, a DEM is required, which in this case is the pre-event DEM from 2011 (INEGI 2019).
- **Layers:** In case of different geological conditions, their spatial distribution can be addressed by defining different layers. The elevation of the lower boundary of each layer has to be indicated, which means that the lowest layer has no boundary and is assumed to be infinitely deep. However, the upper boundary of the shallowest layer is determined by the DEM (Reid et al. 2015). Here, two layers are determined, with Layer 1 consisting of tuff and slope deposits (comparable to Region 2 and 3 from Step III-A), and Layer 2, representing the geological unit 'basalt' (comparable to Region 1 from Step III-A).
- **Material properties**: For each layer the material properties cohesion, friction angle, partially saturated, and fully saturated unit weight need to be defined. Layer 1 integrates values resulting from Step I and Layer 2 those from literature according to Selby (1982).
- **Hydrological conditions**: The final task is to define the hydrological conditions. In this case, a piezometric surface was used, which enables to compute the pore pressure by multiplying the vertical depths beneath the piezometric surface with the unit weight of water (Reid et al. 2015). In this case, the piezometric surface ($piezo_{surface}$) is calculated as follows:

$$piezo_{surface} = DEM_{AI} - \Psi \tag{3.12}$$

where DEM_{AI} is the digital elevation model representing the area of interest, and Ψ corresponds to a parameter to be determined with:

$$\Psi = T * (1 - sat) \tag{3.13}$$

where T is the layer thickness (equation 3.9, described in chapter 3.3.3), and sat the saturation raster (equation 3.11, described in chapter 3.3.3).

3.3.5 Step IV – Evaluation process

The comparison of the FoS maps is carried out in order to assess prediction effectiveness and suitability of the different models. The assessment of the obtained results integrates two different approaches. First, the absolute area and their relative share of the FoS classes are calculated for each model and compared. They are calculated for the complete study area and furthermore for each process region individually.

Secondly, a pixel based difference model is created to determine the discrepancy between the FoS classes. The model indicates the class deviations between the maps and simultaneously enables the detection of spatial patterns.

4. Results of the geomorphological analyses

4.1 Geomorphological characterization of the Capulín landslide

In the year of 2013, the coastal state of Veracruz (Mexico) experienced a period of intensive rainfalls due to numerous storms of different intensities. Several flood events and over 650 landslides took place as consequences of these rainfalls (Guzmán Lagunes and Morales Barrera 2014). The landslides concentrate in the center of the state of Veracruz, due to its mountainous terrain. During the period between the 12 to 17 September (2013), a category 1 hurricane (Hurricane Ingrid) passed by the coast of Veracruz causing intensive rainfalls in the entire state. In the following days (21-22 September), a cold front (No. 1) occurred causing extreme rainfalls, especially in the study area and its close surroundings (Guzmán Lagunes and Morales Barrera 2014). Subsequently to this heavy rainfall period, the Capulín landslide was initiated on October 1st in the year of 2013 and represents one of the largest landslides of the corresponding period (Guzmán Lagunes and Morales Barrera 2014). It is situated near the villages El Capulín and El Escalanar in a slope area with elevations ranging from 1,900 to 1,100 m a.s.l. The steepest parts of the slope are between 1,900 and 1,650 m a.s.l., with slope inclination values between 35 and 65°. The scarp of the Capulín landslide is located at 1,445 m a.s.l., while the landslides toe reaches down to approx. 1,190 m a.s.l. related to slope inclinations with a mean value of approx. 20° (Figure 4-1/1). Even though the initial movements cannot clearly be determined in retrospect, it can be supposed that the first movements started in the lower parts of the slope, in close proximity to the stream (Figure 4-1/1). Various eyewitnesses, mostly farmers from the village El Capulín, who already recognized movements on their terrains prior to the event, support this assumption. The movements continued further upslope resulting in a landslide with a maximum length of approx. 1,000 m (Figure 4-1-1). The main movement endured for three days, whereas smaller movements occurred for a longer time. The scarp is approx. 180 m wide and the slide reaches its maximum width of 300 m in the lower parts (below the current road, Figure 4-1/1). The height of the semicircular scarp is up to 35 m with a steep slope (> 45°, Figure 4-1/1). The inclination decreases towards the slide mass, where loose material of the upper areas accumulates. The transition to the slide mass is fluent, continuing to the more plane surface (< 10°) of the accumulation area (Figure 4-1/1, 2). On this plane surface the original vegetation remained vital, indicating that this part of the slide mass moved as a coherent slide block (Figure 4-1/2). It is approx. 90 m wide, with

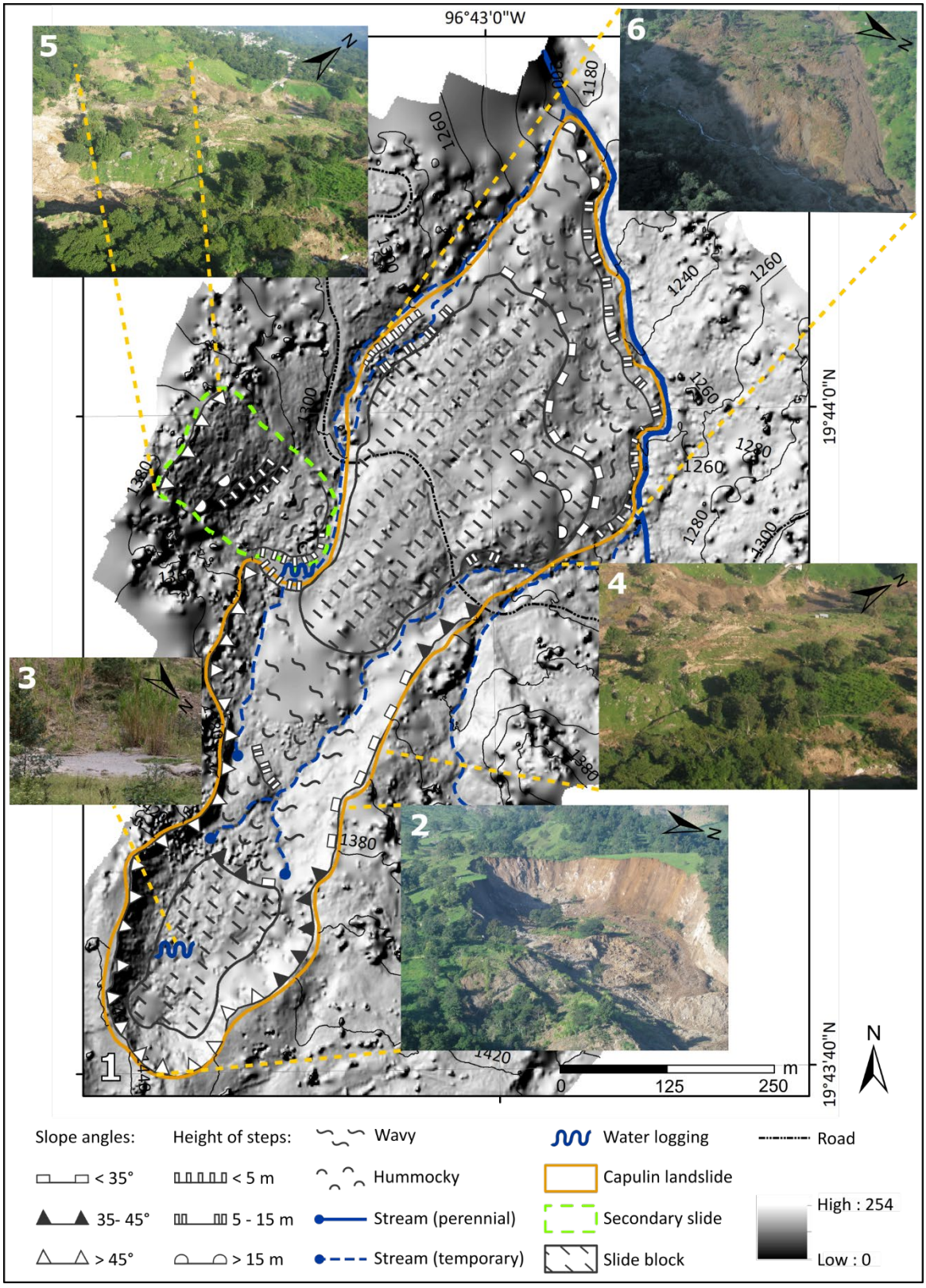

Figure 4-1. Geomorphological map of the Capulín landslide (1) and photographs of different landslide sections: 2 = upper part including scarp, upper slide block (vegetated area in the slide mass), area of severe distortion, and eastern flank; 3 = water logging (Source: Wilde, 2018); 4 = lower slide block; 5 = secondary landslide; 6 = foot area. Source: Geomorphological symbols: modified after Leser et al. (1975) and Terhorst (1997). Photographs 2, 4-6: S. Rodríguez Elizarrarás, 2013.

a maximum length of 170 m, and is slightly tilted backward toward the scarp, which indicates a rotational movement. Water logging occurs at the western side of the slide block (Figure 4-1/3). Subsequently to this upper slide block, the inclination increases suddenly (> 35°) and this part of the slide mass extends for over 200 m and is limited by a complex step with heights between 2 and 4 m (Figure 4-1/1). Photographs from 2013 show that this part of the slide mass experienced severe distortion resulting in a wavy to hummocky surface (lower right corner of Figure 4-1/2). Various temporary streams emerge in this section and are incised approx. 1 to 4 m into the slide mass (Figure 4-1/1). One of the streams is located at the western flank and the others flow along the eastern flank (Figure 4-1/1). In this area, the eastern flank shows inclinations of less than 35° while the western flank is very steep, with inclinations of more than 45° (Figure 4-1/1). A secondary landslide, which has a length of approx. 90 m and a width of 80 m, interrupts the western flank (Figure 4-1/5). As a consequence to the occurrence of this secondary process, the main slide mass is shifted eastwards. The foot of the secondary landslide is south east facing and has a height of approx. 2 to 4 m. A temporary stream at the margins of this foot separates the secondary from the primary process. Here, the main slide mass is characterized by a large slide block, which has a width of approx. 240 m and with 380 m it is twice as long as the upper slide block (Figure 4-1/2/4). It contains original vegetation, such as coffee plants, shrubs, and trees that survived the movement and remained vital (Figure 4-1/4). The small coffee plantations were still under cultivation three years after the movement. The fairly intact vegetation indicates that this lower slide block experienced only minor internal distortion and moved as a coherent mass.

At approx. 1,260 m a.s.l., the inclination increases up to 35°, which marks the transition from the lower slide block into the foot area (Figure 4-1/1). A hummocky and wavy surface characterizes the foot. The photograph of the foot from 2013 (Figure 4-1/6) shows flow-type processes present in this area, which most likely are responsible for the development of this surface forms. Towards the stream, which runs along the landslides foot, the slide mass forms a distinctive step with heights ranging from 5 to 15 m, and a maximum height of 20 m at the northwestern toe (Figure 4-1/1). It is highly probable that the stream removed material from the slide mass, which, as a consequence, resulted in this steep step (> 35°, Figure 4-1/1).

4.2 Digital elevation models

In order to document successive changes of the Capulín landslide DEMs representing different temporal survey periods were generated (method description see chapter 3.1.1) and compared with the available DEM data from 2011, reflecting the conditions prior to the landslide event. The DEM 2013 is based on data derived from photographs taken from a helicopter one day after the landslide event and photographs collected from an unmanned aerial vehicle (UAV) form the base for the DEM 2016.

The main parameters of the photogrammetric surveys are reported in Table 4-1. The comparison of both DEMs demonstrates that data derived from the photographs collected by the UAV is more precise than the helicopter photographs. With 0.09 m/pixel the DEM 2016 shows a higher resolution than the DEM 2013 with 0.24 m/pixel. This difference can be observed in the ground resolution as well (cf. Table 4-1). The higher number of tie points (twice as much) and projections result from the substantially higher amount of available photographs (Table 4-1) as from the 2016 survey over 400 photographs are available and only 88 from 2013. A further difference consists in the number of GCPs, which are utilized in the generation process. For the DEM 2013 only 7 out of 21 GCPs are suitable, whereas all GCPs were used for the DEM 2016.

Table 4-1. Main acquisition parameters of the 2016 and 2013 surveys.

	December 2016	**October 2013**
Number of images	423	88
Number of aligned images	367	57
Coverage area (km²)	0.585	1.66
Ground resolution (cm/pixel)	4.77	11.8
Number of tie points	99,717	49,052
Number of projections	227,093	121,455
Reprojection error (pixel)	0.296	0.395
Number of GCPs	21	7
Orthomosaic resolution (m/pixel)	0.05	0.12
DEM resolution (m/pixel)	0.09	0.24

4.2.1 Analysis of the DEM 2016

Based on the data collected in 2016 and the resulting 3D-model generated in Agisoft, a digital terrain model (DTM) as well as a digital surface model (DSM) were produced. The DTM 2016 generated from the dense cloud (in Agisoft) has a resolution of 0.09 m (Table

4-1). However, considering the accuracy (total error) of the applied GCPs (Table 4-2) the DEM was exported with a cell size of 1 m (Figure 4-2a) and, for further calculations with the LiDAR DEM (DEM 2011), with a cell size of 5 m as well. The resulting orthomosaic was furthermore exported with a cell size of 1 m (Figure 4-2b).

Accuracy assessment of the GCPs: As a first step of the accuracy assessment the Root Mean Square Error (RMSE) of the control and check points was calculated (Table 4-2). The check points record a total error of 1.39 m and the total error of the control points is 0.96 m. The check points with highest error are mainly located inside the landslide area, while control points with highest errors are mostly located in external areas (Figure 4-2b). Simultaneously, check and control points reflecting low errors are situated outside the landslide, preferentially located in areas with low vegetation (primarily grassland). However, some GCPs located on grassland or bare ground also show high errors. Consequently, the surrounding environment seems to be not the only determining factor for high accuracy.

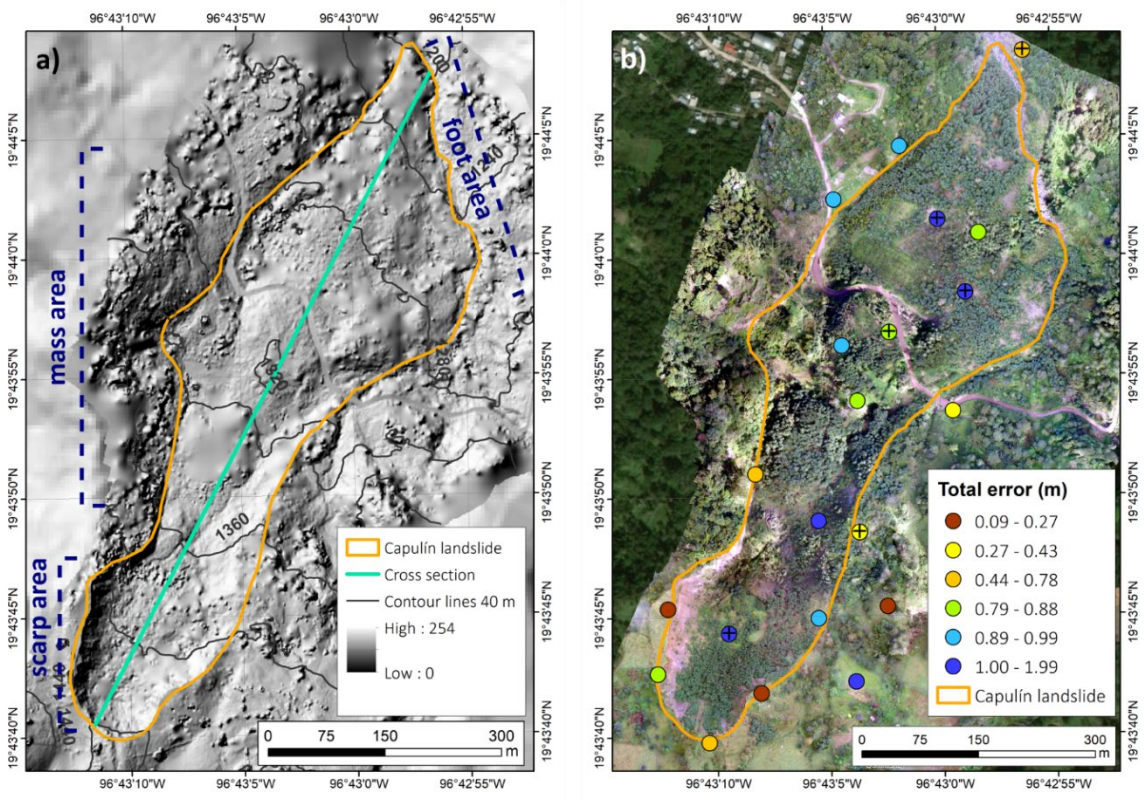

Figure 4-2. a) Resulting DEM 2016 visualized by a hillshade (cell size of 1 m). Furthermore, the approx. division into scarp, slide mass, and foot area is shown. Source of background map: INEGI (2019). b) Orthomosaic acquired from the photographs collected by the UAV. Location of the GCPs (showing their horizontal errors) used as control points (colored circles) and check points (colored circles with cross) for the DEM 2016. Source: Own illustration. Source of background map: Esri World Imagery (2019).

Table 4-2. Ground Control Point accuracy for the 2016 data.

Type	Count	XY error	Z error	Error (pixel)	Total error (m)
Control points	15	0.50923	0.813895	2.887	0.9601
Check points	6	1.23926	0.632639	4.946	1.3914

Most of these GCPs are difficult to identify on the photographs, which reveals that image resolution has to be regarded as a further decisive factor. The attempt to generate a 3D-model with fewer, more precise GCPs resulted in a less accurate DEM and was consequently rejected.

Vegetation classification results: Overall, the DSM is applied to assess the result of the vegetation classification process (according to chapter 3.1.1) by comparing it with the DTM. The difference between vegetation (DSM 2016) and ground surface (DTM 2016) is clearly visible in Figure 4-3. In areas without vegetation both cross sections coincide (e.g. between 440 and 460 m at the cross section, cf. Figure 4-3). However, the DTM 2016 cross section shows surface unevenness in the first segment of the cross section in Figure 4-3 (red box). In some cases, this is related to insufficient filtering, however, in this particular case the unevenness reflects the disturbed surface caused by the mass movement.

As already stated in chapter 3.1.1, best classification occur when NDVI is calculated prior to the dense cloud creation, which is further classified in Agisoft Metashape with the tool 'classify points'. Figure 4-4 presents the classified dense cloud results, with (Figure 4-4a)

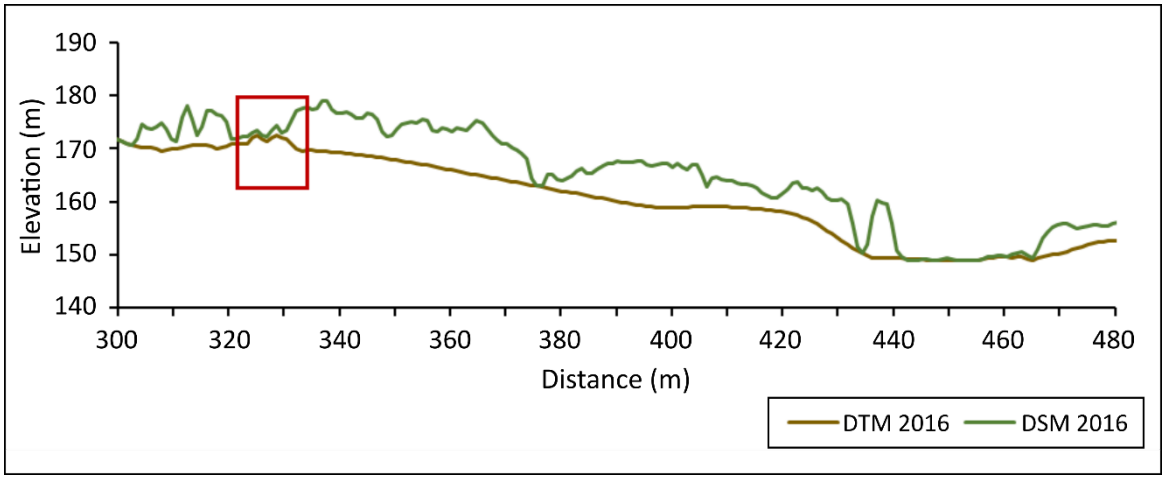

Figure 4-3. Exemplary cross section extract along the Capulín landslide transect (Figure 4-2a) comparing the DEMs before (DSM) and after the filtering process (DTM). Unevenness of the DTM 2016 marked in red. Source: Own illustration.

and without previous NDVI calculation (Figure 4-4b). The cross sections prove that the first approach (DEM A) leads to enhanced filtering of the vegetation as the resulting line exhibits less peaks (cf. Figure 4-4c). However, the filtering process has the disadvantage of simplification, which is obvious in the first segment of the cross section in Figure 4-4c (blue box) where DEM A cuts a depression. Since the error range of the classification without NDVI preparation is higher, the generation of the 2016 DTM integrates the first approach (with NDVI preparation). The automated point classification in Agisoft Metashape leads to three classes (cf. Figure 4-4a and b). The major part of the dense clouds is identified as 'high vegetation' (green), followed by the class 'ground points' (brown). The remaining class is referred to as 'buildings' (red; cf. Figure 4-4a, b). The 'buildings' class contains steep areas with mainly white and gray colors, which, in this case, represent non-vegetated areas and part of the scarp area (without vegetation as well). The classification as 'building' objects is therefore incorrect and requires adjustment. In order to avoid this type of misclassification the 'buildings' class from dense cloud a)

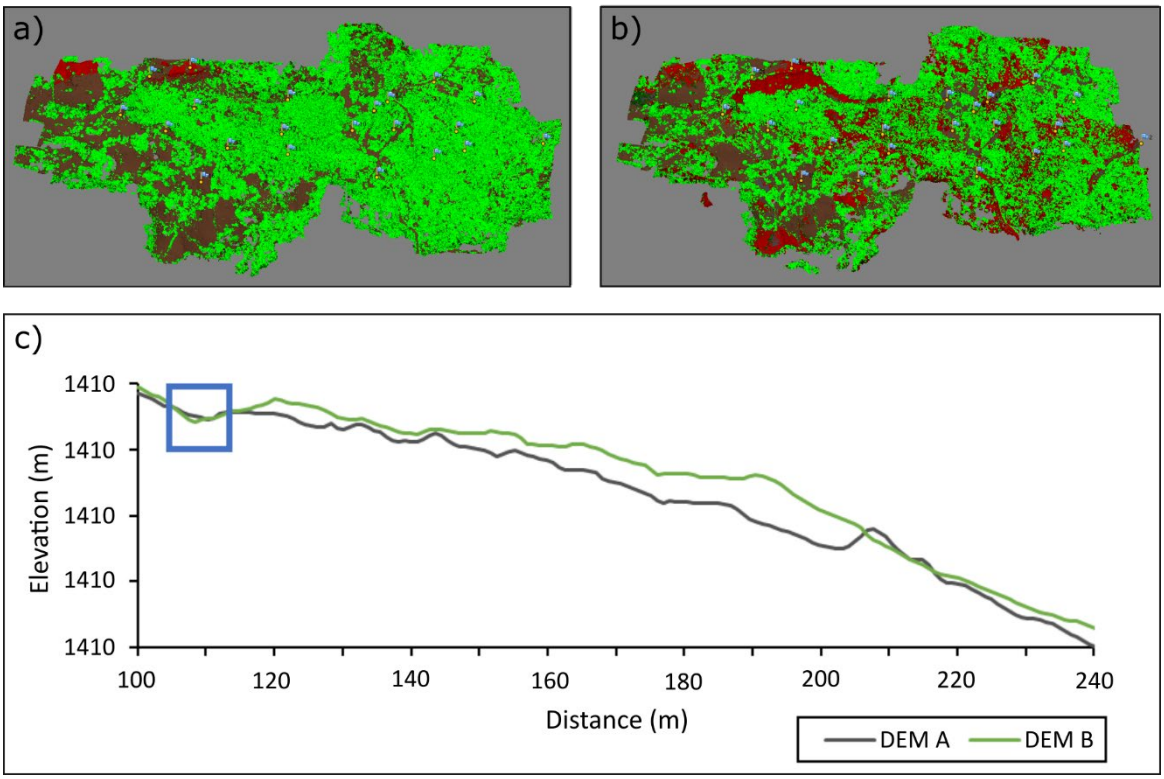

Figure 4-4. Classified dense cloud derived from Agisoft: a) with preliminary NDVI preparation and b) without preliminary preparation. Green color represents the class 'high vegetation', brown represents 'ground points' and red represents the class 'building'. c) Exemplary extract of DEM cross sections with (DEM A) and without (DEM B) preliminary NDVI preparation of the dense cloud. Depression, which is cut out in DEM A is marked in blue. Source: Own illustration.

(Figure 4-4a) is transferred into the 'ground' class. However, for dense cloud b) this transfer is not possible as the 'buildings' class includes points from 'ground points' and 'high vegetation' class (cf. Figure 4-4a, b). Thus, the transfer would lead to additional misclassification and thus, was rejected. Accordingly, dense cloud a) forms the base to generate the DTM 2016.

When considering Figure 4-5a some misclassifications in the DEM can be observed although filtering was applied. A critical point consists in the fact that in some parts vegetation is still visible (cf. Figure 4-5d, e). This leads to the conclusion that filtering is not sufficient in all areas. In the center (Figure 4-5b, c) and in the foot area of the slide mass (Figure 4-5a) the surface is too generalized, as a consequence of very dense vegetation. These observations demonstrate the importance to include the calculated error in subsequent analyses in order to avoid overestimation of the surface height.

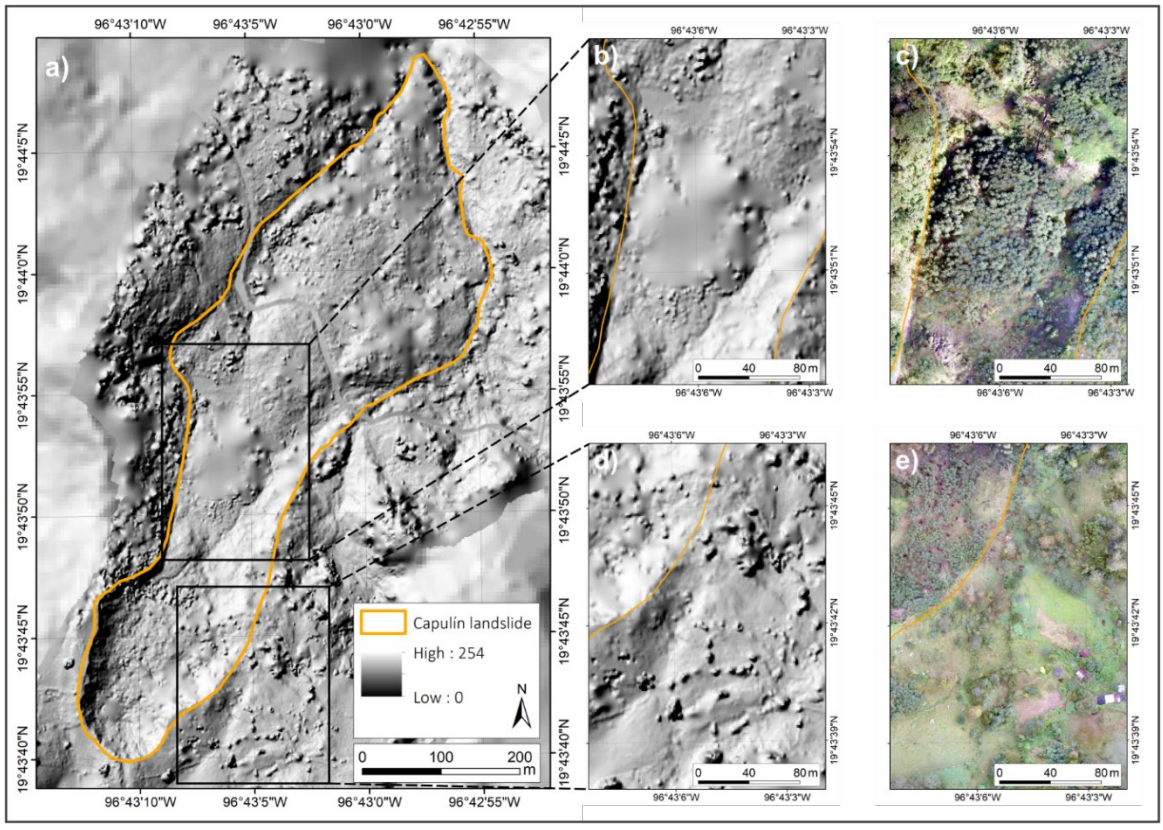

Figure 4-5. a) Hillshades derived from the DEM 2016. Source of background map: INEGI (2019). b) Detailed close-up of the hillshade and c) related orthomosaic acquired from the photographs collected by the UAV. d) Detailed close-up of the hillshade and e) related orthomosaic. Source: Own illustration.

Accuracy assessment of the DTM 2016: In the second step of the accuracy assessment, the DTM 2016 was adjusted to the LiDAR DEM 2011 (detailed description see chapter 3.1.1). It has a mean absolute difference (ME) of 1.0 m in comparison to the DEM 2011 (Figure 4-6a) and therefore, it ranges in the same magnitude as the resulting error of the georeferencing (GCP accuracy). The comparison of the DEM 2016 and DEM 2011 shows a very strong correlation without clear outliers and a coefficient of determination (R^2) of 0.99 (Figure 4-6b). The elevation differences are normally distributed and allow for the calculation of the standard deviation (STD; cf. Figure 4-6a). Thus, the STD (2.27 m) is applied to estimate the accuracy of the DEM 2016 and as threshold for the DoD calculations.

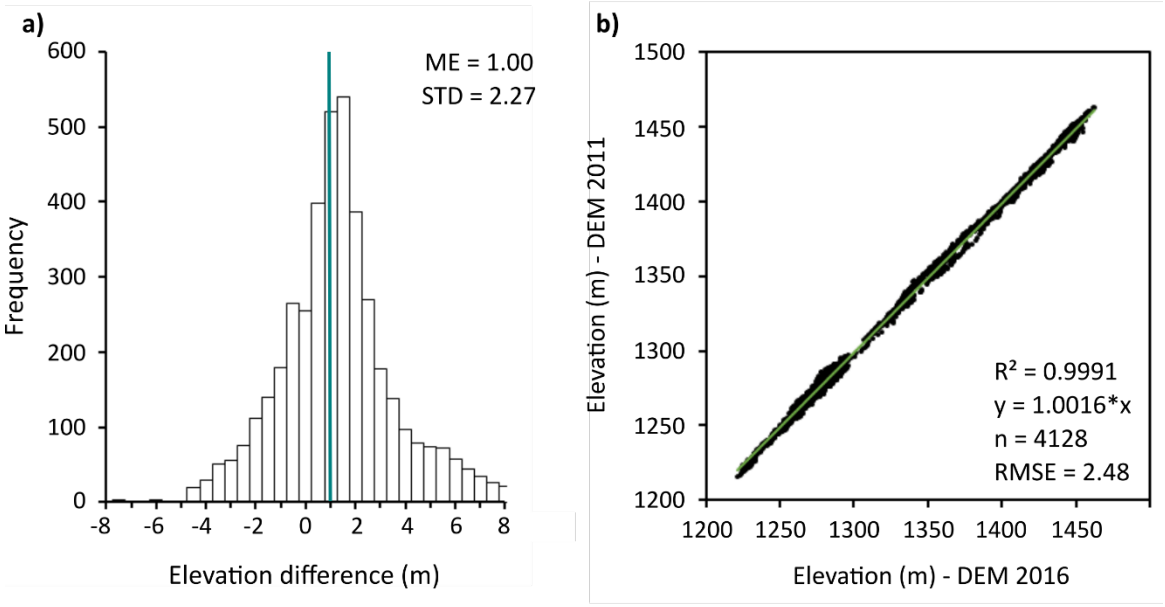

Figure 4-6. a) Elevation difference between the stable areas of DEM 2011 and DEM 2016. b) Simple linear regression of the DEM 2016 in comparison to the DEM 2011. Source: Own illustration.

4.2.2 Analysis of the DEM 2013

The DTM 2013 provides a resolution of 0.24 m/pixel (Table 4-1), however, it was exported with a cell size of 1.80 m (Figure 4-7a), considering the total error of the GCPs (Table 4-3). Additionally, the generation of a 5 m DTM allows for an overlay with the LiDAR DEM (DEM 2011). The created DSM has a cell size of 1.80 m and the calculated orthomosaic could not be applied due to low quality.

Table 4-3. Ground Control Point accuracy for the 2013 data.

Type	Count	XY error (m)	Z error (m)	Error (pixel)	Total error (m)
Control points	4	1.610	0.925	19.202	1.857
Check points	3	1.943	1.815	6.608	2.659

Accuracy assessment of the GCPs: The georeferencing error is determined by calculating the RMSE of the check points (cf. Table 4-3). With a value of 2.66 m it is considerably higher than the error from the 2016 data (1.39 m). It can be supposed that the calculated error results from the missing GCP markings as the photographs were taken prior to the GCPs generation. Due to permanent changes in the slide mass during the years 2013 and 2016 many GCP locations could not be detected anymore. Therefore, the location of the GCPs had to be estimated which is reflected by higher error values. As a consequence, the generation process includes four control points and three check points (Figure 4-7b). This low number is due to the fact that only GCPs located outside the landslide area or close to recognizable structures are suitable.

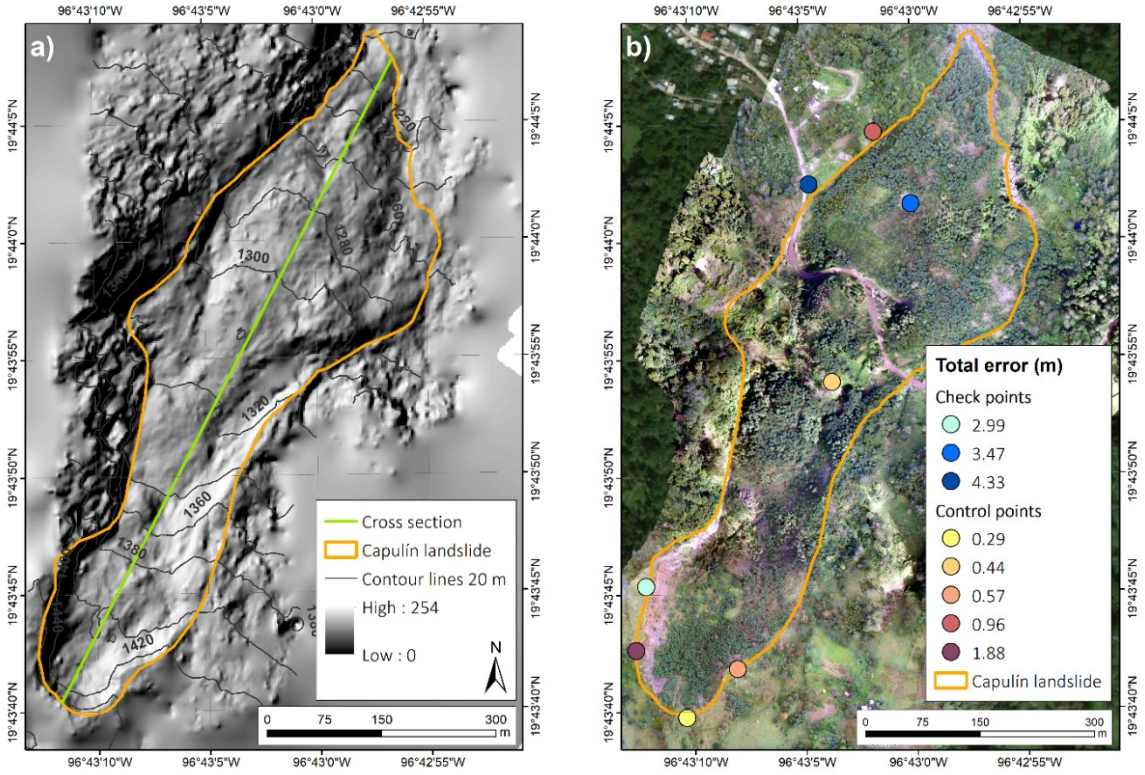

Figure 4-7. a) Resulting DEM 2013 visualized by a hillshade with a cell size of 1.8 m. b) Orthomosaic acquired from the photographs collected by the UAV. Location of the GCPs (showing their horizontal errors) used as control points and check points for the DEM 2013. Source: Own illustration. Source of background map: Esri World Imagery (2019).

Vegetation classification results: In order to evaluate the process of the vegetation classification, the terrain and surface models are compared against one another (Figure 4-8). As stated in chapter 3.1.1 a preliminary preparation of the dense cloud is not necessary as major parts of the landslide area were not vegetated. This is due to the fact that most of the vegetation got destroyed during the landslide event, with some exceptions in the central part and the foot area of the landslide (cf. Figure 4-8a, 4-9b and c). In this case, the simple ground point classification is sufficient as it correctly identifies the majority of the dense point cloud as 'ground points' (cf. Figure 4-8b; chapter 3.1.1). As mentioned above, a few coherent areas containing higher vegetation remained after the mass movement occurred (Figure 4-8a). The major part of the vegetation captured in the 3D-model is located outside the landslide area. The significant peak in the cross section corresponds to the vegetation identified in the central part of the dense cloud (Figure 4-8b) and the DTM line shows its successful removal (cf. Figure 4-8c, approx. between 450 and 530 m). Although the filter removed the majority of the vegetation, in some cases it leads

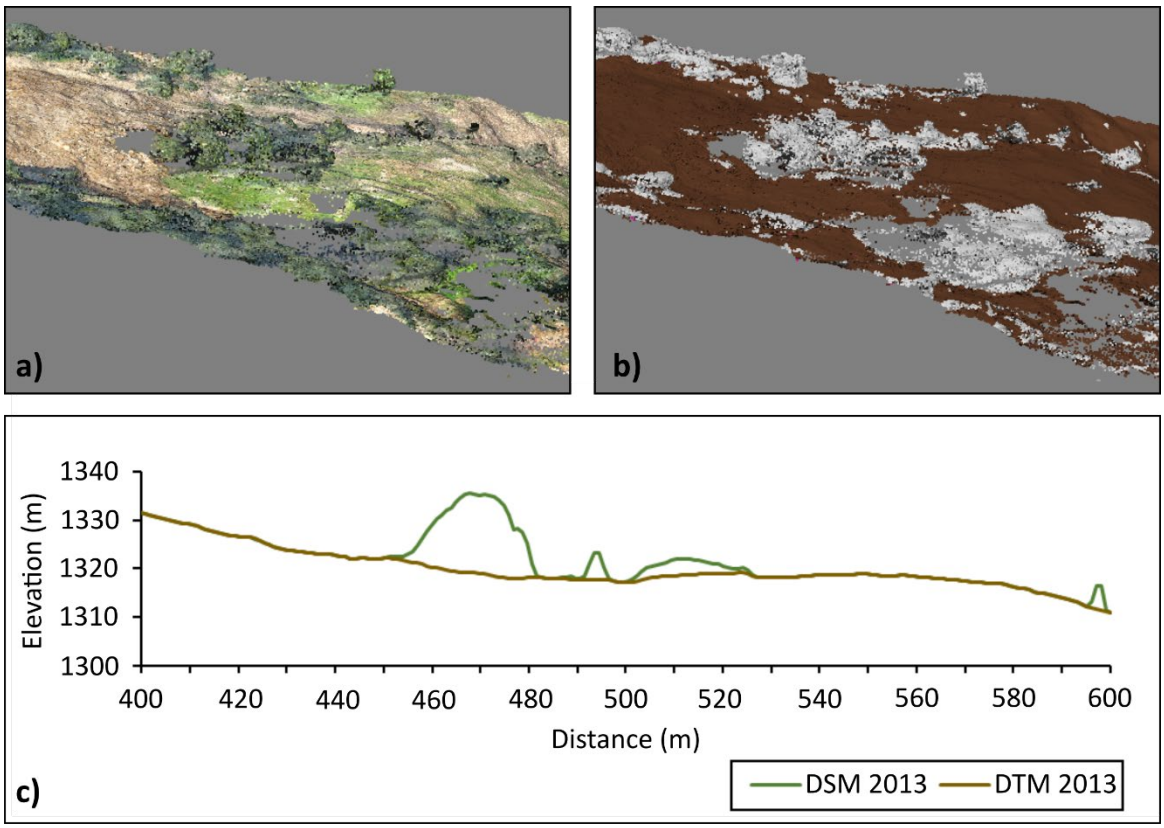

Figure 4-8. a) Extract of the dense cloud (center part) of the Capulín landslide (illustration derived from Agisoft). b) Classified dense cloud, with ground points in brown and not further specified vegetation in gray (illustration derived from Agisoft). c) Cross section along the Capulín landslide (roughly the same section as depicted in dense clouds above) comparing the DEMs before (DSM) and after the filtering process (DTM). Source: Own illustration.

to a misclassification as 'ground points' resulting in vegetation residuals. These residuals can be observed especially on the western flank where the vegetation is very dense (cf. Figure 4-9a). Within the landslide area, few residuals can be found in the lower part of the slide mass and in the middle of the foot area (Figure 4-9b). Due to the sliding process only small areas with dense vegetation remained and consequently, only these areas are generalized due to the filter. This can be seen at the eastern flank close to the foot (cf. Figure 4-9c). The lack of data causes a smooth surface in the peripheral areas.

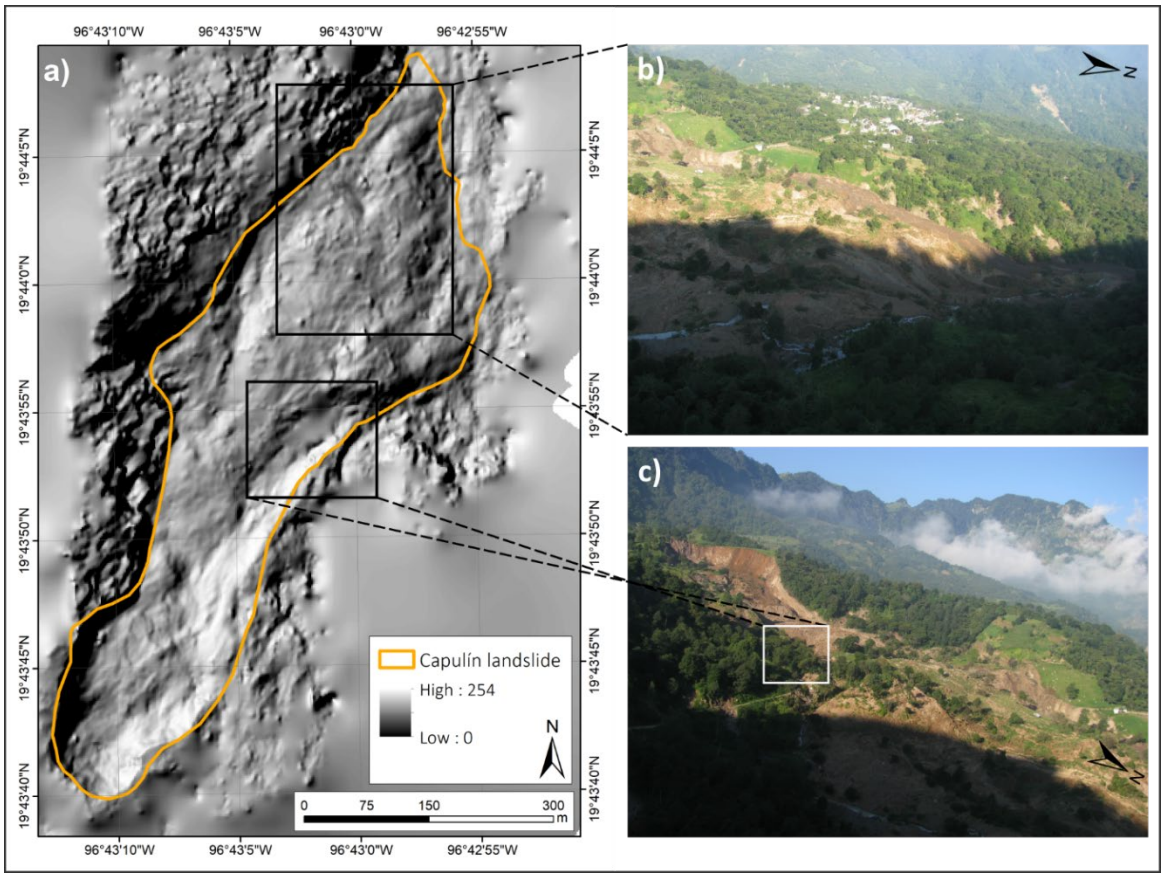

Figure 4-9. a) Hillshade derived from the DEM 2013. b) Photograph of the landslide's foot area (view from the northeast to the west). c) Photograph of the Capulín landslide (view from the northeast to the southwest). Photographs: S. Rodríguez Elizarrarás, 2013. Source: Own illustration.

Accuracy assessment of the DTM 2013: The second part of the accuracy assessment consist of adjusting the DTM 2013 to the LiDAR DEM 2011. Both elevation models (DEM 2011 and DEM 2013) correlate very strongly, with a coefficient of determination (R^2) of 0.99 (Figure 4-10). With 5.79 the RSME is higher compared to the 2016 data (RMSE of 2.48). The STD cannot be used in this case as it requires a normal distribution, which was not given here. Thus, the RMSE determines the resulting error of the DTM 2013.

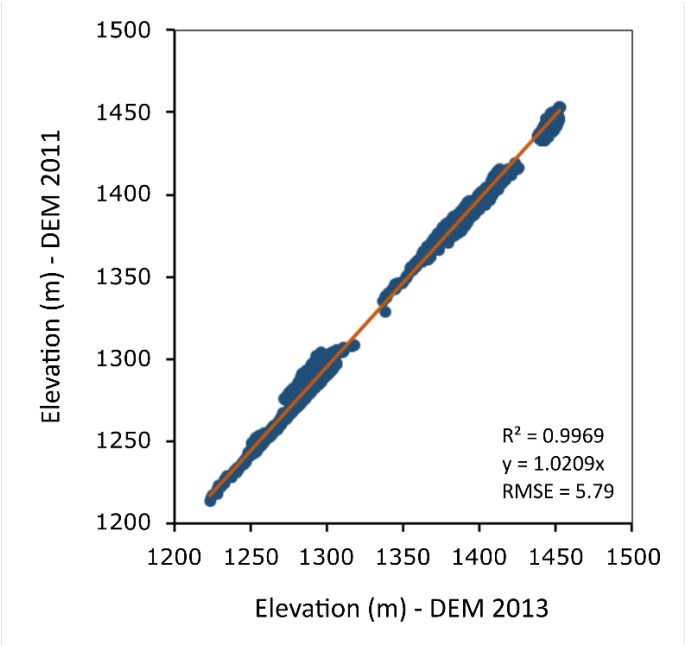

Figure 4-10. Simple linear regression of the DTM 2013 against DEM 2011. Source: Own illustration.

4.3 Analysis of the landslides in the Chiconquiaco Mountain Range

An inventory map is created by visually interpreting hillshades, slope maps (synonymously with the term 'slope gradient map'), and satellite images to display the landslides in the study area. The spatial distribution of the mapped landslides is illustrated in Figure 4-11. With a regional scale of 1 : 30,000 the map represents a medium-scale geomorphological, historical landslide inventory map (according to Guzzetti et al. 2012). The focus of the mapping procedure is on sliding processes, such as rotational, translational, and complex slides, while further gravitational processes (e.g. falls, topples) are not considered.

The landslides are mapped as polygons, since the distinction of the scarp area and slide mass is not possible in all cases. Thus, a polygon represents a combination of scarp and slide mass. Whenever the identification of a landslide mass is hampered, the scarp signature is assigned (Figure 4-11). In total, twelve landslides and ten scarps were mapped (based on slope map, hillshade, satellite images, and contours) covering an area of approx. 18 % of the study area. If the potential landslide area (landslide no. 10) is not taken into account, the coverage area of the landslides is reduced to 9 %. Since landslide no. 10 cannot be clearly identified, it is characterized as 'uncertain'. This landslide covers a large area and exhibits signs of further progression over time related to smaller slope movements and other erosional processes.

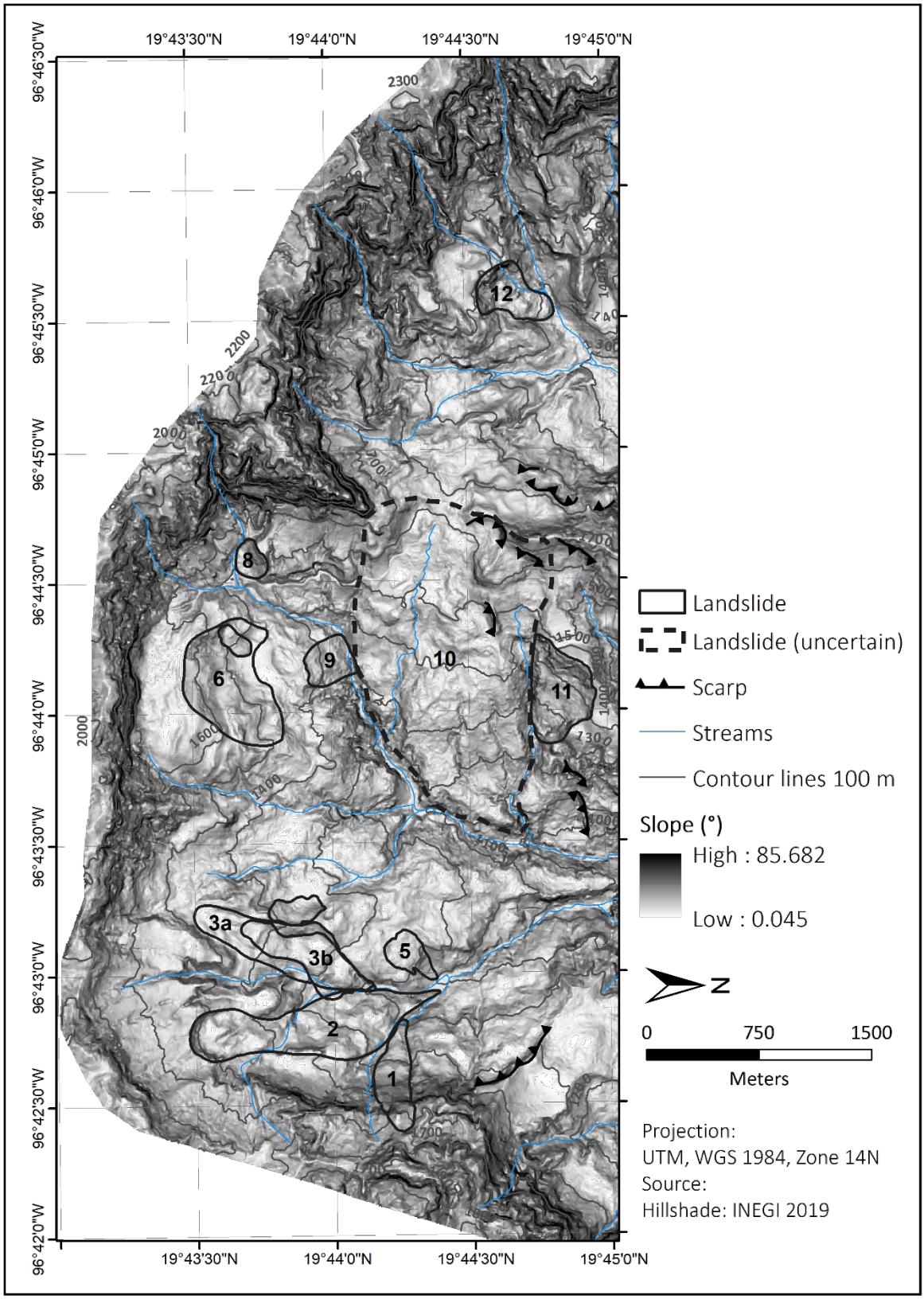

Figure 4-11. Slope gradient map of the study area showing the location of slope failures and streams. Source: Own illustration.

Landslides nos. 1, 6, and 10 occupy the highest positions in the inventory map, with an altitude of 1,650 m a.s.l. (Figure 4-11). The highest scarp is at 1,740 m a.s.l. and the scarp of landslide no. 5 is the lowest with 1,250 m a.s.l. (Figure 4-11). The foot of landslide no. 10 reaches lowest with 1,040 m a.s.l. and the foot areas of landslides nos. 2 and 5 are situated at 1,105 m a.s.l. (Figure 4-11). The landslide with the largest area is no. 10 covering 51 % of the total landslide area (10 % of the study area). The Capulín landslide (no. 3b) comprises approx. 4 % and the Escalanar landslide 1 % of the total landslide area (Figure 4-12). Landslide no. 3a almost coincides with the recent Capulín landslide (no. 3b). The polygon of slide no. 3b represents the extent of the event from 2013, whereas the polygon of no. 3a is based on the hillshade from 2011 (Figure 4-11). Thus, no. 3a represents a former landslide, which occurred before the slide from 2013.

Some of the landslides show similarities, e.g. the highest point is the same for the landslides 1, 6, and 10 (1,650 m a.s.l.) as well as for landslides nos. 3b and 9 (1,445 m a.s.l.). With the exception of landslide nos. 4 and 7, the majority of the foot areas end at or are located near streams. Furthermore, it can be stated that streams cut landslides nos. 2, 10, and 12. In the northern part of the foot area of landslide no. 6 runs a small creek, which is not captured in this map due to its small size. None of the landslides are located at the very steep slopes (> 50°) close to the border of the study area. Even though some landslides (nos. 2, 8, 11, and 12) have steep scarp areas (< 50°), they do not reach the highest inclination values from the study area.

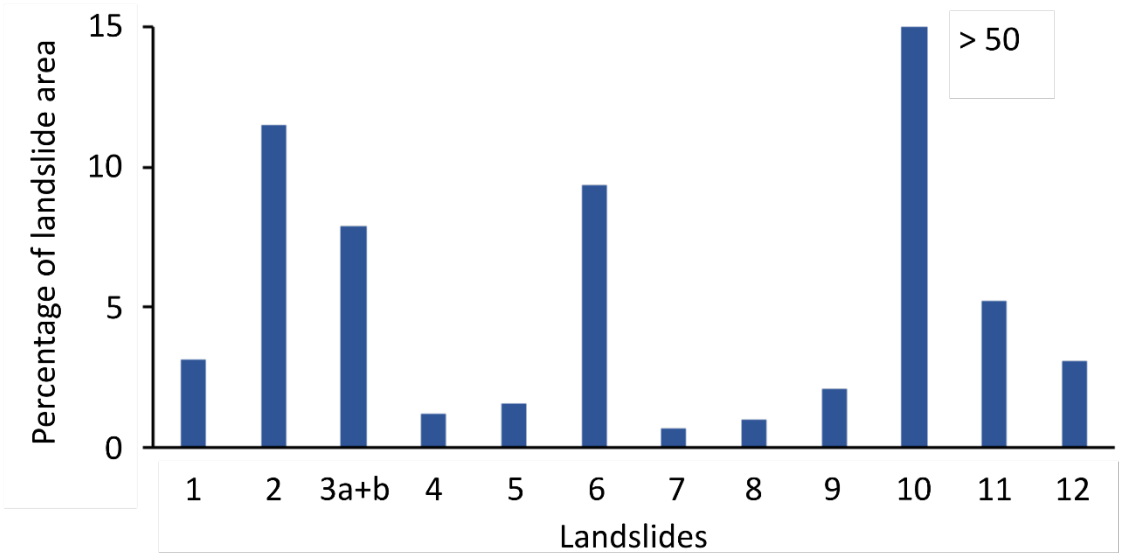

Figure 4-12. Proportion of each landslide in relation to the total landslide area in percentage. Source: Own illustration.

4.4 DEMs of Difference (DoDs)

The available DEMs form the base for the identification of topographical changes in the Capulín landslide area (see chapter 4.2). The first step overlays the pre-event DEM 2011 and the one derived from the helicopter flight in the year 2013. The second step comprises the comparison of the pre-event DEM 2011 with the DEM 2016 from the photogrammetric survey. In addition, to track successive changes of the landslide, it is necessary to compare both post-event DEMs with each other.

4.4.1 Analysis of the DoD 2013

The DEMs of difference (DoD) and elevation change distributions derived from the 2011 and 2013 data are presented in Figure 4-13. Figure 4-13a displays the unthresholded (raw) DoD and Figure 4-13b represents the DoD thresholded by the minimum level of detection (LoD_{min}). This threshold distinguishes actual from model-induced changes. Areas, which experienced erosion (negative values), are indicated in red and areas where material was accumulated (positive values) are indicated in blue. The colorless sections inside the landslide are below threshold and therefore, excluded from the DoD calculations (cf. Figure 4-13b).

In total, 76 % of the area experienced detectable changes, which are significant enough to be distinguished from noise (Figure 4-13b, c). Accordingly, 24 % of the area changes from the raw DoD are unreliable and must be handled with caution. Consequently, the following analyses use the thresholded DoD due to a higher level of reliability. The threshold (δ_{DoD}) is at 5.79 m, which means that surface changes in the order of +/-5.79 m or more are adequately captured (cf. chapter 3.1.3).

The application of the threshold leads to the spatial reduction of the area with detected surface changes from 167,175 m² to 126,400 m² (cf. Table 4-4). Altogether, the erosional area comprises a volume of 1,714,872 m³ and the area of accumulation a volume of 270,873 m³. The DoD ranges from -36.80 m to 23.60 m. With an average depth of 16.58 m, the surface lowering is higher than the average depth of the surface increase with 11.80 m. This relation is further reflected in the quantified volumetric elevation change distributions shown in Figure 4-13c. From 76 % of significant detected changes 62 % correspond to eroded areas and only 14 % to areas of accumulation. The volumetric change is calculated by multiplying the area with the magnitude of the detected elevation change (Wheaton et al. 2010).

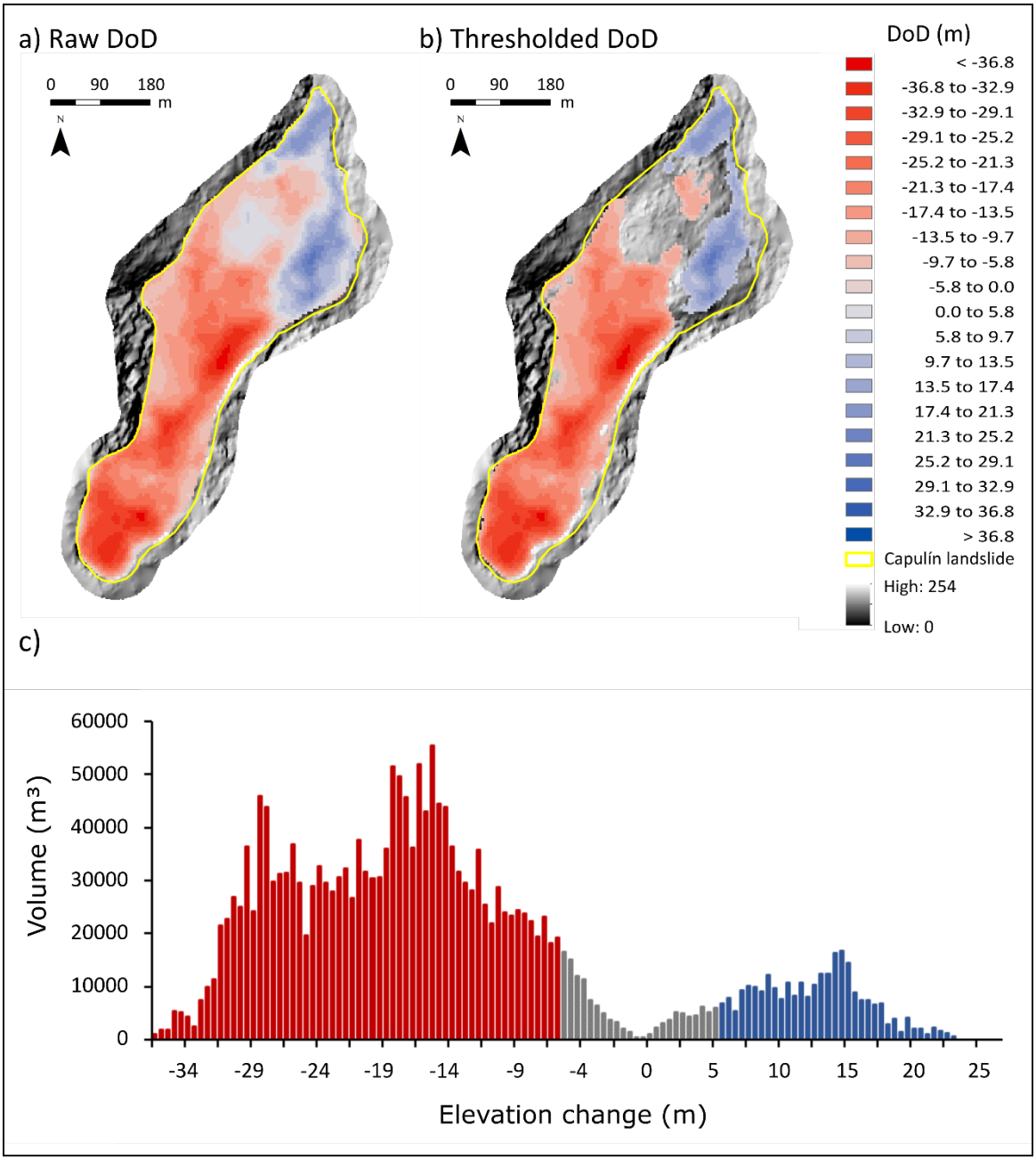

Figure 4-13. Comparison of raw (a) and thresholded (b) DoDs of 2013. c) Elevation change distribution from the thresholded DoD. Red colors correspond to erosional, the blue colors to areas of accumulation. Gray color represents areas below threshold. Source: Own illustration.

Table 4-4. Comparison of areal and volumetric values of raw and LoD_{min} thresholded 2013 DoDs.

DoD	Areal change detection (m²)			Volumetric change detection (m³)		
	Erosion	Accumulation	Total change	Erosion	Accumulation	Total change
Raw	127,700	39,475	167,175	1,792,848	315,115	2,107,963
Threshold	103,450	22,950	126,400	1,714,872	270,873	1,985,745

The spatial pattern of erosion and accumulation is illustrated in Figure 4-14, where the combination of hillshade and lateral view clearly visualizes the elevation changes. The area where the scarp has collapsed, exhibits the highest elevation differences with up to -35 m (cf. Figure 4-14a). Similar values occur in the region of the eastern flank (max. -35 m), whereas the western flank is characterized by the lowest elevation differences (about -5 m). At a distance of approx. 750 m (Figure 4-14b), the area of surface

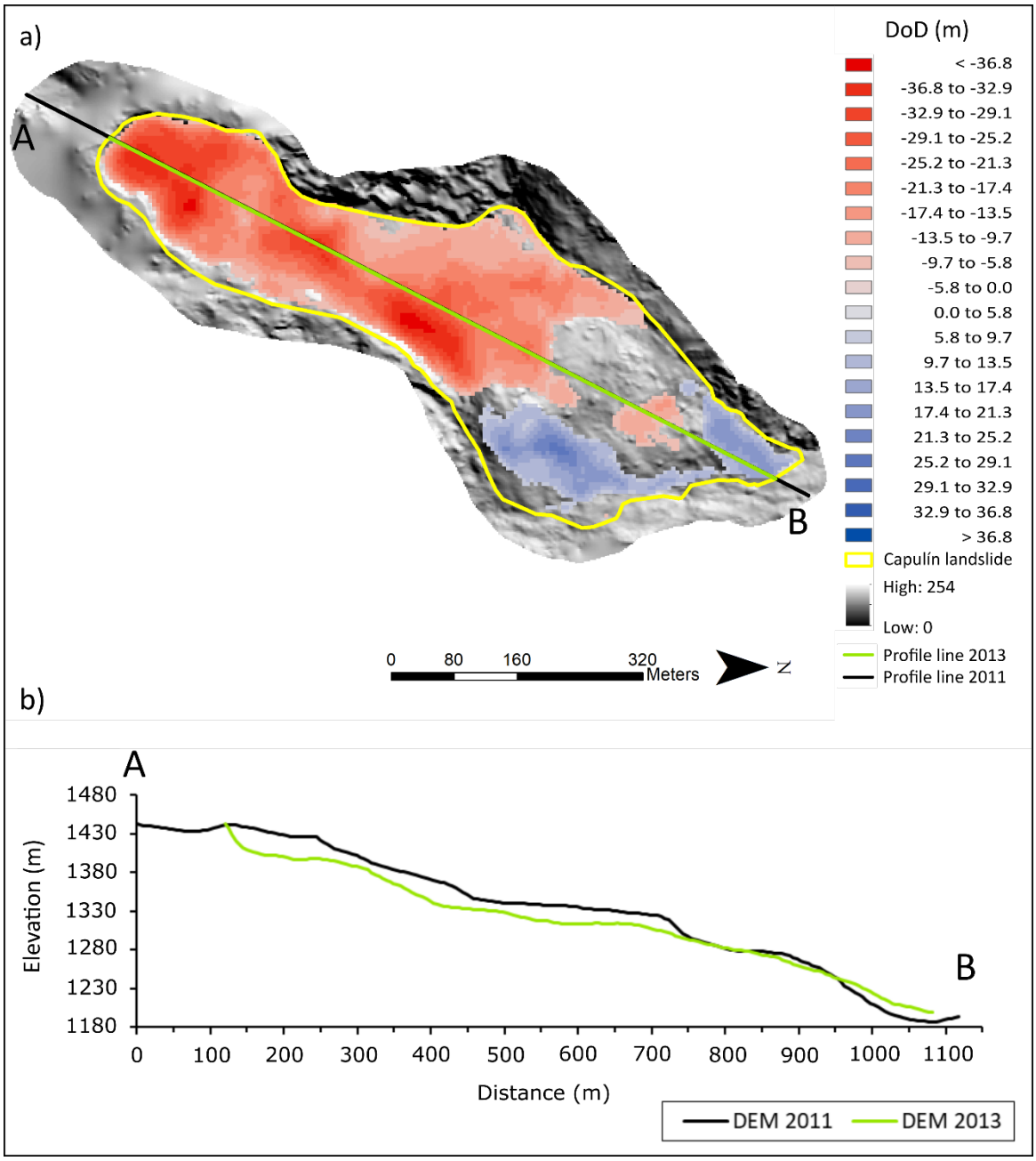

Figure 4-14. a) Difference between the DEMs of 2013 and 2011 illustrating the surface changes. Underlying map: Hillshade from 2013 (1.8 m grid). b) Cross sections (marked in green in a)) along the Capulín landslide comparing the pre- and post-event DEMs (5 m grid). Source: Own illustration.

lowering ends in most parts and the surface raising area begins. Comparing Figure 4-14a with 4-14b it is interesting to note that the areas where both cross sections are approx. at the same elevation (750 - 850 m distance, Figure 4-14b) further coincide with the areas, situated below the threshold. These areas are excluded from the calculations and correspond to areas, within the landslide, where the hillshade is visible (Figure 4-14a). The highest elevation differences (< 20 m) in the accumulation area occur at the eastern landslide foot. In the northwestern part, the elevation differences are lower and the foot area appears to be less inclined.

4.4.2 Analysis of the DoD 2016

The DoD of the DEMs 2011 and 2016 displays the vertical movements in the landslide area (Figure 4-15). The minimum level of detection (LoD_{min}) of 2.27 m (δ_{DoD}) is used for the calculation of the thresholded DoD. Thus, the DoD considers only vertical displacements larger than +/-2.27 m (Figure 4-15b). With the application of the threshold, detectable changes are identified in 88 % of the area. Consequently, 12 % of the changes from the raw DoD are inaccurate (cf. Figure 4-15a and b). Furthermore, applying the threshold reduces the total detectable areal change from 167,175 m² to 146,975 m² (cf. Table 4-5). The total net volume shows smaller differences between the raw (-487,220 m³) and thresholded DoD (-482,694 m³). For the latter, the erosional area accounts for a volume of 1,136,163 m³ and the area of accumulation comprises a volume of 653,469 m³ (Table 4-5). The DoD ranges from -29.50 m to 38.40 m. The average thickness of the areas of erosion (12.44 m) and accumulation (11.74 m) are in the same order of magnitude. However, the area of erosion (55 %) is larger than the area of accumulation (33 %). Additional to the spatial distribution of detectable changes (Figure 4-15a and b), Figure 4-15c shows the quantified volumetric elevation change distributions of the DoD 2016.

Table 4-5. Comparison of areal and volumetric values of raw and LoD_{min} thresholded 2016 DoDs.

DoD	Areal change detection (m²)			Volumetric change detection (m³)		
	Erosion	Accumulation	Total change	Erosion	Accumulation	Total change
Raw	102,875	64,300	167,175	1,149,395	662,175	1,811,571
Threshold	91,325	55,650	146,975	1,136,163	653,469	1,789,632

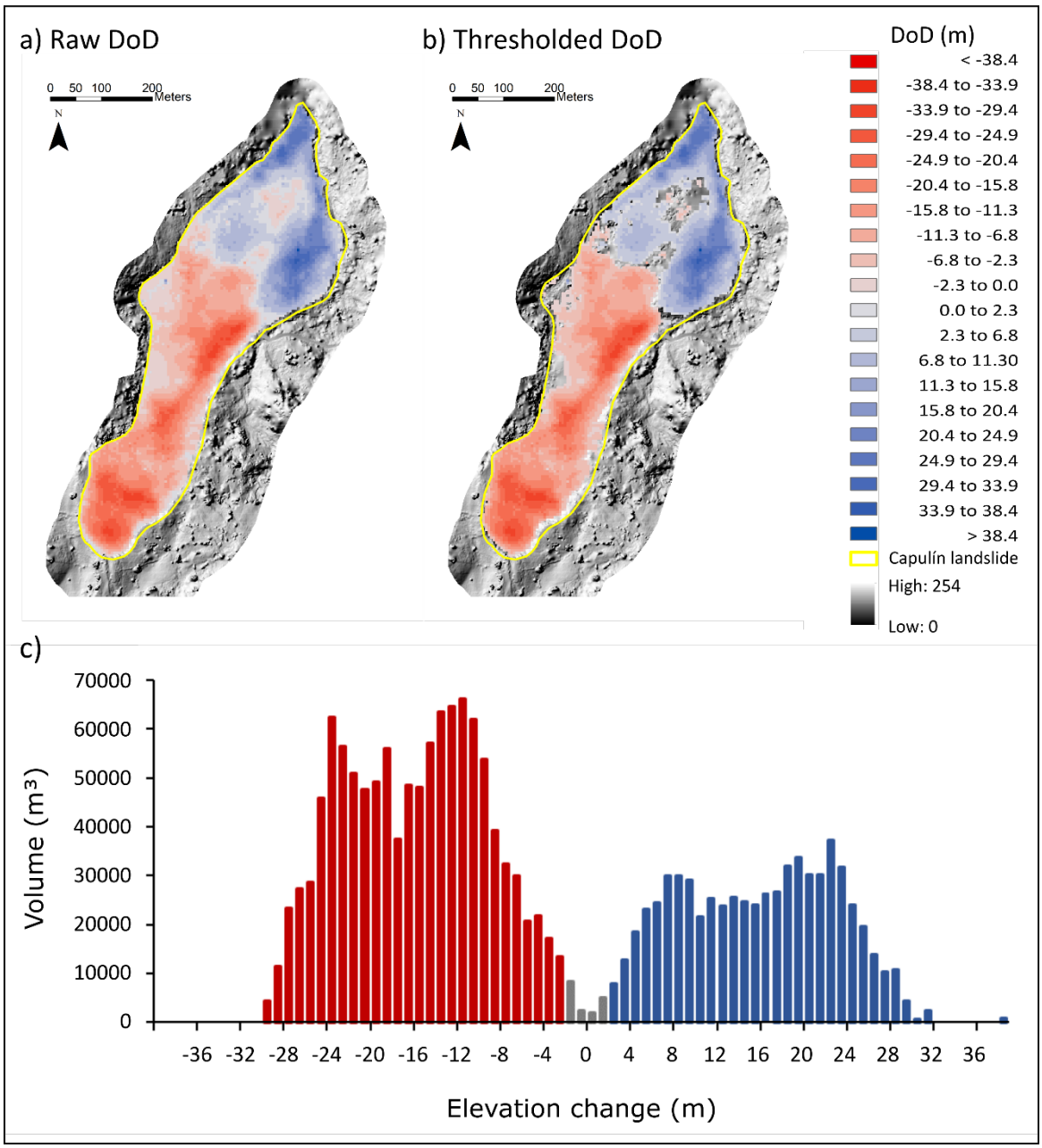

Figure 4-15. Comparison of raw (a) and thresholded (b) DoDs of 2016. c) Elevation change distribution from the thresholded DoD. Red colors correspond to erosional, blue colors to accumulated areas. Gray color represents areas below threshold. Source: Own illustration.

The lateral view (Figure 4-16b) provides further insight into the areas of erosion and accumulation. The area close to the scarp (approx. at 150 m) shows the highest elevation differences (up to -29 m). The remaining areas of erosion are characterized by surface lowering as well, although lowering differences remain smaller in most parts (cf. Figure 4-16a). At the distance of approx. 700 m, the area of surface lowering ends and the accumulation area begins (Figure 4-16b). Here, the highest elevation differences occur in

the eastern part of the slide mass. Low elevation differences appear clearly visible in the central part of the cross section (Figure 4-16b). The elevation difference increases in the foot area and the morphology is steeper compared to the pre-event conditions. Areas below the detection limit are located in the western flank and the center of the foot area (Figure 4-16a).

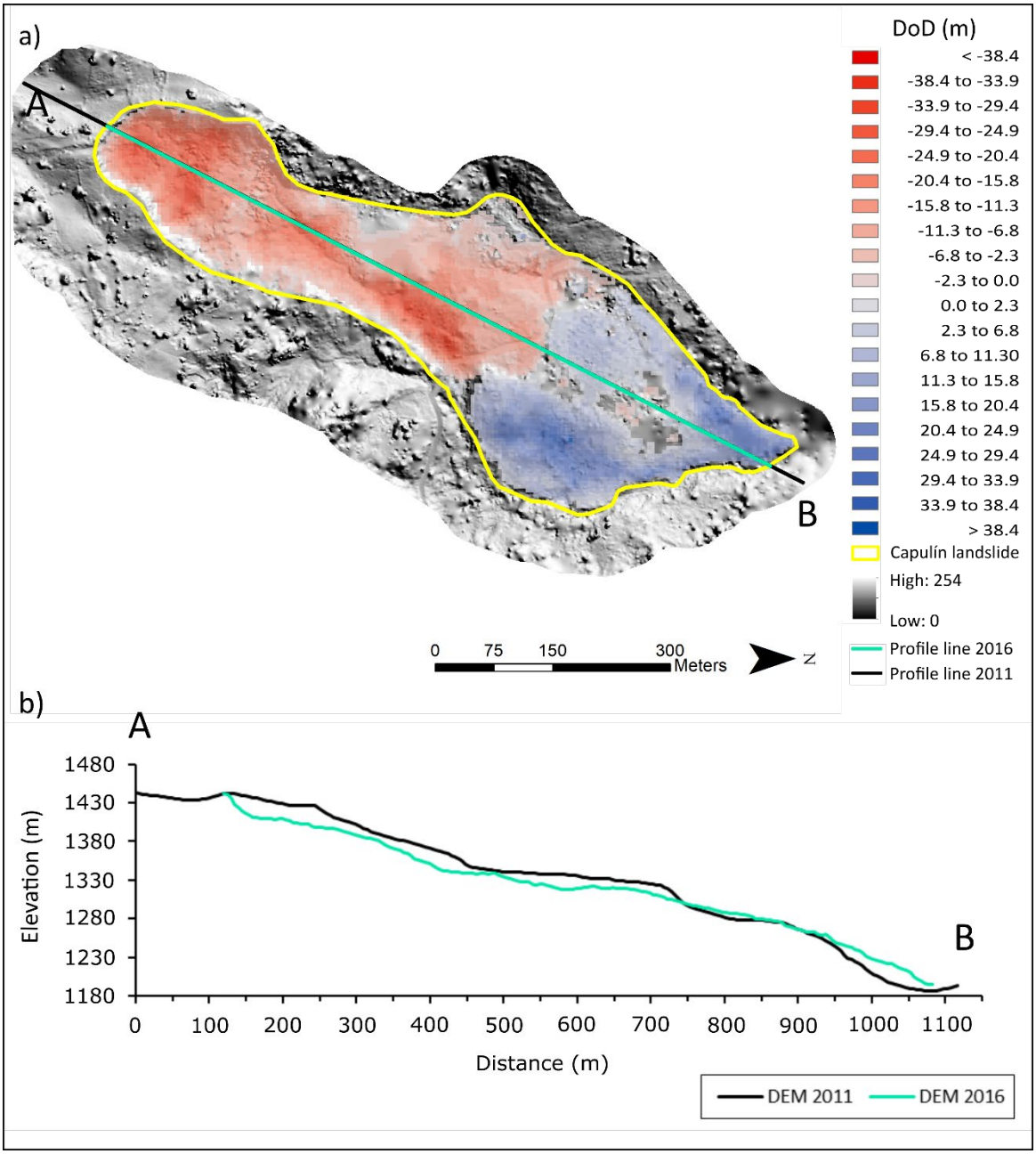

Figure 4-16. a) Difference between the DEMs from 2016 and 2011 illustrating the surface changes. Underlying map: Hillshade from 2016 (1 m grid). b) Cross sections (marked in green in a)) along the Capulín slide comparing the pre- and post-event DEMs (5 m grid). Source: Own illustration.

4.4.3 DoD of the post-event DEMs

In order to track further erosion and accumulation processes, both post-event DEMs (2013 and 2016) are compared (Figure 4-17). For this task, the DEM 2013 was adjusted to the DEM 2016 due to its higher accuracy (cf. chapter 4.2.1). The STD (2.98 m) is used as LoD_{min} threshold for the DoD calculation. For further results of the accuracy assessment and the volumetric elevation change distribution of this DoD see Appendix B.

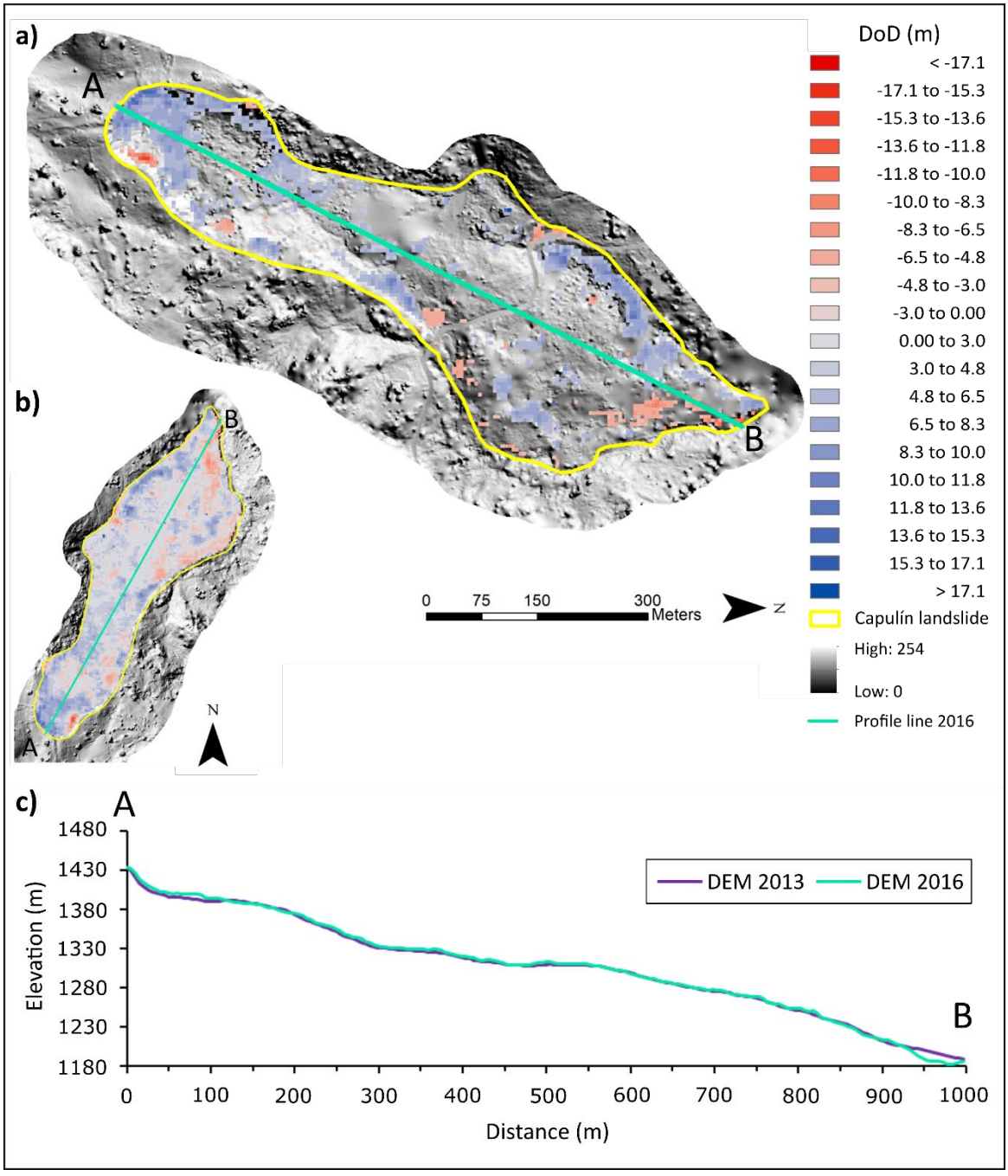

Figure 4-17. a) Thresholded DoD from the 2013 and 2016 data. Underlying map: Hillshade from 2016 (1 m grid). b) Raw DoD; c) Cross sections (marked in green in a)) along the Capulín landslide comparing the 2013 and 2016 DEMs (5 m grid). Source: Own illustration.

The major part of the elevation changes are in the same magnitude range as the threshold. Hence, after the application of the threshold changes are detected in only 27 % of the area (cf. Figure 4-17a and b). This means that in 73 % of detected changes cannot be clearly distinguished from noise. Figure 4-17c proves that both cross sections are rather similar, however, do not coincide completely. It is interesting to note that in this case the relation between areas of surface lowering and increase differ compared to the former described DoDs. Here, 37,825 m² record an increase in elevation and only 6,825 m² show surface lowering (Figure 4-17a). The volume relation between areas of erosion and accumulation reflects this distribution as well. With approx. 86 %, the volume of accumulation areas is more than six times higher than those of the eroded areas with 14 %. The major part of the changes ranges between 3 and 6 m (cf. Appendix B). The maximum values are at -13 m and 17 m, but only few outliers show such high values (mainly individual pixels). The accumulation is mostly located close to the scarp and further at the flanks. Despite of this, erosional areas are primarily located at the slide's toe. One exception exists at the eastern part of the scarp area. Results of erosional processes at the landslide foot can be traced in the cross section (Figure 4-17c), where the surface of the DEM 2016 is steeper and is situated below the older surface.

4.4.4 Comparison of the DoD 2013 and DoD 2016

In general, there are differences between the above described DoDs. In this context, it can be observed that the area with detectable changes of the DoD 2016 (88 %) is larger than the area of the DoD 2013 (76 %). A further deviation appears in the relation between the average depth of the areas of erosion and accumulation. In this case, the average depth difference amounts to 0.70 m for the DoD 2016, whereas the DoD 2013 records 4.77 m. Furthermore, areas of erosion are deeper in the DoD 2013 (with a maximum of -36.8 m) as in the DoD 2016 (with a maximum of -29.5 m). This is clearly visible in the scarp area as well as in the eastern flank (cf. Figure 4-18a, b). Moreover, the distribution pattern reveals differences. In the DoD 2013 the area of erosion reaches further downslope compared to the DoD 2016 and consequently, the area of accumulation is larger in the latter DoD. This can also be observed in the cross sections, where the surface lowering of the 2016 DoD already ends at a distance of about 600 m, whereas in the DoD 2013 the end occurs at approx. 750 m (cf. Figures 4-14 and 4-16). These distribution differences are reflected in the ratio between the eroded and accumulated areas as well. While for the DoD 2016 the

relation between areas of surface lowering and raising is approx. 60 to 40 %, the DoD 2013 shows a relation of approx. 85 to 15 %. Furthermore, the distribution of areas below threshold show different patterns in each DoD. The thresholded areas of the DoD 2013 are mostly coherent and concentrated in the lower part of the landslide, while in the DoD 2016 they spread over a wider area (Figure 4-18a, b). Overall, it appears that the erosion was stronger directly after the main landslide event in 2013 and the redistribution of sediments started afterwards as suggested by the DoD 2016 (Figure 4-18a, b).

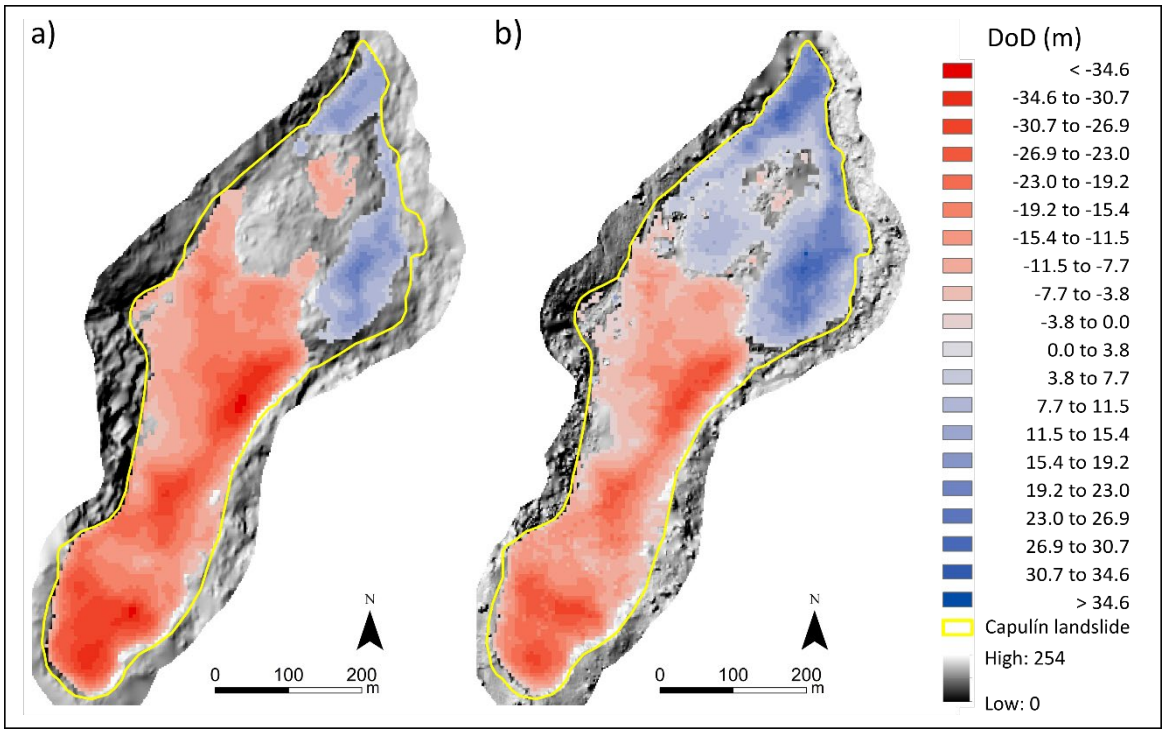

Figure 4-18. Results of the thresholded DoDs of 2013 (a) and 2016 (b). Landslide marked in yellow. Underlying map: Hillshade from 2016 (1 m grid). Source: Own illustration.

4.5 Slip surface determination for the Capulín landslide

The slip surface of the Capulín landslide is reconstructed by interpolating elevation information of the potential slip surface derived from geophysical analyses. With the combined application of ERT and SRT measurements the slide mass can be distinguished from the underlying surface. This allows for the identification of the potential slip surface in the resulting subsurface models (cf. Appendix C, Wilde et al. 2017a, b).

In total, 97 points are generated based on the subsurface models (Figure 4-19). A total number of 36 points in the Transects 1, 2, and 4, form the base for interpolation. The

remaining 25 points are further classified as validation points (Group 2). The interpolation process does not include Transects 5 and 6 and therefore, they are used for validation (Group 1; cf. Figure 4-19). The evaluation procedure comprises the calculation of the RMSE for each interpolation algorithm and a cross section of the interpolation results for visual assessment (Figure 4-20).

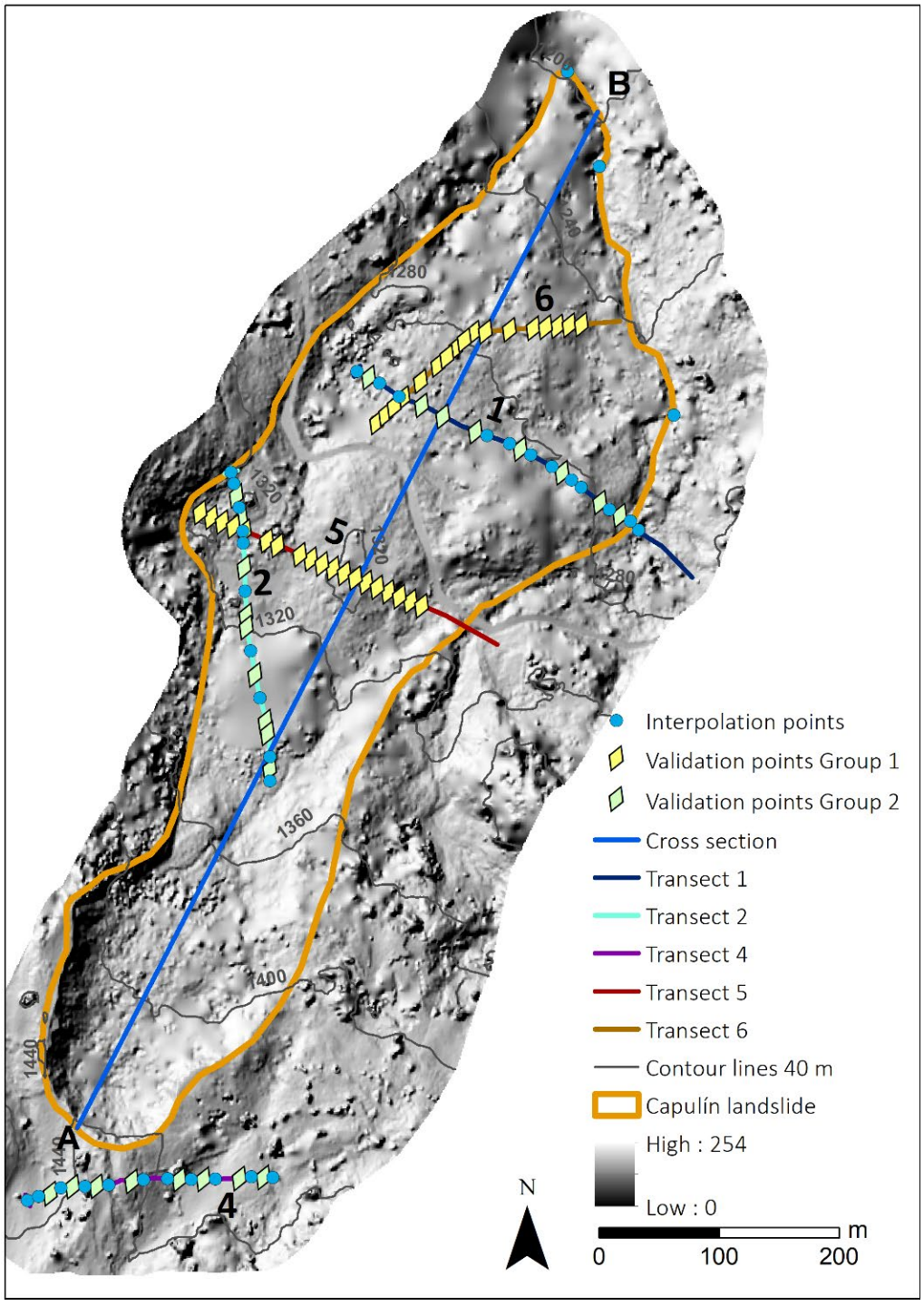

Figure 4-19. Location of the geophysical transects with interpolation- and validation points. Underlying map is the hillshade of 2016. Source: Modified after Wilde et al. (2017a, b).

The RMSE was computed for each validation group as well as for their combinations (Table 4-6). Overall, Group 2 records the lowest RMSE values and Group 1 the highest ones. Relatively high values occur in the combined group, however, they remain below those from Group 1. The natural neighbor method shows the highest RMSE for the Groups 1 and 2, and the spline method has the highest errors for the combined group. While the results from the natural neighbor and spline interpolations are similar, the kriging method deviates considerably, and at the same time, shows the lowest values (Table 4-6).

The cross sections of each interpolation result as well as the pre- (DEM 2011) and post-event (DEM 2016) surfaces are illustrated in Figure 4-20, which represents the differences between the methods. The interpolated slip surfaces start at an elevation of around 1,400 m (at a distance between 0 and 50 m) and are located below the scarp area (elevation of approx. 1,450 m). This is due to the fact that the first interpolation points are located outside the landslide area (Figure 4-19). Although, the surface from 2016 represents lower elevation values than the former surface from 2011, both surfaces show almost equal heights at approx. 600 m distance. A change occurs at a distance of approx. 800 m (Figure 4-20) where the pre-event surface lies above the post-event surface. At this distance, the slip plane remains below the post-event surface (DEM 2016), however, coincide with the pre-event surface (DEM 2011).

Overall, the three interpolation algorithms show comparable results in the cross section. Especially, the natural neighbor and kriging results are very similar, while the result of the spline method shows some deviations (Figure 4-20). Between 50 m and approx. 200 m, the spline technique calculates higher elevations. At approx. 100 m, the line almost coincides with the surface from the year 2016. The reverse situation occurs between 210 m and 300 m distance, where the spline algorithm displays the lowest elevations (Figure 4-20). This divergent structure is further visible in the 3D illustration (Figure 4-21 (1)).

Table 4-6. RMSE results of the different interpolation algorithms.

Method	RMSE		
	Group 1	**Group 2**	**Group 1+2**
Natural neighbor	11.73	2.14	9.02
Spline tension	11.72	1.97	9.09
Kriging (ordinary)	10.73	1.90	8.33

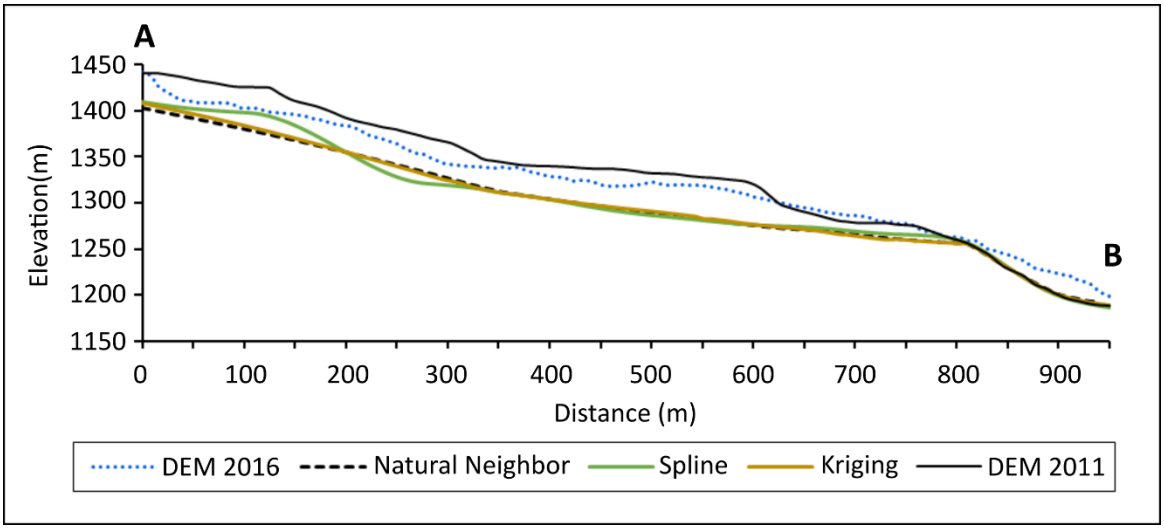

Figure 4-20. Cross section (A-B) of the Capulín landslide, representing the pre- (DEM 2011) and post-event (DEM 2016) surface, and the results of the different interpolation techniques. The location of the cross section is depicted in Figure 4-19. Source: Own illustration.

Compared to the topographic and geological information, the divergence cannot be explained and represents a more unrealistic structure. Further on, considering the relatively high RMSE values, it is reasonable to exclude this interpolation result.

The three-dimensional scheme of the natural neighbor slip surface shows a more even distribution of the contours (Figure 4-21 (2)), compared to the spline results. However, one disruption appears clearly at the 1,250 m contour line. A cross check with the topographical and geological data provides no reason for this unrealistic spatial pattern. In general, it can be stated that areas with abrupt elevation changes tend to be strongly smoothed (Figure 4-21 (2)). Similar to the conclusion to reject the slip surface from the spline interpolation, this natural neighbor result also appears to be partially unrealistic and with the highest RMSE values of all results (Table 4-6), it is disregarded for further analyses as well.

The ordinary kriging method is characterized by the smallest RMSE values and even though contour shifts occur as well, they appear to be less sharp. Moreover, the related three-dimensional model from the kriging method displays detailed and significant elevation changes, mostly caused by dense data coverage (Figure 4-21 (3)). Based on the visual assessment of the spatial pattern, the ordinary kriging method produces a geomorphological and geological plausible result, and in addition has the lowest RMSE values. Hence, this interpolated slip surface forms the base for further analyses.

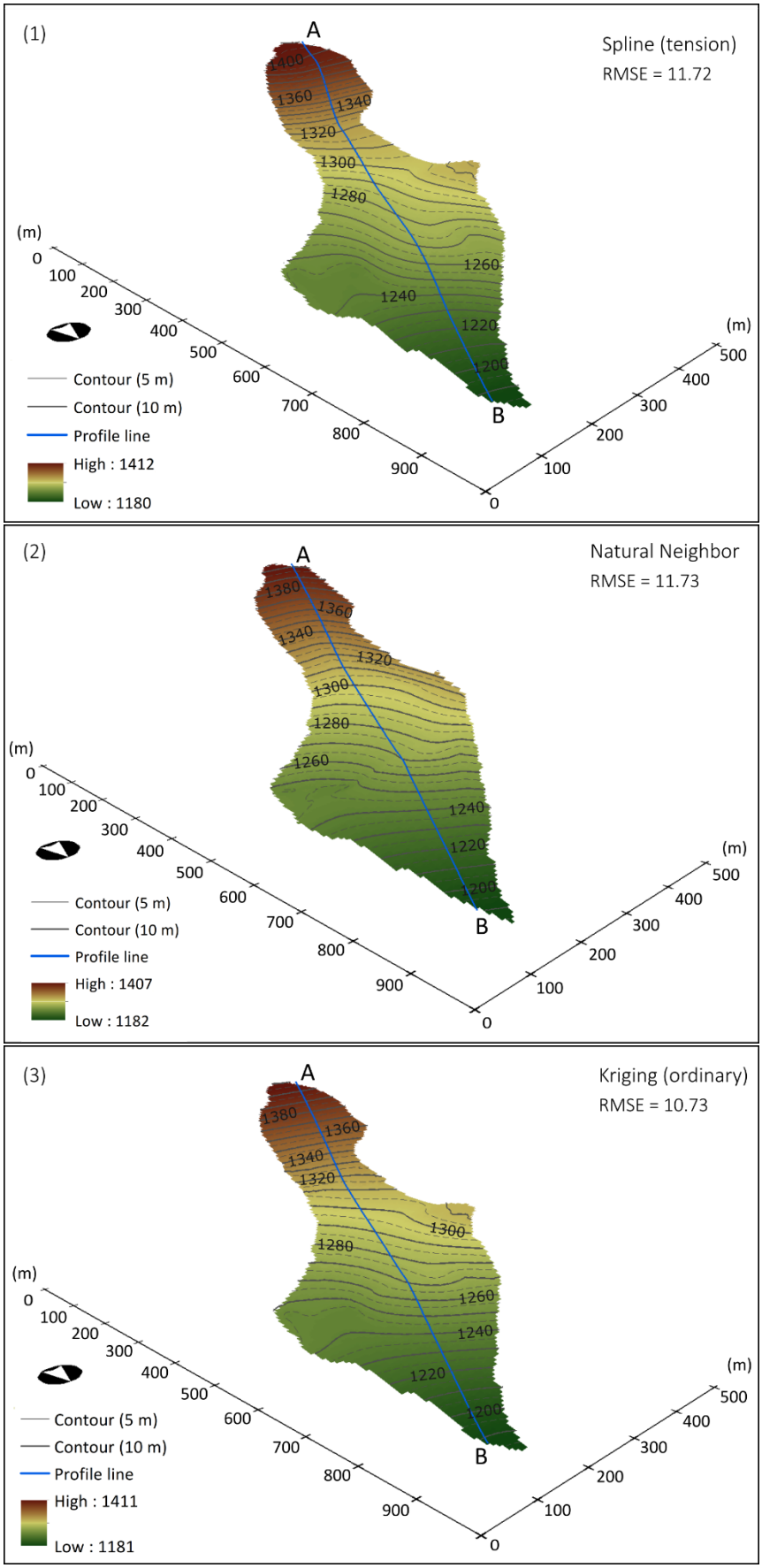

Figure 4-21. 3D illustration of the interpolated slip surfaces using (1) spline algorithm, (2) natural neighbor technique, and (3) ordinary kriging algorithm. Source: Own illustration.

4.6 The volume of the Capulín landslide

For the estimation of the landslide volume five approaches are applied here (cf. chapter 3.1.5). Three of them (Approaches I, II, and III) calculate the volume of the transported material, while Approaches IV and V estimate the volume before the landslide event (Table 4-7).

The parameters used in Approach I (half ellipsoid method, V_d) are shown in Figure 4-22. Besides the depth value (D_d), which is derived from the geophysical measurements along the cross section, the values are measured based on the DEM 2016.

Approach II calculates the volume of the displaced mass relative to the pre-event surface (V_{DoD}). In this context, the areas of erosion and accumulation are derived from the DoD of the pre- and post-event DEMs (cf. chapter 4.4). To calculate the volumes for erosion (V_e) and accumulation (V_a), each zone is further multiplied by the according average thickness of the respective area (Table 4-8). Overall, V_{DoD} represents the smallest volume (Table 4-7).

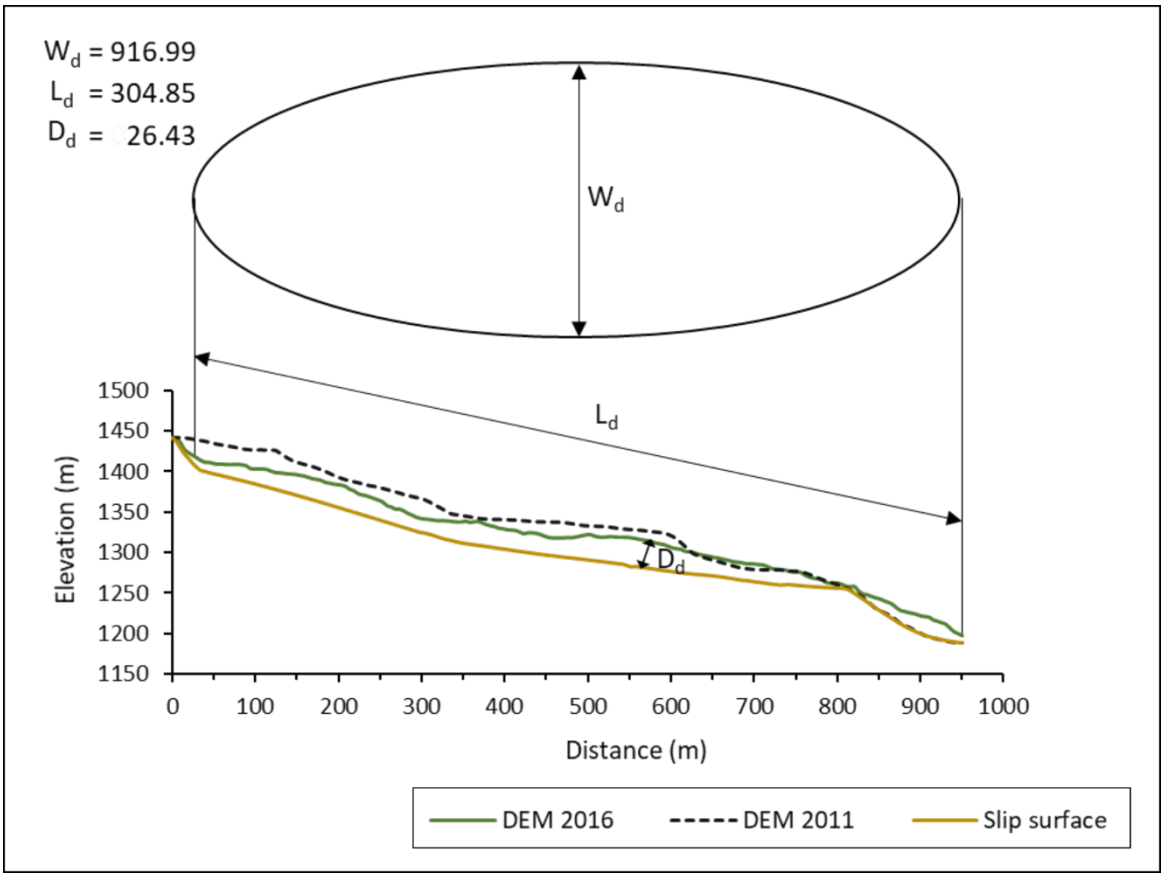

Figure 4-22. Cross section of the Capulín landslide, including the pre- and post-event surfaces, the interpolated slip surface as well as the ellipsoid with the associated parameters for the volume calculation. Source: Own illustration.

Table 4-7. Results of the landslide volume calculation.

Approach	Method	Volume (m^3)	
Approach I	V_d	3.9×10^6	Post-event
Approach II	V_{DoD}	1.8×10^6	
Approach III	V_{post}	3.9×10^6	
Approach IV	V_{total}	4.2×10^6	Pre-event
Approach V	V_{pre}	4.4×10^6	

Table 4-8. Volume calculation for the areas of erosion (V_e) and accumulation (V_a). V_x represents the difference of V_e and V_a.

Name	Volume (m^3)
V_e	1.1×10^6
V_a	7.3×10^5
V_x	3.5×10^5

This is consistent with the chosen approach that only considers the volume of the difference between the pre- and post-event surfaces and does not compute the total volume of the slide mass.

In the case of Approach III, the calculation of the post-event volume (V_{post}) integrates the interpolated slip surface derived from the geophysical measurements (cf. chapter 4.5) and the post-event DEM. Table 4-9 shows the values of the resulting DoD, which is based on the subtraction of the slip surface grid from DEM 2016. In comparison, V_d and V_{post} are rather similar, with a deviation of less than 1 % (Table 4-7).

Approach IV combines the results from I and II with the aim to calculate the volume of the material before the landslide occurred. The resulting volume V_{total} records the second highest volume with 4.2×10^6 m^3 (Table 4-7).

The difference between the slip surface and the pre-event DEM is calculated in Approach V, which represents the second pre-event volume (Table 4-9). The comparison

of the two pre-event volumes shows that V_{pre} displays the larger volume, however, with 4 % the difference remains very low.

Furthermore, the pre-event volume V_{pre} is compared to the post-event volumes. Therefore, V_e is added to the post-event volume (V_{post}) and V_a is subtracted. With a volume of 4.3 x 10^6 m^3 it shows a strong similarity to V_{pre}, with a difference of about 3 %.

Table 4-9. Results of the DoDs. DoD-2011 represents the difference between the pre-event and the interpolated slip surface. DoD-2016 represents the difference between the post-event and the interpolated slip surface (chapter 4.5).

Attributes	DoD - 2011	DoD - 2016
Areal		
Total area of erosion (m^2)	148,875	165,975
Total area of accumulation (m^2)	9150	200
Vertical averages		
Average depth of erosion (m)	29.02	23.47
Average depth of accumulation (m)	7.53	2.69
Volumetric		
Total volume of erosion (m^3)	4.3 x 10^6	3.9 x 10^6
Total volume of accumulation (m^3)	68,911	538
Total volume of difference (m^3)	***4.4 x 10^6***	***3.9 x 10^6***

5. Results of the sediment analyses

In order to characterize the landslide-related properties, a number of 154 samples was collected and analyzed. The resulting dataset is further used for validation in the modeling process (chapter 6). The samples are subdivided into three main local groups (Figure 5-1):

- Capulín
- Surrounding areas
- Escalanar

Location- and sample name are synonymous, if the location consists of only one sample. Continuous numeration after the location name indicates that it comprises more than one sample (e.g. location S 3, comprises 3 samples: S 3-1, S 3-2, and S 3-3). All coordinates and depth information are indicated in Appendix D. The results of the laboratory analyses are show in Appendix E to G, and the data, which were analyzed in the course of the thesis projects of M. Füssl and A. Lenz, is indicated in the Appendix.

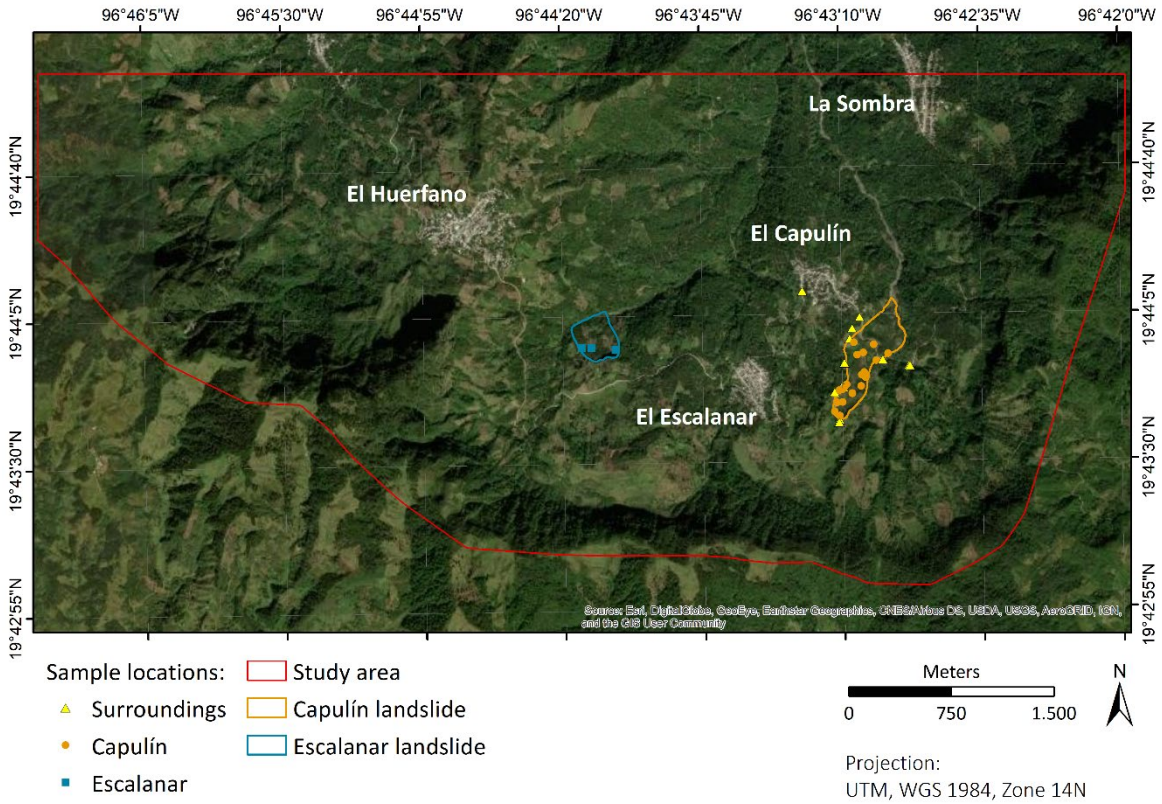

Figure 5-1. Sample locations. Samples located within the Capulín landslide are depicted in orange, sample in the surrounding areas are marked in yellow, and samples of the Escalanar landslide are depicted in blue. Source: Own illustration. Source of background map: Esri World Imagery (2019).

5.1 Sediments in the Capulín landslide area

5.1.1 Scarp area

Four locations were sampled in the scarp (S 1 - S 4), in areas with more than 50° slope angle, where S 1 and S 2 lie in the center of the scarp, S 3 as well as S 4 in the western part (Figure 5-2).

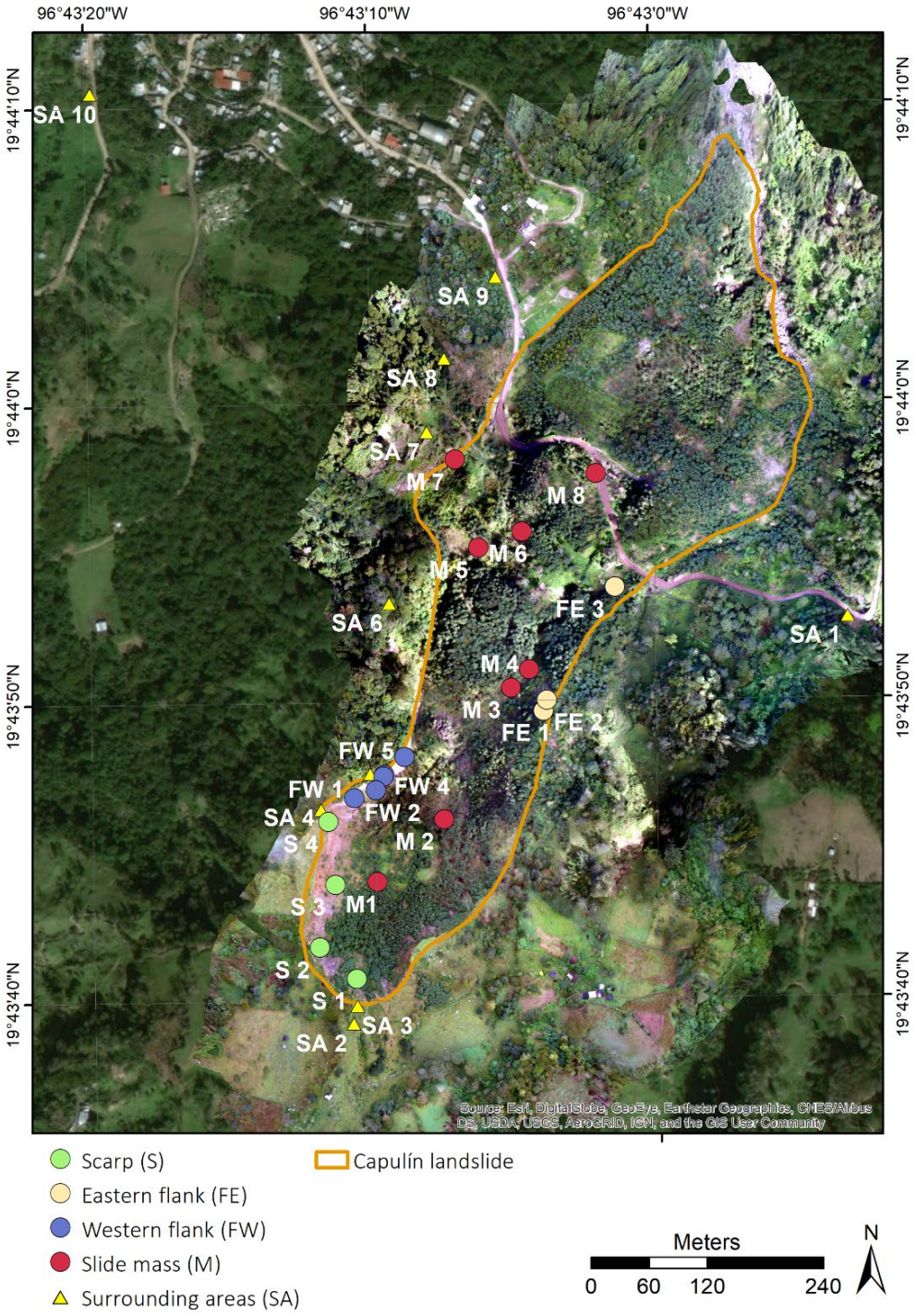

Figure 5-2. Sample locations inside and in the surrounding areas of the Capulín landslide. Source: Own illustration. Source of background map: Esri World Imagery (2019).

Figure 5-3 documents the general sediment structure for the locations S1, S2, and S3. The upper parts consist of large blocks (max. about 2 x 3 m) in a fine matrix, whereas fine materials dominate the lower parts. In location S 4, the blocky layer reaches down to depths of more than 20 m (Figure 5-4). At this site, it was possible to sample the entire exposure and therefore, S4 comprises 19 samples in total (Figure 5-4). The uppermost samples (4-1 to 4-4) differ significantly from those of the lower exposure, due to darker colors and the higher amounts of total carbon (TC), which range between 2.1 to 6.4 % (cf. Table 5-1). The TC values for all remaining scarp samples are below 0.8 %. Further differences can be observed in the results of the grain size distribution (Figure 5-5). With less than 20 % the clay content remains very low and the silt contents (65 - 76 %) are remarkably high.

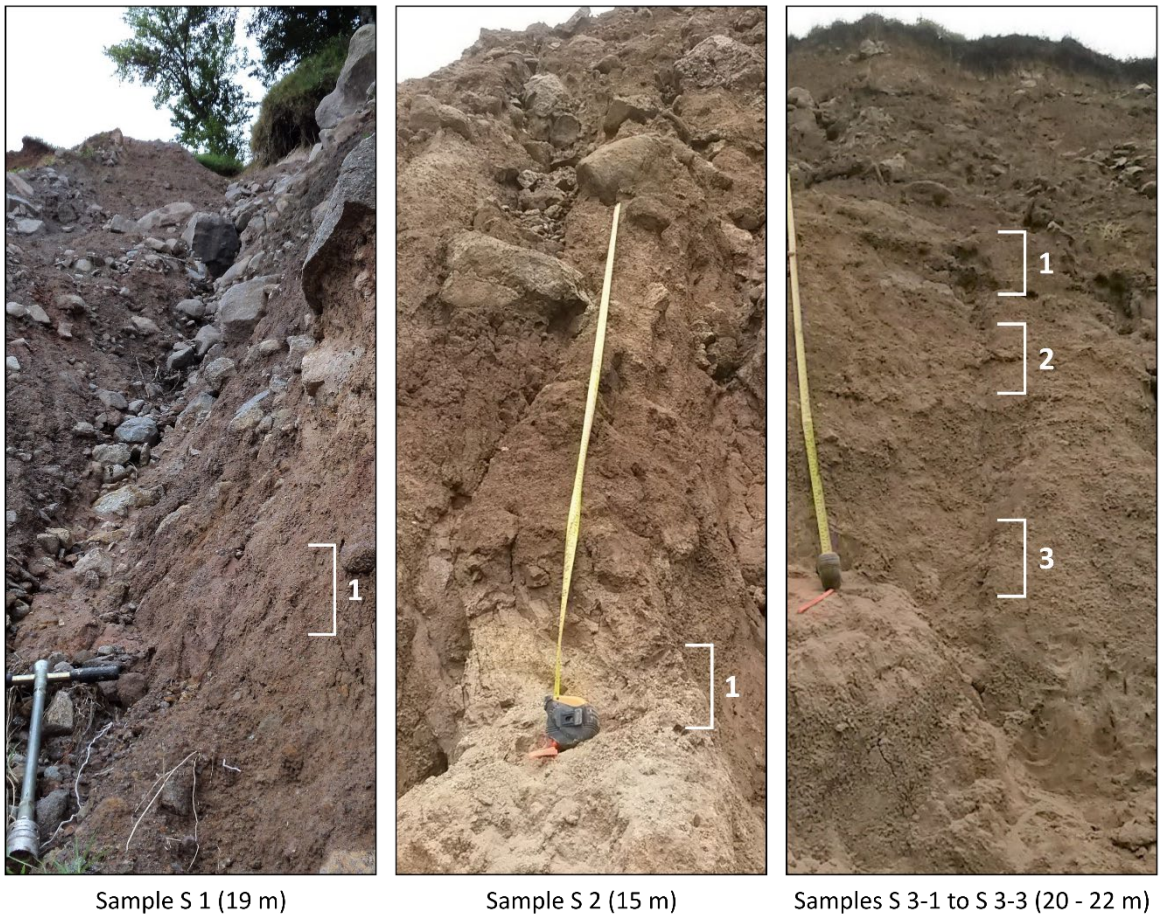

Figure 5-3. Location of the scarp samples (Capulín landslide). S 1 and S 2 are located in the center of the scarp, S 3 is located in the western part. The sampling areas are marked with white squared brackets. The sampling depths as indicated in the labels are measured from the top of the scarp. Source: Own photographs (2018).

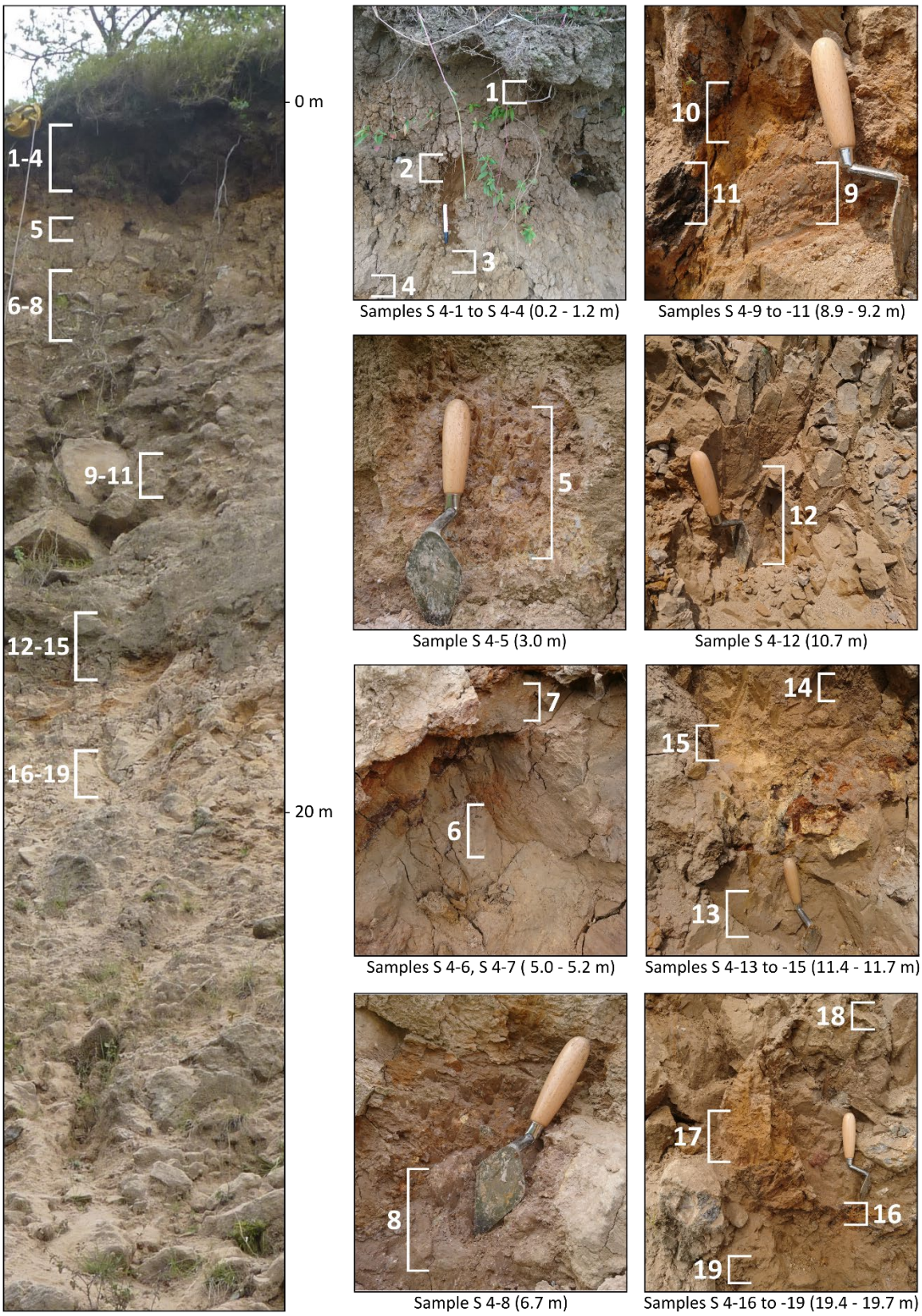

Figure 5-4. Sample location S 4. Left-hand side: Photo of the scarp exposure, from the top of the scarp down to the slide mass (not scaled). Right-hand side: detailed sampling areas. The sampling areas are marked with white squared brackets. The sampling depths as indicated in the labels are measured from the top of the scarp. Source: Own photographs (2018).

All other S4 samples as well as the samples from S 3 show clay contents between 26 and 70 % (Figure 5-5). In general, the silt contents range between 26 and 67 %, and the coarse material (sand and gravel) can reach up to 15 %. Whereas samples S 1 and S 2 have high

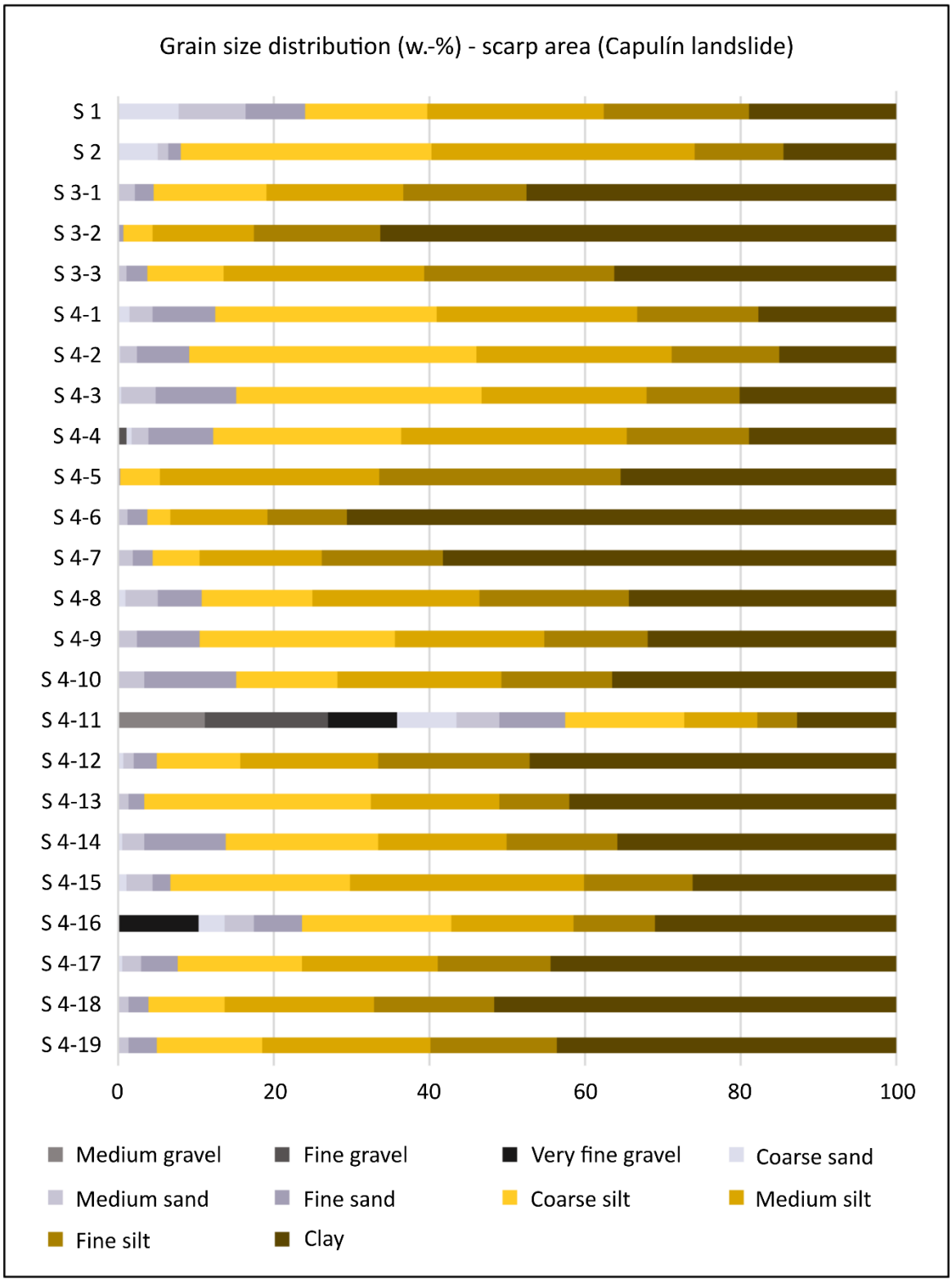

Figure 5-5. Grain size contents (weight-percentage) of the Capulín scarp. Source: Own illustration.

silt contents as well (48 - 77 %), they show lower clay contents (S 1, 24 %; Figure 5-5). In total, the scarp samples can be classified as clay (3), silty clay (6), silty clay loam (7), silt loam (7), and loam (1) (Appendix H, IUSS Working Group 2014).

Limits of consistency were analyzed for seven samples of the scarp area. Cohesion, unit weight values, and friction angle are derived by combining the limits of consistency results with the grain size distribution (cf. Appendix F and G). Sample S 3-2 as well as the five samples from location S 4 are classified as elastic silts, and sample S 3-3 is classified as low plastic silt (Figure 5-6). The latter has the highest unit weight and cohesion values, whereas S 3-2 has the lowest. The friction angle is the same (15.0°) for S 3-2 and all samples from S 4, only S 3-3 differs with a value of 22.5°.

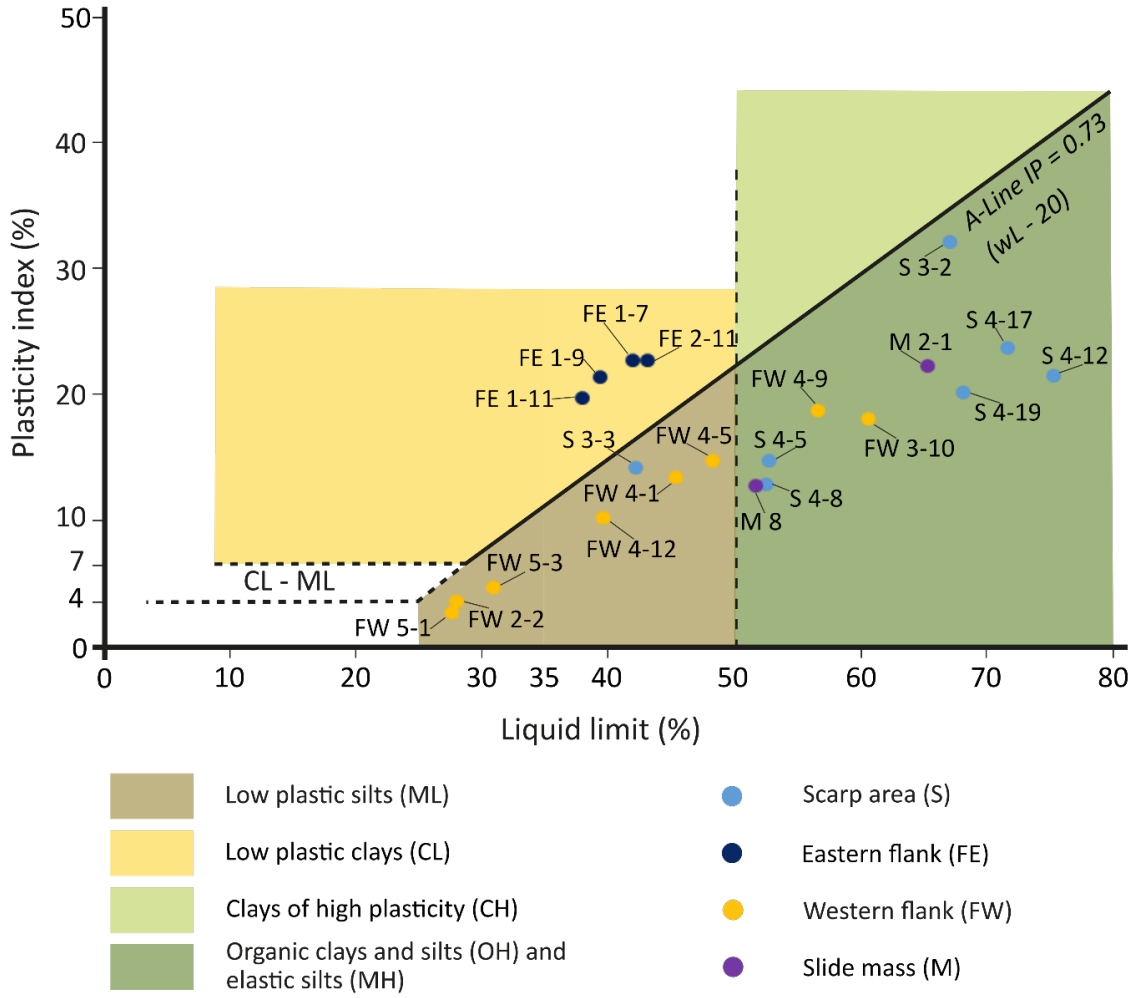

Figure 5-6. Limits of consistency analysis for the samples of the Capulín landslide (see also Appendix G). Plasticity chart according to ASTM (2006). Source: Own illustration.

The pH values are in a range of 4.5 to 7.5 (Table 5-1), and over 50 % are classified as moderately acidic according to DIN 4220 (2008). The carbonate pre-test was negative for all scarp samples. The hydraulic conductivity was measured for seven samples and four samples are classified as very low and two as low (Table 5-2). Only sample 3-3 is classified as 'high' according to DIN 4220 (2008). In general, the bulk density is very low (DIN 4220; Table 5-2).

Table 5-1. Results of the pH and total carbon (TC) analyses for the scarp area.

Name	pH	pH classification (DIN 4220)	Total carbon (%)
S 1	7.5	very slightly alkaline	-
S 2	6.7	very slightly acidic	-
S 3-3	6.9	neutral	-
S 4-1[1]	4.9	slightly acidic	6.36
S 4-2[1]	5.1	slightly acidic	3.21
S 4-3	5.2	moderately acidic	2.05
S 4-4	5.1	moderately acidic	0.82
S 4-5[1]	4.5	moderately acidic	0.08
S 4-6[1]	4.6	very slightly acidic	0.70
S 4-7[1]	4.7	slightly acidic	0.29
S 4-8	4.8	moderately acidic	0.16
S 4-9	5.0	moderately acidic	0.46
S 4-10	4.9	moderately acidic	0.41
S 4-11	5.3	moderately acidic	0.20
S 4-12	5.0	moderately acidic	0.29
S 4-13	5.5	strongly acidic	0.62
S 4-14	6.4	strongly acidic	0.29
S 4-15	5.2	strongly acidic	0.23
S 4-16	5.0	moderately acidic	0.20
S 4-17	5.1	moderately acidic	0.22
S 4-18	5.4	moderately acidic	0.24
S 4-19	6.0	moderately acidic	0.32

[1] = Füssl (2020); '-' = method not applied.

Table 5-2: Results of the dry bulk density and hydraulic conductivity analyses for the scarp area.

Name	Dry bulk density (g/cm³)	Bulk density classification (DIN 4220)	Constant hydraulic conductivity (cm/h)	Hydraulic conductivity classification (DIN 4220)
S 1	1.22	low	-	-
S 2	1.16	very low	-	-
S 3-3	0.96	very low	4.00	high
S 4-12	0.59	very low	0.03	very low
S 4-13	0.61	very low	0.04	very low
S 4-14	0.52	very low	0.21	low
S 4-15	0.49	very low	0.03	very low
S 4-18	0.82	very low	0.07	low
S 4-19	0.98	very low	0.01	very low

'-' = method not applied.

5.1.2 Eastern flank

Similar to the scarp area, the eastern flank is characterized by steep slopes with inclinations of more than 30° and relative height differences of more than 15 m. Depth and slope angle of the flank decrease towards the foot area of the slide. Three locations represent the eastern flank (Figure 5-2). FE 1 and FE 2 are at a distance to each other of approx. 10 m, and FE 3 is at a distance of 135 m north of FE 2. All three sites show different characteristics (Figure 5-7), especially the amount of coarse material (including large blocks of 1 x 2 m) differs strongly. FE 1 contains coarse material mainly in the upper parts (0 - 1 m), while in FE 2 and FE 3 coarse material is present in the entire exposures. The dominant color of FE 1 is gray, while brown to red colors dominate in FE 2 and FE 3 (see Figure 5-7). However, the first meter of FE 1 displays brown to red colors as well.

The silt fraction is dominant in almost all samples of the eastern flank (with the exception of FE 1-3, FE 2-2, and FE 2-10) and ranges between 30 and 58 % (Figure 5-8). Higher gravel and sand contents mainly occur in the upper parts of FE 1 (FE 1-1 to 1-4) as well as in FE 2, and in FE 3. The majority of the samples are classified as loam (cf. Appendix H; WRB, IUSS Working Group 2014). With the with the highest clay contents (33 - 39 %), FE 1-5 to 1-13 correspond to silty clays and FE 2-11 to silty clay loam (WRB, IUSS Working Group 2014). The limits of consistency were analyzed for four samples (FE 1-7, FE 1-9, FE 1-11, FE 2-11)

and all of them belong to the class of low plastic clays (Figure 5-6). With a friction angle of 22.5° and unit weights of 19.0 kN/m³, respectively 20.5 kN/m³, the geotechnical values record similarities for all four samples. Only the effective cohesion values differ clearly with 10 kN/m² for FE 1 samples and 0 kN/m² for sample FE 2-11 (details see Appendix G).

With pH values between 7.0 and 7.6, the samples of the eastern flank reveal slightly alkaline to neutral conditions (Table 5-3, Ad-hoc-AG Boden 2005). Although the pH values are relatively consistent for all samples, the carbonate contents show significant differences. While the carbonate values of FE 2 (with the exception of FE 2-11) and FE 3 range between 1 and 11 %, samples FE 1-5 to 1-13 and FE 2-11 show values between 25 and 39 % (Table 5-3). This difference can be observed in the TC values as well. The values for FE 1-1 to 1-4, and FE 2 range between 0.1 and 1.2 %, while samples FE 1-5 to 1-13 and FE 2-11 show values between 4.0 and 4.9 % (Table 5-3). The bulk density was analyzed for ten of the eastern flank samples (Table 5-4), with a predominance of high and very high bulk density (DIN 4220 2008). The hydraulic conductivity ranges from very low to very high according to DIN 4220 (2008; Table 5-4).

Figure 5-7. Photos of the sample locations of the eastern flank (Capulín landslide). The sampling areas are marked with white squared brackets. The sampling depths as indicated in the labels are measured from the ground surface. Source: Own photographs (2018).

Table 5-3. Results of pH, total carbon (TC), and carbonate analyses for the Capulín landslide's eastern flank.

Name	pH	pH classification (DIN 4220)	Total carbon (%)	Carbonates (%)
FE 1-1[1,2]	7.4	very slightly alkaline	0.29	-
FE 1-2[1,2]	7.1	neutral	0.17	1.88
FE 1-3[2]	7.3	very slightly alkaline	0.18	2.92
FE 1-4[2]	7.4	very slightly alkaline	0.09	1.00
FE 1-5[1,2]	7.5	very slightly alkaline	4.49	38.09
FE 1-6[1,2]	7.1	neutral	4.12	36.71
FE 1-7[2]	7.5	very slightly alkaline	4.31	25.29
FE 1-8[1,2]	7.4	very slightly alkaline	4.86	38.92
FE 1-9[1,2]	7.3	very slightly alkaline	4.81	37.89
FE 1-10[2]	7.2	neutral	4.88	38.41
FE 1-11[1,2]	7.1	neutral	4.48	36.94
FE 1-12[1,2]	7.2	neutral	4.39	37.69
FE 1-13[2]	7.3	very slightly alkaline	4.33	35.34
FE 2-1	7.5	very slightly alkaline	0.19	2.53
FE 2-2	7.6	very slightly alkaline	1.13	9.85
FE 2-3	7.5	very slightly alkaline	0.17	1.20
FE 2-4	7.6	very slightly alkaline	0.49	5.28
FE 2-5	7.3	very slightly alkaline	0.07	-
FE 2-6	7.2	very slightly alkaline	1.15	11.32
FE 2-7	7.2	very slightly alkaline	0.40	6.55
FE 2-8	7.2	very slightly alkaline	0.77	5.97
FE 2-9	7.0	neutral	0.09	-
FE 2-10	7.2	neutral	0.10	1.12
FE 2-11	7.2	neutral	4.02	35.48
FE 3	7.2	neutral	-	-

[1] = Füssl (2020); [2] = Lenz (2019); '-' = method not applied.

Table 5-4. Results of the dry bulk density and hydraulic conductivity analyses for the eastern flank.

Name	Dry bulk density (g/cm³)	Dry bulk density classification (DIN 4220)	Constant hydraulic conductivity (cm/h)	Hydraulic conductivity classification (DIN 4220)
FE 1-1[1,2]	1.36	low	0.06	low
FE 1-2[1,2]	2.94	very high	0.01	very low
FE 1-5[1,2]	1.79	high	-	-
FE 1-6[1,2]	1.90	very high	-	-
FE 1-8[1,2]	1.85	very high	-	-
FE 1-9[1,2]	1.76	high	-	-
FE 1-10[2]	1.81	very high	0.16	low
FE 1-11[1,2]	1.75	high	1.09	intermediate
FE 1-12[1,2]	1.77	high	3.78	high
FE 3	1.18	very low	4.54	very high

[1] = Füssl (2020); [2] = Lenz (2019); '-' = method not applied.

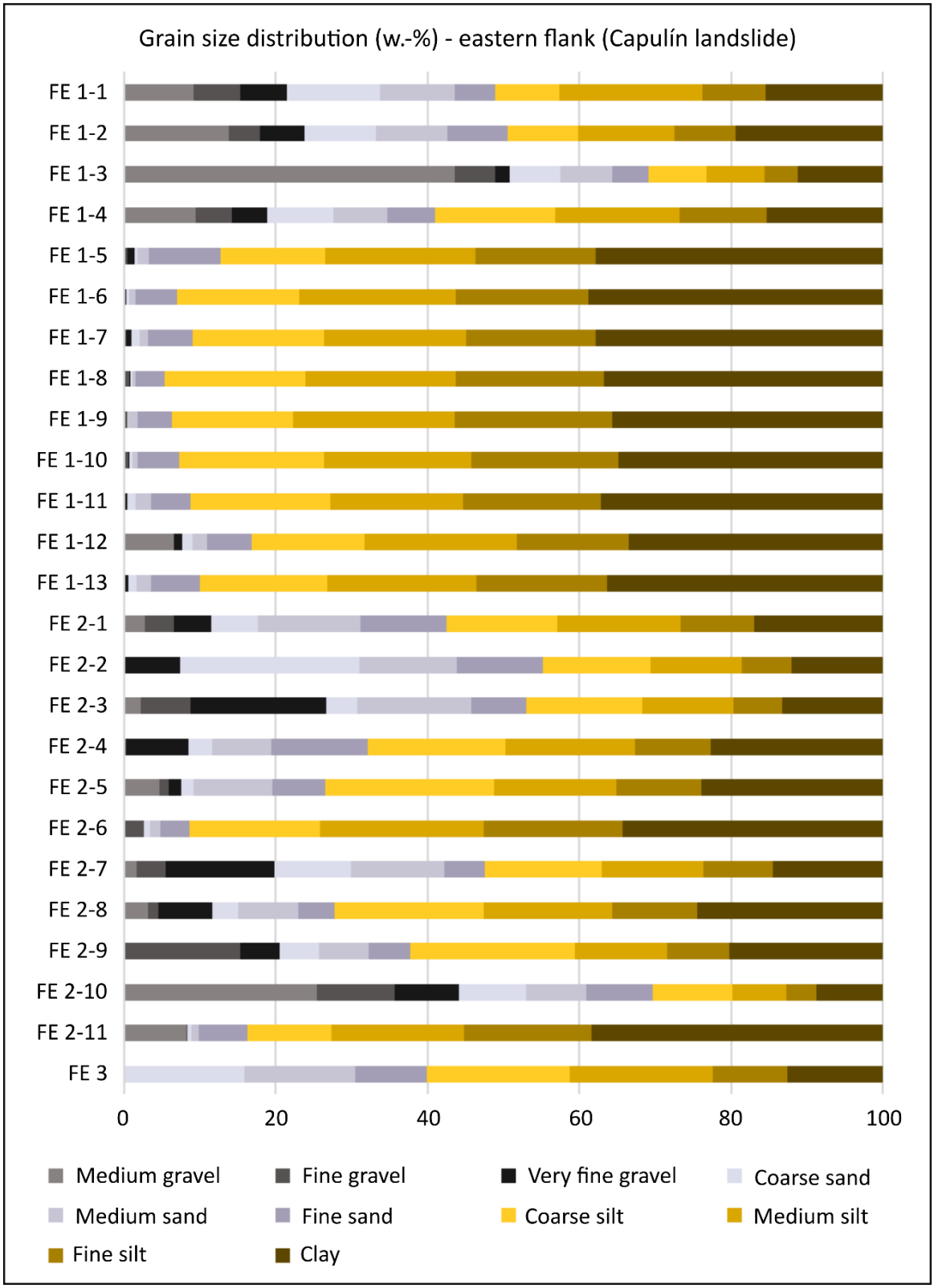

Figure 5-8. Grain size contents (weight-percentage) of the eastern flank (Capulín landslide). Source: Own illustration.

In summary, the results can be classified into two different groups, with one group consisting of FE 1-1 to FE 1-4, and samples of locations FE 2 and FE 3, and the second group comprising samples FE 1-5 to FE 1-13, and FE 2-11.

5.1.3 Western flank

Sampling of the western flank comprises five locations within a distance of about 70 m (Figure 5-2, 5-9). Steep slopes (> 40°) with vertical displacements of more than 20 m characterize the western flank. In contrast to the eastern flank, the steep slopes of the

Sample FW 1 (13 m) | Samples FW 2-1 to 2-3 (12 - 13 m) | Samples FW 3-1 to 3-13 (5 - 6 m)

Samples FW 4-1 to 4-13 (4 - 5 m) | Sample FW 5-1 to 5-4 (5 - 6 m)

Figure 5-9. Sample locations of the western flank (Capulín landslide). The sampling areas are marked with white squared brackets. The sampling depths as indicated in the labels are measured from the ground surface. Source: Own photographs (2018).

western flank reach down to the lower areas of the landslide. Samples FW 1 and FW 2-1 to 2-3 are located approx. 13 m below surface, and sample locations FW 3 to FW 5 are at depths between 4 and 6 m (Figure 5-2). FW 1, FW 2, and FW 5 show similar characteristics such as color (light grayish brown to light brown) or the presence of large blocks (about 0.5 x 1 m). Whereas FW 3 and FW 4 macroscopically differ from the other locations, especially in color, which range from brown to red, and the absence of larger blocks (Figure 5-9).

According to the WRB (IUSS Working Group 2014), 38 % of the samples can be classified as loam, and 38 % as silt loam (cf. Appendix H). Furthermore, 15 % correspond to sandy loam, and 9 % to silty clay loam (WRB, IUSS Working Group 2014). In more than 50 % of the samples the silt fraction is dominant (37 - 72 %), and the sand fraction ranges between 16 and 60 %, with the exception of FW 3-8 (10 %), FW 3-9 (4 %), and FW 3-12 (3 %). The clay contents show a wide range, with values between 3 and 34 % (Figure 5-10). The same can be observed for the gravel fraction, which ranges between 0 and 55 %. More than 60 % of the samples have gravel contents of less than 10 %, and only 9 % show values over 25 %.

In total, limits of consistency were determined for eight of the western flank samples. FW 3-10 and FW 4-9 are determined as elastic silts, whereas all other samples as low plastic silts (Figure 5-6). The geotechnical values form three main groups (Table 5-5). FW 5-1, 5-3, and FW 2-2 represent the group with the highest values, with a friction angle of 27.5°, a unit weight value of 21.0 kN/m³, and effective cohesion of 5.0 kN/m² (group A, marked in yellow, Table 5-5). FW 3-10 and FW 4-9 correspond to the group with the lowest values,

Table 5-5. Results of the geotechnical analyses for the western flank of the Capulín landslide. Group A (yellow) records the highest values. Group B (green) has the lowest values, Group C (blue) represents the remaining values with similar range.

Name	Unit weight (kN/m³)	Friction angle (°)	Cohesion c' (kN/m²)
FW 2-2	21.0	27.5	5.0
FW 3-10	17.0	15.0	0.0
FW 4-1	19.5	22.5	5.0
FW 4-5	19.0	22.5	0.0
FW 4-9	17.0	15.0	0.0
FW 4-12	19.0	22.5	0.0
FW 5-1	21.0	27.5	5.0
FW 5-3	21.0	27.5	5.0

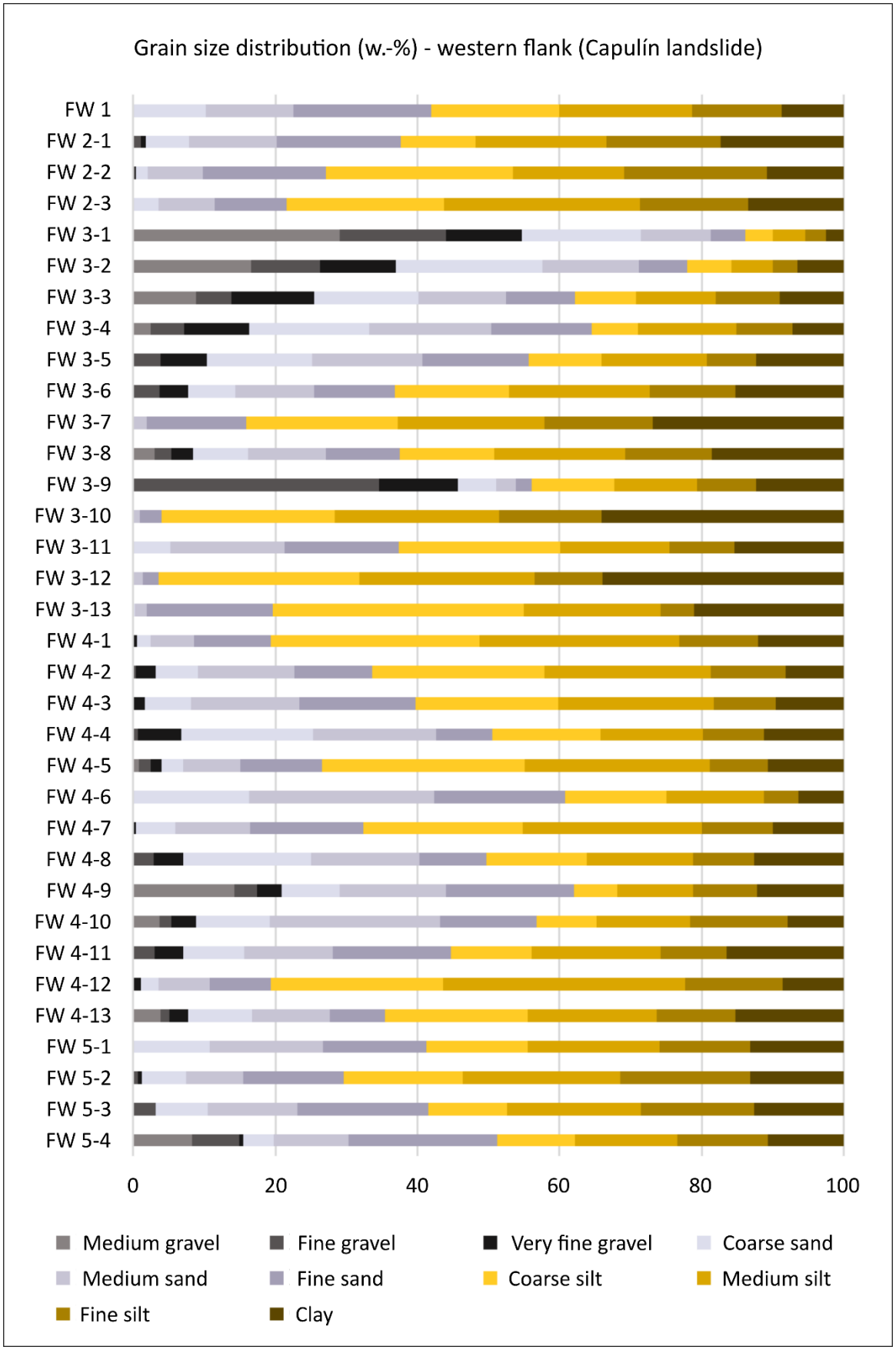

Figure 5-10. Grain size contents (weight-percentage) of the Capulín landslide's western flank. Source: Own illustration.

with a friction angle of 15°, a unit weight value of 17 kN/m³, and cohesion of 0 kN/m² (group B, marked in green, Table 5-5). FW 4-1, FW 4-5, and FW 4-12 have similar results and therefore, can be combined in one group (group C, marked in blue, Table 5-5). All three samples have a friction angle of 22.5°, the unit weight values range between 19.0 and 19.5 kN/m³, and the effective cohesion values are between 0 and 5 kN/m². The bulk density was analyzed for seven samples and the results range between very low (3), low (3), and intermediate (1) (Table 5-6). The western flank sediments have very low carbonate content values (0.04 to 0.80 %) and the pH values range between 4.9 and 7.0 (Table 5-6 and 5-7), whereas approx. 66 % are classified as slightly acidic, 22 % as very slightly acidic, 6 % as neutral, and 6 % as moderately acidic. All samples show TC contents of less than 0.1 % (Table 5-7). The hydraulic conductivity was analyzed for seven samples and is predominantly classified as low (according to DIN 4220), with the exception of sample FW 4-5, which is classified as intermediate (cf. Table 5-6).

Table 5-6. Results of the dry bulk density, hydraulic conductivity, and carbonate analyses for the western flank of the Capulín landslide.

Name	Dry bulk density (g/cm³)	Dry bulk density classification (DIN 4220)	Constant hydraulic conductivity (cm/h)	Hydraulic conductivity classification (DIN 4220)	Carbonates (%)
FW 3-2[2]	-	-	-	-	0,22
FW 4-1[1,2]	0.97	very low	-	-	0.10
FW 4-2[1,2]	1.49	intermediate	0.27	low	0.26
FW 4-3	-	-	-	-	0.08
FW 4-4	-	-	-	-	0.80
FW 4-5[1,2]	1.35	low	0.55	intermediate	0.04
FW 4-6[1]	1.37	low	0.06	low	-
FW 4-7	-	-	-	-	0.42
FW 4-9[1]	0.99	very low	0.07	low	-
FW 4-10[1]	1.01	very low	0.38	low	-
FW 4-11[1,2]	1.37	low	0.35	low	0.32
FW 4-12	-	-	0.06	low	-
FW 4-13	-	-	-	-	0.32

[1] = Füssl (2020); [2] = Lenz (2019); '-' = method not applied.

Table 5-7. Results of the pH and total carbon (TC) analyses for the western flank of the Capulín landslide.

Name	pH	pH classification (DIN 4220)	Total carbon (%)
FW 2-1	5.6	slightly acidic	0.08
FW 2-2	6.0	slightly acidic	0.03
FW 3-1[2]	6.9	neutral	0.04
FW 3-2[2]	5.8	slightly acidic	0.05
FW 3-3[2]	5.7	slightly acidic	0.02
FW 3-4[2]	7.0	neutral	0.02
FW 3-5[2]	5.7	slightly acidic	0.02
FW 3-6[2]	6.6	very slightly acidic	0.02
FW 3-7[2]	6.0	slightly acidic	0.03
FW 3-8[2]	6.7	very slightly acidic	0.03
FW 3-9[2]	5.8	slightly acidic	0.03
FW 3-10[2]	5.9	slightly acidic	0.05
FW 3-11[2]	5.9	slightly acidic	0.04
FW 3-12[2]	5.8	slightly acidic	0.03
FW 3-13[2]	6.0	slightly acidic	0.03
FW 4-1[1]	5.8	slightly acidic	0.02
FW 4-2[1]	5.7	slightly acidic	0.02
FW 4-3	6.6	very slightly acidic	0.02
FW 4-4	5.8	slightly acidic	0.03
FW 4-5[1]	5.6	slightly acidic	0.02
FW 4-6[1]	6.7	very slightly acidic	0.02
FW 4-7	6.4	very slightly acidic	0.02
FW 4-8	6.7	very slightly acidic	0.02
FW 4-9[1]	5.3	moderately acidic	0.03
FW 4-10[1]	5.7	slightly acidic	0.03
FW 4-11[1]	4.9	moderately acidic	0.04
FW 4-12	6.5	very slightly acidic	0.06
FW 4-13	5.7	slightly acidic	0.04
FW 5-1	6.0	slightly acidic	0.06
FW 5-2	6.0	slightly acidic	0.09
FW 5-3	5.8	slightly acidic	0.10
FW 5-4	5.9	slightly acidic	0.08

[1] = Füssl (2020); [2] = Lenz (2019).

5.1.4 Slide mass

The sample locations of the slide mass (Figure 5-11) are mostly concentrated in the center and the upper parts of the slide, however, they appear to be very heterogeneous (Figure 5-2). M 1 is located in a relatively flat area in close proximity to the scarp, while M 2 belongs to an area with steep slopes (> 30°). A small incised creek formed the exposures of M 3 and M 4, which lie in the center of the slide mass and near the eastern flank (Figure 5-2). M 5 is located in a flat area in the center of the slide, close to the western flank. This flat area has a width of approx. 70 m and is surrounded by higher terrain, where M 6 is located.

Figure 5-11. Sample locations of the slide mass. The sampling areas are marked with squared white and black brackets. The sampling depths as indicated in the labels are measured from the ground surface. Source: Own photographs (2016, 2018).

M 6 represents a soil profile with a depth of approx. 1 m. M 7 is situated at a contact point between the main slide mass and a secondary slide mass, which originated from the western flank. At location M 8, a road cut exposed the slide mass (Figure 5-2).

Grain size analyses for the slide mass yields a texture of silt loam for 75 % of the samples, and silty clay loam for 19 %. As the only one (6 %), the texture of sample M 5 (Figure 5-12) belongs to sandy loams (WRB, IUSS Working Group 2014), with almost equal silt (50.0 %) and sand contents (44.5 %). In general, silt is the predominant grain size fraction throughout all samples of the slide mass, with values between 41.0 and 75.1 % (Figure 5-12). In M 1, the sand content with 29.7 % is relatively high, and the clay fraction

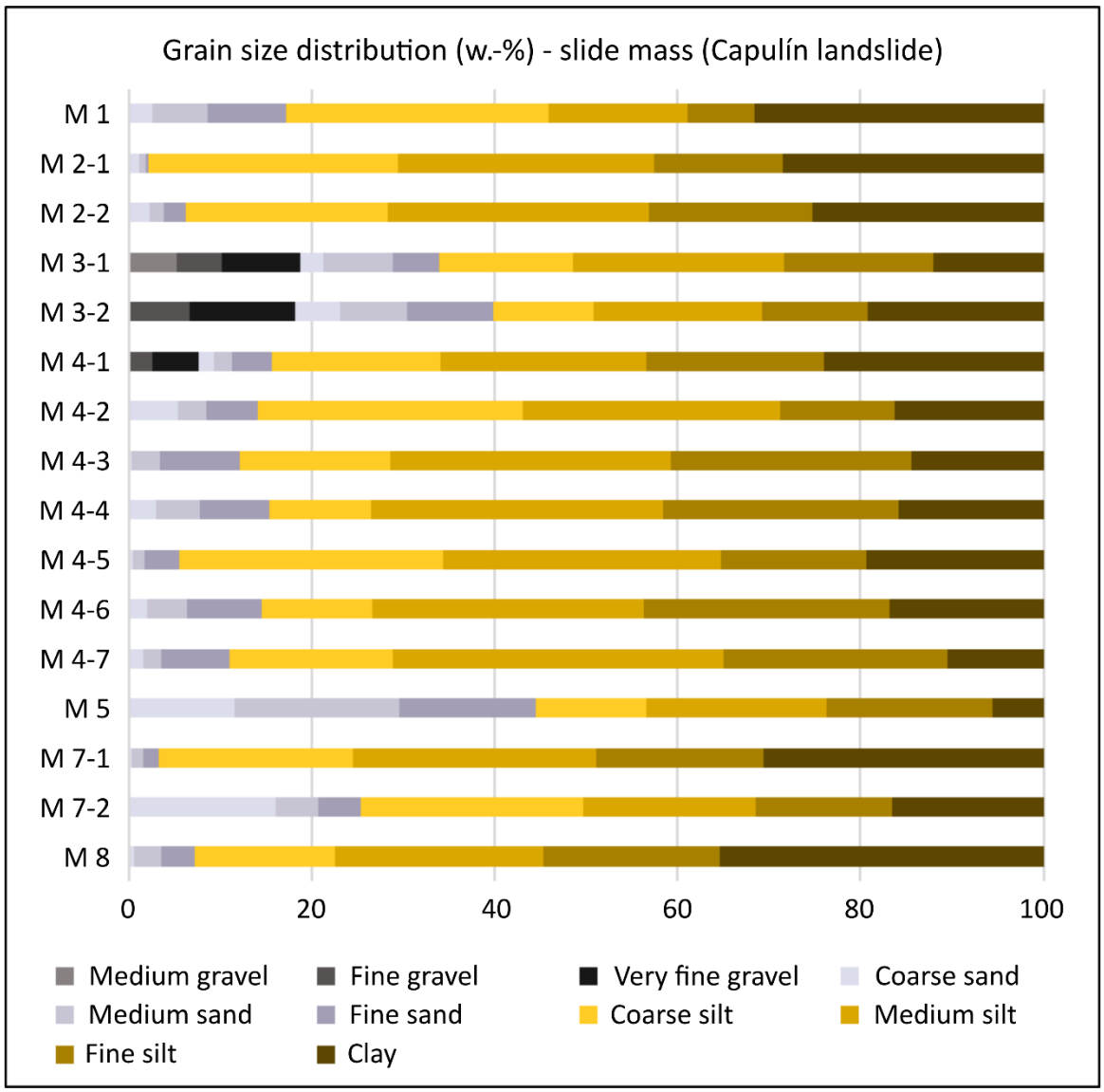

Figure 5-12. Grain size content (weight-percentage) of the Capulín slide mass. Source: Own illustration.

plays a minor role with 14.4 %. M 2 contains high amounts of clay between 25.2 % (M 2-2) and 28.5 % (M 2-1), while the sand remains very low. For M 3, sand and clay occur in equivalent amounts, with sand contents between 15 and 21 %, and clay contents between 12 and 19 % (Figure 5-12). In location M 4, the sand contents range between 5.5 and 15.4 % and the clay contents between 10.5 and 23.9 %. With 30.5 % the clay fraction in M 7-1 is high, while the sand content is very low (3.3 %). Despite of this, the clay content of M 7-2 reaches 16.5 %, and the sand fraction 25.3 %. M 8 shows a similar distribution as M 7-1, with a clay content of 35.3 %, and a low sand content of 7.3 % (Figure 5-12).

Table 5-8. Results of pH, total carbon, and dry bulk density analyses for the Capulín slide mass.

Name	pH	pH classification (DIN 4220)	Total carbon (%)	Dry bulk density (g/cm³)	Dry bulk density classification (DIN 4220)
M 1	6.6	very slightly acidic	-	1.33	low
M 2-1	7.5	very slightly alkaline	-	0.88	very low
M 2-2	7.1	neutral	-	0.99	very low
M 3-1	5.4	moderately acidic	0.06	-	-
M 3-2	5.2	moderately acidic	0.57	-	-
M 4-1	5.7	slightly acidic	0.06	-	-
M 4-2	5.6	slightly acidic	0.06	-	-
M 4-3	5.7	slightly acidic	0.06	-	-
M 4-4	5.6	slightly acidic	0.04	-	-
M 4-5	5.6	slightly acidic	-	-	-
M 4-6	5.7	slightly acidic	0.04	-	-
M 4-7	5.6	slightly acidic	0.04	-	-
M 5	7.4	very slightly alkaline	-	1.40	low
M 6-1	4.9	moderately acidic	7.54	-	-
M 6-2	5.7	slightly acidic	3.16	-	-
M 6-3	5.7	slightly acidic	1.67	-	-
M 6-4	5.4	slightly acidic	1.15	-	-
M 6-5	5.3	moderately acidic	0.97	-	-
M 6-6	5.3	moderately acidic	0.99	-	-
M 6-7	5.3	moderately acidic	1.20	-	-
M 7-1	-	-	-	-	-
M 7-2	-	-	-	-	-
M 8	6.7	very slightly acidic	-	1.02	very low

'-' = method not applied.

The bulk density was determined for five samples and ranges between very low (3) and low (2) according to DIN 4220 (2008; Table 5-8). Limits of consistency were analyzed for two samples (M 2-1, M 8) and both classify as elastic silts, with a friction angle of 15°, unit weight of 14 kN/m³, and effective cohesion value of 10 kN/m² (Figure 5-6, Appendix G).

The pH values for M 1, M 3, M 4, and M8 are between 5.2 and 6.7 and therefore, show moderately acidic to very slightly acidic conditions (Ad-hoc-AG Boden 2005, DIN 4220 2008). M 2-2 is classified as neutral (7.1), and M 2-1 (7.5) and M5 (7.4) as very slightly alkaline (DIN 4220, Ad-hoc-AG Boden 2005). The carbonate test was negative for all samples and the TC contents are very low (Table 5-8).

As mentioned above, location M 6 corresponds to a soil profile, consisting of seven horizons, and is situated within the slide mass (Figure 5-2). The horizons are Ah, AB, Bw1, Bw2, Bw(t)1, Bw(t)2, Bw(t)3 (Figure 5-13), and the determined soil group is Andosol (WRB, IUSS Working Group 2014). The first horizon (M 6-1) is a dense, compact Ah horizon with dark brown to black colors and a thickness of 12 cm. The structure of the soil matrix is granular containing few small rock fragments, and fine roots are numerous. Below a clear and wavy boundary, a dark brown, loose AB horizon (M 6-2) is located between 12 and 25 cm depth (Figure 5-13). Illuviated organic material from the overlying horizon is related to the dark color. Fine roots penetrate the matrix, whereas rock fragments are not present in this horizon. The structure of the soil matrix is granular to (sub-)angular, and the lower

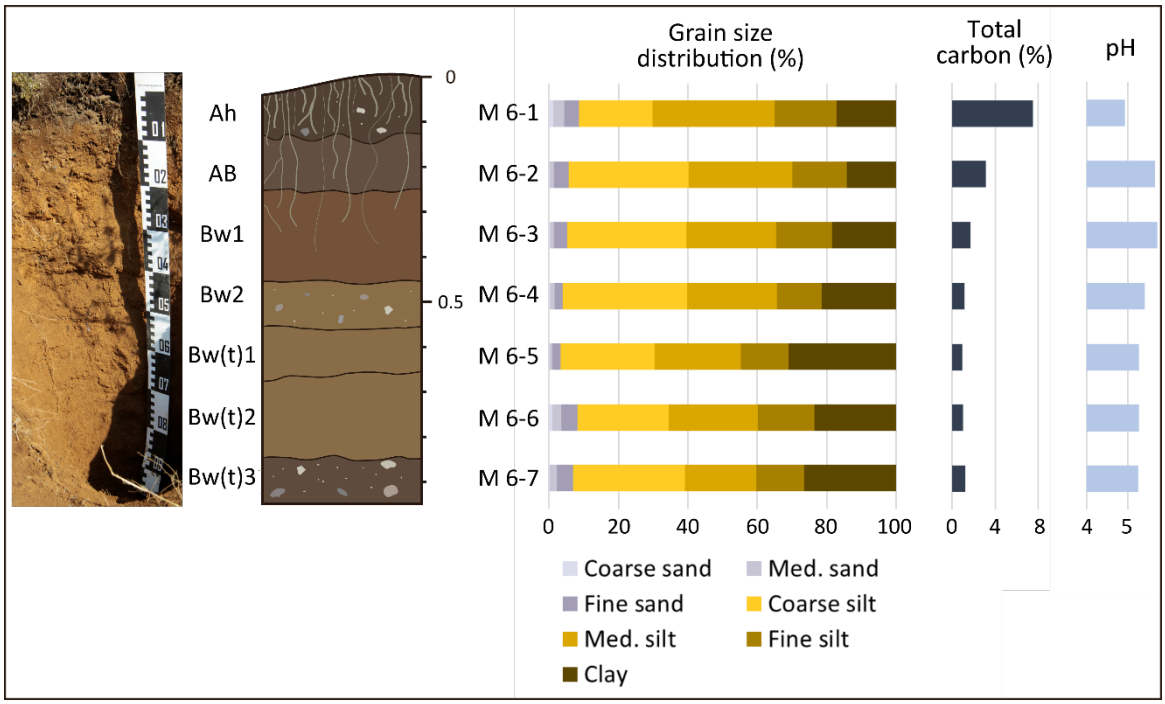

Figure 5-13. Profile and laboratory results of M 6. Source: Own photograph (2016) and illustrations.

boundary is wavy and diffuse. A reddish brown Bw1 horizon (M 6-3) follows between 25 and 45 cm depth. In general, it is slightly denser than the horizon above, but still loose, and has a (sub-)angular to granular structure. Few small clay coatings can be observed and fine roots are still present. The basal boundary is clear and relatively straight. The following Bw2 horizon (M 6-4; 45 - 55 cm) is more densely packed, has a brown color and a (sub-)angular to granular structure. Single small rock fragments are present and the aggregate surfaces have thin clay coatings. A loose and brownish Bw(t) horizon (M 6-5; 55 - 65 cm) follows below a straight boundary. The soil structure is (sub-)angular to weak granular, with a weak platy structure as well. Rock fragments and clay coatings are not present, and the boundary towards the lower horizon is clear and straight. At a depth of 65 to 85 cm the second Bw(t) horizon (M 6-6) is determined. In this part, the soil is more dense and shows a (sub-)angular to weak platy structure. The color is brown and few clay coatings are present, while rock fragments are absent. The basal horizon is a Bw(t) horizon (M 6-7) at a depth of 85 to 110 cm, which corresponds to the end of the pit, however, it does not mark the end of the soil. This horizon is denser and of dark brown color. The structure is (sub-)angular, and size and proportion of rock fragments increase (Figure 5-13).

The grain size analysis for M 6 yielded textures of silt loam and silty clay loam (according to WRB, IUSS Working Group 2014), with silt as the predominant component (cf. Appendix H). In general, the four upper horizons M 6-1 to 6-4 have higher silt contents (74.1 - 80.0 %), while the lower three horizons (M 6-5 to M 6-7) show higher clay contents (23.6 - 30.9 %). The sand fraction lies below 10 % in all horizons (Figure 5-13).

Horizon M 6-1 is classified as silt loam (according to WRB, IUSS Working Group 2014) with a silt content of 74.1 %. The medium silt represents the highest proportion, with 35.4 %, within the silt fraction (Figure 5-13). The clay content lies at 17.2 % and the sand content has the lowest amount with 8.7 %. M 6-2 has the highest silt content (80.0 %) and the lowest clay content (14.3 %) within the profile (Figure 5-13). Here, the silt fraction is dominated by coarse silt (34.4 %). In M 6-3 the clay content raises again to 18.5 %, and the silt content slightly decreases (76.2 %). Equal to the former horizon, coarse silt remains the dominant silt fraction (34.4 %). M 6-4 shows values similar to the former horizons and has the highest coarse silt content (35.7 %) within the profile. M 6-5 is determined as silty clay loam and has the highest clay content (30.9 %) of all soil horizons. Simultaneously, sand (3.3 %) and silt contents (65.7 %) remain very low (Figure 5-13). M 6-6 is classified as silt

loam as the clay content decreases again (23.6 %). With 8.2 % M 6-6 shows high amount of sand fraction. The basal horizon (M 6-7) is determined as silty clay loam (same as M 6-5) as well, with 26.6 % of clay, 66.4 % silt, and 7.0 % of sand (Figure 5-13).

The TC content is highest in the uppermost horizon (M 6-1; 7.5 %) and is decreasing with depth, from 3.16 and 0.97 % (Table 5-8). The pH values of profile M 6 are between 4.9 and 5.7. The uppermost horizon (M 6-1; 4.9) as well as the lower three horizons (M 6-5 to M 6-6; 5.3) are classified as moderately acidic, while the remaining three horizons (M 6-2 to M 6-4) are classified as slightly acidic (cf. Table 5-8).

5.2 Sediments in the surrounding areas

The surrounding areas of the Capulín landslide were sampled at ten different locations. The majority of the sample sites (SA 2 to SA 9) are in close proximity to the slide, mainly concentrated on the western side and on top of the scarp (Figure 5-2). SA 1 represents an outcrop approx. 200 m west of the Capulín landslide (Figure 5-14), next to the road leading from El Capulín (in northern direction) to La Sombra (Figure 5-1). The location comprises two samples, SA 1-1 and SA 1-2, in depths of 4.0 m and 4.2 m, respectively (Figure 5-14). SA 10 is located at the same road, however, leading in the opposite direction (southwest) towards the village El Escalanar. It has a linear distance of about 500 m northwest to the Capulín landslide, and a 30 m distance to the entrance of the village El Capulín (Figure 5-2). The samples of this site are at depths of 2.0 m (SA 10-1) and 2.4 m (SA 10-2). Primarily, according to field observations, all four samples appear to be very similar, especially due to their gray colors (Figure 5-14). However, laboratory analyses record some differences as well. Although the silt fraction is predominant in all samples (43.8 - 71.4 %), SA 1-1 and SA 1-2 have higher clay contents (32.2 - 34.9 %) and are classified as silty clay loam (according to IUSS Working Group2014), while samples SA 10-1 (20.2 % clay) and 10-2 (18.9 % clay) are classified as silt loam (cf. Appendix H). Interestingly, the contents of the coarse materials vary strongly within the locations.

SA 1-1 shows low contents of gravel (0.9 %) and sand (3.2 %), while SA 1-2 has a larger proportion of coarse material, with 8.6 % of gravel, and 15.4 % of sand. SA 10-1 and SA 10-2 have similar contents of coarse material (11.9 and 9.7 %, respectively), however, differ in their distribution (Figure 5-15). SA 10-1 shows an almost even distribution of gravel (5.7 %) and sand (6.2 %), whereas SA 10-2 has a very low gravel (0.2 %), and a high sand

proportion (9.5 %). Hydraulic conductivity was determined for samples SA 1-1 and SA 1-2, and is classfied as low (0.17 cm/h) and intermediate (0.44 cm/h) according to DIN 4220. The bulk density is classified as very high for SA 1-1, and for SA 1-2 as high (Table 5-9). The pH values are very homogenous, with a range of 7.4 to 7.6 and thus, can be classified as very slightly alkaline (Table 5-9). Carbonate contents are within a similar range for SA 1-1, SA 10-1, and SA 10-2, with the exception of SA 1-2, which shows a lower value with 18.7 %. The same distribution can be observed considering the TC contents, while SA 1-1, SA 10-1, and SA 10-2 lie within a range of 4.5 % to 4.8 %, SA 1-2 shows a lower value with 2.3 % (Table 5-9).

Study site and location of samples SA 1-1 and 1-2 (4.0, 4.2 m)

Study site and location of samples SA 10-1 and 10-2 (2.0, 2.4 m)

Figure 5-14. Study site and sampling locations SA 1 and SA 10. The sampling depths as indicated in the labels are measured from the ground surface. Source: Own photographs (2018).

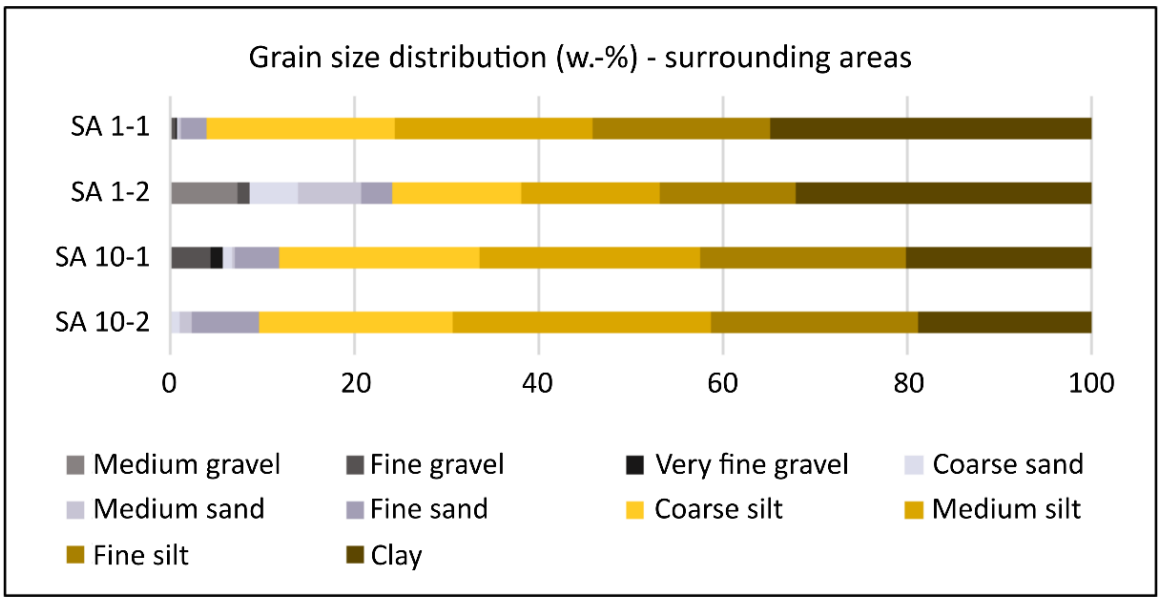

Figure 5-15. Grain size content (weight-percentage) of the sample locations SA 1 and SA 10 from the surrounding areas. Source: Own illustration.

Table 5-9. Results of pH, TC, carbonates, and dry bulk density analyses for the surrounding areas.

Name	TC (%)	pH ($CaCl_2$)	pH classification (DIN 4220)	Dry bulk density (g/cm^3)	Dry bulk density classification (DIN 4220)	Carbonates (%)
SA 1-1[1]	4.44	7.4	very slightly alkaline	2.00	very high	35.33
SA 1-2[1]	2.34	7.6	very slightly alkaline	1.80	high	18.66
SA 10-1	4.60	7.6	very slightly alkaline	-	-	38.23
SA 10-2	4.83	7.6	very slightly alkaline	-	-	40.28

The results of the limits of consistency anlyses prove low plastic clays for the three samples (Figure 5-16; ASTM 2006). These results combined with the grain size classification result in a friction angle of 27.5°, an effective cohesion value of 5 kN/m^2, and a unit weight of 21.0 kN/m^3 for samples SA 10-1 and SA 10-2. Even though SA 1-1 is classified as low plastic silt as well, with 41.5 % its liquid limit is higher (< 30 % for sample location SA 10), and

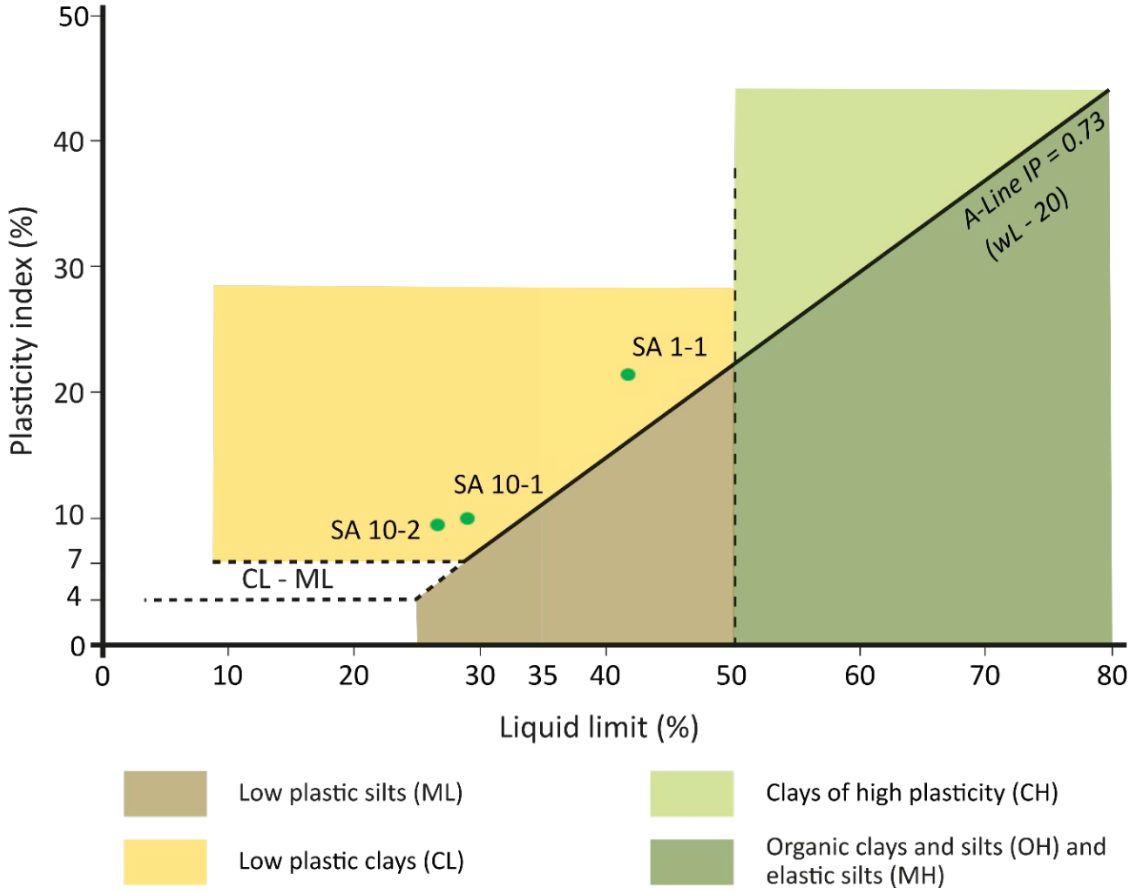

Figure 5-16. Limits of consistency analysis for the samples in the surrounding areas of the Capulín landslide (cf. Appendix G). Plasticity chart according to ASTM (2016). Source: Own illustration.

therefore, the derived geotechnical values differ from the SA 10 results. The unit weight for SA 1-1 is slightly lower, with 20.5 kN/m³, the friction angle is also smaller (22.5°). However, the effective cohesion shows a higher value with 10 kN/m² (Appendix G).

Figure 5-17 shows further sampling locations of the surrounding areas. SA 2 to SA 9 are at the western flank as well as above the scarp of the Capulín landslide (Figure 5-2) at a depth between 0.1 to 1.6 m below the surface (Figure 5-17, Appendix D). These samples are characterized by brown to reddish brown colors. Fine material is predominant in all locations. Furthermore, coarser material (max. 2 x 10 cm) is present in locations SA 6 to SA 9 (Figure 5-17).

Grain size analysis for sample locations SA 3 to SA 9 yields a texture of silt loam (according to WRB, IUSS Working Group 2014) for 43 % of the samples, and a texture of silty clay loam for 43 % (Appendix H). All other samples correspond to silty clays (SA 4-2),

Figure 5-17. Sample locations (SA 2 - SA 9) of the surrounding areas of the Capulín landslide. The sampling areas are marked with white squared brackets. The sampling depths as indicated in the labels are measured from the ground surface. Source: Photographs T. Sprafke (2016).

and clay (SA 4-3). In samples SA 3 to SA 9, the silt fraction is dominant (52.3 - 75.0 %), with the exception of SA 4-2 and SA 4-3, where clay has the largest proportion (49.2 and 59.9 %). The clay contents for the remaining samples (SA 3, SA 5 - SA 9) range between 15.4 and 34.7 %, and the contents of the coarse material (including gravel and sand fraction) lie between 2.2 and 29.4 % (Figure 5-18).

TC contents are below 1.0 % for 67 % of the samples, and the remaining 33 % range between 1.3 and 2.8 % (Table 5-10). The pH values range between 4.1 and 6.0, whereby 26 % are classified as strongly acidic, 58 % as moderately acidic and 16 % as slightly acidic (Table 5-10). Unlike sample locations SA 1 and SA 10, the carbonate pre-test was negative. The dry bulk density analyses comprises 14 samples and the results range between very low and intermediate (cf. Table 5-10).

Table 5-10. Results of pH, total carbon (TC), carbonates, and dry bulk density analyses for the surrounding areas (SA 2 – SA 9).

Name	pH	pH classification (DIN 4220)	Total carbon (%)	Dry bulk density (g/cm³)	Dry bulk density classification (DIN 4220)
SA 2-1	4.9	moderately acidic	2.81	-	-
SA 2-2	5.4	moderately acidic	1.65	-	-
SA 2-3	5.3	moderately acidic	1.66	-	-
SA 2-4	5.0	moderately acidic	1.34	-	-
SA 2-5	5.0	moderately acidic	0.88	-	-
SA 3	6.0	slightly acidic	-	0.97	very low
SA 4-1	4.7	strongly acidic	0.72	0.52	very low
SA 4-2	4.3	strongly acidic	0.51	0.73	very low
SA 4-3	4.1	strongly acidic	0.25	0.93	very low
SA 5-1	4.3	strongly acidic	1.57	1.19	very low
SA 5-2	5.4	slightly acidic	0.17	1.53	intermediate
SA 6-1	4.4	strongly acidic	0.27	1.25	low
SA 6-2	5.1	moderately acidic	0.07	1.23	low
SA 7	5.6	slightly acidic	0.46	1.24	low
SA 8	4.8	moderately acidic	0.46	1.38	low
SA 9-1	4.9	moderately acidic	2.04	1.01	very low
SA 9-2	5.2	moderately acidic	0.94	1.32	low
SA 9-3	5.2	moderately acidic	0.56	1.33	low
SA 9-4	5.2	moderately acidic	0.34	1.23	low

'-' = method not applied.

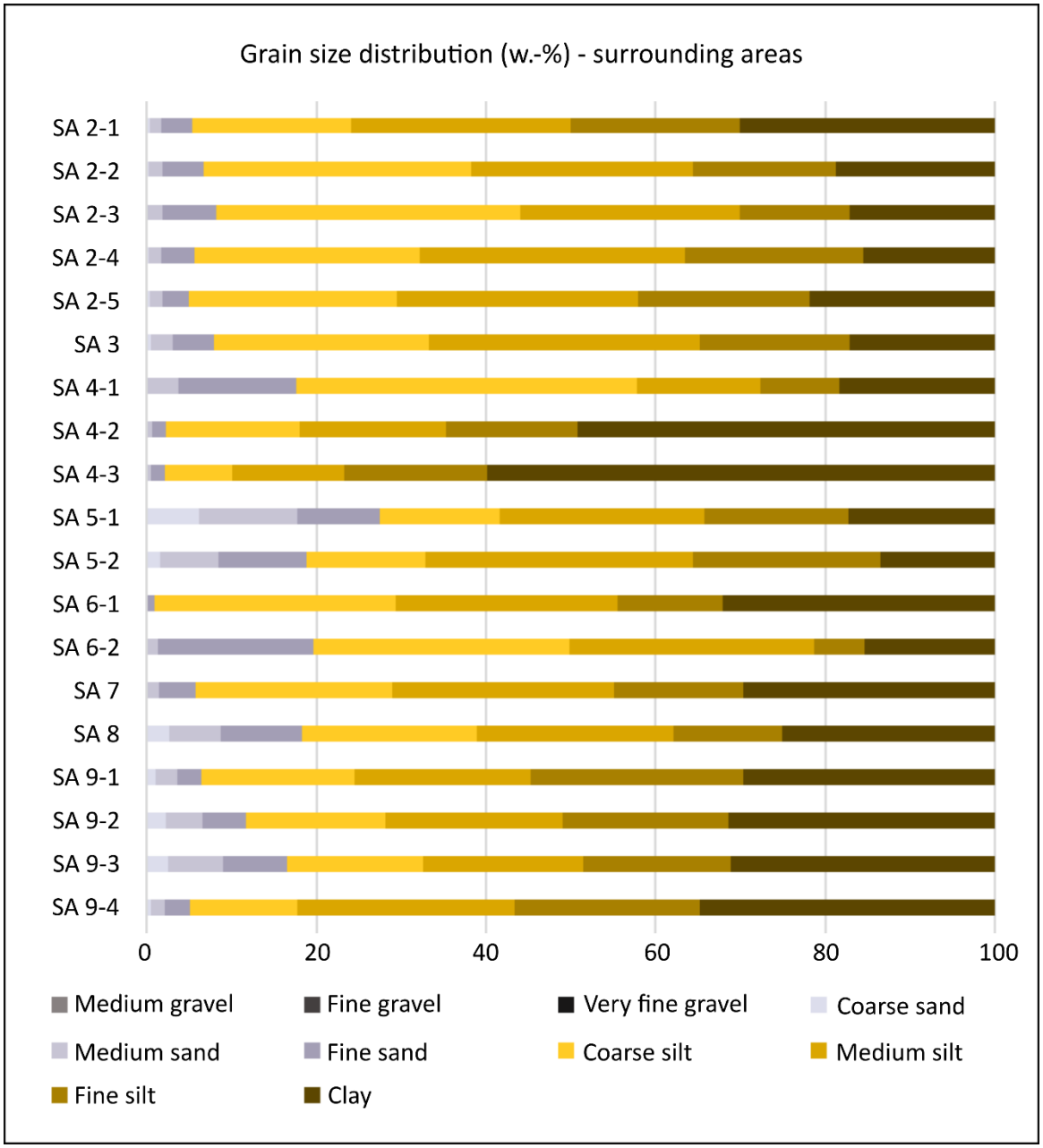

Figure 5-18. Grain size content (weight-percentage) of the sample locations SA 2 to SA 9 from the surrounding areas of the Capulín landslide. Source: Own illustration.

SA 2 represents a characteristic soil profile, located in the area above the scarp (Figure 5-2). The profile consists of five horizons with the sequence of Ah, Bw1, Bw2, Bw(t)1, Bw(t)2, indicating the soil group Andosol (Figure 5-19; WRB, IUSS Working Group 2014). The first horizon (SA 2-1) is a 20 cm thick, brown, dense Ah horizon with a weak structure. Small, angular shaped rock fragments occur with diameters up to 3 cm and roots of different sizes (mostly medium and fine sized) are present. The structure of the soil matrix is granular. The lower boundary is gradual, almost diffuse, with pockets (Figure 5-19). A 25 cm thick, brown Bw1 horizon (SA 2-2) follows, which shows weak cohesion of the

matrix. A granular to (sub-)angular structure is developed. Roots are present, while rock fragments are missing. A weak, wavy boundary separates the 1st from the 2nd Bw horizon (SA 2-3). The latter has a thickness of 15 cm (Figure 5-19) and an overall slight reddish brown color. The structure is subangular to granular. Large, rounded rock fragments, with diameters ranging between 5 and 10 cm occur as well as few clay coatings on aggregates. A boundary with large waves marks the transition towards the lower horizon. The underlying Bw(t)1 horizon (SA 2-4, 60 - 90 cm) has a slight reddish brown color, and a subangular to granular structure. Massive clay coatings cover the aggregates, and the matrix includes large, rounded rock fragments (10 - 15 cm diameter) are included. The lower boundary is wavy and weakly developed. The basal horizon (90 - 140 cm) corresponds to a Bw(t)2 (SA 2-5). This grayish brown horizon is of platy to (sub-)angular structure and very dense. Many large rock fragments (10 - 15 cm diameter) and few clay coatings are present.

Grain size analyses of profile SA 2 generally yield a silt loam texture (WRB, IUSS Working Group 2014), with silt as predominant grain size faction (64.5 - 78.9 %). Due to the high amount of clay (30.1 %) combined with a silt content of 64.5 %, SA 2-1 is the only horizon, which is determined as silty clay loam (cf. Appendix H). SA 2-2 and SA 2-3 have very similar textures, with silt contents of 74.5 to 74.7 %, and 18.8 and 17.2 % of clay (Figure 5-19). Coarse silt represents the main component within the silt fraction in both horizons.

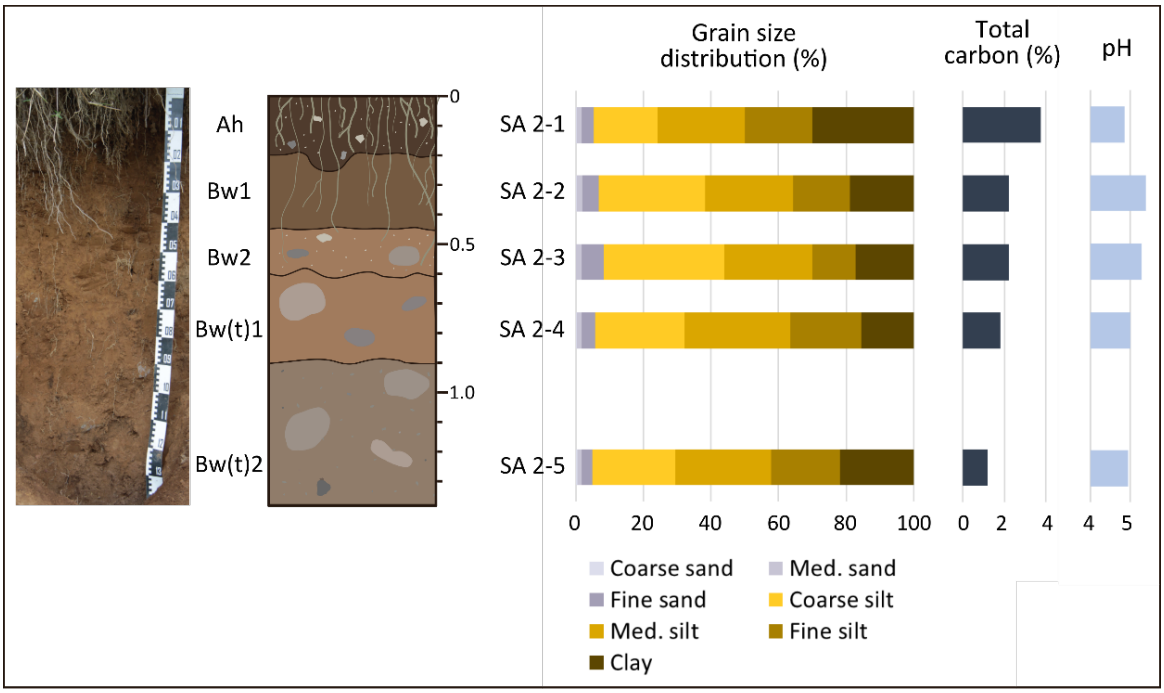

Figure 5-19. Profile and laboratory results of SA 2. Source: Own photograph (2016) and illustrations.

SA 2-4 has the highest silt content (78.9 %) within the profile. Clay content is low with 15.5 %, and the sand fraction lies at 5.7 %. Fine silt dominates the silt fraction in SA 2-5 (28.4 %) as well. In the basal horizon, sand remains very low and clay fraction is at 21.8 % (Figure 5-19). The pH values are homogenous and in the moderately acidic milieu, between 4.9 and 5.4 (Table 5-10). The TC content is high in the uppermost horizon (2.8 %) and decreases with depth. All horizons are free of carbonates.

5.3 Sediments in the Escalanar landslide area

The Escalanar landslide is located at about 900 m linear distance west of the village El Escalanar and 200 m inland next to the road leading from El Escalanar to El Huerfano (see Figures 5-2, 5-20). Sampling of the Escalanar landslide took place at the eastern flank (EFE 1) close to the scarp, in the slide mass (EM 1), and at the western flank (EFW 1). The scarp area was not accessible for sampling.

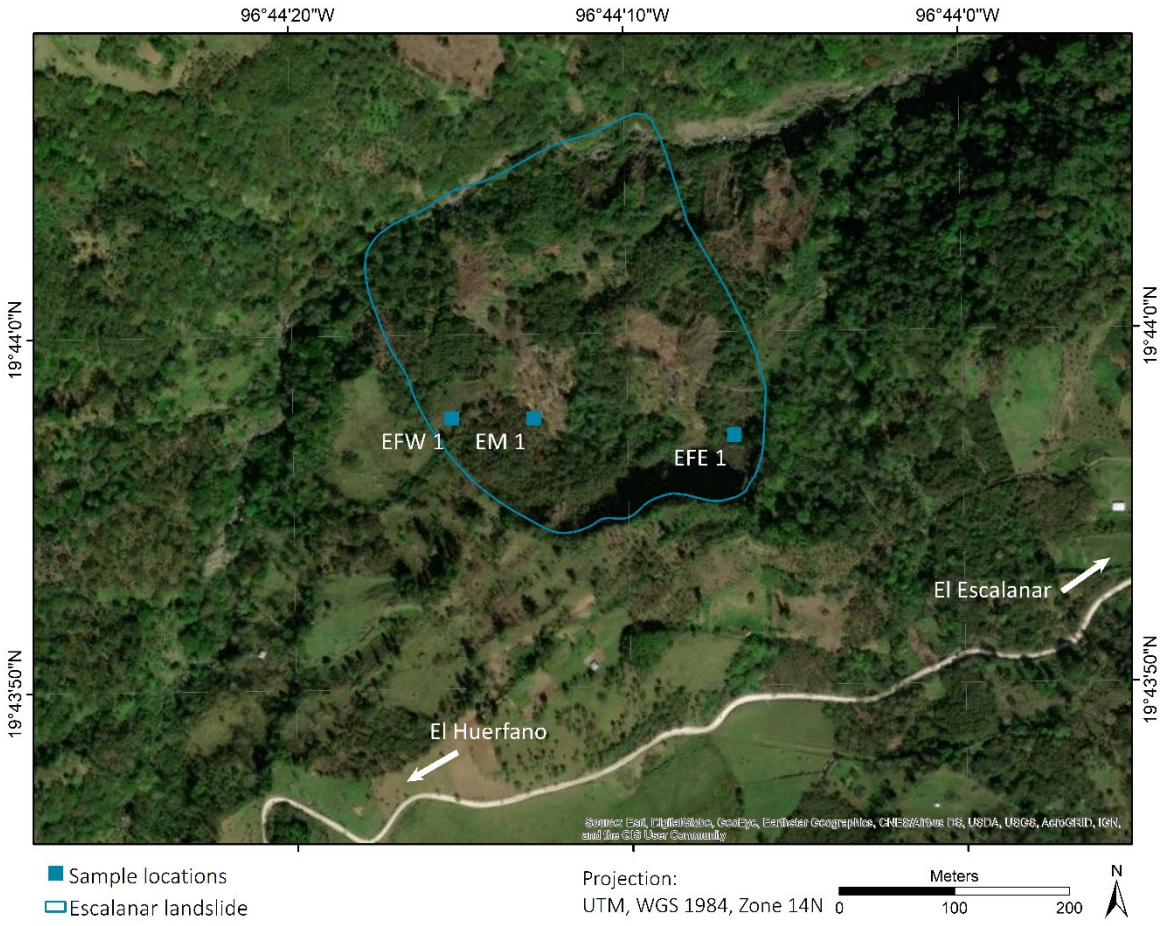

Figure 5-20. Locations of the samples of the Escalanar landslide. Source: Own Illustration. Source of background map: Esri World Imagery (2019).

Limits of consistency were determined for eleven samples of the Escalanar landslide (Figure 5-21). The sample from the eastern flank (EFE 1-3) is the only low plastic clay, whereas the other samples correspond to low plastic silts (27 %) and elasitc silts (64 %; according to ASTM 2006). EFE 1-3 has an effective cohesion of 5.0 kN/m², the highest unit weight with 21.0 kN/m³, and a friction angle of 27.5°. EM 1-5, EM 1-11, and EM 1-12 have the same friction angle (22.5°) and similar unit weights (19.5 - 20.5 kN/m³), however, they represent different cohesion values, 10.0 kN/m² for EM 1-5, EM 1-11, and 5.0 kN/m² for EM 1-12. The remaining samples record the same geotechnical values, with 0 cohesion, a friction angle of 15°, and a unit weight of 15 kN/m³. The only exception is EM 1-10, which has a unit weight of 14 kN/m³ (Appendix G).

The location EFE comprises three samples and is located 13 to 14 m below surface (Figure 5-22). At a first glance, the three samples seem rather homogenous as they are

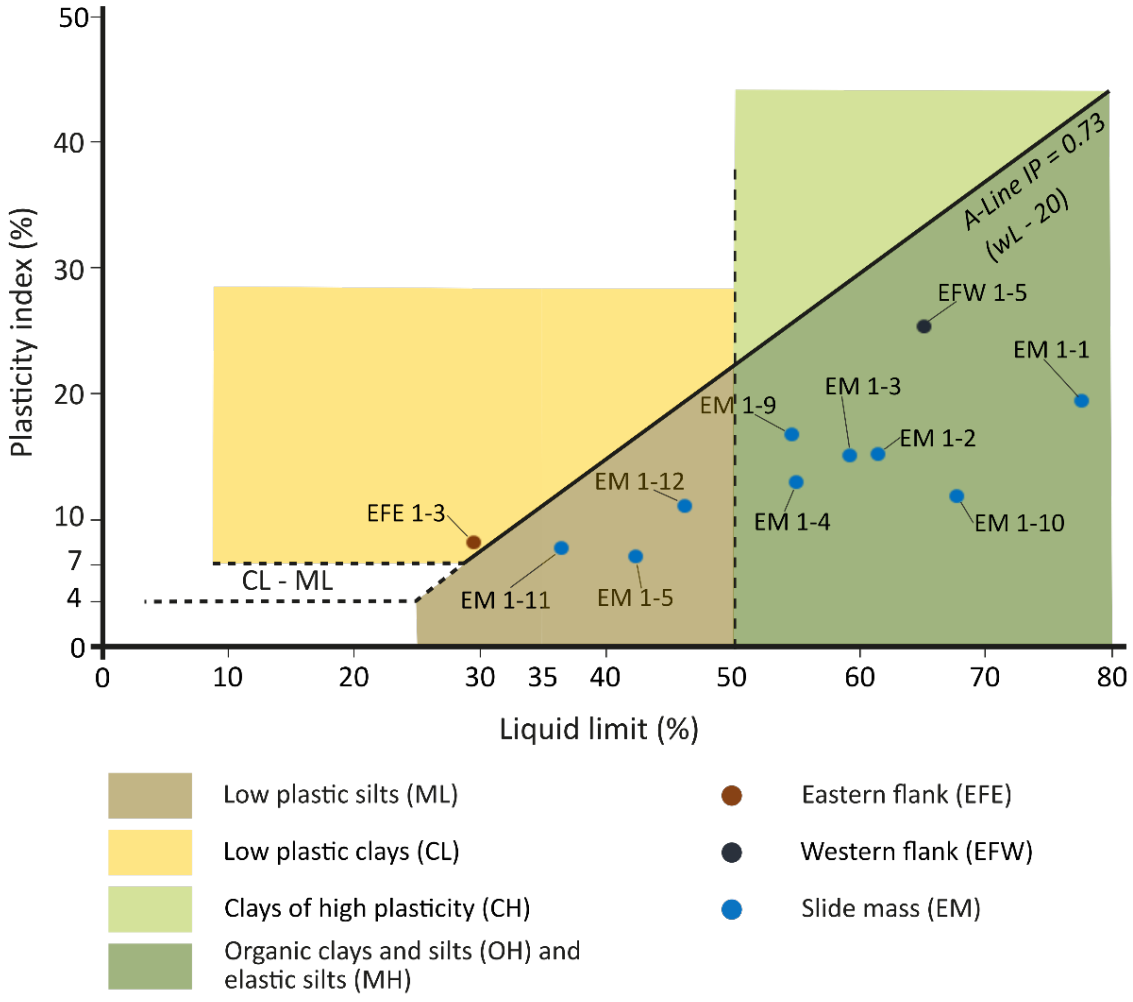

Figure 5-21. Limits of consistency analysis for the samples of the Escalanar landslide (see also Appendix G). Plasticity chart according to ASTM (2016). Source: Own illustration.

classified as silt loam (EFE-1, EFE-2) and loam (EFE-3). However, a closer look reveals the differences between the grain-size distributions. While the dominant fraction of EFE-1 is silt, with 51.0 %, EFE-2 shows the highest proportion in the gravel fraction (41.2 %), and EFE-3 has similar amounts of sand (37.0 %) and silt (33.2 %). The clay contents for all three samples are below 10 % (cf. Figure 5-23). In turn, the pH values are homogenous and within the very slightly acidic range (6.2 - 6.3). TC contents are very low and remain below 0.1 % (Table 5-11). All samples of EFE are free of calcium carbonates.

Figure 5-22. Study site and sampling locations at the eastern flank of the Escalanar landslide. The outlines of the sampling areas are marked with white dashed lines. The sampling depths as indicated in the labels are measured from the ground surface. Source: Own photographs (2018).

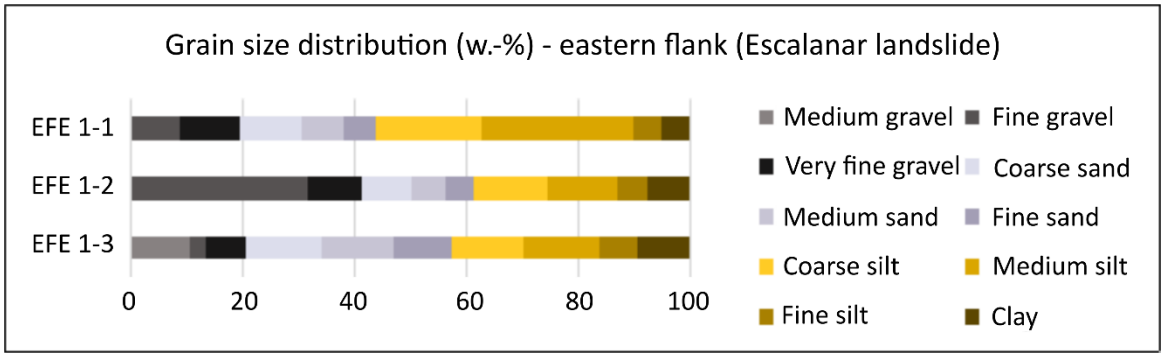

Figure 5-23. Grain size content (weight-percentage) of the eastern flank of the Escalanar landslide. Source: Own illustration.

Table 5-11. Results of pH and total carbon (TC) analyses for the eastern flank of the Escalanar slide.

Name	pH	pH classification (DIN 4220)	Total carbon (%)
EFE 1-1	6.2	very slightly acidic	0.08
EFE 1-2	6.3	very slightly acidic	0.05
EFE 1-3	6.3	very slightly acidic	0.05

Profile EM is located about 70 m to the east of EFW in the Escalanar slide mass (Figure 5-20). In this location, the slide mass forms a parallel step to the scarp. The profile can be subdivided into twelve horizons (Figure 5-24). In general, location EM is characterized by dark brown colors in the upper part and lighter brown colors in the lower part, only the area between 60 and 86 cm displays a light gray color (Figure 5-24). The grain size analyses yielded a classification of silt loam for 83 % of the samples, only EM 1-9 and EM 1-10 are classified as silty clay loam (according to WRB, IUSS Working Group 2014, Appendix H). Silt represents the predominant grain size fraction (45.4 - 69.2 %) and a relatively high clay amount (14.2 - 33.0 %) in 75 % of the samples (Figure 5-25). Sand as second highest fraction is represented in EM 1-6 (24.0 %) and EM 1-11 (17.4 %), whereas EM 1-8 shows the highest gravel content with 32.3 %. Overall, sand fraction ranges between 6.9 and 24.0 %, gravel between 0 and 32.3 %, and clay between 14.2 and 33.0 %.

The pH values range between 4.4 and 6.0, representing strongly acidic to slightly acidic conditions and all samples are carbonate-free (Table 5-12, Ad-hoc-AG Boden 2005). The TC content is high in the upper four samples (2.4 to 4.8 %) and decreases with depth.

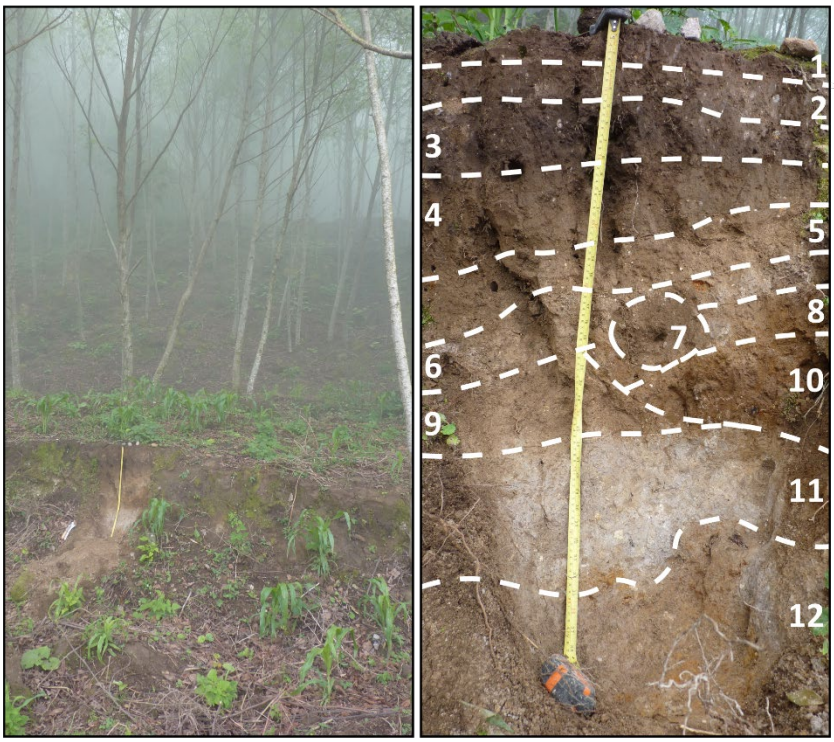

Figure 5-24. Study site and sampling locations in the slide mass of the Escalanar landslide. The outlines of the sampling areas are marked with white dashed lines. The sampling depths as indicated in the labels are measured from the ground surface. Source: Own photographs (2018).

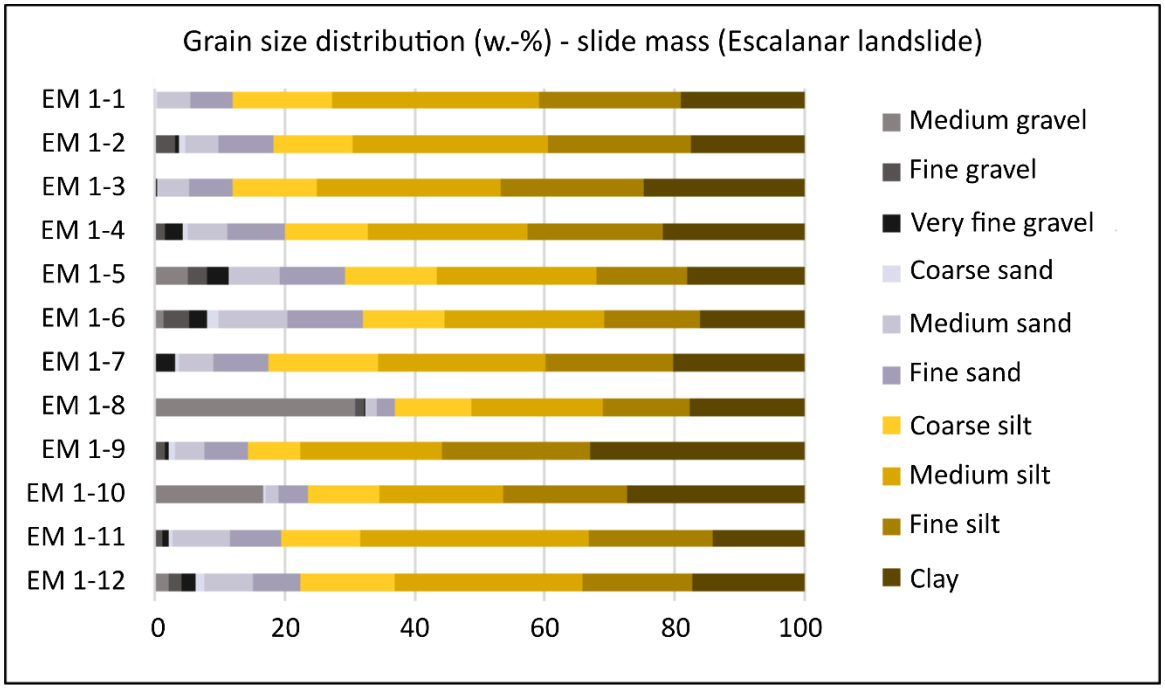

Figure 5-25. Grain size distribution (w.-%) of the Escalanar slide mass. Source: Own illustration.

Table 5-12. Results of the pH and total carbon (TC) analyses for the slide mass of the Escalanar landslide.

Name	pH	pH classification (DIN 4220)	Total carbon (%)
EM 1-1[2]	4.4	strongly acidic	4.77
EM 1-2[2]	4.5	strongly acidic	2.59
EM 1-3[2]	4.7	moderately acidic	2.94
EM 1-4[2]	5.4	slightly acidic	2.39
EM 1-5[2]	5.6	slightly acidic	0.80
EM 1-6[2]	5.5	slightly acidic	0.60
EM 1-7[2]	5.4	moderately acidic	1.34
EM 1-8[2]	5.5	slightly acidic	1.82
EM 1-9[2]	5.1	moderately acidic	0.54
EM 1-10[2]	5.1	moderately acidic	1.12
EM 1-11[2]	6.0	slightly acidic	0.08
EM 1-12[2]	4.8	moderately acidic	0.15

[2] = Lenz (2019).

Sample location EFW is situated on the opposite site of EFE, at the western flank (Figure 5-20, 5-26). At this location the flank has a slope angle of more than 30° and a depth of 2.1 m. EFW can be subdivided into five horizons, where each was sampled twice (Figure 5-26). In the upper horizon the grain size fraction of silt is dominant with 48.8 % (EFW1-1)

and 53.4 % (EFW 1-2). Due to a slightly higher clay content (25.3 %), EFW 1-1 is classified as silty clay loam, and EFW 1-2 as silt loam (23.1 % clay). The underlying horizons (EFW 1-3, EFW 1-4) contain high amount of gravel fraction (34.2 %, 34.3 %), sand ranges between 22.1 and 29.1 %, and silt between 24.1 and 27.5 % (Figure 5-27). While sand and silt are present in relatively equivalent amounts (range between 22.1 - 29.1 %). The clay contents record 12.5 and 16.2 % and both samples can be classified as loam (cf. Appendix H). In contrast to this, the predominant grain size of samples EFW1-5 and EFW 1-6 is silt (51.6 % and 48.8 %), with similar values as the uppermost horizon (cf. Figure 5-27). With clay as dominant fraction, the samples belong to the silty clay loam (Appendix H). The highest amounts of gravel occur in EFW 1-7 (68.0 %), EFW 1-8 (66.3 %), and EFW 1-9 (55.5 %). Here, the sand contents range between 10.0 and 13.8 %, the silt fraction between 14.2 and 19.0 %, and the clay between 6.7 to 11.6 % (Figure 5-27). On the contrary, EFW 1-10 has a low gravel content (7.1 %) and an enhanced silt content with 51.5 %. Furthermore, in this sample sand and silt are equally distributed (25.7 and 25.6 %; Figure 5-27).

The substrate in the entire profile is carbonate free and the pH values range between moderately acidic and very slightly acidic (Table 5-13). EFW 1-1 and 1-2 show TC contents of 2.8 and 2.4 %, respectively, whereas the values of the remaining samples are below 0.6 %

Figure 5-26. Study site and sample locations at the western flank of the Escalanar landslide. The outlines of the sampling areas are marked with white dashed lines. The sampling depths as indicated in the labels are measured from the ground surface. Source: Own photographs (2018).

(Table 5-13). The hydraulic conductivity was determined for eight samples and according to DIN 4220 (2008) can be classified as high (1), very high (4), and extremely high (1). The only exceptions with comparably low values are samples EFW 1-4 (low) and EFW 1-6 (intermediate; Table 5-13).

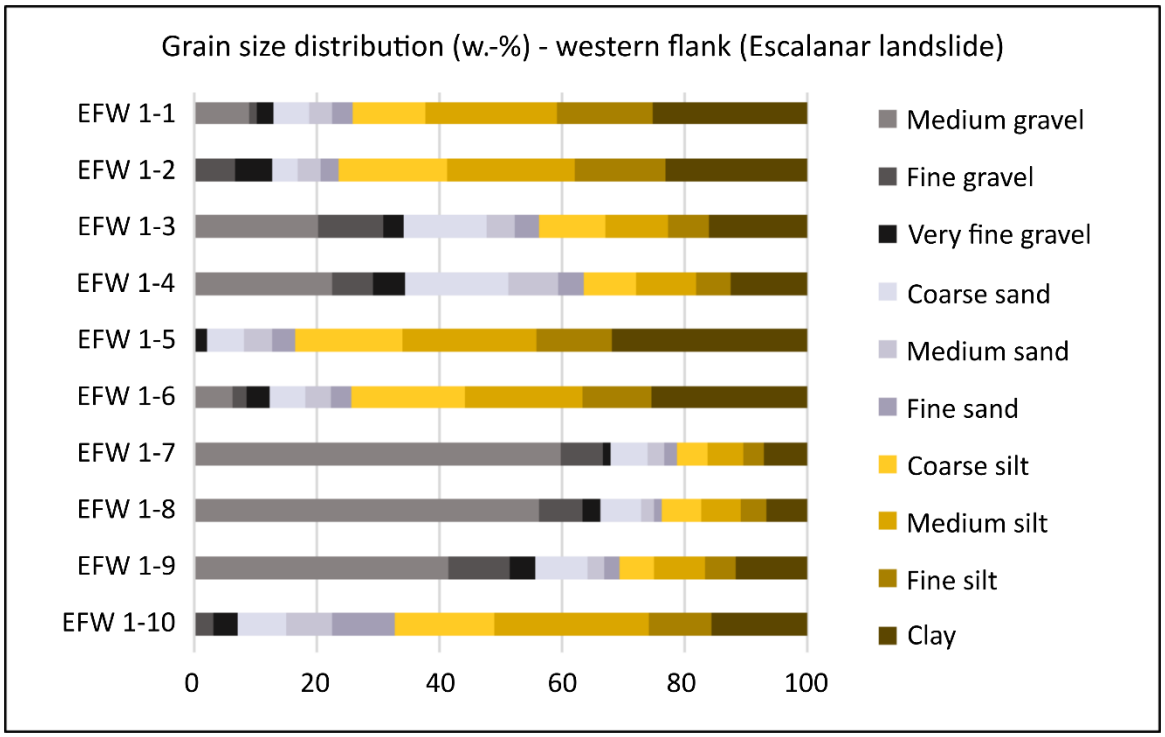

Figure 5-27. Grain size content (weight-%) of Escalanar's western flank. Source: Own illustration.

Table 5-13. Results of the pH, total carbon (TC), and constant hydraulic conductivity analyses for the western flank of the Escalanar landslide.

Name	pH	pH classification (DIN 4220)	Total carbon (%)	Constant hydraulic conductivity (cm/h)	Hydraulic conductivity classification (DIN 4220)
EFW 1-1[1,2]	5.3	moderately acidic	2.82	5.32	very high
EFW 1-2[1,2]	5.4	moderately acidic	2.42	8.04	very high
EFW 1-3[1,2]	5.7	slightly acidic	0.60	10.70	very high
EFW 1-4[1,2]	5.7	slightly acidic	0.53	0.30	low
EFW 1-5[1,2]	6.3	very slightly acidic	0.26	2.87	high
EFW 1-6[1,2]	5.6	slightly acidic	0.32	0.86	intermediate
EFW 1-7[1,2]	6.4	very slightly acidic	0.30	10.20	very high
EFW 1-8[2]	5.8	slightly acidic	0.34	114.59	extremely high
EFW 1-9[2]	6.6	very slightly acidic	0.31	-	-
EFW 1-10[2]	6.0	slightly acidic	0.04	-	-

[1] = Füssl (2020); [2] = Lenz (2019); '-' = method not applied.

6. Results of the slope stability modeling

6.1 Step I – Input parameter generation

The calculation of the geotechnical parameters consists of two phases, whereby the first phase comprises the determination of algorithm-required parameters. In the second phase, the root-finding algorithm (Equation 3.6) calculates the geotechnical parameters by solving the FoS equation (Equation 3.5, cf. chapter 3.3.1).

Table 6-1 shows all required parameters, where the inclination angle β and the average slip surface depth z represent calculation results, while the FoS value and water saturation were determined (estimated values see chapter 3.3.1). The ranges for cohesion, friction angle, and density correspond to the laboratory results (cf. chapter 5). The obtained data set (Table 6-1) forms the base for calculating the final values (Table 6-2), which are used as input parameters for further slope stability modeling.

Performing a second calculation of the geotechnical parameters allows to obtain comparative values. The landslide no. 2, situated in the south of the Capulín landslide (Figure 4-11, chapter 4.3), forms the base for this second parameter set (Table 6-3). With the assumption, that the parameter range for friction angle, density and cohesion remain the same, only the landslide specific components (slope angle and thickness) are different (cf. Table 6-1 and 6-3). The both calculation results show great similarity (Table 6-2 and 6-4).

Parameter	Value (range)
FoS	1.5
β - slope [°]	13.9
z - thickness [m]	29.02
m - saturation	0.5
cohesion [MPa]	0 - 0.01
friction angle [°]	15 - 30
density [g/cm³]	1.4 - 2.0

Table 6-1. Input parameters for the root-finding equation (cf. chapter 3.3.1).

Parameter	Value
cohesion [MPa]	0.03744
friction angle [°]	22.3
density [g/cm³]	1.74

Table 6-2. Calculation results for the geotechnical parameters for the Capulín landslide.

Parameter	Value (range)
FoS	1.5
β - slope [°]	14.1
z - thickness [m]	30.0
m - saturation	0.5
cohesion [MPa]	0 - 0.01
friction angle [°]	15 - 30
density [g/cm³]	1.4 - 2.0

Table 6-3. Input parameters of the landslides no. 2 for the root-finding equation.

Parameter	Value
cohesion [MPa]	0.03881
friction angle [°]	22.6
density [g/cm³]	1.75

Table 6-4. Calculation results for the geotechnical parameters for landslide no. 2.

6.2 Step II – Validation process of the input parameters

As explained in chapter 3.3.2, the calculation approach from Step I is validated by the method of slices.

Input parameters: Figure 6-1 illustrates the geotechnical model, where the surface (bold green line) corresponds to the cross section of the Capulín landslide. The results from Step I provide the material properties (Table 6-2). The 'fully specified' tool allows for the indication of the exact slip surface form as determined in chapter 4.5. The piezometric line divides the potential slide mass between the terrain surface and the slip surface in half and represents a saturation of approx. 50 % (Figure 6-1a). At the meeting point of the slip surface with the terrain surface (at a distance of approx. 800 m), the piezometric line rises to the surface and at a distance of about 900 m ends at a stream, located at the slope's foot (Figure 6-1). The piezometric line can be modified in order to represent different saturation stages, i.e. if the line is equal to the slip surface, it records dry conditions without saturation (0 %), and in case the piezometric line reaches the surface line, saturation is at 100 %. The resulting geotechnical model combines all parameters described above and forms the base for the limit equilibrium calculations.

Slope stability calculations: The limit equilibrium result shows the division of the slide mass into 51 slices (Figure 6-1b). The resulting FoS, calculated with the Bishop's simplified method (FoS_{Bishop}) is at 1.8, and at 1.6 with the Morgenstern-Price method (FoS_{MP}, Figure 6-2).

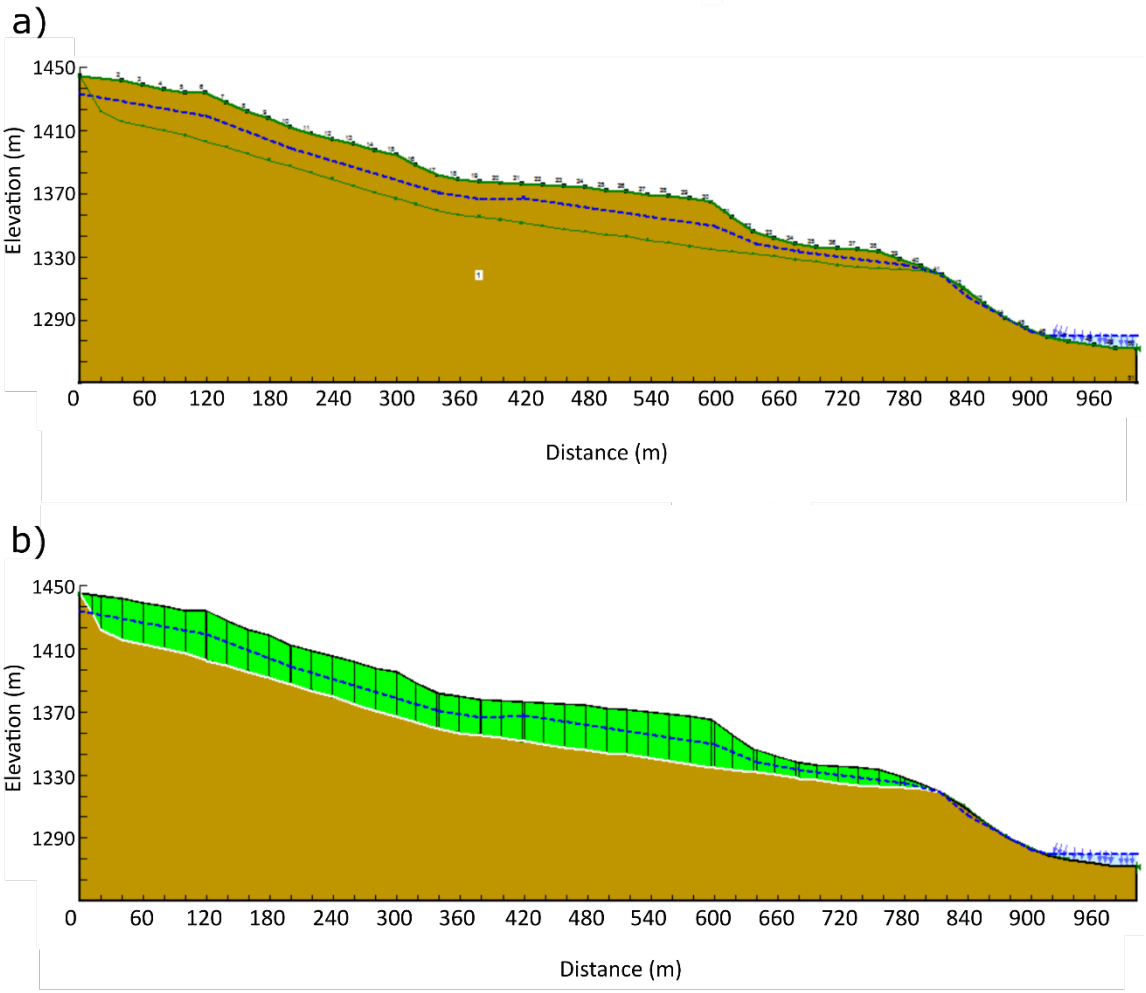

Figure 6-1. a) Geotechnical model, designed in Slope/W. The cross section represents the Capulín landslide, including the surface (upper green line), predefined slip surface (lower green), material properties (brown area), and piezometric line (blue, dashed line). For the location of the cross section, see Figure 3-10. b) Slices, dividing the slide mass, are marked in green. Source: Own illustration, based on the model derived from Slope/W.

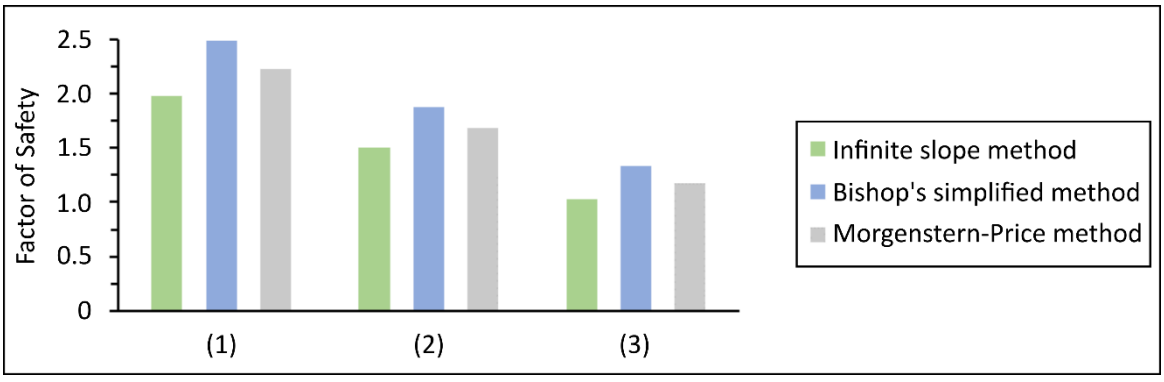

Figure 6-2. Comparison of the different limit equilibrium methods. Results represent the FoS calculated for three different levels of saturation, utilizing the same geotechnical parameters as input. (1) Zero saturation, (2) 50 % saturation, (3) 100 % saturation. Source: Own illustration.

Validation process: The next step consists of the computation of comparative values and enables the analysis of the differences between the infinite slope result ($FoS_{infinite}$) and the Slope/W results (FoS_{Bishop}, FoS_{MP}; Figure 6-3). Thus, the three FoS are calculated with the same geotechnical parameters, however, for three different saturation conditions, with (1) zero saturation, (2) 50 % saturation, and (3) 100 % saturation. Figure 6-2 proves that FoS_{Bishop} represents the highest values for all three saturation conditions, while the $FoS_{infinite}$ produces the lowest ones. The differences between the $FoS_{infinite}$ and FoS_{MP} (0.2) as well as between FoS_{MP} and FoS_{Bishop} (0.3) are smaller than the difference between $FoS_{infinite}$ and FoS_{Bishop} (0.5).

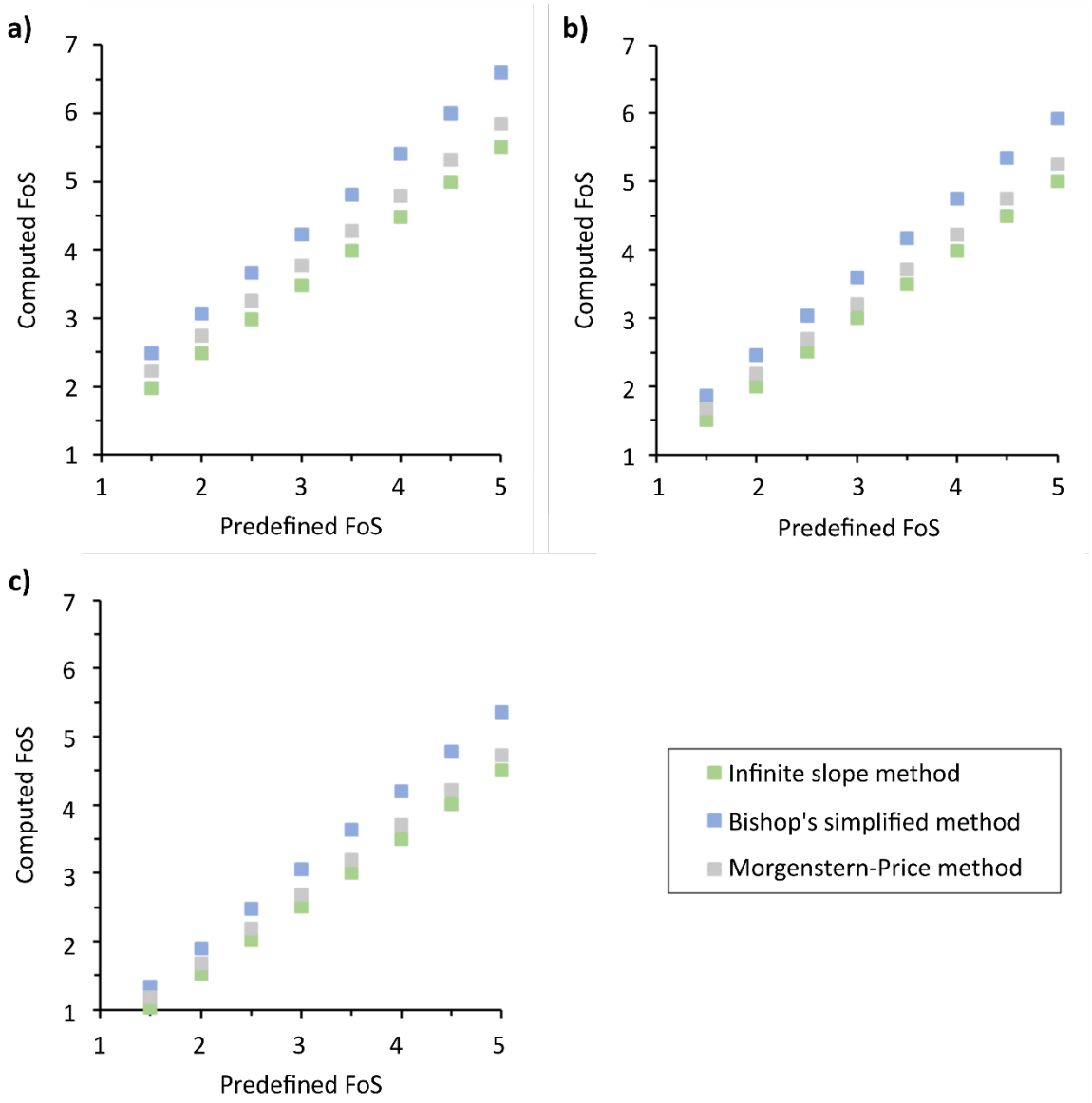

Figure 6-3. Comparison of the limit equilibrium methods. Results represent the computed FoS, utilizing eight geotechnical parameter sets as input. The different parameter sets were computed for a) zero saturation, b) 50 % saturation, and c) 100 % saturation. Source: Own illustration.

Furthermore, the FoS are computed for different geotechnical parameter sets at varying saturations. The root-finding algorithm generates geotechnical parameters with eight different FoS values as input data. These datasets are applied in the limit equilibrium calculations and the results are listed in Figure 6-3. As already pointed out in Figure 6-2, the results from the Bishop's simplified method show the highest FoS values. It can also be observed that the difference between the Factors of Safety slightly decreases with smaller FoS values. The FoSs show good consistency among the three modeling approaches as the differences remain relatively constant.

6.3 Step III (A) - Slope stability modeling based on infinite slope method

6.3.1 Input parameters for SAFETYFACTOR

In Step I and II the slope stability is exemplary calculated for one slope. Step III comprises the transfer of the results from the site-specific to a regional approach in order to model slope stability for the whole study area, starting with the infinite slope analysis. As described in chapter 3.3.3, the software 'SAFETYFACTOR' in SAGA GIS allows for calculating the FoS for a larger area, based on the infinite slope method. However, before the slope stability analysis with SAFETYFACTOR can be performed, various input parameters, such as depth of the slip surface (thickness), water saturation, and geotechnical data need to be determined. The result of the thickness calculation is illustrated in Figure 6-4. The raster map represents the layer thickness for the entire study area (Figure 6-4 (1)). The class with the lowest thickness (0 - 10 m) corresponds with approx. 4 % to the smallest part of the area. The class with the highest values (30 - 35 m) follows with 10 %. Considering the spatial distribution of these two classes, the margins of the study area record the lowest values, whereas the highest values show a distribution over a wider area and they are more concentrated towards the center (Figure 6-4). The third group, with a thickness between 25 and 30 m, accounts with 30 % for the largest area. The remaining two classes represent less than 30 % of the area.

The relationship between slope and layer thickness is illustrated in Figure 6-4 (2). At the initial point of the cross section (starting from A), the layer thickness is very low, and simultaneously the slope very steep. With decreasing slope angle, the layer thickness increases. Considering the cross section at a distance of approx. 1400 m, this fact becomes particularly apparent. As the slope becomes steeper, the thickness considerably decreases (15 m), and where the slope becomes less inclined the layer increases in depth (31 m).

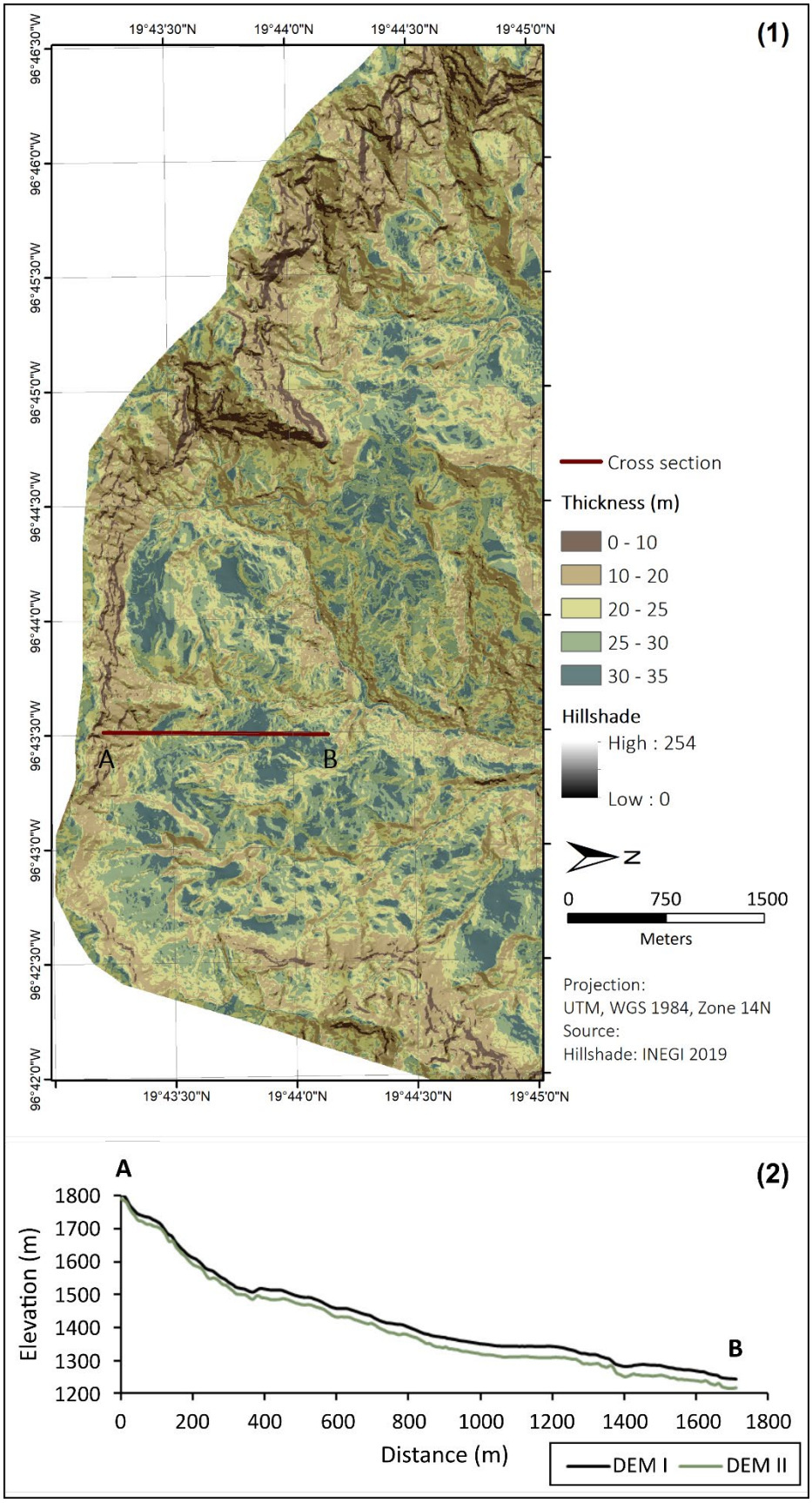

Figure 6-4. Input parameters for SAFETYFACTOR (SAGA): (1) Raster map of layer thickness with transect AB (2). DEM I representing the ground surface and DEM II the potential slip surface. Source: Own illustration.

The geotechnical input data is determined for each process region (Region 1 to 3; Table 6-5). Region 1, with the geological unit basalt and steep slopes, covers an area of 21 %. The region is located at the margins of the study area (cf. Figure 3.3-5). Region 2 accounts for around 6 % of the study area. It mainly consists of steep slopes and the geological unit is characterized as tuff. Region 3 accounts for the majority of the study area, with a proportion of 73 %. It is characterized by moderate to flat slopes and the geotechnical values of this region represent the results from Step I (cf. Table 6-2, 6-5). For Regions 1 and 2, minimum and maximum values are specified for each parameter. Region 3, however, is defined especially for this study area and therefore, only one value per parameter is specified instead of a value range. Region 1 has the highest values for each parameter, whereas the values of Region 2 and 3 are more comparable. Especially the minimum values of Region 2 show a high similarity to the values from Region 3.

Furthermore, the water saturation distribution in the entire study area is determined (Figure 6-5). The highest saturation values (75 - 100 %) occur in less than 0.5 % of the area and are concentrated at accumulation lines. The next saturation class with 50 to 75 % represents a small area with around 8 %, and is mainly concentrated at accumulation lines as well. Consequently, the majority of the area is divided into the two remaining classes. The class with saturation values between 25 - 50 % accounts for 43 % of the area, while the class with the lowest saturation values (0 - 25 %) covers an area of 48 %.

Table 6-5. Geotechnical input parameters for SAFETYFACTOR. Region 1: geotechnical properties for basalt according to Selby (1982), Region 2: geotechnical characteristics for tuff according to Asniar et al. (2019), Region 3: geotechnical values derived from Step I (cf. Table 6-2). Proportion of the area in brackets.

Calibration Region	**Region 1 (21 %)**	**Region 2 (6 %)**	**Region 3 (73 %)**
Cohesion min. (MPa)	35.00	0.00	0.04
Cohesion max. (MPa)	55.00	1.45	0.04
Friction angle min. (°)	35.00	24.00	22.30
Friction angle max. (°)	45.00	45.00	22.30
Density min. (g/cm³)	2.55	1.83	1.74
Density max. (g/cm³)	3.10	2.54	1.74

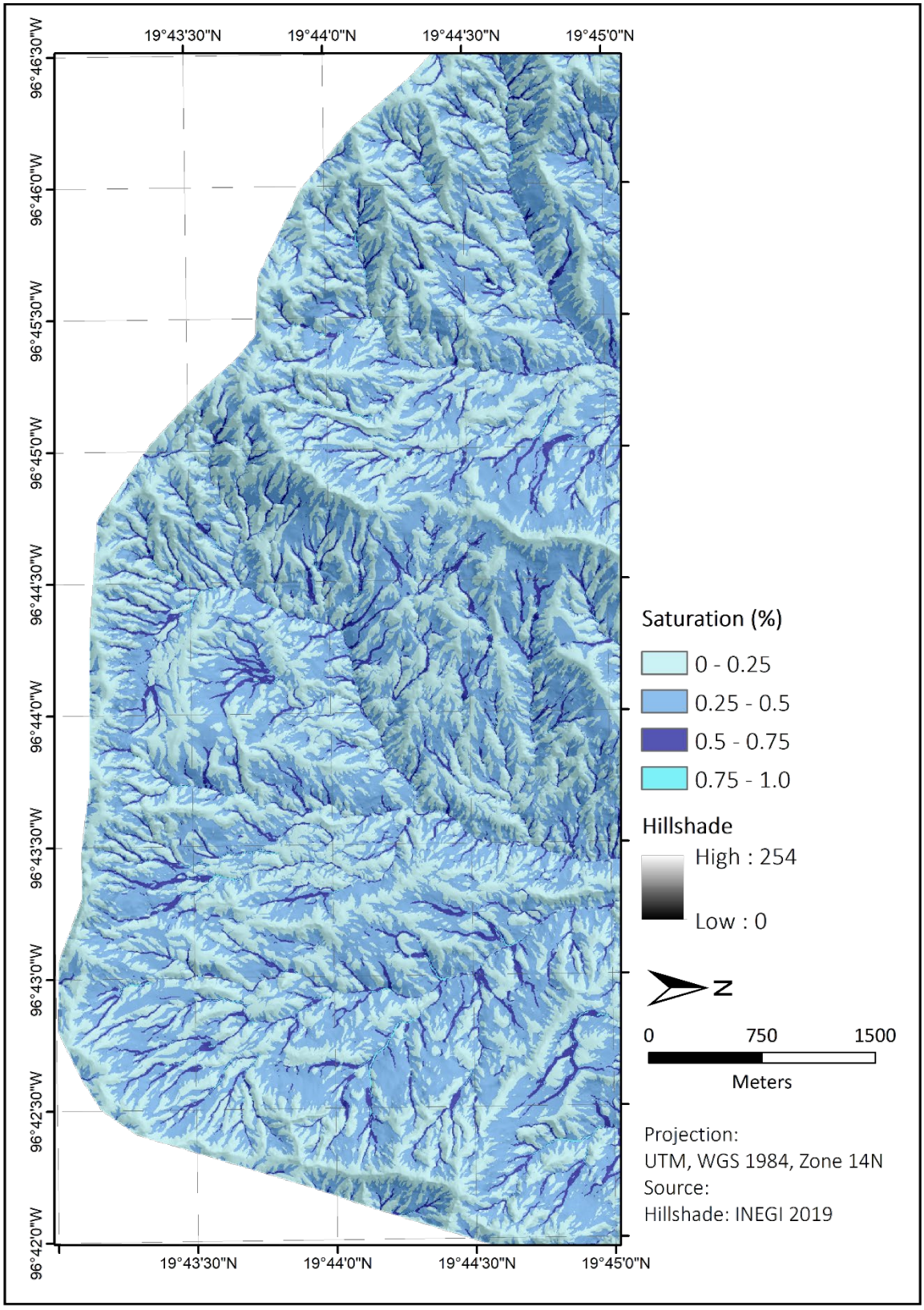

Figure 6-5. Distribution of the water saturation in the study area. Source: Own illustration.

6.3.2 Slope stability modeling with SAFETYFACTOR (infinite slope method)

Based on the input parameters described in the previous chapter, the slope stability is calculated with the SAFETYFACTOR program. The results of the slope stability analysis (here referred to as '**simple SAFETYFACTOR map**') are illustrated in Figures 6-6 and 6-7. Figure 6-6 records the proportion of the stability classes in relation to the study area. It proves that Class 5 ('highly stable') with FoS values above 1.5 covers the largest area with 44 %. On the one hand, highly stable areas (Class 5) can be identified in relatively flat areas in the center of the study area (cf. Figure 6-7). On the other hand, this class is concentrated at the margins of the study area (Figure 6-7) and is mainly represented by Process Region 1. Consequently, this parameter combination corresponds to stable conditions. Classes 3 (defined as 'moderate') and 4 (classified as 'stable') represent the smallest classes with 12 and 7 % (Figure 6-6). Both are widely distributed over the entire area and specific concentrations cannot be observed (Figure 6-7a). Class 2 ('unstable') corresponds to the second largest area, however, with 22 % it is only half the size of Class 5. Class 1, which represents the 'highly unstable' zones, accounts for 15 % of the entire region, and is mostly concentrated at steep slopes in the center. In summary, the classes corresponding to moderate, high-, and highly stable areas account for 63 % of the study area, and consequently, less than 40 % are defined as unstable.

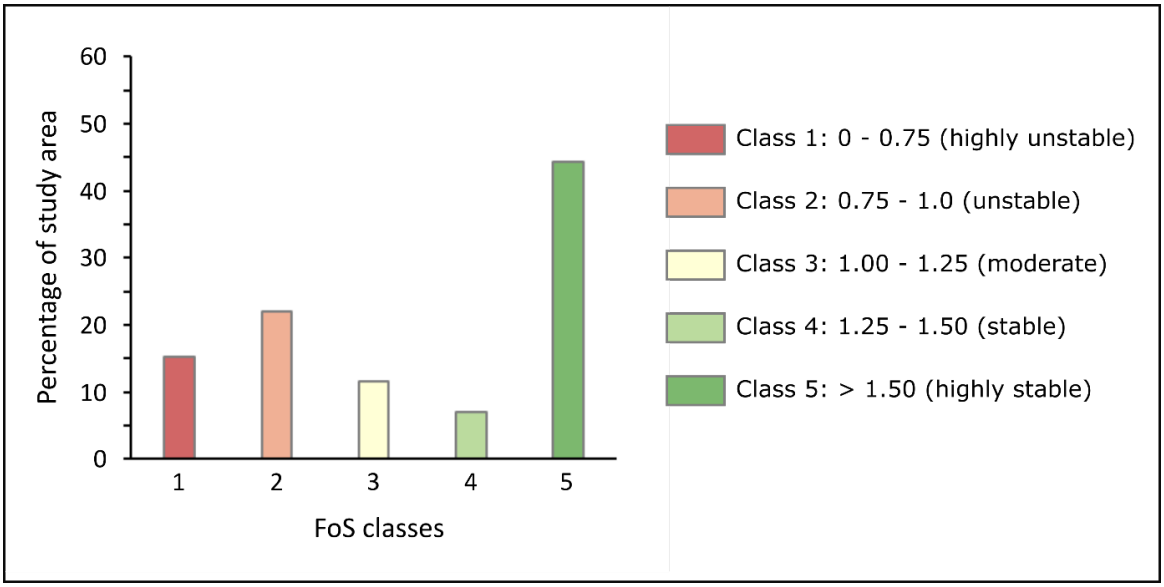

Figure 6-6. Proportion of the stability classes in relation to the study area in percentage for the simple SAFETYFACTOR map. Susceptibility classification modified after Teixeira et al. (2015). Source: Own illustration.

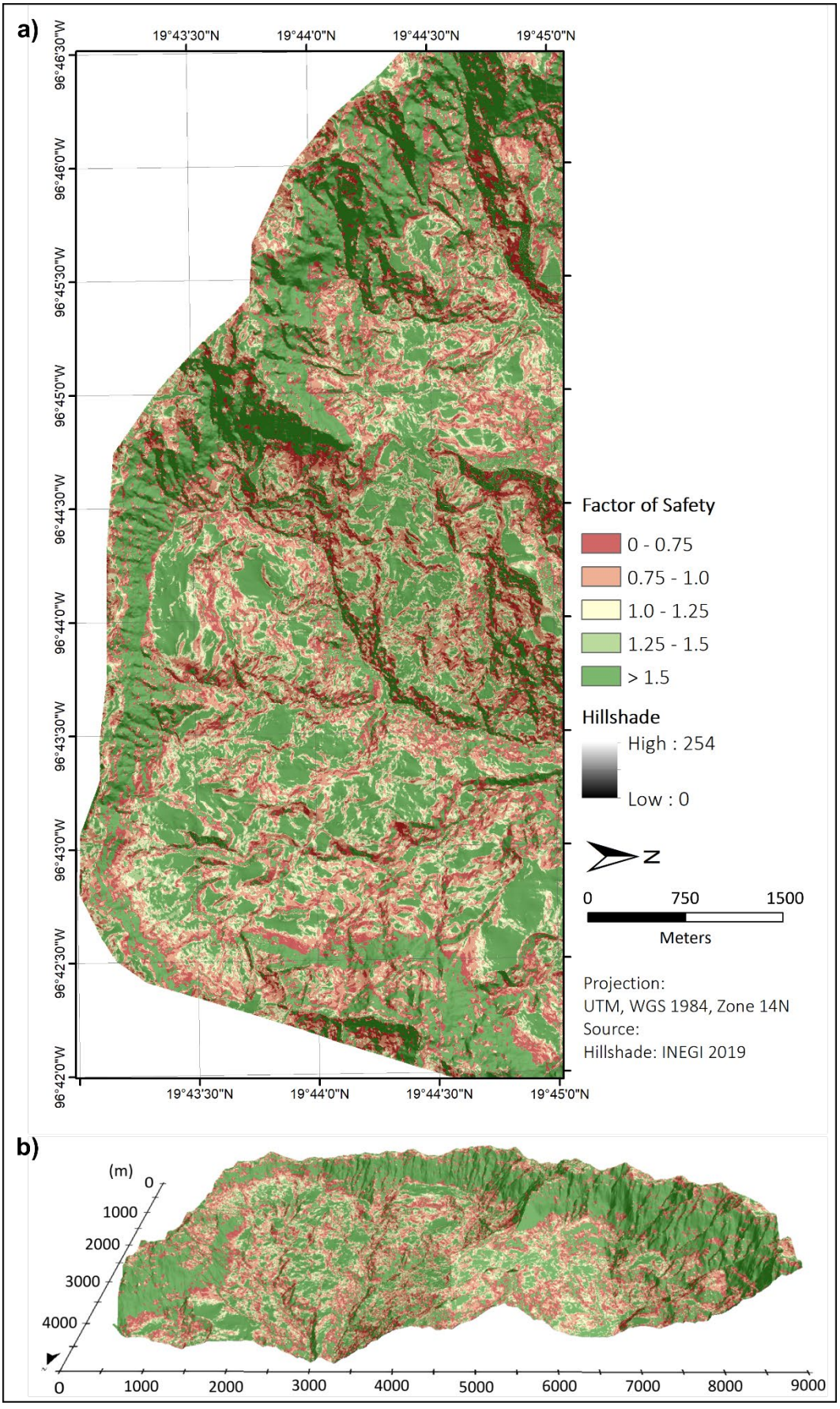

Figure 6-7. a) Factor of Safety map for the study area modeled with the infinite slope method (simple SAFETYFACTOR map). b) 3D-view of the slope stability map. Source: Own illustration.

Considering the relationship between instability and slope inclination, their quantitative evaluation within the different classes is not practical in this case as the distribution of the inclination values is comparatively homogeneous, when considering the mean values. For example, Classes 1, 2, and 5 have mean values of approx. 30°, and Classes 3 and 4 show mean values of about 20°. Hence, a qualitative assessment is required in order to detect correlations between slope instability and slope inclination. This relationship becomes clear in the three-dimensional presentation of the slope stability map (cf. Figure 6-7b). As mentioned before, the steep ridges are mainly classified as 'highly stable' (FoS values > 1.5). Even though areas with inclinations under 20° are also classified as 'highly stable', steeper inclinations (> 40°) prevail in this class. The unstable classes (1 and 2) are mostly located in areas with slope inclinations between 20° and 40°.

SAFETYFACTOR calculates slope stability in a pixel-based approach. This leads to the effect that the FoS classes are not distributed contiguously, causing difficulties for map interpretation. In order to improve the informative value of the map, the majority filter in SAGA GIS is applied and the resulting map (referred to as '**filtered SAFETYFACTOR map**') is illustrated in Figure 6-8a. A comparison of the two maps (Figure 6-7a and 6-8a) shows that the application of the majority filter leads to an elimination of isolated pixels. Thus, the 'filtered SAFETYFACTOR map' shows a more coherent distribution of the FoS classes (cf. Figure 6-8). This effect is clearly visible in the 3D maps (cf. Figure 6-7b and 6-8b), where the ridges at the margins are mainly classified as 'highly stable' in the filtered map (Figure 6-8b), whereas Figure 6-7b exhibits more separate pixels of unstable classes (including 'highly unstable', 'unstable', and 'moderate'). Overall, it can be stated that the parameter classes are more coherent (cf. Figure 6-8). The distribution and patterns of stable and unstable zones in both maps are comparable, however, the quantities of the FoS classes are shifted. The wide distribution of the FoS Class 5 also becomes evident in Figure 6-9. FoS Class 5 shows with approx. 52 % a wide distribution and represents the largest FoS class. Together with the classes 'moderate' (3) and 'stable' (4), they account for approx. 70 % of the entire area (Figure 6-9). Class 2 ('unstable') comprises 19 % and therefore, is almost twice as large as Class 1, which accounts for 11 % of the study area (Figure 6-9). Figure 6-8 further illustrates the landslide distribution in the study area (cf. chapter 4.3). It shows that the scarp areas in the western part can be associated with unstable zones, whereas the other scarps are not in direct connection with unstable zones (Figure 6-8a, b). Out of the 12 mapped landslides, landslide no. 8 shows the lowest amount of unstable

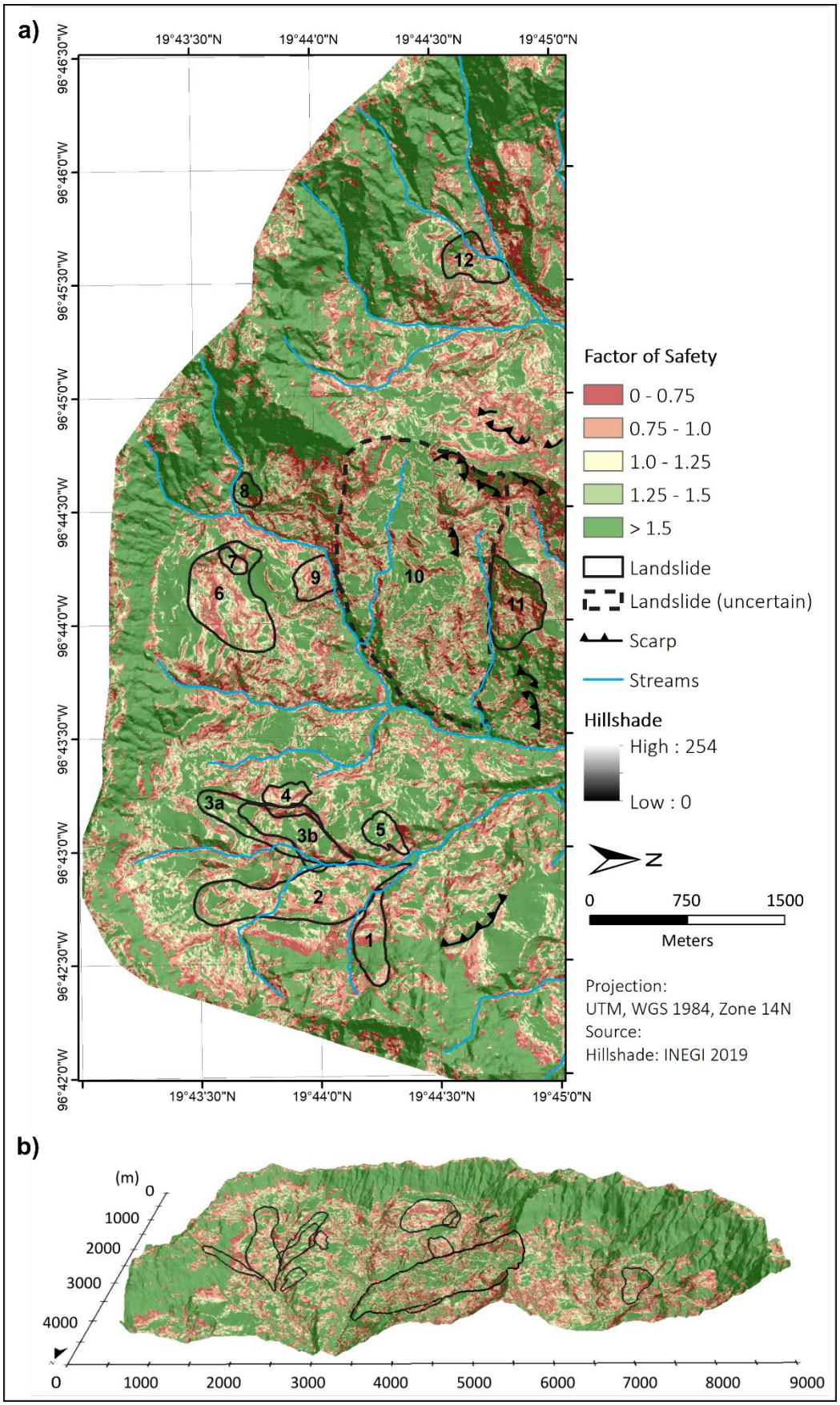

Figure 6-8. a) Filtered SAFETYFACTOR map for the study area modeled with the infinite slope method. b) Three-dimensional view of the slope stability map. Source: Own illustration.

classes (Classes 1 and 2). Landslide no. 3 (Capulín landslide) and no. 5 records a low amount of instability classes (about 20 % of the landslide area). Landslides 1, 2, 6, 7, 10, 11, and 12 have a relatively high correspondence to the unstable classes and the remaining two landslides (4 and 9) account for the highest correspondences (cf. Figure 6-8a, b).

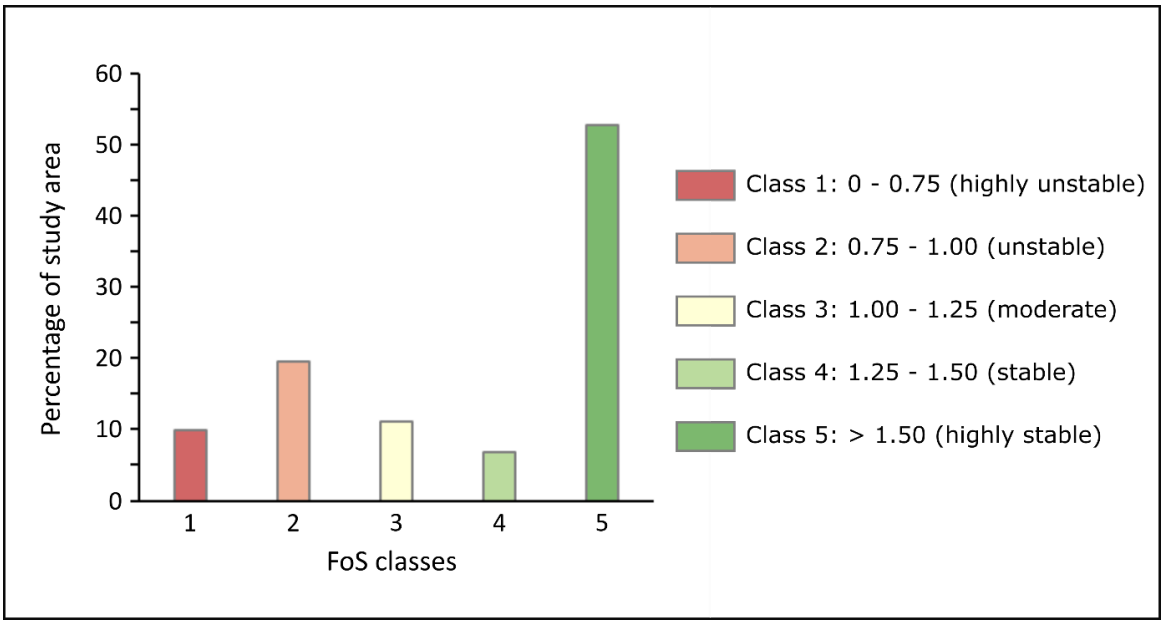

Figure 6-9. Proportion of the stability classes in relation to the study area in percentage for the filtered SAFETYFACTOR map. Susceptibility classification modified after Teixeira et al. (2015). Source: Own illustration.

6.4 Step III (B) - Slope stability modeling based on Bishop's simplified method

6.4.1 Input parameters for Scoops3D

In this step, the method of slices is transferred from one slope to the whole study area by calculating slope stability with Scoops3D (see chapter 3.3.4). The main input parameter for Scoops3D is a digital elevation model (DEM), representing the surface. Here, the surface of the study area corresponds to the DEM 2011 (Figure 6-10 (1)). In this study, two layers are defined. The lower boundary of Layer 1 is calculated by subtracting the layer thickness from the DEM, and the lower boundary of Layer 2 is assumed to be infinitely deep (cf. chapter 3.3.4). Figure 6-10 (2) illustrates a cross section (C, D) of the study area, including the distribution of the layers and the piezometric surface. The blue line indicates the piezometric surface, which runs very close to the surface in steep sections and for lower inclinations, its distance from the surface increases (Figure 6-10 (2)).

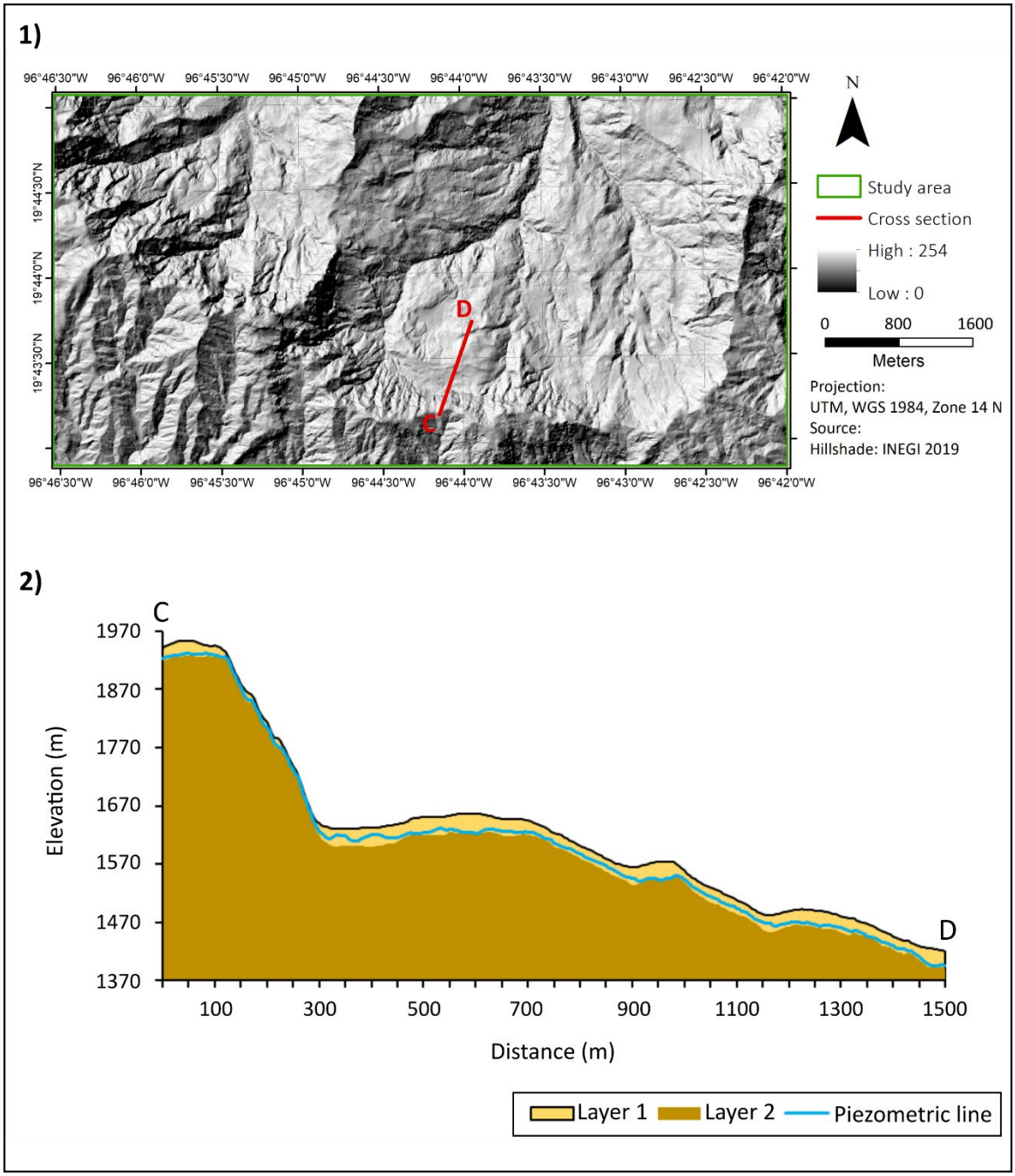

Figure 6-10. Input parameters for Scoops3D. 1) Hillshade of the study area (based on the DEM 2011), with the cross section (C-D) marked in red. 2) Cross section C-D, including layers and piezometric line as specified for modeling in Scoops3D. Source: Own illustration.

Layer 1 integrates cohesion and friction angle from Step I (Table 6-6). The density value derived in Step I (cf. Table 6-2) is used to calculate the partially saturated unit weight (see chapter 3.2.2), and for the saturated unit weight, the maximum unit weight value from the laboratory results is utilized for this layer (cf. Appendix G). Layer 2 comprises literature-based values according to Selby (1982).

Table 6-6. Input parameters for Scoops3D. Values from Layer 1 were derived in Step I (see chapter 6-1). Values from Layer 2 represent mean values for basalt according to Selby (1982).

Layer	Layer 1	Layer 2
Cohesion (kPa)	37.44	45,000.00
Friction angle (°)	22.30	40.00
Partially saturated unit weight (kN/m³)	17.07	27.50
Saturated unit weight (kN/m³)	21.00	27.50

6.4.2 Slope stability modeling with Scoops3D (method of slices)

The slope stability is computed in Scoops3D, using the input data described in the previous chapter. The result of this modeling approach is a map (here referred to as '**Scoops3D map**'), which represents the minimum FoS for each pixel of the DEM (Figure 6-11). The classification range differs from the one used in the SAFETYFACTOR approach, which is due to the FoS usually being overestimated by the methods of slices compared to the infinite slope method (Selby 1982, Abramson et al. 2002). The map indicates that the most extensive areas of highest stability (FoS > 2.25) are located at the ridges in the margins of the study area. There is one interruption, which is located in the southeastern part (Figure 6-12). Central areas, which are also classified as stable (from 2.0 upwards), are characterized by low slope inclination.

Together with the areas classified as 'moderately stable' (FoS from 1.75 to 2.00) the three classes account for about 61 % of the study area. Figure 6-12 shows the proportion of the FoS classes in relation to the study area. Thus, 39 % of the area is classified as unstable, where 17 % have a FoS between 1.5 and 1.75 ('unstable'), and 22 % are defined as 'highly unstable' with FoS values between 0 and 1.5 (Figure 6-12). Latter represents the second largest class, even though Class 5 is twice as large. Classes 1 and 2 are located in the center of the study area and both are characterized by similar slope inclinations with a mean inclination of 29° for Class 1 and a mean inclination of 25° for Class 2. The distribution of the FoS classes in connection with the slope inclination is illustrated in Figure 6-11b. Considering the landslide distribution in the study area, it can be stated that the majority of the landslide areas primarily contain unstable areas (Figure 6-11a). Exceptions to this are recorded by the landslides 8 and 12, which mainly show FoS values above 2.0 and only

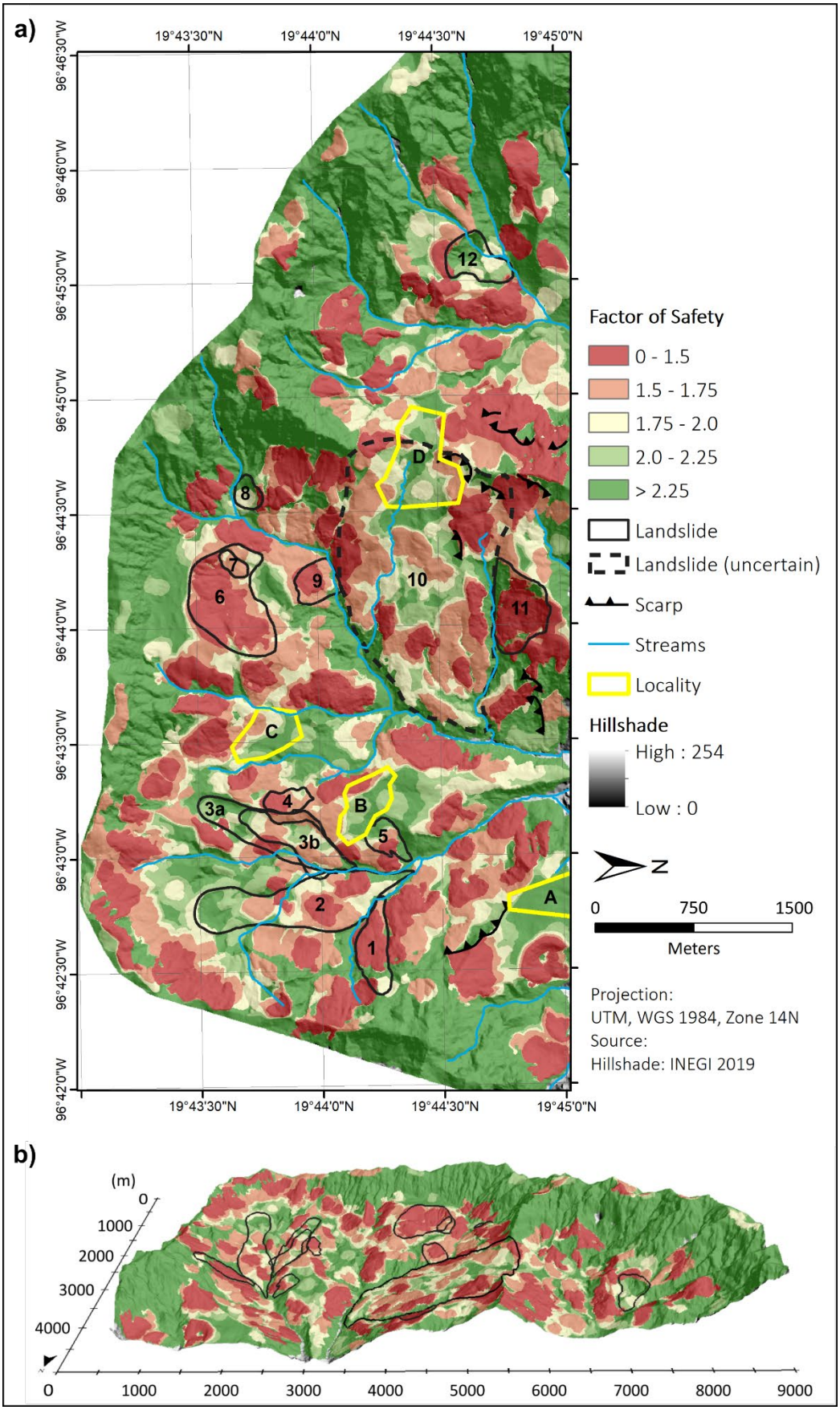

Figure 6-11. a) Factor of Safety map for the study area modeled with the method of slices (Scoops3D). b) Three-dimensional view of the slope stability map. Localities: A: La Sombra, B: El Capulín, C: El Escalanar, D: El Huerfano. Source: Own illustration.

smaller parts display values between 1.75 and 2.0. The scarp areas and partially the foot areas of landslides 1, 2, 3a, 3b (Capulín landslide), and 5 exhibit high FoS values, whereas the remaining slides are classified as unstable (< 1.75). Landslide 10 comprises a large area (approx. 2.2 km²) and even though some parts of the slide are characterized as unstable, the area is not classified as one continuous mass, but a set of smaller potentially unstable zones (cf. Figure 6-11a). Landslides 4, 6, 7, 9, and 11 are also classified as unstable with FoS values less than 1.75. Considering the scarp areas, it becomes clear that the northeastern scarps are not in direct connection with unstable zones, while those of the western part are within unstable zones (Figure 6-11a).

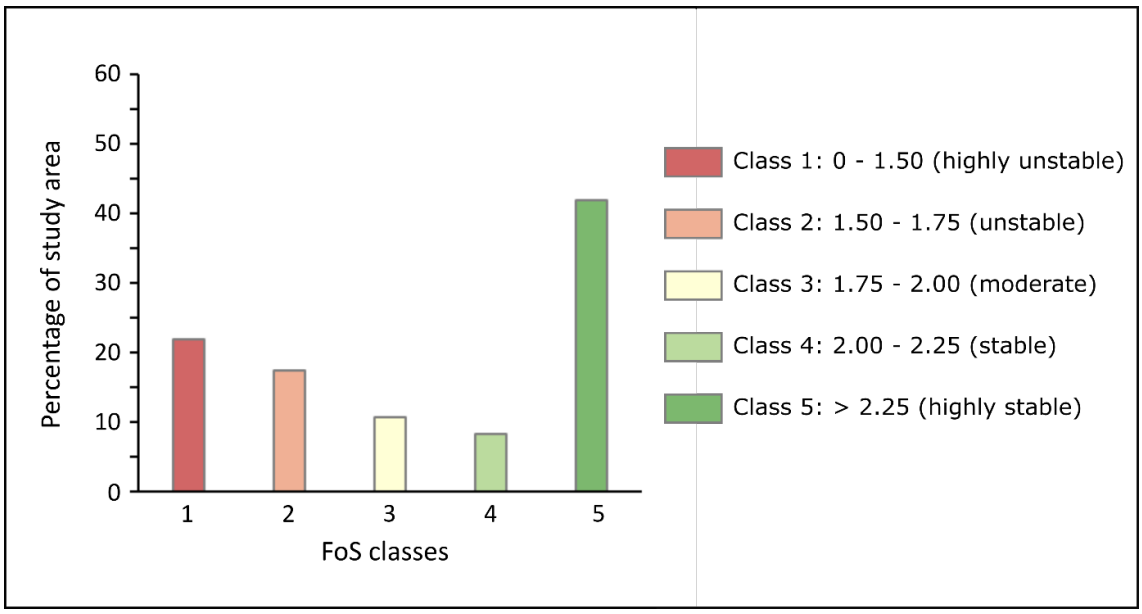

Figure 6-12. Proportion of the stability classes in relation to the study area in percentage for the Scoops3D map. Source: Own illustration.

6.5 Step IV – Comparison of the slope stability approaches

6.5.1 Simple SAFETYFACTOR map vs. filtered SAFETYFACTOR map

In order to evaluate the strengths and weaknesses of the different approaches, the 'simple SAFETYFACTOR map' and the 'filtered SAFETYFACTOR map' are compared (Figure 6-13). The main difference between the two maps consists in the application of a majority filter. Even though both maps are based on the same analysis, the filtering process causes shifts within the FoS classes (Figure 6-14). Classes 3 and 4 remain almost unchanged and there is a difference of approx. 2 % for class 2. A more noticeable change (approx. 5 % difference) is detected when comparing the proportions in Class 1. Class 5 records with

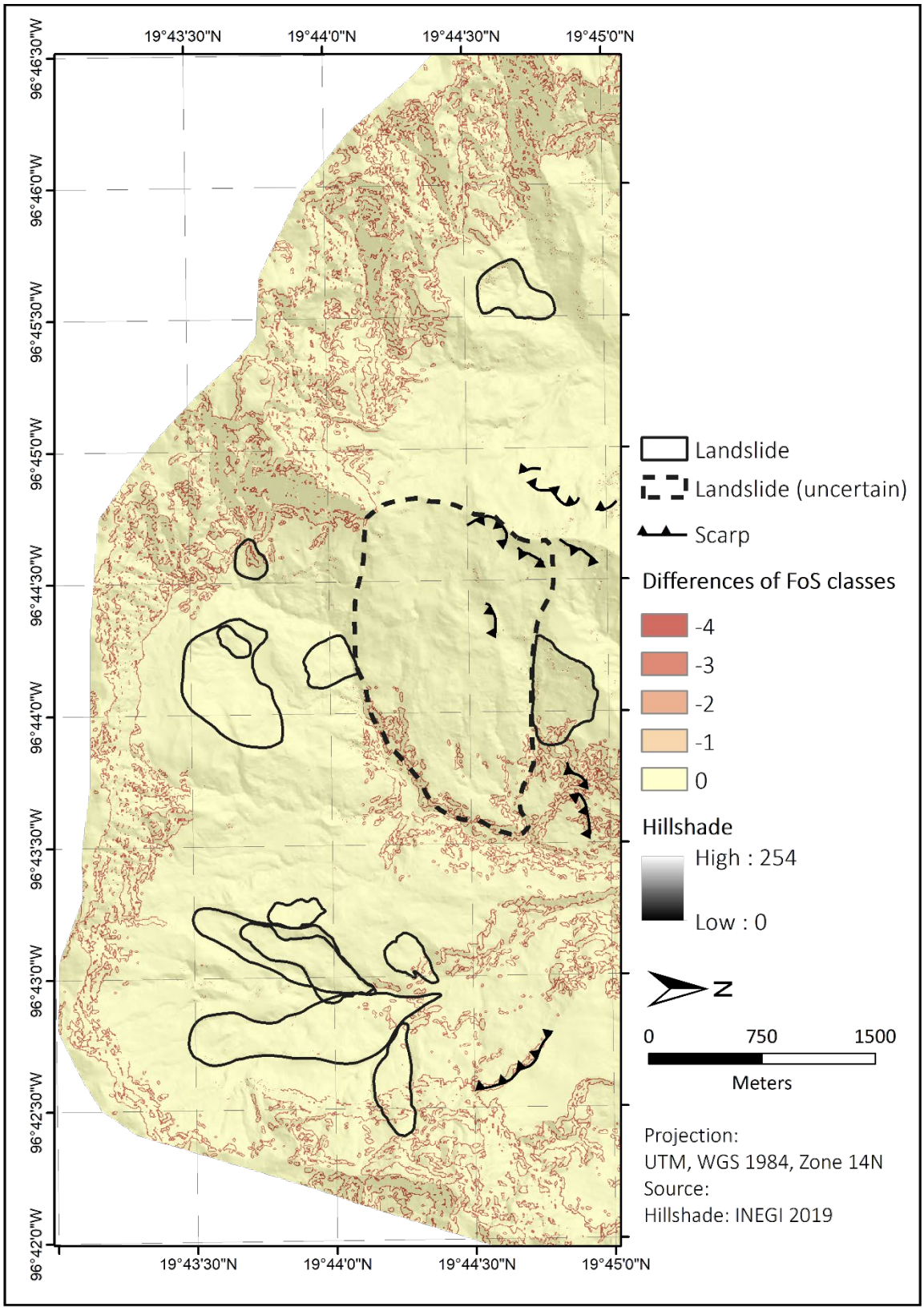

Figure 6-13. Pixel-based difference model of the SAFETYFACTOR maps (with and without filter application). Negative values represent classes from the simple map that are below the filtered SAFETYFACTOR classes. Source: Own illustration.

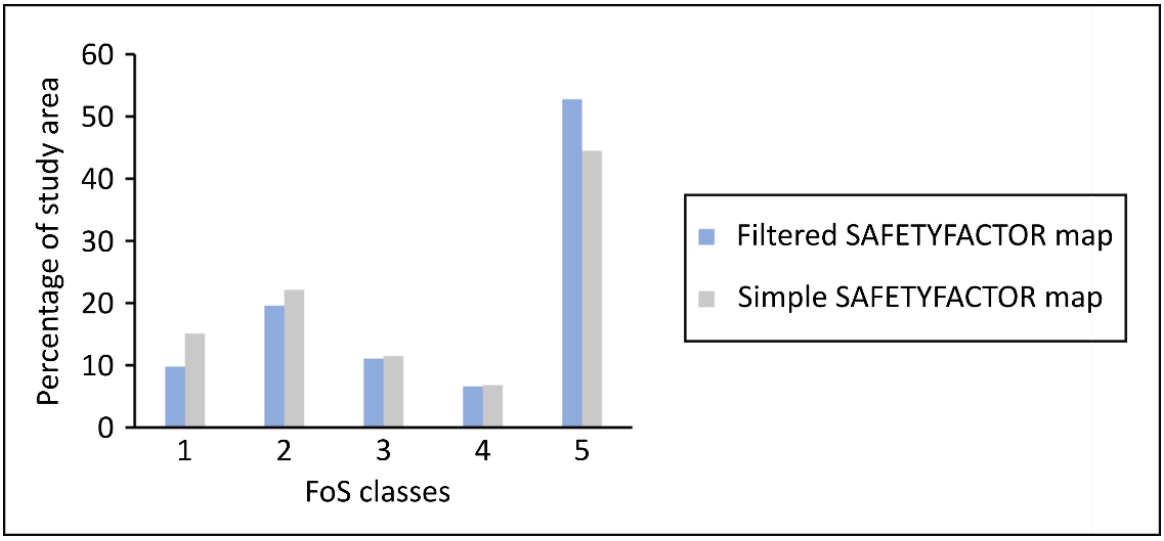

Figure 6-14. Comparison of the FoS classes of the simple SAFETYFACTOR map (gray) and filtered SAFETYFACTOR map (blue). The bars show the proportion of the classes in relation to the study area in percentage. Source: Own illustration.

approx. 8 % a significant difference (Figure 6-14). Overall, it can be summarized that after the filtering process the proportion of the stable areas (Class 3, 4, and 5) increases (53 %) in the filtered SAFETYFACTOR map, compared to the simple SAFETYFACTOR map (44 %).

Both maps show similar distributions of the FoS classes in Region 1 and 2 (cf. Figure 3-5), however, in Region 3, differences between the two maps are visible (Figure 6-15). In the latter region, the largest group of the simple SAFETYFACTOR map corresponds to Class 2, whereas Class 5 comprises the largest part of the filtered map. Comparing Class 1 of both maps results in a difference of approx. 7 %, whereas Classes 3 and 4 remain the same (Figure 6-15).

Figure 6-13 shows the pixel-based difference model of the two SAFETYFACTOR maps. Here, the two maps correspond to the same classes in the major part of the area (92 %). The deviation by one or two classes accounts for less than 1 % of the study area, whereas the deviation of three classes comprises 3 %. The highest deviation, with a difference of four classes, accounts for approx. 5 %. Furthermore, in Figure 6-13 the distribution of the differences and similarities is illustrated. The class differences are mainly located at the exterior parts of the study area as well as in smaller areas in the northwest. The agreement between the classes is remarkably good within the landslide areas (Figure 6-13).

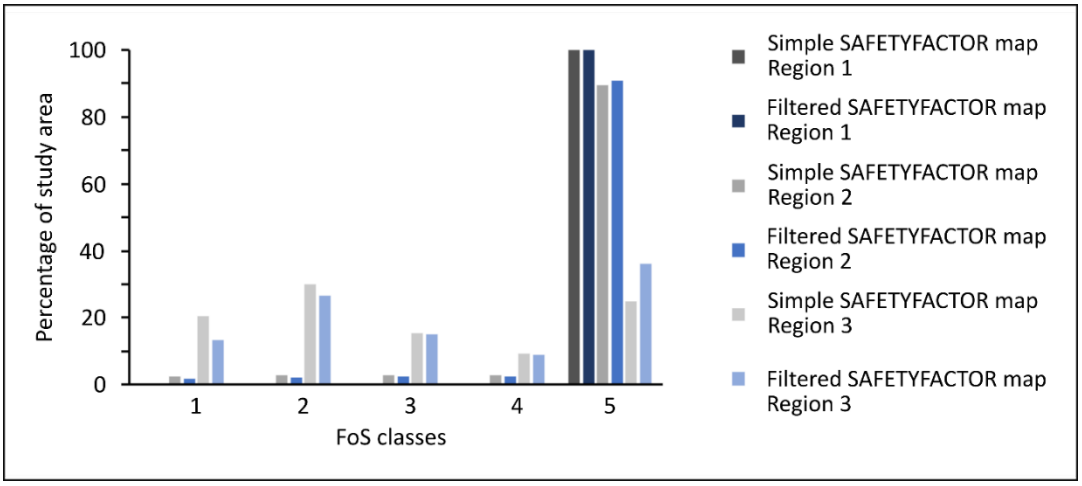

Figure 6-15. Proportion of the FoS classes within the process regions, comparing the simple SAFETYFACTOR map (grays) and the filtered SAFETYFACTOR map (blues). Source: Own illustration.

6.5.2 Filtered SAFETYFACTOR map vs. classified slope map

The second analysis compares the filtered SAFETYFACTOR map with a classified slope map (Figures 6-17, 6-18). Related to this, a slope map was derived from the DEM 2011 and then classified. To allow the comparison of both maps, the slope map is divided into five classes. The classes are determined with the goal to be comparable to the FoS classes. The slope values, between 22° and 86° are subdivided in two classes, and the values below 22° into three classes. In Figure 6-18, it can be observed that the class containing the highest slope values (Class 5) represents the group with the largest area (57 %). Class 2 follows with a share of 17 %, and Classes 3 and 4 each account for approx. 11 %. With around 4 %, Class 1 represents the smallest spatial distribution (Figure 6-16). The varying group sizes result from the adjustment of the classes to the SAFETYFACTOR map. Figure 6-17 shows the pixel-based difference model of the simple SAFETYFACTOR map and the slope map. In this case, the latter was compared to the SAFETYFACTOR map. In about 39 % of the study area, there are no classification differences between the two maps. The deviation of one class (both negative and positive) accounts for a share of 11 %, and the difference of two classes sums up to 9 %. Similar to this, the difference of four classes accounts for 15 %. An exception consists in the deviation of three classes, which comprises a larger area with 27 % (Figure 6-17). Overall, the percentage of positive values is higher than those of the negative values. Furthermore, the spatial distribution of the class differences can be seen in Figure 6-17. Areas without class differences are located at the margins. In general, there is a good agreement between the maps in areas with steep slopes, whereas in areas with low slope inclinations (0° - 17°), the correspondence is significantly weaker.

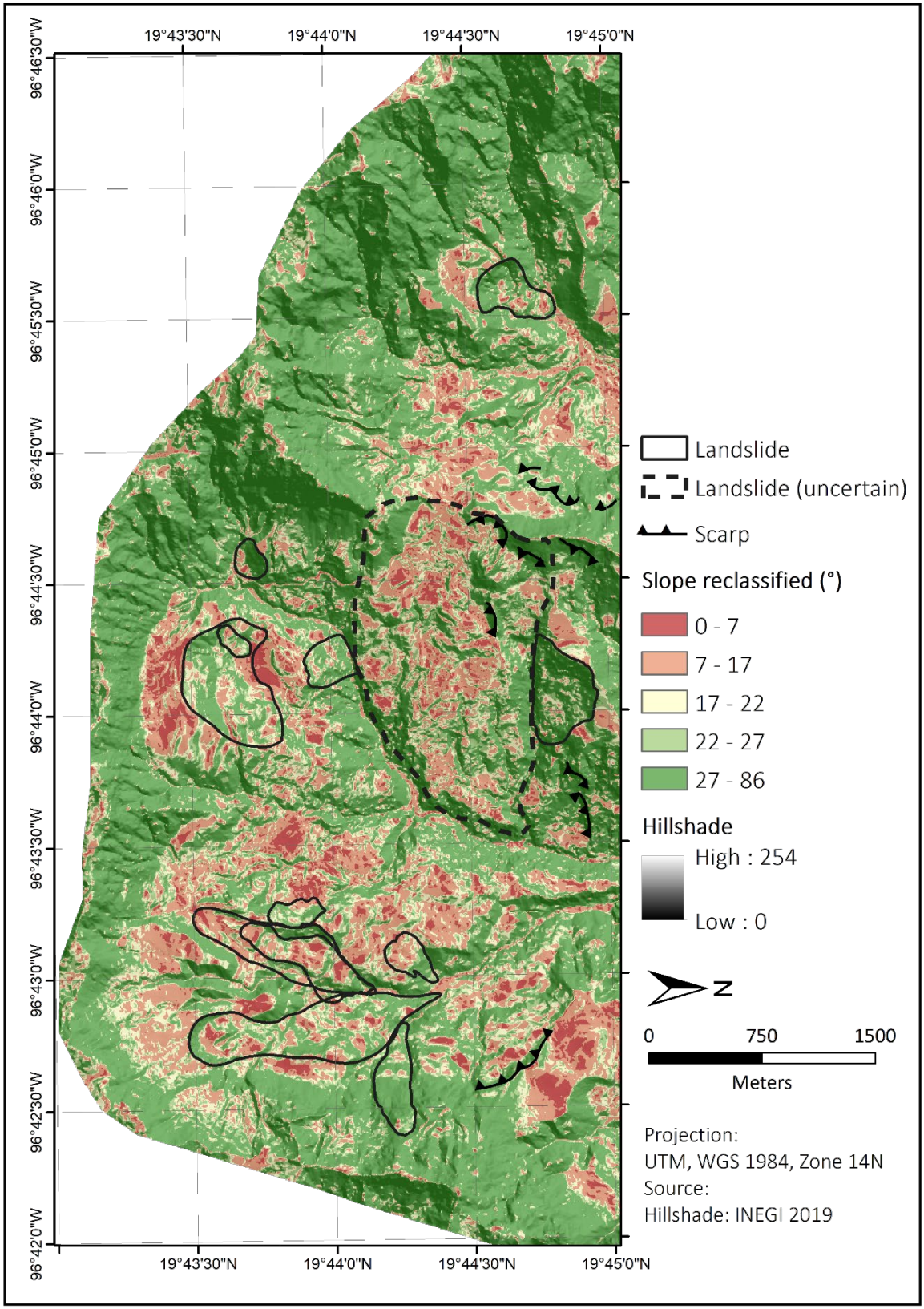

Figure 6-16. Slope map, calculated based on the DEM 2011, and classified into five classes. Source: Own illustration.

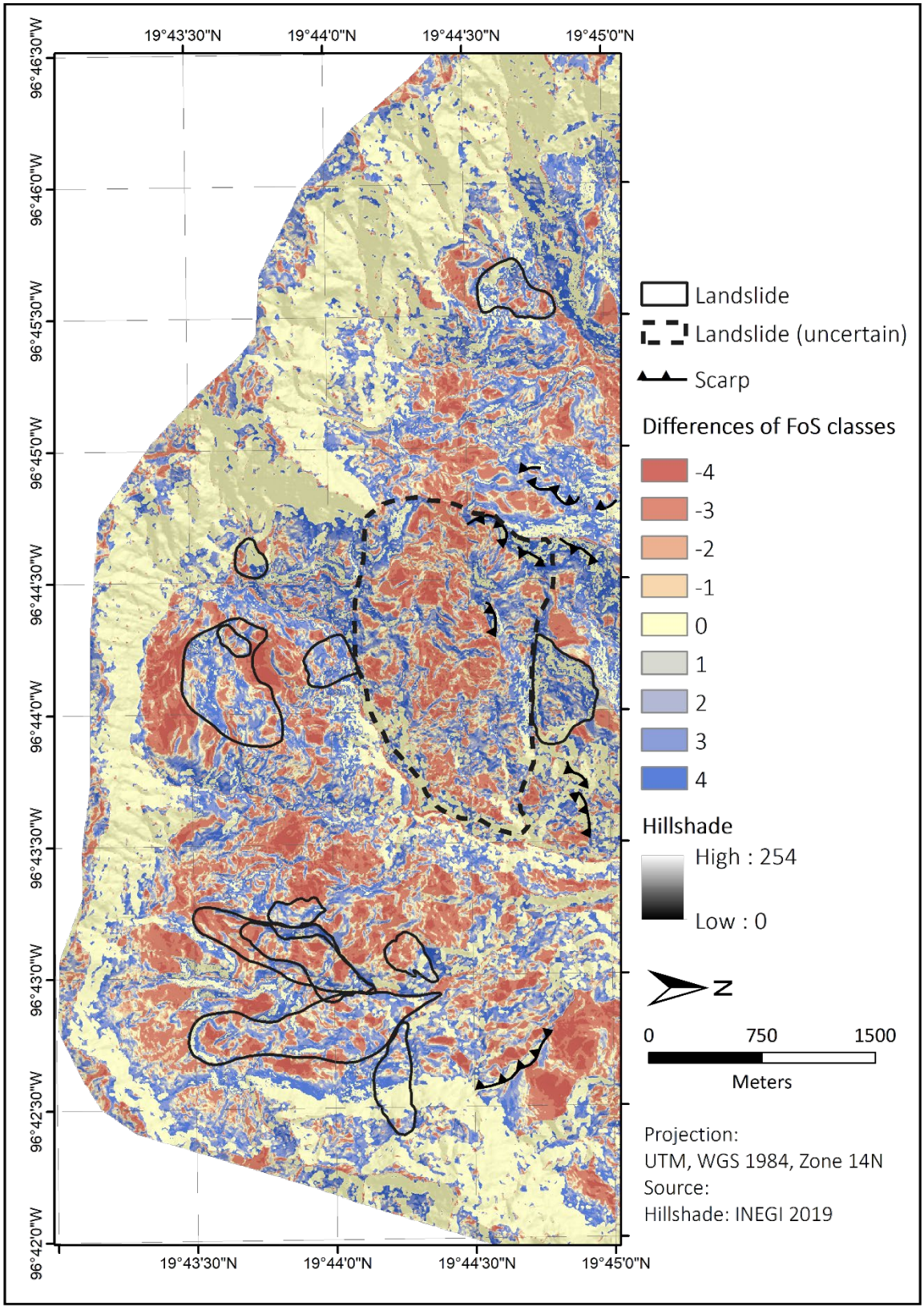

Figure 6-17. Pixel-based difference model of the filtered SAFETYFACTOR map and the classified slope map. The difference classes indicate the deviation of the slope map from the filtered SAFETYFACTOR map. Negative values signify that the slope map classes are below and positive values above, the SAFETYFACTOR classes. Source: Own illustration.

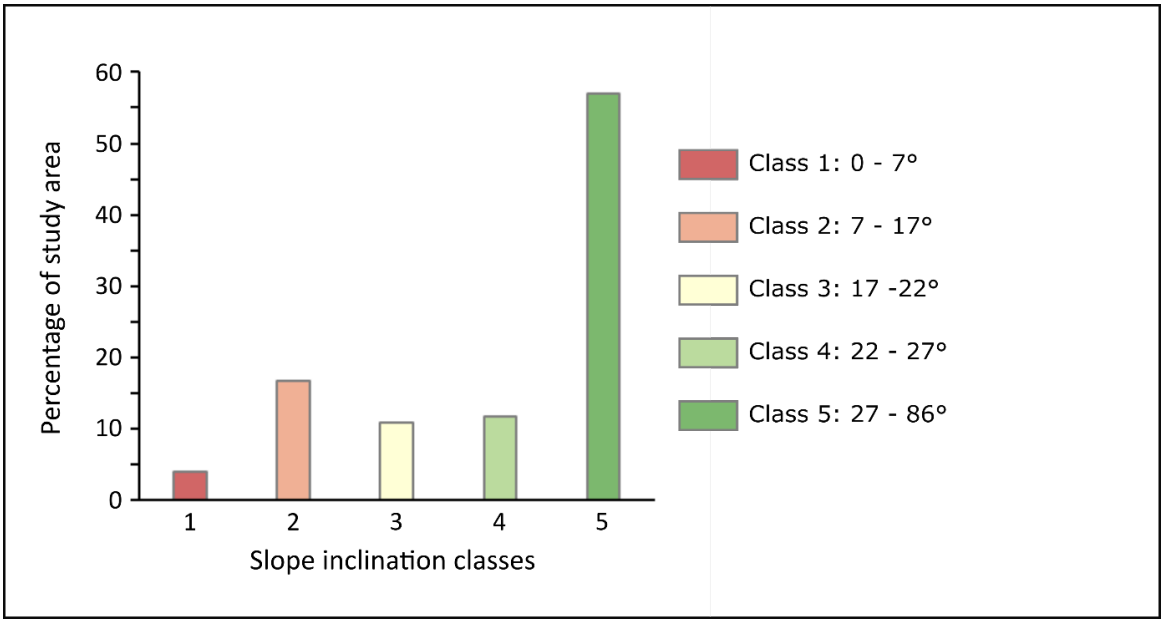

Figure 6-18. Proportion of slope classes in relation to the study area (in %). Source: Own illustration.

6.5.3 Filtered SAFETYFACTOR map vs. literature-value SAFETYFACTOR map

For this analysis, literature values form the base for the generation of the SAFETYFACTOR map (referred to as 'literature-value SAFETYFACTOR map'). The resulting map is compared to the filtered SAFETYFACTOR map. The literature-value SAFETYFACTOR map solely comprises geotechnical values derived from literature, whereas the filtered SAFETYFACTOR map is based on a combination of literature values (Region 1 and 2) and calculated values (Region 3, cf. chapter 6.3.1). Accordingly, the input values only differ in Region 3, where the same literature values as Region 2 are applied for the literature SAFETYFACTOR map (Table 6-7). The resulting literature-value SAFETYFACTOR map is illustrated in Figure 6-19. It is important to notice that the classification of this map does not correspond to the filtered SAFETYFACTOR map. The FoS values are higher compared to the latter map and had to be adjusted in order to enable a comparison. At first glance, the comparison shows a high similarity. However, a more detailed look reveals differences (Figures 6-21, 6-22, and 6-23). Figure 6-20 shows that both maps correspond to the same classes in more than 60 % of the study area, with small differences occurring between the classes (< 5 %; Figure 6-21). The differences increase (Figure 6-22) related to the FoS distribution in the three process regions (cf. Figure 3-5) as for instance in Region 1. In this case, interestingly, 90 % are classified as highly stable (Class 5) in the filtered SAFETYFACTOR map, whereas the literature-value based map shows a wider

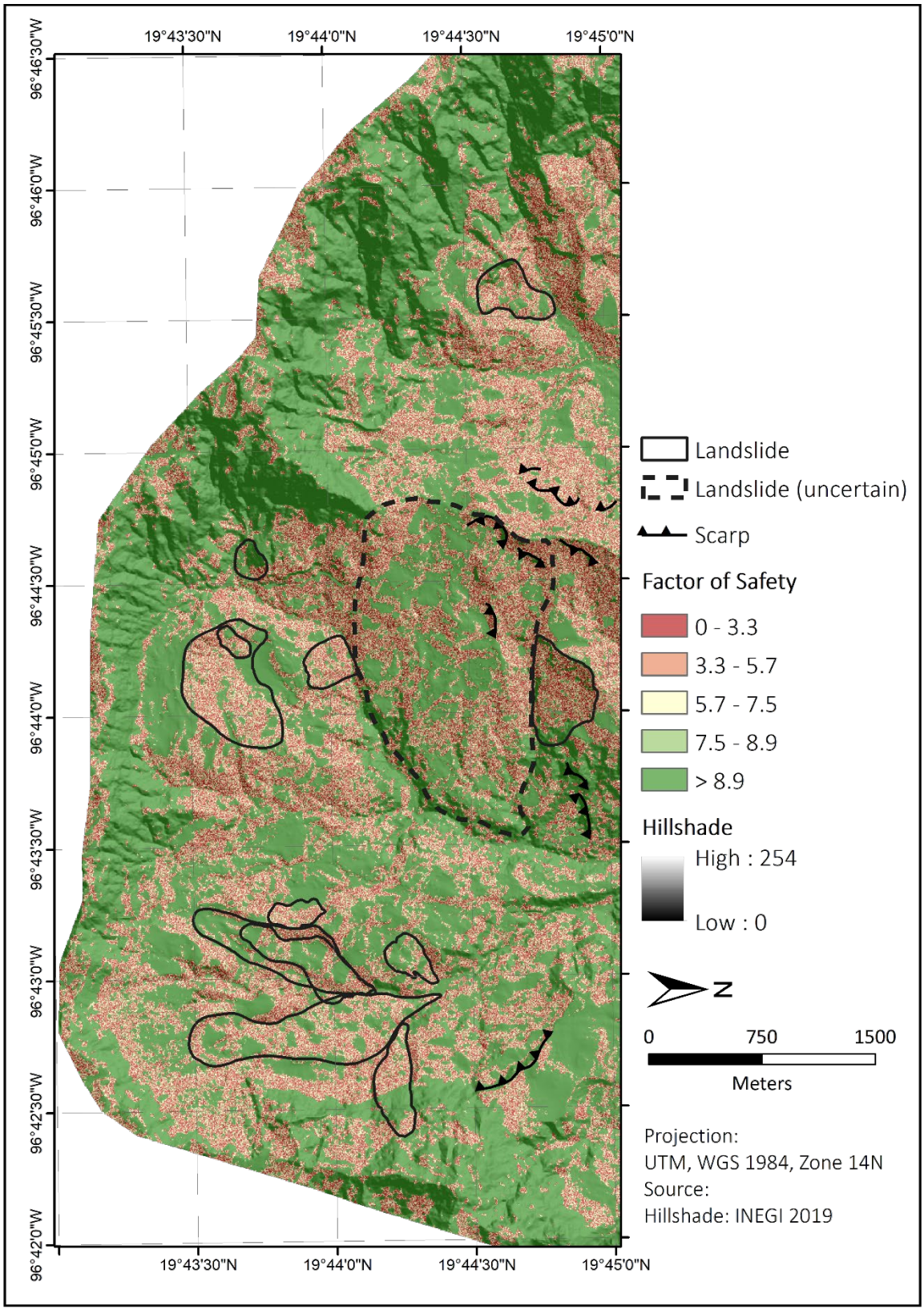

Figure 6-19. Factor of Safety map calculated exclusively using literature values (according to Selby 1982 and Asniar et al. 2019), and further processed with a majority filter. Source: Own illustration.

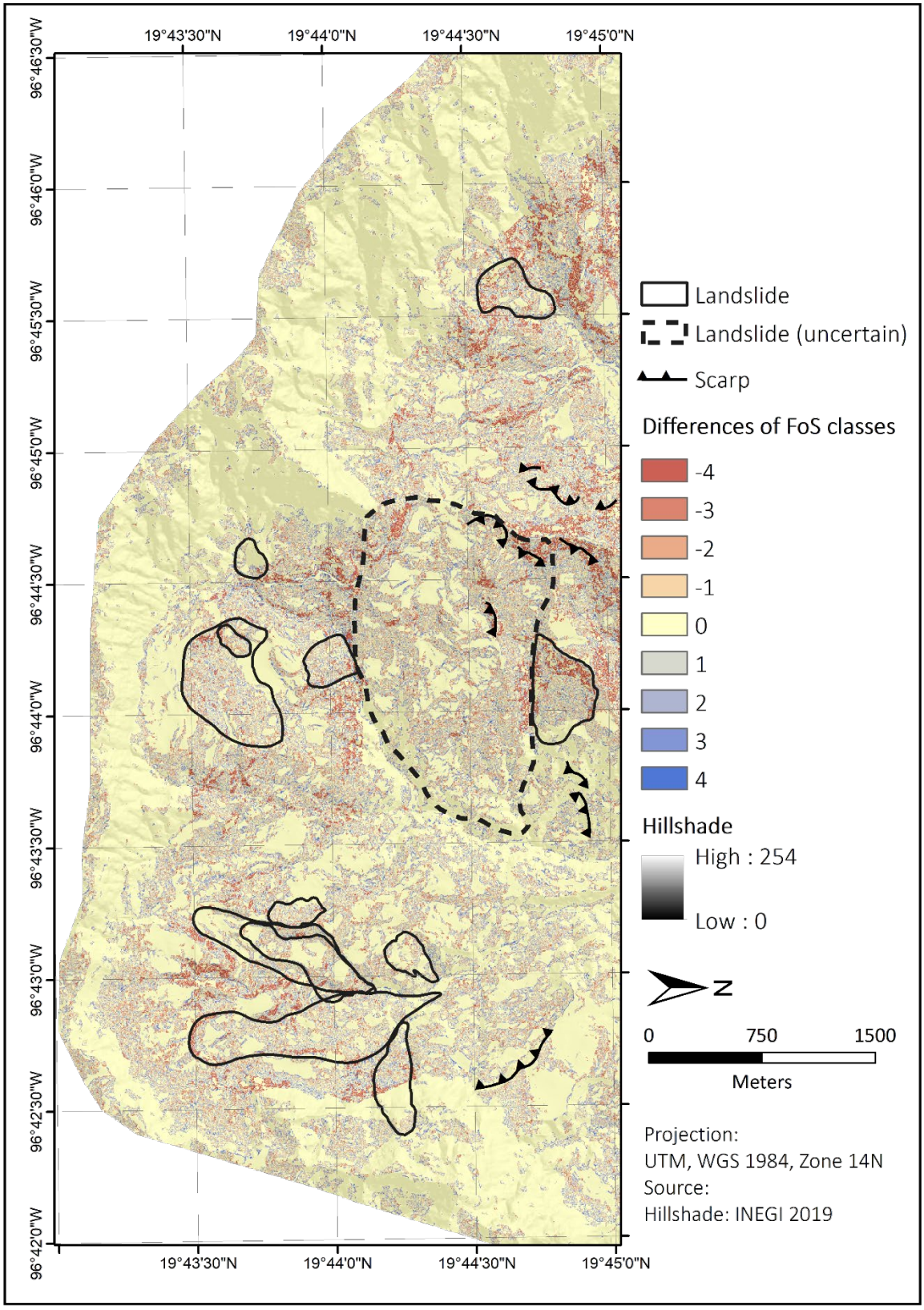

Figure 6-20. Pixel-based difference model of the filtered SAFETYFACTOR map and the literature-value SAFETYFACTOR map. The difference classes indicate the deviation of the literature-based from the filtered SAFETYFACTOR map. Negative values signify that the classes are below (positive values above) the SAFETYFACTOR classes. Source: Own illustration.

distribution of the FoS classes. Figure 6-22 illustrates the distribution of the FoS classes within the process regions and for Region 2 an almost homogenous distribution can be observed. Despite this, Region 3 accounts for minor class differences between both maps, ranging from 3 to 8 %. Region 1 can be disregarded as both maps do not show differences (Figure 6-20, 6-22).

Table 6-7. Geotechnical input parameters for the literature-value SAFETYFACTOR map. Region 1: geotechnical properties for basalt according to Selby (1982), Region 2 and Region 3: geotechnical characteristics for tuff according to Asniar et al. (2019). Proportion of the area in brackets.

Calibration Region	Region 1 (21 %)	Region 2 (6 %)	Region 3 (73 %)
Cohesion min. (MPa)	35.00	0.00	0.00
Cohesion max. (MPa)	55.00	1.45	1.45
Friction angle min. (°)	35.00	24.00	24.00
Friction angle max. (°)	45.00	45.00	45.00
Density min. (g/cm³)	2.55	1.83	1.83
Density max. (g/cm³)	3.10	2.54	2.54

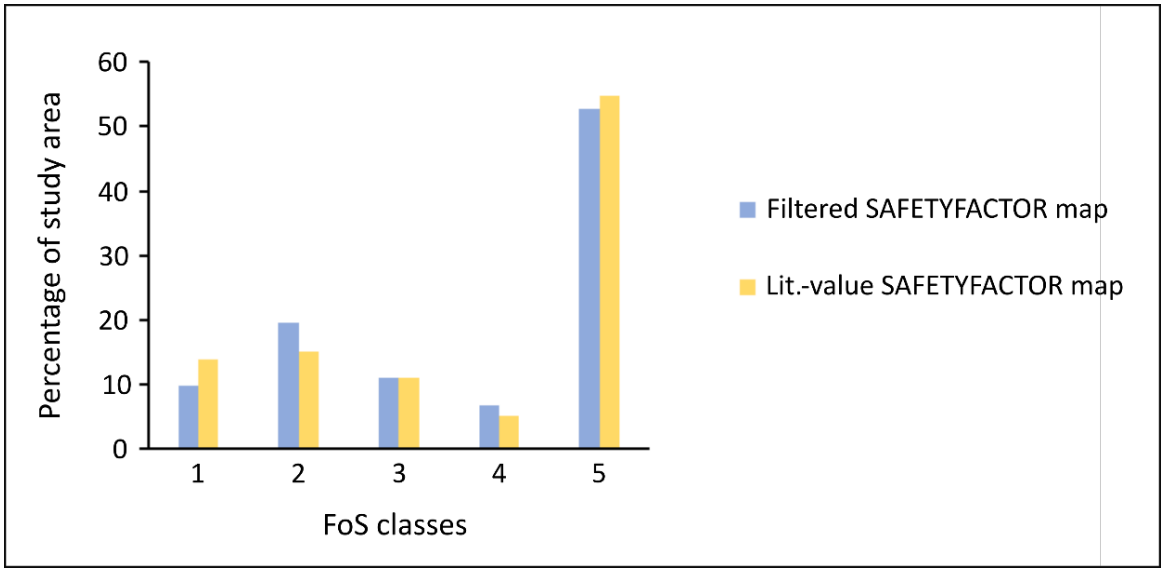

Figure 6-21. Comparison of the FoS classes of the filtered SAFETYFACTOR map (blue) and the literature-value SAFETYFACTOR map (yellow). The bars show the proportion of the classes in relation to the study area in percentage. Source: Own illustration.

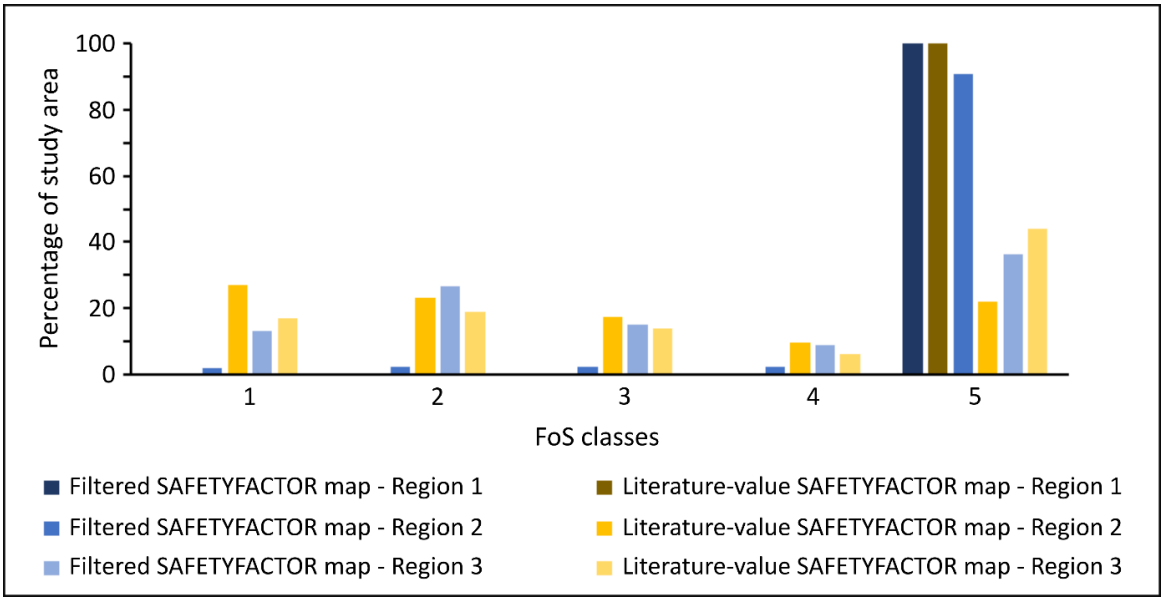

Figure 6-22. Proportion of the FoS classes within the process regions, comparing the filtered SAFETYFACTOR map (blues) and the literature-value SAFETYFACTOR map (yellows). Source: Own illustration.

6.5.4 Scoops3D map vs. filtered SAFETYFACTOR

In this analysis, the resulting maps from Step III A and B are compared. Here, the SAFETYFACTOR map is compared to the Scoops3D map (Figures 6-23, 6-24, and 6-25). Adding the areas with stable FoS classes (Classes 3, 4, and 5), it turns out that with 70 % the SAFETYFACTOR map exhibits a higher share of stable areas than the Scoops3D map with 60 % (Figure 6-23). Larger deviations can further be observed in Class 1 (12 %) and Class 5 (11 %). This divergent classification is also apparent in Figure 6-24, which considers the FoS distribution within the three process regions (cf. Figure 3-5).

In the Scoops3D map, the FoS classes are represented in all three regions, while the SAFETYFACTOR map displays a concentration of Class 5 in Region 1 and 2. Exclusively in Region 3, the FoS values of the SAFETYFACTOR map are more widely distributed over all classes. Thus, in Region 3, the proportions of the FoS classes are similar for both maps (Figure 6-24). In the remaining regions, there is a deviation between the FoS classes, especially in Region 2. For example, Class 5 of the SAFETYFACTOR map has a share of 90 %, while Class 5 of the Scoops3D map only comprises 44 % (Figure 6-24).

Furthermore, Figure 6-25 represents the result of the pixel-based difference model. The two maps correspond to the same classes in about 40 % of the area. Positive values correspond to 40 % and negative values to 20 % of the study area (Figure 6-25).

Considering the landslide polygons in Figure 6-25 it can be stated that positive values are prevailing. The only exception occurs in the northwestern landslide (no. 12), where negative values dominate. In summary, the SAFETYFACTOR map generally represents higher FoS values for the landslides compared to the Scoops3D map (Figure 6-25).

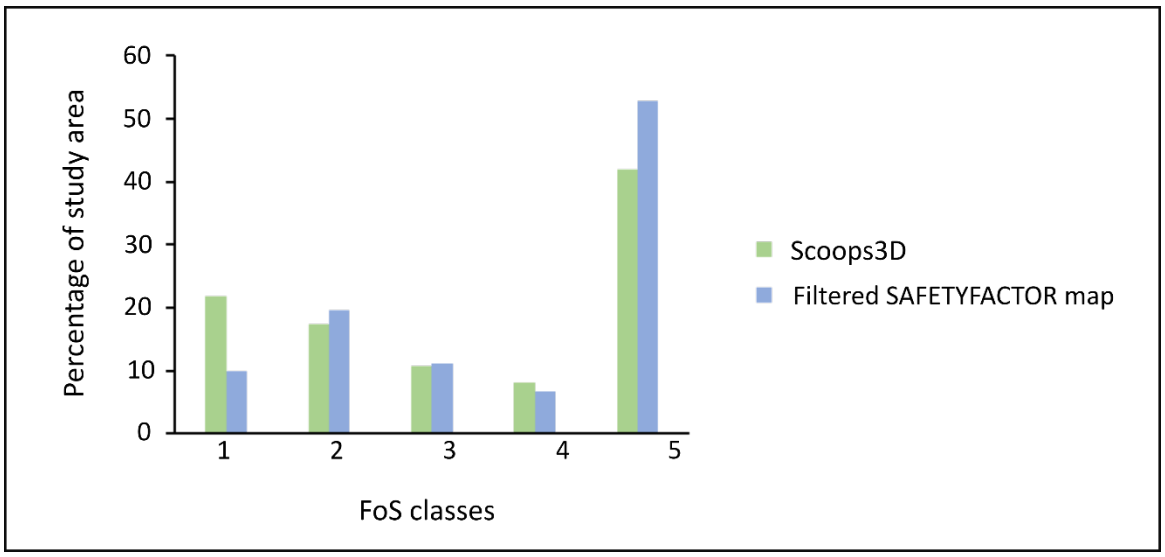

Figure 6-23. Comparison of the FoS classes of the Scoops3D map (green) and the filtered SAFETYFACTOR map (blue). The bars show the proportion of the FoS classes in relation to the study area in percentage. Source: Own illustration.

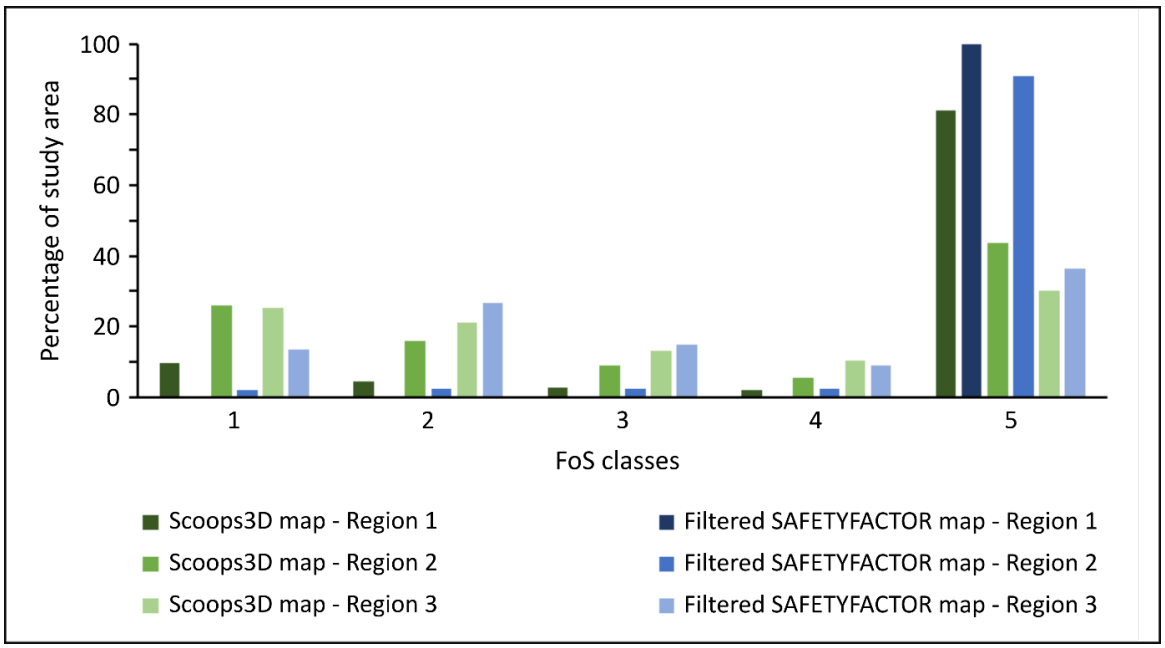

Figure 6-24. Proportion of the FoS classes within the process regions, comparing the filtered SAFETYFACTOR map (blues) and the Scoops3D map (greens). Source: Own illustration.

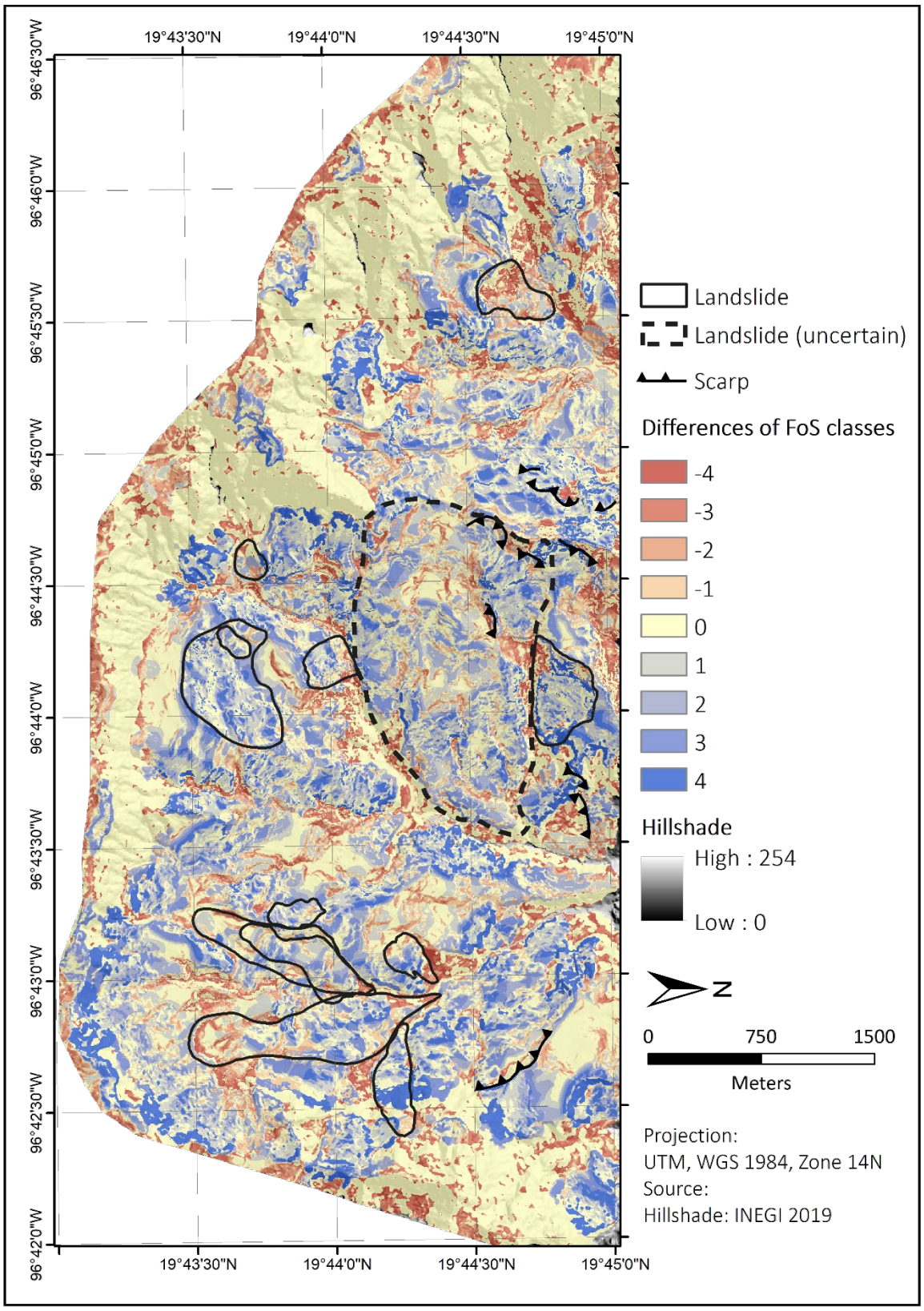

Figure 6-25. Pixel-based difference model of Bishop's simplified method (Scoops3D map) and infinite slope method (filtered SAFETYFACTOR map). The difference classes indicate the deviation of the SAFETYFACTOR map from the Scoops3D map. Negative values signify that the classes are below and positive values above, the Scoops3D classes. Source: Own illustration.

7. Discussion

The overall objective of this study is the assessment of landslide susceptibility in the Chiconquiaco Mountain Range area. The subdivision into a site-specific (local) and a regional approach allows for analyzing the causes and processes as well as to model the susceptibility for the entire study area. The following sections discuss the applied approaches and the methodological concepts.

7.1 Site-specific approach

For the site-specific approach, the focus lies on establishing a data basis, which allows for a better understanding of the occurring processes in the study area. Thereby, one focal point is the characterization of the selected landslide and the other is the evaluation of the methodological concepts. Chapter 7.1.1 provides a characterization of the Capulín landslide, including the analyses of the **causes**, **triggers,** and **process types**, which contribute to a deeper insight into the local conditions and thus, to a better understanding of the Capulín landslide (chapter 1; Varnes 1978, Cruden and Varnes 1996, Wieczorek 1996, Lu and Godt 2013). The following chapter (7.1.2) addresses the second focal point as it includes the discussion of the methodological approaches.

7.1.1 Classification and characterization of the Capulín landslide

7.1.1.1 Precondition and preparatory factors

When considering the preconditions and preparatory factors, a comparison with other landslides from this area supports the identification of the individual components, and therefore, the following considers the landslide in relation to the other landslides of the study area.

The Capulín landslide occurred at a moderate to steep slope (slope gradient between 10 and 35°), located below the extremely steep slopes (> 45°) mainly formed by basalts and andesites (Figure 7-1, Gómez-Tuena et al. 2003, Lascurain-Rangel et al. 2017). The highest point of the Capulín landslide (no. 3b) is at 1,440 m a.s.l., which is slightly lower compared to the scarps of the registered landslides in the study area, where 62 % lie above 1,500 m a.s.l. (Table 7-1; chapter 4.3). The landslide foot extends down to 1,190 m a.s.l., which is similar to the remaining landslides as 54 % are below 1,200 m a.s.l. (Table 7-1). Thus, the

location of the Capulín landslide lies within the range of the other identified landslides (Table 7-1; chapter 4.3).

The mean **slope values** of all mapped landslides range from 20 and 35°, and with 20° the Capulín landslide is at the lower end (Table 7-1). The values are in good agreement with the typical range for landslides, which usually is between 20 and 40° (Highland and Bobrowsky 2008, Terhorst and Damm 2009, Neuhäuser et al. 2012a, Ramírez-Herrera and Gaidzik 2017).

Besides the slope gradient, **proximity to streams** is another important precondition as water level changes affect slope stability through saturation of the slope material and erosion at the foot area (e.g. Cruden and Varnes 1996, Wieczorek 1996, Neuhäuser et al. 2012a, Sujatha et al. 2012). The foot of the Capulín landslide ends at a stream, which most likely is responsible for erosional processes before and after the landslide event, causing steep inclined slopes (> 35°) in this area (with heights over 15 m, Figure 7-1; chapter 4.1). This corresponds well with the mapping results, which reveal that 77 % of the registered landslides are at a distance between 0 and 20 m to streams and 23 % at a distance > 200 m (Table 7-1; chapter 4.3). Close proximity to rivers is not only frequent in this area, but a common phenomenon (e.g. Wieczorek 1996, Zêzere et al. 1999, Terhorst 2001, Terhorst and Kreja 2009, Peduzzi 2010, Neuhäuser et al. 2012a, Deng et al. 2017, Wang et al. 2020).

Table 7-1. Characteristics of the landslides mapped in the study area (chapter 4.3), including the Capulín landslide (no. 3b).

Landslide no.	Highest point of scarp (m a.s.l.)	Lowest point of foot (m a.s.l.)	Mean slope value (°)	Distance to streams (m)
1	1650	1170	35	0 - 5
2	1550	1110	23	10 - 20
3a	1480	1190	20	0 - 5
3b	1440	1190	20	0 - 5
4	1420	1320	25	200 - 250
5	1260	1110	21	10 - 20
6	1630	1450	24	250 - 700
7	1570	1460	24	250 - 700
8	1620	1510	32	10 - 20
9	1450	1310	28	0 - 5
10	1670	1020	24	0 - 5
11	1520	1200	34	0 - 5
12	1590	1370	31	0 - 5

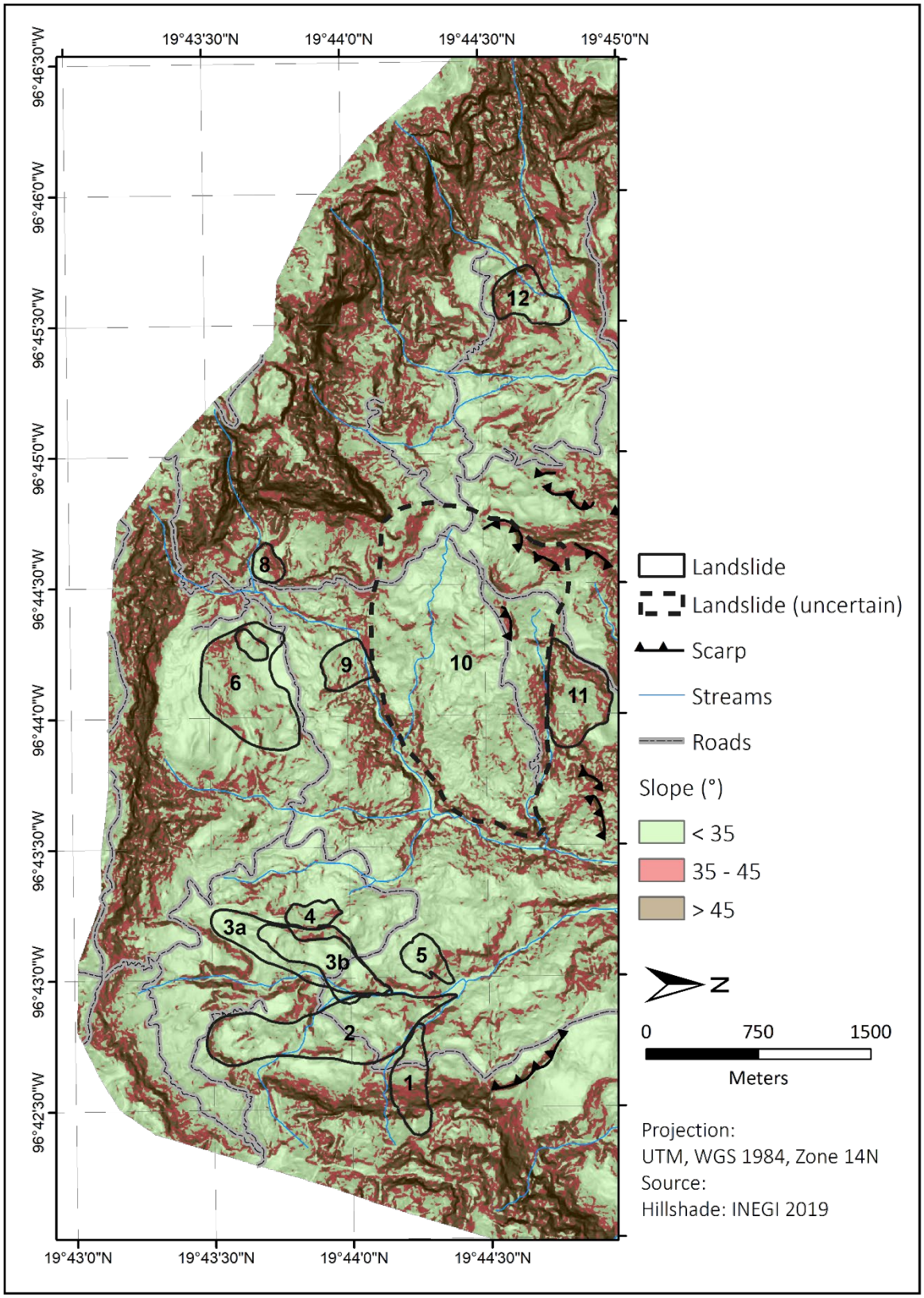

Figure 7-1. Classified slope map of the study area, including the registered landslides. Subdivision into moderate to steep slopes (< 35 °), steep slopes (35 – 45°), and extremely steep slopes (> 45°). Polygons represent mapped landslides (combining scarp and slide mass areas) and line feature mark single scarps, where the slide mass was not identifiable. Brown areas mainly correspond to basalts and andesites, the green area to slope deposits. Source: Own illustration.

In addition to the geomorphological factors mentioned above, **lithology** represents an important precondition (e.g. Varnes 1978, Cruden and Varnes 1996, Prinz and Strauß 2011, Lu and Godt 2013). There are two main lithological units in the study area. One being basalts and andesites, which form the abrupt slopes (> 45°) and surround the study area in a north-opened U-shape (chapter 2, Lascurain-Rangel et al. 2017). The other consists of massive slope deposits (also referred to as talus deposits) covering the moderate to steep slopes (< 35°). All landslides registered in the study area, including the Capulín landslide (no. 3b) occurred in latter unit (Figure 7-1, Wilde et al. 2017a). These massive slope deposits consist of a mixture of fine material and rock fragments of various sizes and are often the result of different slope processes, such as falls, slides, or creeps (Turner 1996, Jiménez Sánchez 2002, Guzmán Lagunes and Morales Barrera 2014). Alternating sandstone and shale deposits, corresponding to a Tertiary terrigenous sequence, form another, smaller lithological unit, since they only occur in outcrops scattered throughout the study area (Lopez-Infanzon 1991, Guzmán Lagunes and Morales Barrera 2014, Wilde et al. 2017a).

As no detailed information on these lithological units is available for the study area, it was necessary to collect basic and crucial data in order to gain knowledge about the lithological conditions (Cruden and Varnes 1996). To obtain a comprehensive overview, sampling included sediments of the Capulín landslide, a second landslide (Escalanar slide) southwest of the village El Capulín, and the surrounding areas in close proximity to the Capulín landslide (cf. Figure 5-1, chapter 5). The characteristics of the analyzed materials vary between sample locations, which is particularly evident in the field observations, where the sampling sites show variations primarily in color as well as in size and content of rocks (Figure 7-2; chapter 5). Furthermore, the results of the sediment analyses reveal interesting similarities and differences as well as certain ranges of values that allow a subdivision into three main groups:

- Group I: Samples from the eastern flank of the Capulín landslide (FE 1 - FE 3) and samples from the surrounding areas (SA 1, SA 10).
- Group II: Soil profile within the slide mass of the Capulín landslide (M 6) and samples from the surrounding areas (SA 2 - SA 9).
- Group III: Samples from the scarp (S 1 - S 4), the western flank (FW 1 – FW 5), and the slide mass (M 1 - M 5; M 7 - M 8) of the Capulín landslide. Samples from the Escalanar landslide (EFE 1, EM 1, EFW 1).

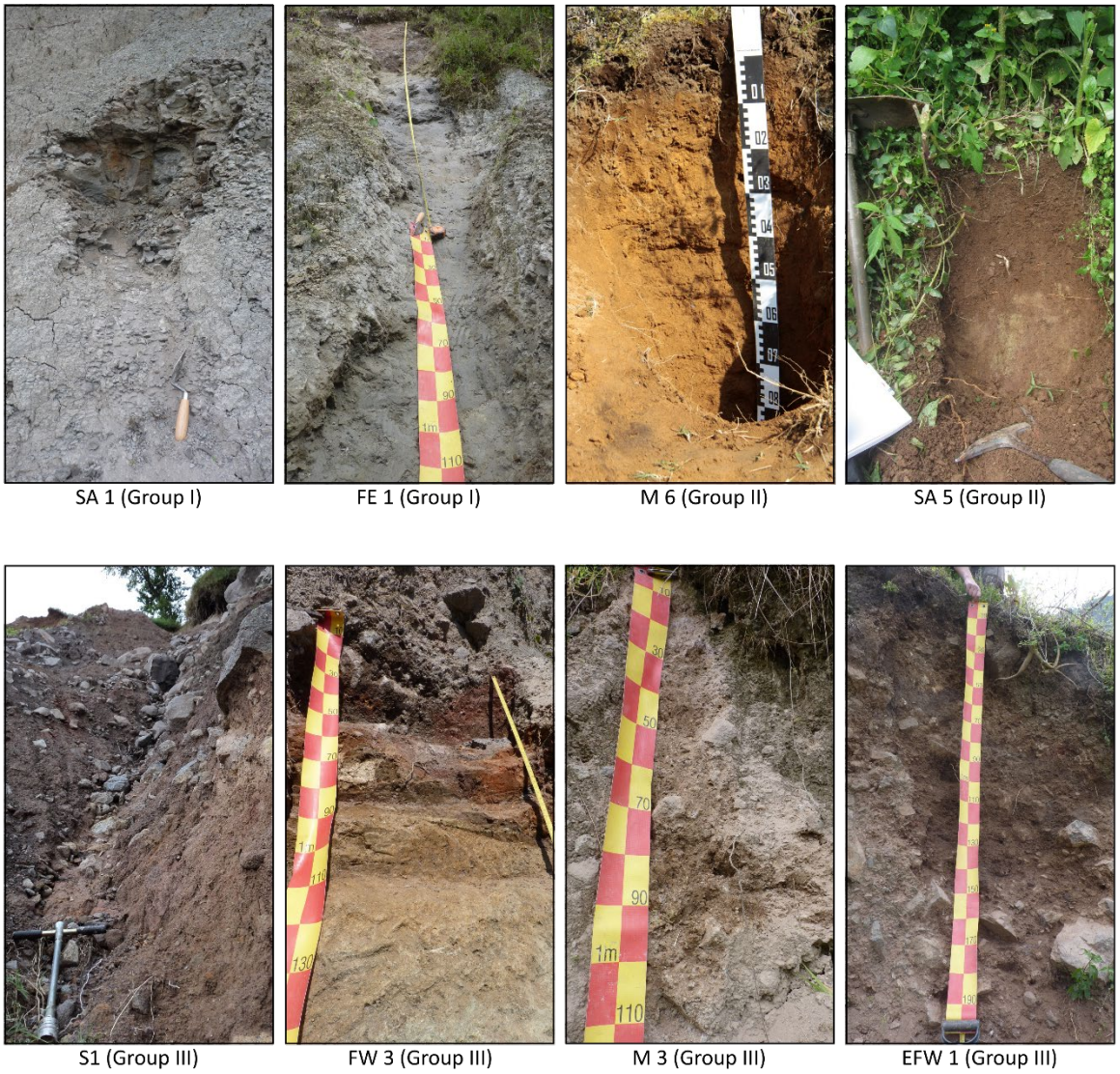

Figure 7-2. Exemplary sample locations from each sediment group. Source: Own photographs (2016, 2018).

Comparing the laboratory analyses of these three groups, some properties are particularly striking (Table 7-2). First of all, it is noticeable that the silt fraction accounts for the largest proportion within the grain size distribution for all groups, with mean values over 50 %, followed by clay with more than 20 % (Table 7-2). Secondly, the carbonate and pH-values record the most significant differences within the groups. While Group II and III have similar ranges, values of Group I clearly deviates from the others (Table 7-2). This remarkable aspect is of particular interest since sample locations SA 1 and SA 10 specifically targeted outcrops, which were related to the above mentioned sedimentary (mainly shale) deposits from the Tertiary terrigenous sequence (Lopez-Infanzon 1991, Wilde et al. 2017a). Thus, the similarity between these samples and the samples of the eastern flank of the Capulín landslide show that latter is most probably associated with

Table 7-2. Subdivision of the sediment analyses results into three main groups. Green marks the most significant similarities and orange the differences between the groups.

Analysis	Group I			Group II			Group III		
	Min.	Max.	Mean	Min.	Max.	Mean	Min.	Max.	Mean
∑ gravel (%)	0.0	26.6	6.4	0.0	2.0	0.1	0.0	68.0	8.7
∑ sand (%)	3.2	47.8	15.3	0.9	27.4	9.0	0.3	60.7	19.7
∑ silt (%)	32.8	71.4	50.5	38.0	80.0	65.6	11.5	78.6	50.8
∑ clay (%)	12.0	38.8	27.8	13.6	59.9	25.4	2.5	70.6	20.8
Carbonates (%)	1.2	40.3	25.5	-*	-*	-*	0.0	0.8	0.3
pH	7.0	7.6	7.3	4.1	6.0	5.1	4.4	7.5	5.8
TC (%)	0.1	4.9	2.8	0.1	7.5	1.3	0.0	6.4	0.6
Dry bulk dens. (g/cm³)	1.2	2.0	1.8	0.5	1.5	1.1	0.0	1.5	1.0
Hydr. conduct. (cm/h)	0.2	4.5	1.7	-	-	-	0.0	17.4	2.8
Liquid Limit (wL) (%)	26.5	51.5	38.9	-	-	-	27.5	77.3	52.6
Plastic limit (wP) (%)	16.8	38.5	21.6	-	-	-	21.2	57.9	37.8
Plasticity Index (%)	9.7	22.7	18.3	-	-	-	2.2	32.1	14.4

'-*' = method not applied due to negative pre-test; '-' = method not applied.

these shale deposits and therefore, of different origin than the remaining samples. Lopez-Infanzon (1991) mentioned gray-colored clayey mudstone in the area of La Sombra, which corresponds well with the colors of these samples, however, they did not provide any further information. Consequently, there is no data on these sediments that could certainly confirm that these samples are related to this lithological unit, nevertheless, relative comparison with the other sample results strengthens the assumption that they are material of different origin, most probably related to sedimentary rocks and their weathered components (Rothe 2015, Wilde et al. 2017a). This assumption leads to a very important information on the disposition and enables to distinguish between two different layers. Meaning that the material assigned to **Group I** represents the underlying lithological unit. This corresponds well to previous findings, which allowed for the identification of a more compact layer underneath the material related to the slide mass (Wilde et al. 2017a, b). Moreover, the hydraulic conductivity is lower compared to Group III (Table 7-2). This could indicate that the material from Group I is less permeable, which would increase the susceptibility to sliding (e.g. Terhorst and Damm 2009, Damm and Terhorst 2010, Neuhäuser et al. 2012a, Prokešová et al. 2013).

Sampling of Group I and III mostly targeted sediments at large outcrops in order to capture sediments that are considerably below the original ground surface (with depths

of up to 20 m below ground surface). In contrast, **Group II** focused on near-surface samples in the range of 0.1 to 1.6 m below the ground surface (chapter 5), and therefore, mainly captured soils. Thus, in the context of lithological preconditions, Group II plays only a subordinated role, since the processes of the Capulín landslide go beyond the depth of soil profiles and soil characteristics are primarily important for the analysis of shallow landslides (e.g. Dietrich et al. 1995, Dou et al. 2015, Schilirò et al. 2019).

Group III includes the largest number of samples and even though they are relatively heterogeneous, as reflected by a wider range of values, they remain within a specific range and record no significant differences, which would allow for a separation into further groups based on the laboratory analyses (Table 7-2). Furthermore, field analyses reveal that most sampling locations of Group III consists of fine material mixed with rock fragments of different sizes and decomposition stages (Figure 7-2). This observation and the fact that the samples representing different landslide features, such as flanks and the slide mass, show no significant differences that would allow for a clear separation, supports the assumption that the source material consists of slope deposits, which already exhibit a certain heterogeneity (e.g. Turner 1996, Ehrlich et al. 2021). Jiménez Sánchez (2002) describes similar characteristics, where complex slides (especially the combination of slide and flow processes) occur at slopes with slope deposit overlying bedrock. Latter consists of sandstone and lutite and the slope deposits include different types of deposits, such as talus-colluvium and old landslides, with blocks of different sizes and over 50 % of fine sediments (Jiménez Sánchez 2002). This reinforces the assumption that the Capulín landslide occurred in slope deposits, which form the moderate to deep slopes in the study area.

Furthermore, **land use, especially** d**eforestation** represent an important preparatory factor, since vegetation has an impact on water availability at slopes and particularly treeless areas can increase landslide susceptibility (e.g. Vanacker et al. 2003, Knapen et al. 2006, Kamp et al. 2008, Mugagga et al. 2012, Neuhäuser et al. 2012a, b, Neuhäuser 2014).

The very steep areas of the slopes above the Capulín landslide record mainly forest-dominated vegetation and with decreasing steepness, agricultural- and grassland prevails (Figure 7-3). In latter area cultivation of coffee and other crops as well as livestock breeding prevails. Small forest areas are within this primarily agriculturally used region and mostly correspond to steeper slopes (Figure 7-3). Mainly below the road that crosses the lower part of the slope, a vegetation change begins and forest predominates, with few coffee

plantations (Figure 7-3). Thus, the majority of the landslide and the area above were cultivated and mainly treeless before the landslide occurred in 2013. This corresponds well with the observation of increased landslide activity in agricultural areas, including shrub- and grassland (e.g. Caballero et al. 2006, Kamp et al. 2008, Neuhäuser 2012a). In general, land-use change, especially deforestation poses a major problem in Mexico, which leads to an increasing susceptibility to landslides in the mountainous regions (Alcántara-Ayala et al. 2006, Caballero et al. 2006, Restrepo and Alvarez 2006, Alcántara-Ayala and Dykes 2010, López-García and Alcántara-Ayala 2012).

The most important anthropogenic activity, beside land use, is road construction (e.g. Nyssen et al. 2002, Highland and Bobrowsky 2008), which represents another crucial preparatory factor for the Capulín landslide. In the case of the Capulín landslide, a road cuts through lower parts of the slope (Figure 7-3). Similar situations are observable in the entire study area, where roads cut or run along landslides. In fact, seven of twelve mapped landslides are in close proximity to or intersected by roads (Figure 7-1). Anthropogenic interventions like these are problematic, especially when built in slope deposits as it is the

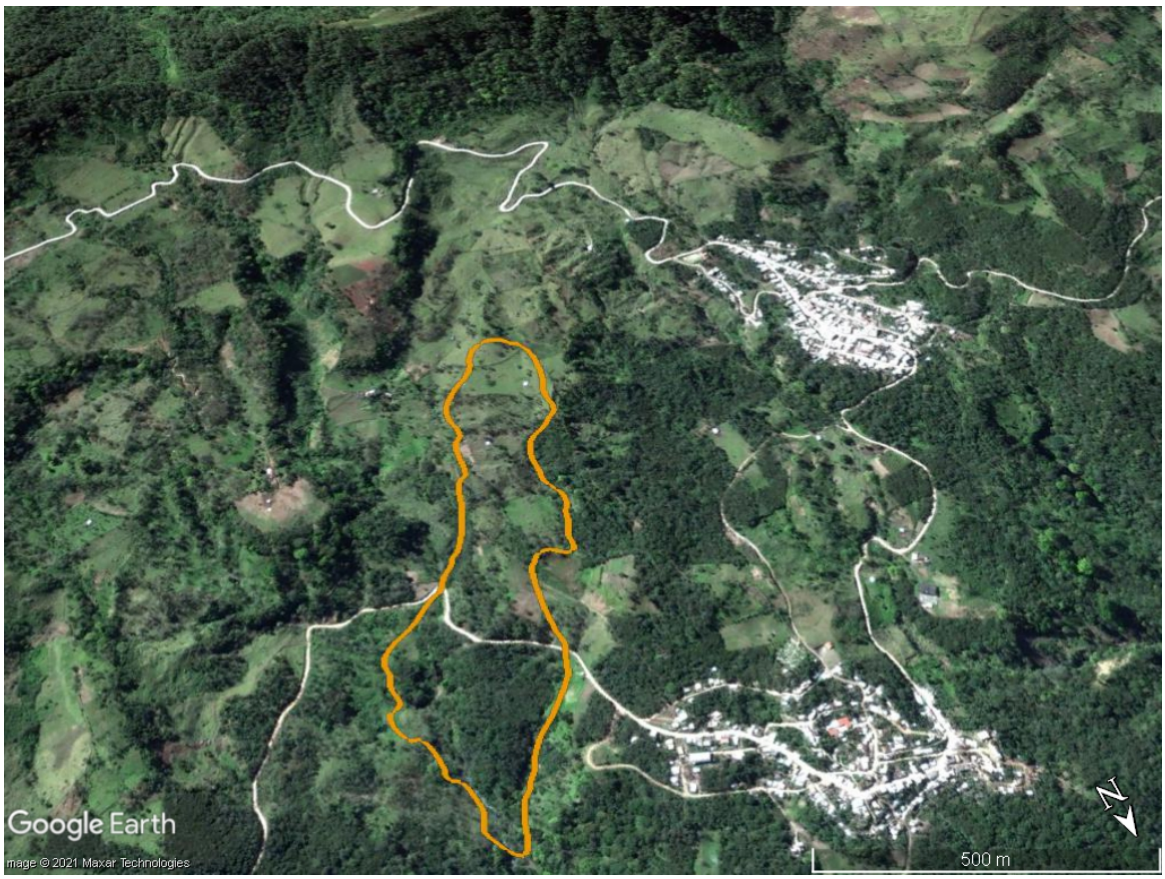

Figure 7-3. Satellite image from 2010. Outline of the present Capulín landslide marked in orange. Source: Google Earth Image © 2021 Maxar Technologies.

case in the study area. While these materials have a natural tendency to being unstable, road cuts additionally contribute to the instability, increasing the susceptibility to slope movements (e.g. Turner 1996, Zêzere et al. 1999, Ehrlich et al. 2021).

7.1.1.2 Trigger

2013 was a year of extreme precipitation events, with prolonged and intense rainfalls causing numerous landslides, not only in Mexico but in other countries, such as Italy, Germany, Norway and India, as well (e.g. Guzmán Lagunes and Morales Barrera 2014, Gupta et al. 2016, Devoli et al. 2018, Fleuchaus et al. 2021). In Mexico, Veracruz was one of the most affected states and especially the central part documented the most landslides within the state (chapter 1; Guzmán Lagunes and Morales Barrera 2014). In September 2013, the month before the Capulín landslide occurred, the meteorological station in Acatlán (closest station to the study area) recorded a precipitation of over 550 mm (22 % of the annual precipitation), which is more than twice as high as the mean monthly precipitation for September (252 mm between 1981 and 2010; Figure 7-4). Thus, during the ten days (21.- 30.09.2013) preceding the landslide event, with 223 mm the Acatlán meteorological station recorded almost the same amount of precipitation as the mean precipitation value for September (Figure 7-5). Figure 7-4 shows that the year of 2013 stands out and the years before and after as well as the mean monthly precipitation are significantly below the values for 2013. This highlights the extreme nature of this year with an unsually high number of hurricanes and other storms in Veracruz and Mexico (cf. chapter 2, Blake 2014). These long-lasting rainfalls in September, which are connected to the cold front No. 1, lead to a rise in the water level of the streams in this region as well (Guzmán Lagunes and Morales Barrera 2014). The meteorological station at Acatlán did not record any precipitation the day the landslide occurred, however, inhabitants of the El Capulín village reported rainfall in the area where the landslide occurred. Thus, it is most likely that the extreme and long-lasting rainfalls that preceded the event are the main factor that triggered the Capulín landslide (Guzmán Lagunes and Morales Barrera 2014, Ramírez-Herrera and Gaidzik 2017). Due to the lack of discharge data from the stream located at the foot of the landslide, it is not clear, which role the water level rise of the stream played, causing erosional processes at the foot area. However, farmers from the Village El Capulín registered first movements in the lower parts of the slope. Therefore, it cannot be excluded that a combination of oversaturation of the slope material due to

intense rainfall and a water-level rise of the stream triggered the landslide event (e.g. Wieczorek 1996, Zêzere et al. 1999, Deng et al. 2017, Wang et al. 2020). A very similar event occurred in the west of Mexico, only few days earlier (16.09.2013), where a rainfall event of four days, causing oversaturation of soil, triggered a landslide of a similar type (Ramírez-Herrera and Gaidzik 2017). Furthermore, comparable precipitation conditions occurred in the case of the San Juan Grijalva landslide, one of the largest landslides of Mexico, which occurred in 2007 after a 30 day-long rainfall period, with over 67 % of the average annual rainfall (Hernández-Madrigal et al. 2011).

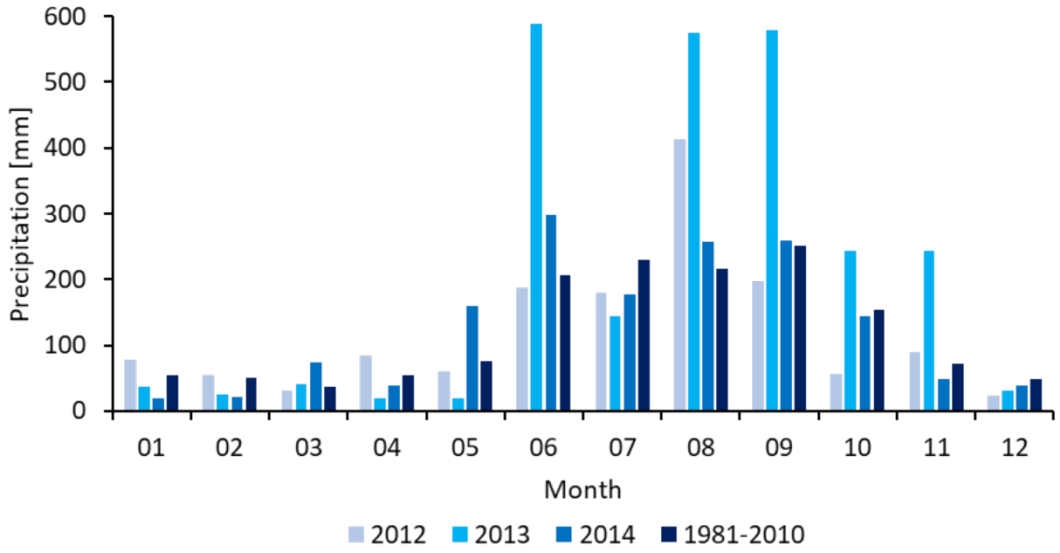

Figure 7-4. Accumulated monthly precipitation at Acatlán, for the years of 2012, 2013, 2014 and the mean monthly precipitation from 1981 to 2010. Source: SMN (2020a, b).

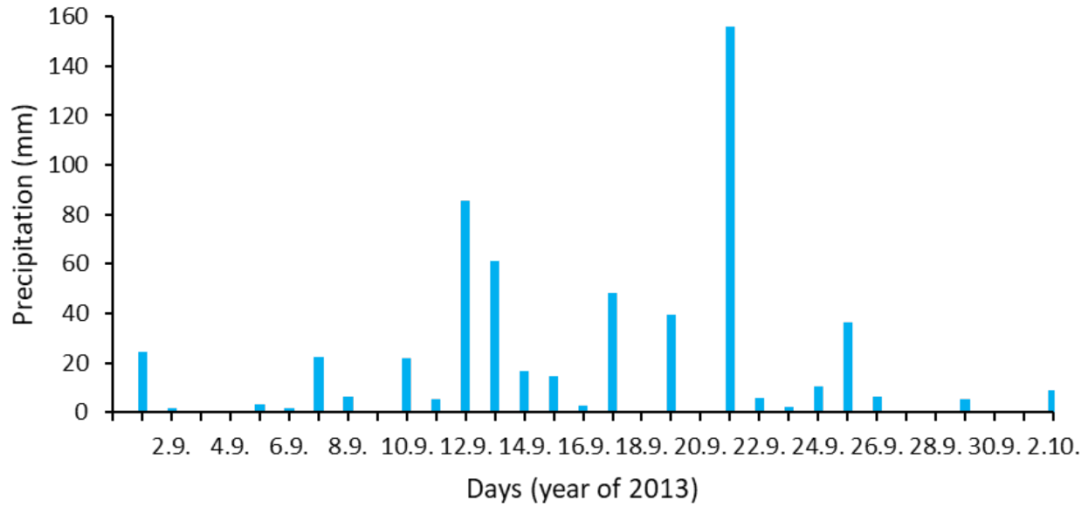

Figure 7-5. Daily precipitation at Acatlán, for the year of 2013. Source: SMN (2020b).

7.1.1.3 Landslide characterization and type classification

The analyses of **activity state**, **velocity**, **water content**, **material** and **type** allow for the classification of the process type (e.g. WP/WLI 1993, Cruden and Varnes 1996, Hungr et al. 2014). These components are discussed in the following sections.

Activity state and movement process

For the activity assessment, it is crucial to distinguish between an active and a dormant state as well as between a first-time and reactivated process (WP/WLI 1993, Cruden and Varnes 1996, Corominas et al. 2014). This determination is an important contribution to the evaluation of landslide susceptibility as it provides crucial information on the type and spatial distribution of activity that has to be expected (e.g. WP/WLI 1993, Temme et al. 2020).

When evaluating the current activity state, the post-event DoD (2013/2016) detected changes in only approx. 30 % of the landslides area (differences of max. +/- 15 m) and the remaining 70 % fell below the threshold (< +/- 2.98 m, chapter 4.4.3). These changes are mainly linked to surficial processes of erosion and weathering (Varnes 1978). Thus, based on the present data the Capulín landslide classifies as active. However, with the available data, the differentiation between an active movement of the entire landslides (not only surficial processes) and a dormant state is not entirely possible and would require further analyses such as inclinometer measurements (e.g. Stark and Choi 2008, Nikolakopoulos et al. 2017, Eker et al. 2018).

In order to further differentiate the activity state into a first-time movement and a reactivated state, it is required to consider the pre-event slope conditions (e.g. Cruden and Varnes 1996, Van den Eeckhaut 2007a, Corominas et al. 2014, Temme et al. 2020). In this context, the hillshade analysis of the study area gives evidence of a former and larger landslide (no. 3a) in close connection to the recent Capulín landslide (no. 3b; Figure 7-1, chapter 4.1). The hillshade from 2011 represents the surface of landslide no. 3a (marked in black) and in order to spatially relate the former and the recent slide, the extent of the Capulín landslide is marked in orange (Figure 7-6). Figure 7-6/1 shows that the Capulín landslide (no. 3b) is almost completely within the former landslide (no. 3a). The scarp of landslide no. 3a is approx. 300 m above the recent scarp and with a maximum width of 400 m, it is slightly broader than the scarp of the Capulín landslide, which has a width of

300 m (Figure 7-6/1). The foot area of no. 3a, however, is slightly smaller (250 m) and consequently the foot of the recent landslide, with a width of approx. 300 m, extends beyond the former foot area (Figure 7-6/1).

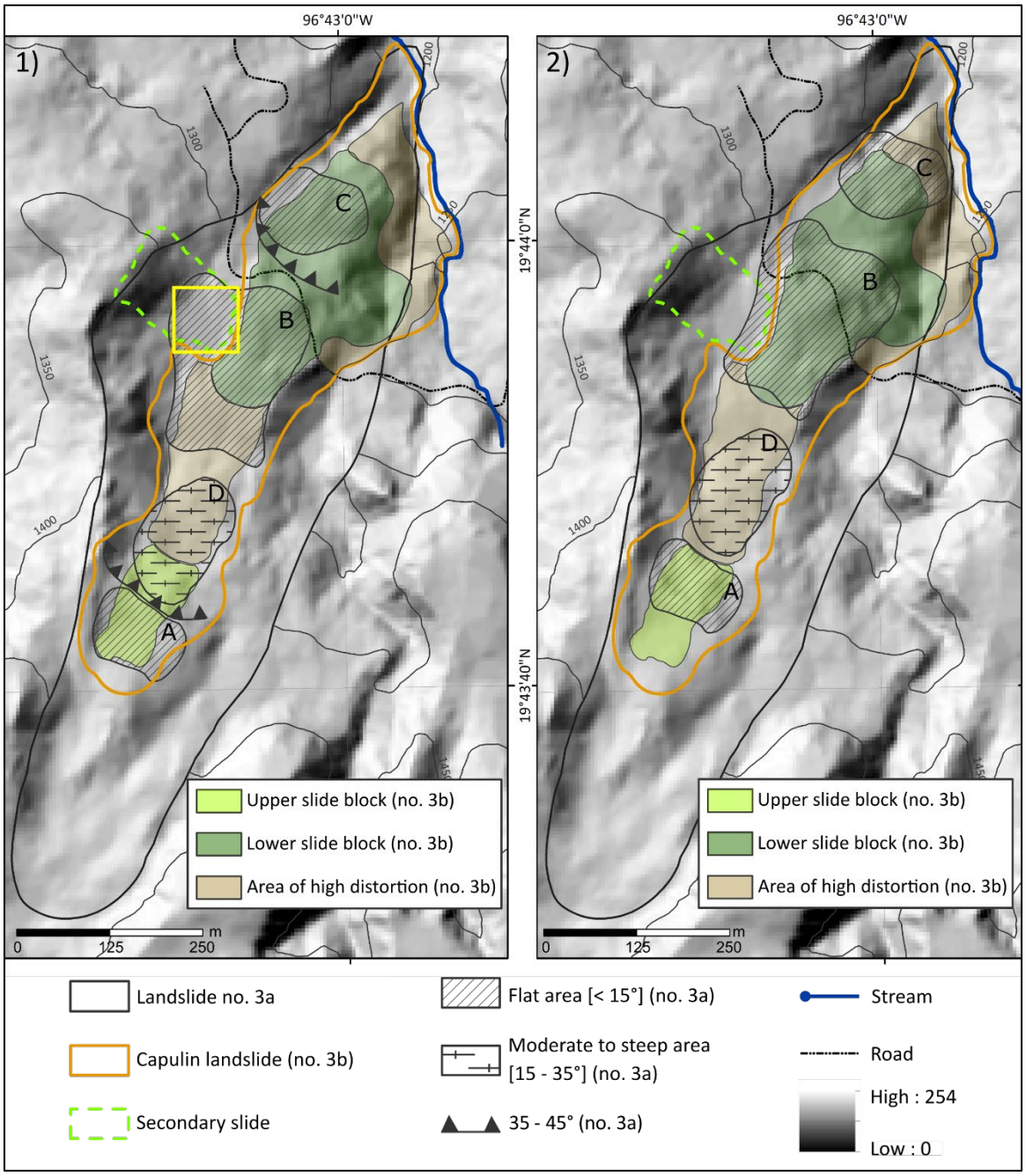

Figure 7-6. Extension of the former landslide (no. 3a) including significant features such as flat (area A - C), moderate to steep areas (area D), and steep slopes (line signature). Extension and elements of the Capulín landslide (no. 3b) marked in color. Estimated location of the pond marked in yellow (1)). 1) Elements based on the 2011 hillshade. 2) Areas A to D are shifted downward in northeast direction by approx. 75 m. Source of Hillshade: INEGI (2019). Own illustration.

In addition, the hillshade from 2011 (INEGI 2019) allows to identify some distinct geomorphological forms of landslide no. 3a, which are concentrated in the same area where the Capulín landslide occurred later (Figure 7-6/1). First, there is a relatively flat area (< 15°) with a length of max. 100 m and a width of 130 m, approx. 40 m below the recent scarp of the Capulín landslide (area A, Figure 7-6/1). This area is limited by a steep inclined slope (35 - 45°), followed by a moderate to steep area with a maximum length of 180 m (area D Figure 7-6/1). Below latter area (D) a less inclined area (< 15°, area B) begins, which has a width of 190 m and a length of 250 m and therefore, is slightly larger than area A (Figure 7-6/1). The last area (C) follows after another steep step and is similar in extent to area A (130 wide, 120 m long, Figure 7-6/1).

A comparison of the geomorphological elements of the former (no. 3a) and the recent (no. 3b) landslides demonstrates that both share common features (Figure 7-6/1, 2). The main elements of the Capulín landslide are an upper and a lower slide block, and steeper areas of high distortion, located between the two slide blocks and in the foot area (Figure 7-6/1, 2). Shifting areas A to D approx. 75 m downslope in a northeasterly direction shows that there is some connection between the two landslides (Figure 7-6/2). Area A corresponds well to the upper slide block, area D has almost the same position as the upper area of high distortion from the Capulín landslide. Furthermore, areas B and C can be well associated with the lower slide block (Figure 6/2). Consequently, this would mean that during the 2013 event (landslide No. 3b), landslide blocks originating from the former landslide (No. 3a) moved downslope about 70 to 80 m to the northeast. Reactivation of old landslide material, especially slide blocks, as it is the case for the Capulín landslide, is a common phenomenon occurring in different regions of the world, demonstrating the need to map old landslides to better assess the occurrence of landslides (e.g. Zêzere et al. 1999, Terhorst 2001, Van den Eeckhaut et al. 2007a, Terhorst and Kreja 2009, Temme et al. 2020).

Further indications of a slope being affected by landslides include signs of disturbed hydrology such as water logging and ponds (e.g. Cruden and Varnes 1996, Terhorst 2001, Terhorst and Kreja 2009). Latter were present before the landslide event in 2013 as well. A satellite image from 2010 recorded a small pond in the area of the former landslide (chapter 4.1), which may indicate that the hydrology was disturbed and water partially logged due to the slide mass (Figure 7-6). Thus, this pond could be an additional evidence of the former landslide as its occurrence is typical for landslide areas (e.g. Varnes 1978, Cruden and Varnes 1996, Terhorst and Kreja 2009). However, it is not possible to exclude

the possibility that the pond is of anthropogenic origin, since there are no information on its formation available. Local farmers stated that the pond was several meters deep (rough estimation), which is a sign that the water in the pond at least remained in a natural way. However, the data basis is not sufficient to reach a conclusion about the ponds origin. On the one hand, in case it was naturally formed, this could mean that the slope hydrology was somehow disturbed (e.g. Varnes 1978, Terhorst 2001, Geertsema and Pojar 2007, Terhorst and Kreja 2009). On the other hand, if it was of anthropogenic origin, there would be no clear evidence of disturbed hydrology as additional water logging was not reported and also not visible in satellite images. Nonetheless, in both cases, the water of the pond had an influence on the movement, especially as ponds can lead to overloading, which could cause reactivation processes (e.g. van den Eeckhaut et al. 2007a, Temme et al. 2020).

In summary, based on the situation described above, a first-time movement of the Capulín landslide is highly unlikely and thus, the overall activity is considered (and hereafter referred to) as ***reactivated*** (Corominas et al. 2014). Nevertheless, it cannot be ruled out that the Capulín landslide is currently dormant.

Velocity and water content (at the time of the movement/event)

According to the classification of Cruden and Varnes (1996) the velocity of the Capulín landslide ranges between '***rapid***' (1.8 m/h) and '***very rapid***' (3 m/min; Guzmán Lagunes and Morales Barrera 2014). This range of values is typical for rotational and translational slides, since their typical motion velocities largely overlap (Highland and Bobrowsky 2008).

The photographs taken one day after the Capulín landslide occurred reveal a spatial differentiation of the water content within the slide mass and allows for the differentiation between ***wet*** and ***very wet conditions***. Most of the landslide area experienced wet conditions as evidenced by numerous areas of standing water (Figure 7-7a), which is typical for wet conditions (Varnes 1978, Cruden and Varnes 1996, Guzmán Lagunes and Morales Barrera 2014). Very wet conditions, which are characterized by flow-type movements were present at the lower western flank and the foot area (cf. Figure 7-7b, chapter 4.1). In this case, the estimation of the water content during the movement process is based on the photos taken directly after the event. However, in order to accurately assess the water content in the landslide material, it would be necessary to carry out further

analyses. For example, Jäger et al. (2014) applied micromorphological studies, which allowed to differentiate between wet and dry conditions within the landslide sediments.

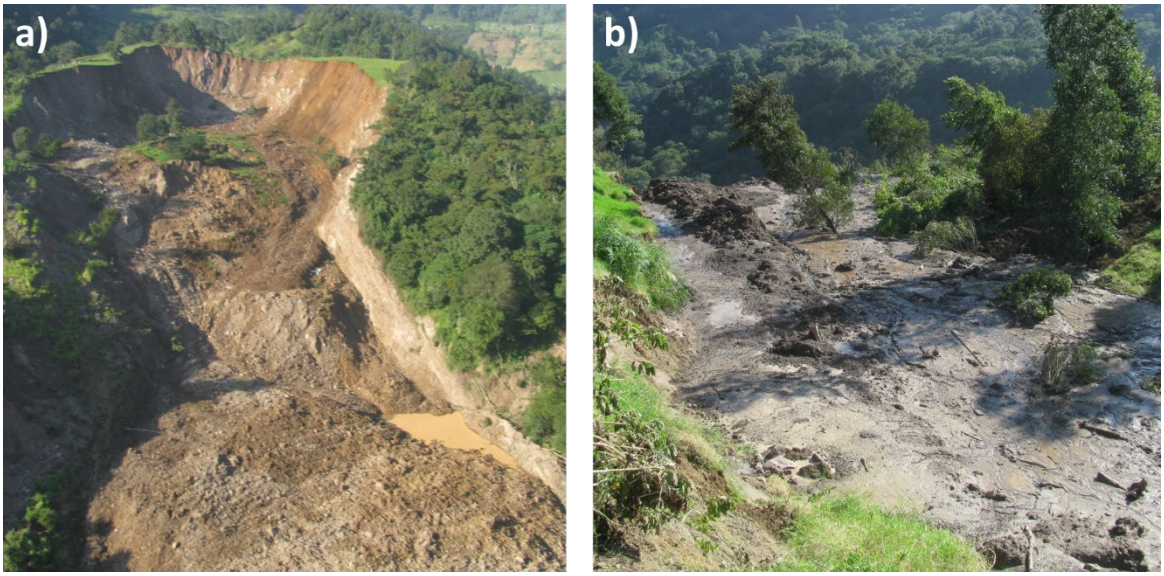

Figure 7-7. a) Upper area of the Capulín landslide with standing water at the western flank. b) Flow-movements at the western flank of the Capulín landslide. Photographs: S. Rodríguez Elizarrarás, 2013.

Material

For the definition of the landslide material, the common classification differentiates between rock, debris and earth, where debris contains 20 to 80 % of coarse material and the class 'earth' requires over 80 % of fine material with a size of less than 2 mm (Varnes 1978, Cruden and Varnes 1996, Highland and Bobrowsky 2008). This is a highly generalized definition of material and does not consider detailed information, nevertheless, it represents important additional information that helps to distinguish processes on an objective basis.

In the case of the Capulín landslide, the determination of the material class is mainly based on field observations as the laboratory analyses focused on the fine sediments (< 8 mm). The photographs of the scarp and slide mass demonstrate that large rocks (> 10 cm) and boulders reduce the overall dominance of fine material, which leads to assigning the '***debris***' instead of 'earth' classification (Figure 7-8a, b; Varnes 1978, Cruden and Varnes 1996). Nonetheless, fine material clearly prevails in areas with flow-type processes, which are located especially at the western flank and the toe area and thus classify as '***earth***' (Figure 7-7b, cf. chapter 4.1, Cruden and Varnes 1996).

Figure 7-8. Photographs of the scarp (a) and slide mass (b) of the Capulín landslide. Source: Own photographs (2018).

Type characterization

The complete identification of the mass movement type requires the consideration of the main landslide features, such as scarp, flanks, slide mass, foot, slip surface as well as volume, and areas of erosion and accumulation in general (cf. chapter 1).

The Capulín landslide is a deep-seated landslide with the sliding surface depth exceeding 28 m (e.g. Wieczorek 1996, Korup 2006, Kaunda 2010). Considering the areas of erosion and accumulation, the DEM of Difference (DoD) of the DEMs 2016 and 2011 (DoD 2016) reveals an unequal distribution, where the area of erosion (62 %) prevails the area of accumulation (38 %, chapter 4.4.2). Additionally, the volumes estimated based on the DoD record the same distribution (erosion 63 %, accumulation 37 %). This is particularly interesting as the accumulation area usually accounts for the larger proportion in sliding processes (e.g. Varnes 1978, Chen et al. 2006, Liu et al. 2021). Similar distributions to the Capulín landslide are recorded in comparable case studies (Eker et al. 2018), and e.g. Prokešová et al. (2010) determined a rather identical unequal distribution in a landslide in Slovakia, with similar volumes of depletion (64 %) and accumulation (36 %). Corsini et al. (2009) and Prokešová et al. (2010) state that the uneven distribution could be due to natural (e.g. erosion in the accumulation area) or artificial processes (e.g. artificial compaction), nevertheless, errors due to the methodological approach must be considered as well. In this context, assuming that the vegetation residuals are responsible for an unequal

distribution in the DoD 2016, the DoD 2013 should have a better equal distribution as the DEM 2013 had less vegetation. However, this is not the case since the area of erosion (82 %) exceeds the area of accumulation (18 %) in the DoD 2013 as well (cf. chapter 4.2). Thus, even though the methodological aspect is a plausible cause and the analyses in the present work show that vegetation filtering is still highly error-prone (cf. chapter 4.2), this is unlikely to be the only explanation in the case of the Capulín landslide (Prokešová et al. 2010).

Additionally, the calculations of the different pre- and post-event volumes (chapter 3.1.5, 4.6) provide further indications of the uneven distribution of erosion and accumulation. Considering the different calculated volumes, it is evident that the values of the pre-events (4.2×10^6 - 4.4×10^6 m^3) exceed those of the post-events (1.8×10^6 - 3.9×10^6 m^3, chapter 4.6). A critical view on this phenomenon requires a detailed discussion at this point, as among others, Cruden and Varnes (1996) as well as WP/WPLI (1990) state that swelling of the sliding material causes an increase in volume as the material becomes less compact. In this context, the conditions of the Capulín landslide are of major importance. Since the post-event volume is smaller, a possible explanation is that originally, the parent material had a low compactness resulting in a limited expansion. Swelling is typical especially for rock slides, where the bedrock transforms into debris and consequently expands in volume, but occurs in other movement types as well (Varnes 1978, Parise and Guzzi 1992, Claude et al. 2014). Liu et al. (2021) analyzed a reactivation process in loess with contact to mudstone where the landslide had a swelling of 10 %, which is clearly lower than reported from bedrock (> 25 %; Parise and Guzzi 1992, Nicoletti and Parise 1995, Cruden and Varnes 1996, Hungr and Evans 2004, Claude et al. 2014). As mentioned above, in the case of the Capulín landslide, the parent material most probably consists of slope deposits and major parts of the slide mass moved as a coherent mass (slide block) with little defragmentation. Consequently, swelling or general volume increase would probably be less than in bedrock as well (e.g. Skempton and Hutchinson 1969, Liu et al. 2021).

A further important aspect, which could explain the imbalance of the pre- and post-event volumes, is erosion of the accumulated material. Photographs of the Capulín landslide, taken one day after the event, show that the stream at the foot of the slope transported material (Figure 7-9). In addition, continuing erosional processes at the foot of the landslide have a retrogressive and steepening effect as shown by the cross section of the DEM 2013 and 2016 (Figure 7-10). Here, the surface line of the DEM 2016 records a steeper

slope and reaches below the surface line of the DEM 2013, indicating that the stream cut into the landslide foot and consequently eroded material in this area (orange square, Figure 7-10). Thus, these erosional processes could be another explanation for the pre-event volume being larger than the post-event volume (Bichler et al. 2004, Deng et al. 2017, Wang et al. 2020).

While the erosion and accumulation areas as well as the volume already provide important information, a close look at the individual landslide components provides additional information, which allows for the complete identification of the landslide type.

Figure 7-9. Stream cutting through the slide mass at the foot area of the Capulín landslide. Photographs: S. Rodríguez Elizarrarás, 2013.

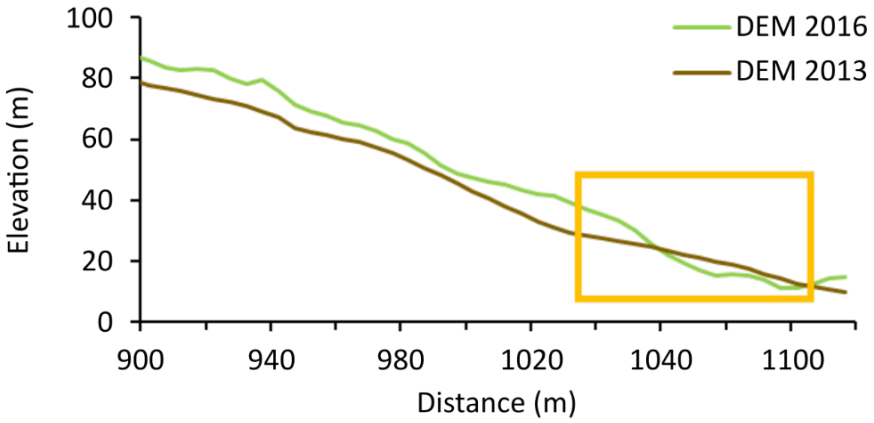

Figure 7-10. Part of the cross sections of the DEMs from 2013 and 2016, showing the toe area (orange box). Source: Own illustration.

A detailed consideration of the landslide features reveals the complexity of the Capulín landslide, which comprises components from different process types (Figure 7-11). Particularly noticeable is the presence of both slide and flow processes. The slide processes account for the majority of the landslide area and the flow processes are mainly present at the lower western flank and the foot (Figure 7-9, 7-11). The two large slide blocks within the slide area are of special interest as they not only differ in size but also have different characteristics.

The **upper slide block** is, with a width of 90 m wide and a length of 170 m long, the smaller one of the two slide blocks (Figure 7-11). The steep (> 45°) scarp surrounds the upper slide block in a semicircular form, whereas the surface of the block has inclinations below 10° (Figure 7-11). Original vegetation, which remained vital after the movement, and the slight backwards tilting of the slide block indicate that this part of the landslide moved as a coherent mass with little internal deformation and a rotational motion (chapter 4.1, e.g. Cruden and Varnes 1996, Miller and Cruden 2002, Highland and Bobrowsky 2008). Furthermore, with a max. depth of 47 m and a length of 160 m, the upper slide block has a depth to length ratio of 0.3, which is in the upper end of the typical range of rotational landslides (0.15 to 0.33; Varnes 1978, Cruden and Varnes 1996, Highland and Bobrowsky 2008). Additionally, water logging is present in the western part of the slide block, indicating a disruption of the drainage system, which is common for rotational movement processes (Figure 7-11, Varnes 1978, Cruden and Varnes 1996, Link 1997, Terhorst 2001, Geertsema and Pojar 2007).

The **lower slide block** is considerably larger (240 m wide and 380 m long) than the upper slide block (Figure 7-11). Various observations indicate that this mass also moved as a coherent mass without strong internal deformation. For example, vegetation within the lower slide block, such as trees and coffee plants, are mostly intact and nearly unaffected by the movement (chapter 4.1). Underlining the relevance of undisturbed vegetation, a rather well-preserved soil occurs in the slide mass (M 6), reflecting high similarities to a second soil profile (SA 2) situated on top of the scarp. The slope-parallel slip surface further contributes to the assumption that this block moved as a coherent mass in a translational motion. Furthermore, with a max. depth of 43 m and a max. length of 380 m, the lower slide block has a depth to length ratio of 0.1, which is in the upper end of the typical range of translational landslides, which usually is not above 0.1 (Skempton and Hutchinson 1969, Cruden and Varnes 1996, Laberg and Vorren 2000).

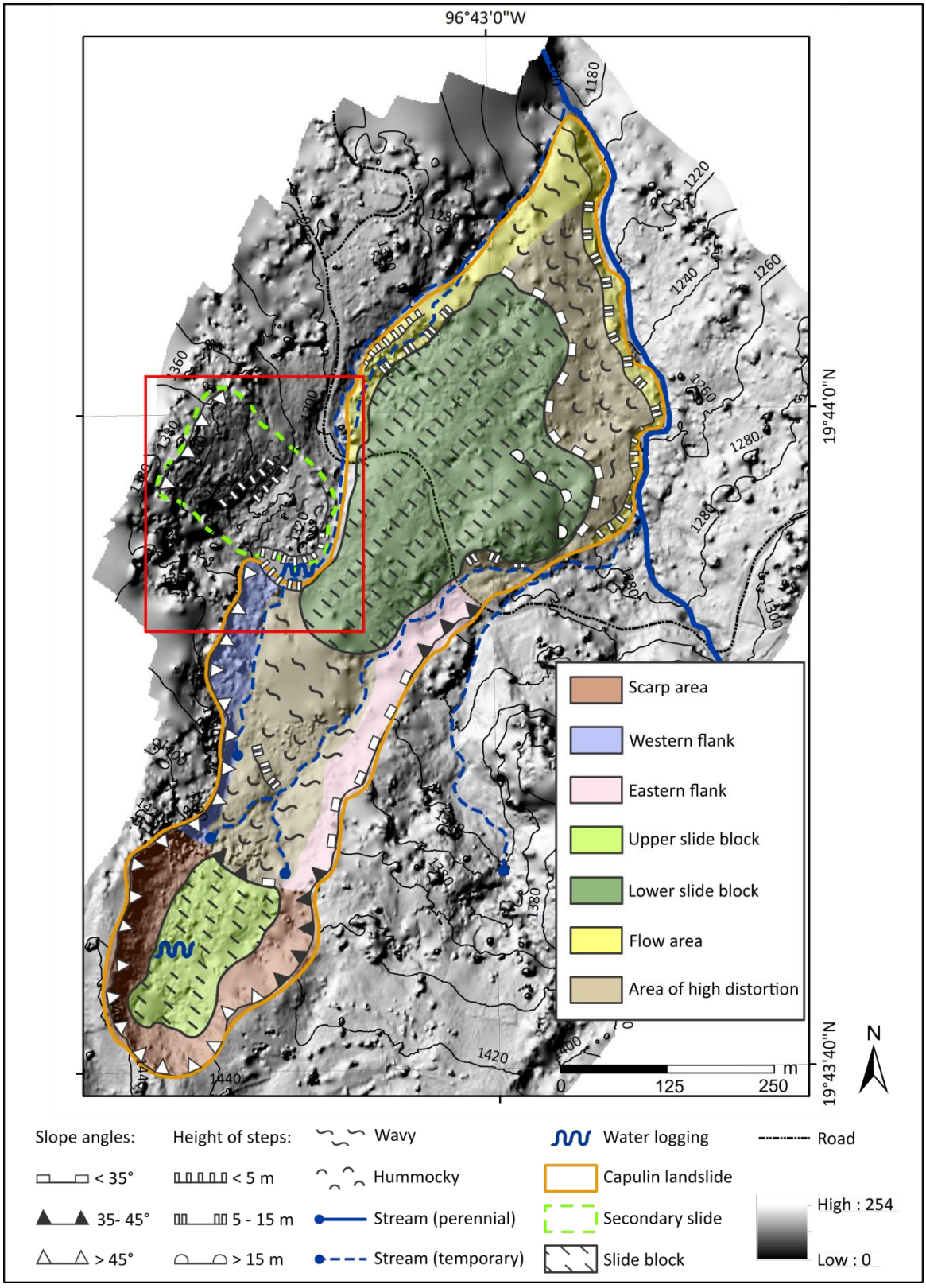

Figure 7-11. Geomorphological map of the Capulín landslide with the different process regions. Red square see Figure 7-13. Source of geomorphological symbols: modified after Terhorst (1997), Leser et al. (1975). Source: Own illustration.

With the upper slide block being related to rotational and the lower slide block to translational movements, the slide process within the Capulín landslide classifies as a compound slide (Skempton and Hutchinson 1969, Varnes 1978, Cruden and Varnes 1996, Zêzere et al. 1999, Chelli et al. 2006). de Bari et al. (2011) and Ramírez-Herrera and Gaidzik (2017) describe landslides with similar characteristics, where a combination of rotational- and translational processes occurred.

Between these slide blocks there is an area of high distortion (deformation), mainly characterized by exposed, unsorted material and a vegetation free surface (Figure 7-11, 7-12). These areas of high distortion are characteristic for compound landslides and usually occur between the rotational- and translational blocks, as it is the case for the Capulín landslide (Skempton and Hutchinson 1969). Compound landslides typically occur in weathered material and slope deposits in general overlying argillaceous layers (Zêzere et al. 1999, Jiménez Sánchez 2002). With regard to the Capulín landslide, this supports the assumption mentioned above that shales underlie slope deposits.

As previously mentioned, besides the sliding features, the Capulín landslide experienced flow movements as well, especially at the western flank and the foot area (Figure 7-9, 7-11). While the presence of the stream could be a possible explanation for the high water content

Figure 7-12. Area of high distortion between the two slide blocks of the Capulín landslide. Upper part of the lower slide block, including intact trees, is at the lower right corner of the photograph. Source: Photographs: S. Rodríguez Elizarrarás, 2013.

and the resulting flow-type movement at the landslide foot, it does not explain the high amount of water at the western flank. However, a closer look at the conditions before the landslide occurred provide information that can explain the water availability in this area. Figure 7-13a shows that the main and secondary slide masses surround a relative plane area. Water logging and a stream running between the different slide masses characterize this plane surface (Figure 7-13a). Furthermore, the satellite image from 2010 shows a pond with a maximum width of 50 m and a length of approx. 90 m (Figure 7-13b).

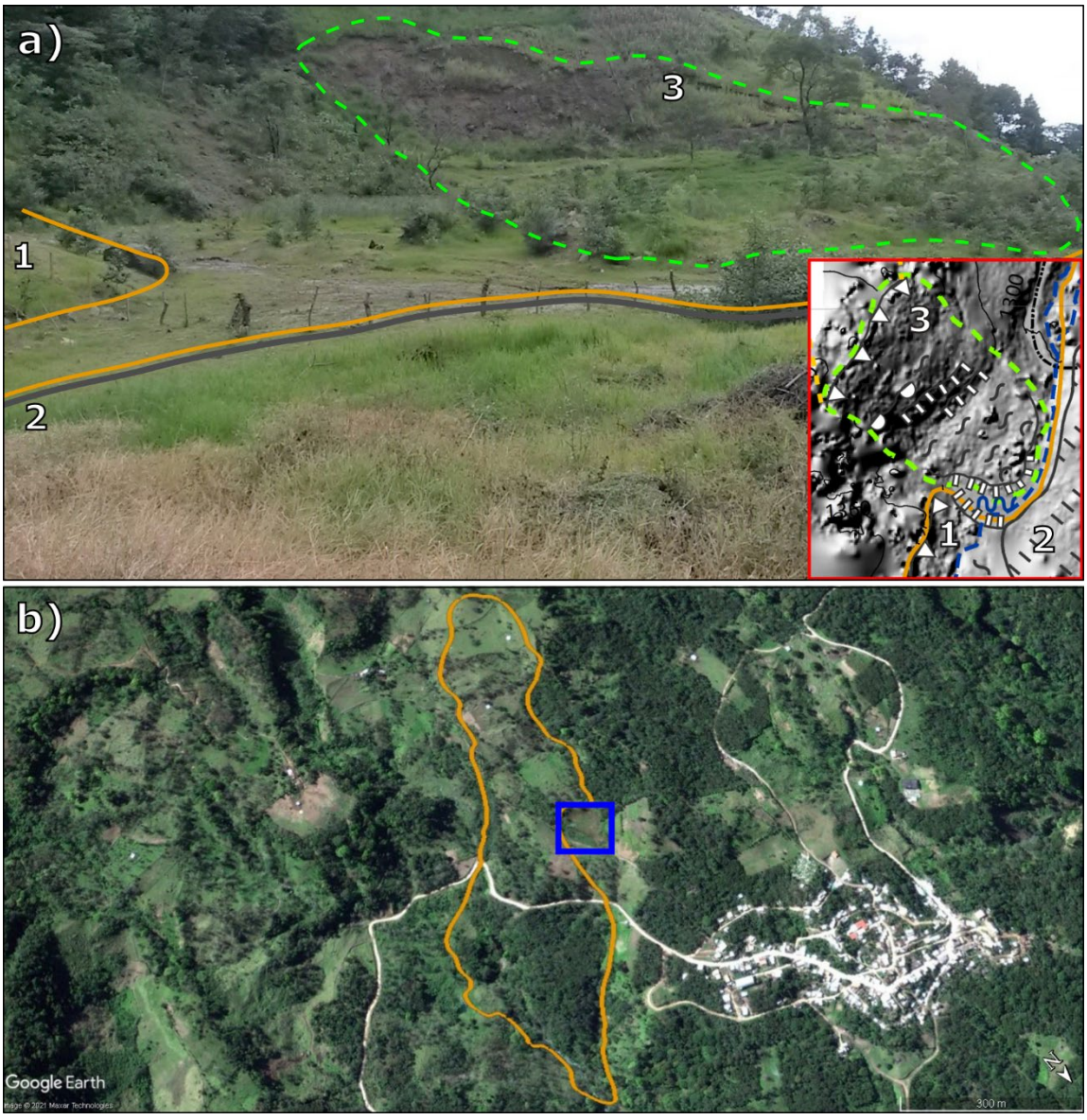

Figure 7-13. a) Photograph of the secondary landslide and the primary slide mass. 1 = upper slide mass; 2 = north-western margin of the lower slide block, 3 = extent of the secondary landslide (dashed green line). Red square: geomorphological map with underlying hillshade from 2016 corresponding to the photograph; location marked in Figure 4-1. b) Satellite image from 2010. Outline of the present Capulín landslide marked in orange and the location of a former pond in blue. Source: Google Earth Image © 2021 Maxar Technologies, own photograph (2016).

The location of this pond roughly coincides with this area and simultaneously corresponds to the section where the flow movement initiated in 2013 (Figure 7-11). A possible scenario is that during the landslide event, the water got released from the pond and thus, the high amount of water caused flow movements along the western flank of the Capulín landslide.

Consequently, with this additional type the Capulín landslide represents a complex mass movement, which is classified as a compound slide flow (Varnes 1978, Cruden and Varnes 1996, de Bari et al. 2011, Ramírez-Herrera and Gaidzik 2017).

Concluding landslide classification of the Capulín landslide

Summarizing all landslide characteristics from the previous sections and following the common classification of Cruden and Varnes (1996), the Capulín landslide classifies as a *reactivated, rapid to very rapid, wet, compound debris slide - very wet earth flow* (Table 7-3). Especially the combination of slide and flow types is a common phenomenon and was already subject in different case studies (e.g. Skempton and Hutchinson 1969, Varnes 1978, Cruden and Varnes 1996, Terhorst 1997, Terhorst 2001, Nikolaeva et al. 2014, Ramírez-Herrera and Gaidzik 2017).

Table 7-3. Overview of the individual properties, leading to the identification and classification of the Capulín landslide according to Cruden and Varnes (1996).

Activity state	Velocity	Water content	Material	Type
Reactivated	Rapid to very rapid	Wet (slide), very wet (flow)	Debris (slide), earth (flow)	Compound slide flow

7.1.2 Methodological approaches

Within the site-specific analysis approach, an important objective was to develop a methodological concept, including a variety of different geomorphological and UAV-based remote sensing methods, which allows for a detailed landslide characterization (Bichler et al. 2004, de Bari et al. 2011, Ausilio and Zimmaro 2017). Figure 7-14 provides an overview of the applied methods and the topic to which they have contributed. The following sub-chapters analyze and evaluate the suitability, strengths, and weaknesses of the applied geomorphological methods. The discussion of the methods related to the modeling approach is in chapter 7.2.

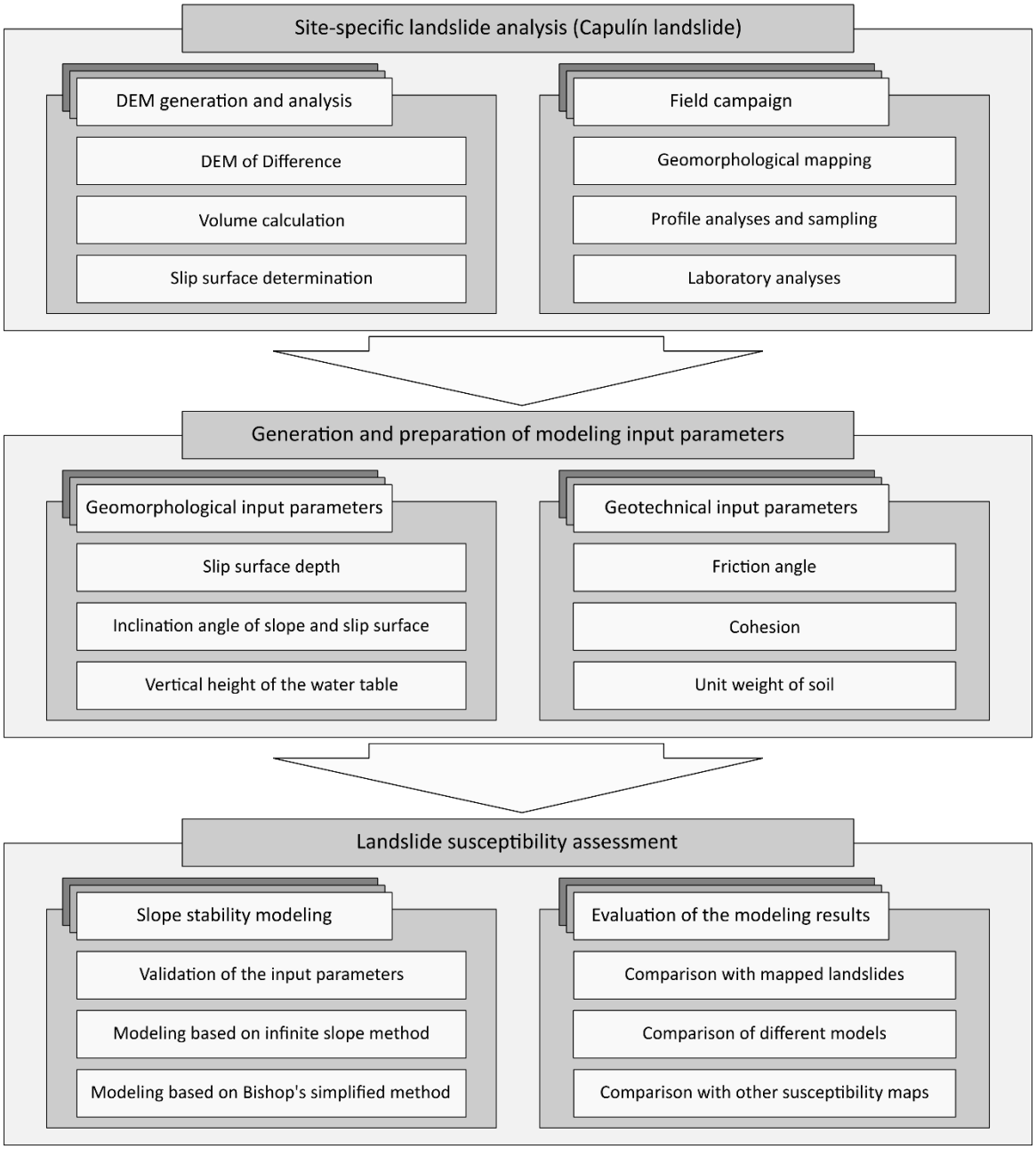

Figure 7-14. Overview of the applied methods and their relation to the main topics of the study. Source: Own illustration.

7.1.2.1 Digital elevation model generation

Digital elevation models play a key role in geomorphological investigations and specifically in landslide research (e.g. Guzzetti et al. 2012, Micheletti et al. 2015, Wilson 2012, Hugenholtz et al. 2013). In particular, post-event DEMs are essential to characterize landslide features and to carry out further analyses such as DoDs (Jaboyedoff et al. 2012, Eker et al. 2018, Mora et al. 2018). In the present work, the generated post-event DEM

essentially supported the results from field observations and contributed to the creation of the geomorphological map (Figure 4-1, chapter 4).

A possibility to generate DEMs is the photogrammetric approach, which usually is based on photographs (mostly collected by UAVs) combined with Ground Control Points (GCPs) or archival imagery such as historical aerial photographs (e.g. Aguilar et al. 2013, Bakker and Lane 2017). This method became common practice in recent years and has the ability to produce high resolution DEMs (e.g. Smith et al. 2016, Mancini et al. 2017, Nikolakopoulos et al. 2017). Furthermore, it represents a cost-effective and highly flexible approach, which extends the applicability to areas with restricted access, e.g. due to steepness or hazardous environments like flood areas (Hashemi-Beni et al. 2018). And thus, represents a good alternative to DEMs derived from LiDAR data, which generally are more expensive and time-consuming (Hackney and Clayton 2015, Jiménez-Jiménez et al. 2021). Therefore, one goal of the present study comprises the generation of DEMs based on aerial photographs of the Capulín landslide. The resolution of the resulting DEM 2016 (UAV-data) reaches a maximum of 0.09 m/pixel, however, in order to consider the overall accuracy it is exported with a resolution of 1 m/pixel. Other studies achieved higher accuracies, but these results are generally obtained in sparsely vegetated or non-vegetated areas (e.g. Lucieer et al. 2014b, Hackney and Clayton 2015, James et al. 2017b). The corresponding hillshades from the DEM 2016 show that the accuracy is adequate for mapping the individual landslide elements (such as scarp, flanks, hummocky surfaces) and the level of detail allows for thorough geomorphological analyses and characterization (cf. Figure 7-11, Niethammer et al. 2012, Van Den Eeckhaut et al. 2007b, 2012). However, minor uncertainties, such as vegetation residuals, in the terrain model remain due to partly insufficient filtering (Figure 7-15, Anders et al. 2019). In the Digital Surface Model (DSM; Figure 7-15) dense vegetation is clearly visible, with higher vegetation at the margins and smaller coffee plants in the center. Cross section AB cuts directly through the coffee plantation (Figure 7-15a) and the hillshade based on the DTM 2016 (Figure 7-15b) shows the same section after removing the vegetation. Especially in the southern area, the filtering process is successful, since it removed most of the vegetated areas (Figure 7-15b). However, the cross section (Figure 7-15c) reveals that some residuals remain. In the first 10 m, the surface line appears relatively straight without significant elevations differences, which changes between 15 and 35 m (Figure 7-15c). Here, the DTM line has a similar pattern as the DSM line, which means that the vegetation removal was

not completely successful in this area. These residuals highlight the problem, which the photogrammetric approach faces when dealing with dense vegetation or other surface elements such as buildings (Anders et al. 2019). There are several methods to filter vegetation from DSMs, but since the quality of the results varies greatly, the filtering process is currently under research (Anders et al. 2019). In this work, the elaborated filtering process with the preliminary NDVI preparation appears to deliver the best results

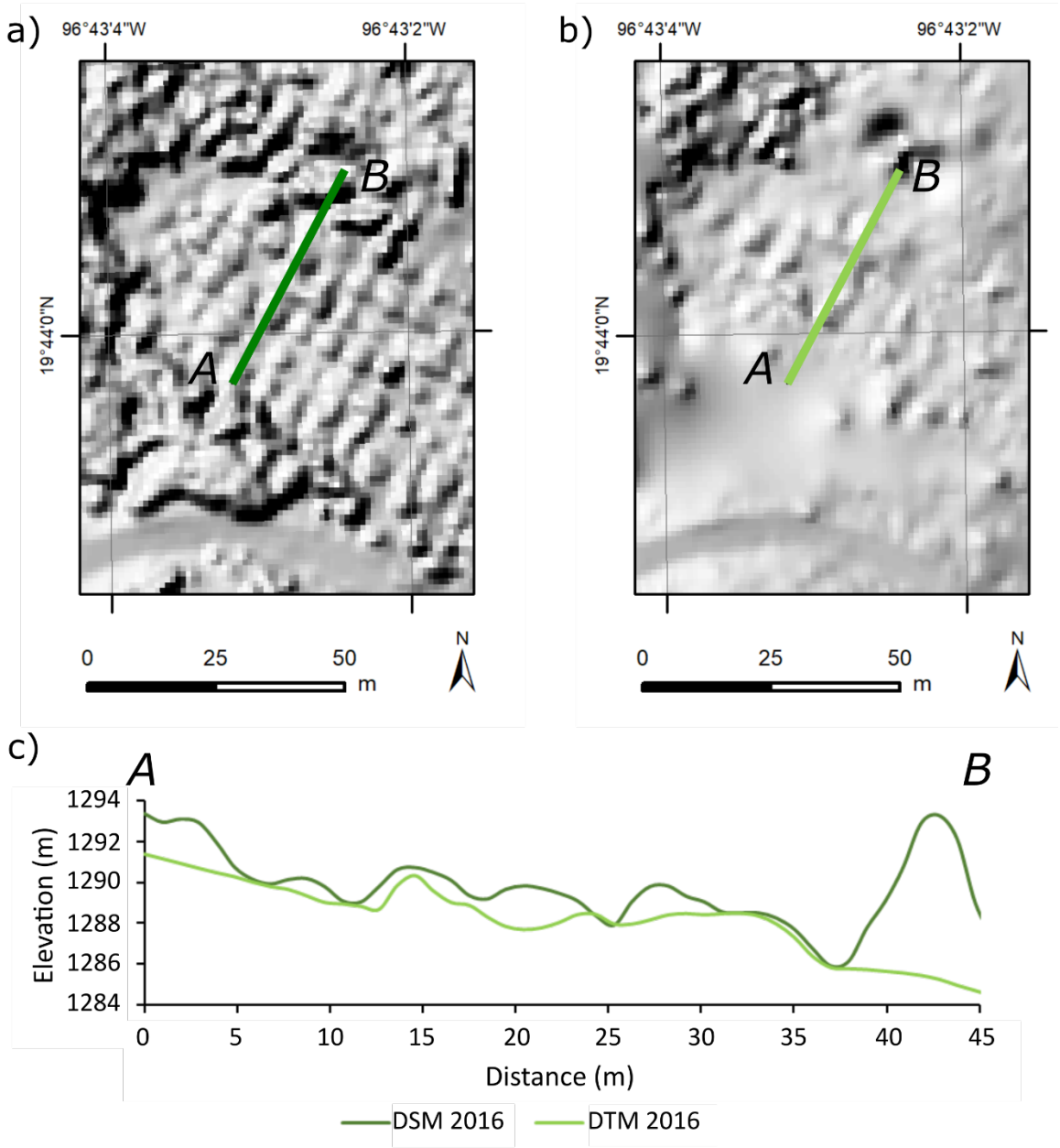

Figure 7-15. Exemplary excerpt of the hillshades from the Capulín landslide. Hillshade a) is based on the surface model (DSM 2016), showing the entire surface, including vegetation. Hillshade b) represents the terrain model (DTM 2016), showing that in this particular section the vegetation removal was not entirely successful, leaving some vegetation residuals. c) Cross section AB through the coffee plantation. Source: Own illustration.

as it classifies the majority of the dense cloud correctly, whereas the other classification systems showed high amounts of misclassification (chapter 3.1.1 and 4.2.1). Anders et al. (2019) also concluded that the classification alone, provided by programs such as Agisoft, is not sufficient in all cases. Furthermore, in order to handle the uncertainties of the filtering process, it is important to carefully examine their impact and to decide if they can be disregarded or not (James and Robson 2012). As for instance, the filtering residuals in this study, which usually are in the range of few meters, play a minor role related to the landslide volume (approx. 4×10^6 m³) and thus, are disregarded. However, in case the goal is to detect changes in the range of centimeters, the accuracy of this DEM is not sufficient as it would require accuracies of centimeters or even millimeters (Wheaton et al. 2010, Turner et al. 2012, Eltner et al. 2017, Glendell et al. 2017).

For the DEM 2013, it is not possible to achieve high accuracy as it is based on data, which did not originate from a photogrammetric survey. The usage of photographs without any camera position or calibration information is rather uncommon and related to various difficulties in the generation process (e.g. estimation of the GCP-positions), which resulted in a lower overall accuracy (chapter 4.2). In particular, missing GCPs lead to a lower resolution as they can essentially influence the DEM accuracy (Sanz-Ablanedo et al. 2018). Although the resulting resolution is at the lower end of spectrum, the DEM 2013 records a similar quality as the DEM 2016. Therefore, it is suitable for further applications and proves to be an acceptable approach (Hugenholtz et al. 2013). This finding is particularly important as it demonstrates that non-georeferenced photographs are applicable for DEM generation, in case GCPs are transferable to them.

In general, GCPs represent an important determining factor for improving DEM accuracy (e.g. James and Robson 2012, Eltner et al. 2016). A high number of GCPs and an even distribution considerably improves the accuracy (Harwin and Lucieer 2012, Smith et al. 2016, Oniga et al. 2018, Villanueva and Blanco 2019). Sanz-Ablanedo et al. (2018) stated that evenly distributed GCPs result in accuracy twice as good as irregularly distributed GCPs. By consequence, these measures require more fieldwork, which in many cases is hampered due to inaccessibility. However, the improvement of GCPs application still has high potential for research (Harwin and Lucieer 2012, Sanz-Ablanedo et al. 2018).

In summary, it can be stated that the accuracy of both DEMs is sufficient for the identification of morphological features, even though the accuracy is lower compared to other studies (e.g. Lucieer et al. 2014a, Fazio et al. 2019).

7.1.2.2 Applicability of DEMs of Difference

For the characterization of the Capulín landslide, the objective is to identify and analyze the areas of erosion (depletion) and accumulation (e.g. Cruden and Varnes 1996, Tofani et al. 2013). The applied analyses reveal that DoDs are a valuable tool for detecting deformation caused by landslides as they are capable to identify erosion and accumulation patterns and to estimate their volumetric changes (e.g. Demoulin 2006, Wheaton et al. 2010, Bossi et al. 2015, Mora et al. 2018, Altmann et al. 2020, Samodra et al. 2020). The main advantage of DoDs is that they allow for monitoring temporal surface changes over large areas and therefore, they represent a good alternative to GPS methods or other geodetic techniques, which usually are more elaborate and time-consuming (Prokešová et al. 2010). This possibility enables to determine the geomorphic changes for the entire Capulín landslide (chapter 4.4). However, when assessing DoDs, it is crucial to consider errors inherited from the DEMs (Lane et al. 2003, Wheaton et al. 2010, Williams 2012). The integration of thresholds allows for a clear differentiation between real changes and DEM errors (Wheaton et al. 2010, Williams 2012, Bangen et al. 2014, Vericat et al. 2017). This is especially important for the present study, as the applied DEMs originated from different sources with varying errors (chapter 4.4). Considering these uncertainties, the DoD approach is most reliable in case the magnitude of changes is higher than related thresholds (Williams 2012). Wheaton et al. (2010) stated that the application of the LoD_{min} leads to a higher information loss especially regarding small-scale changes. This information loss lies in an acceptable range, since the present work focuses on the high magnitude changes caused by the landslide. Thus, the DoDs calculated here prove to be applicable for the characterization of larger surface changes in the landslide area (Bossi et al. 2015, Turner et al. 2015, Hsieh et al. 2016, Lindner et al. 2016). However, as the thresholds in the DoDs of this study are rather high (5.79 m for 2013 and 2.27 m for 2016), small-scale changes or even no changes are not detectable (Wheaton et al. 2010, Bangen et al. 2014). Even though the same elevation does not automatically mean that these areas did not experience any changes, it excludes the possibility to identify unchanged zones. Instead, it only states that the elevation after the landslide event is equal or similar to the one before (Prokešová et al. 2010).

The problem of detecting small-scale changes becomes particularly clear when looking at the DoD of the post-event DEMs (chapter 4.4.3). In this DoD 73 % of the area of interest fell under threshold (+/- 2.98 m). Therefore, it is not possible to distinguish between actual

changes and noise in these areas. On the one hand, this can imply that these regions did not experience any changes, but on the other hand, it is highly possible that minor changes (< +/- 2.98 m) occurred that could not be detected (Wheaton et al. 2010, Bangen et al. 2014). Thus, for the identification of smaller differences, the present DoDs can provide indications, however, due to the rather high thresholds, they are not convenient for detailed analyses (Seier et al. 2018). Consequently, it is recommended to carry out an additional visual comparison of the post-event DEMs.

Overall, it can be stated that the calculated DoDs are very well suited for the detection of large deformations caused by the Capulín landslide. However, the high thresholds prevent a reliable detection of smaller changes.

7.1.2.3 Slip surface determination

The slip surface plays a crucial role in landslide analysis, as the shape allows to determine the type of sliding and represents an important component for landslide stability analyses and volume calculation (e.g. Carter and Bentley 1985, James et al. 2019). There are many different methods to detect the slip surface such as drilling procedures and non-invasive geophysical analyses (cf. chapter 3.1.4; Jongmans et al. 2009, Hibert et al. 2012, Furuya and Jiang 2015). ERT represents the most commonly used geophysical method in landslide research (e.g. Erginal et al. 2009, de Bari et al. 2011, Hibert et al. 2012, Chalupa et al. 2018, Bentivenga et al. 2019). However, when studying complex phenomena such as landslides, it is reasonable to combine different geophysical methods as they complement each other (e.g. Jongmans and Garambois 2007, Jäger et al. 2013, Schwindt et al. 2016). The results obtained by the geophysical investigations at the Capulín landslide confirm this statement. Here, the combination of ERT and SRT measurements makes it possible to distinguish the sliding mass from the underlying substrate (Wilde et al. 2017a, b). In the present work, these results form the base for the slip surface reconstruction of the Capulín landslide (chapter 4.5; Wilde et al. 2017a, b). Due to the fact that the geophysical surveys include only five transects irregularly distributed over the Capulín landslide, the data is insufficient to cover the entire study area and must therefore be interpolated (chapter 4.5). This is a typical problem, which arises when data, available only at certain points or locations, is supposed to cover large areas (e.g. Aguilar et al. 2005, Kalenchuk et al. 2009). This shows that even though geophysical analyses are considered excellent methods for

detecting sliding surfaces, it is not without its challenges (e.g. Bichler et al. 2004, Jongmans and Garambois 2007, Naudet et al. 2008, Perrone et al. 2008). Results highly depend on subsurface complexity, distribution and number of surveys within a study area, and consequently, the less data is available the more error-prone the interpolations are (e.g. Kalenchuk et al. 2009, Travelletti and Malet 2012).

The performance of the different interpolation techniques depends on several components as well, such as data distribution and accuracy, and on the overall objective of the study (Aguilar et al. 2005, Travelletti and Malet 2012, Jaboyedoff et al. 2020). For this reason, the slip surface calculation of the Capulín landslide includes three interpolation methods in order to select the most appropriate one (Kalenchuk et al. 2009, Travelletti and Malet 2012). The here obtained interpolation results of three different methods show good agreement in their main characteristics. All estimated slip surfaces are parallel to the terrain surface with constant depth in the upper regions and diminishing depth towards the foot area (Figure 4-20, chapter 4.5). Due to its low RMSE value and the realistic spatial pattern, the kriging method results to be the most fitting interpolation technique for the reconstruction of the slip surface of the Capulín landslide (cf. chapter 4.5). This finding is consistent with the studies of Kalenchuk et al. (2009), Kalenchuk et al. (2012), and Travelletti and Malet (2012), who found that the kriging method produces the best results.

In addition, since the different interpolation methods display advantages and disadvantages, the results require a thorough evaluation (e.g. Desmet 1997, Aguilar et al. 2005). One method to validate the interpolation results is the cross validation. It is a common technique in geostatistical practice and removes one data point at the time, estimates its value by interpolation and then compares the interpolated point to the original data point (e.g. Voltz and Webster 1990, Kalenchuk et al. 2009). However, Voltz and Webster (1990) state that evaluation with a separate dataset is more reliable, partitioning available data into a set of 'interpolation' and a set of 'validation' points. Therefore, in this study latter approach was preferred over the cross validation approach (chapter 3.1.4, Kalenchuk et al. 2009). Furthermore, the calculation of the RMSE enables the comparison of the spatial prediction of each of the applied interpolation techniques (e.g. Kalenchuk et al. 2009, Aguilar et al. 2005). The evaluation assessment records different RMSE values depending on which and how many validation points are used (chapter 4.5). This can be explained by the distribution of the validation points. Group 1 consists of points that are not involved in the interpolation process and therefore, cover a

region with a sparse distribution of interpolation points. This low coverage leads to inaccuracies and consequently, to higher RMSE values. Group 2, on the other hand, represents points located close to the interpolation points and therefore, they are supposed to be more accurate. Overall, the higher RMSE from Group 1 is likely the more realistic error estimate since it represents a more independent data set (Voltz and Webster 1990).

Generally, more data on the slip surface would significantly improve the interpolation (Aguilar et al. 2005, Kalenchuk et al. 2009). However, besides this being elaborate and time-consuming, the Capulín landslide is not accessible in all areas, therefore, some sections would still not be possible to be analyzed. A good addition would be drilling, this could support the geophysical findings and could provide additional data, but this method is not always easy to implement as well (e.g. Naudet et al. 2008, Furuya and Jiang 2015).

Overall, the determined slip surface geometry is a great improvement over a slip surface that would be estimated based on landslide geometry alone (e.g., spoon shape for rotational slides), and thus leads to more accurate input data for slope stability analyses (Kalenchuk et al. 2009, Bichler et al. 2004).

7.1.2.4 Landslide volume calculations

As mentioned before, volume calculations play an essential role in landslide analyses and therefore represent another important characteristic to be determined (e.g. Guzzetti et al. 2009, Marchesini et al. 2009, Verbovšek et al. 2017). Calculation of landslide volume is subject to a considerable uncertainty factor, which is reflected in the number of different methods that exist for its estimation. An overview of the common methods is provided by Jaboyedoff et al. (2020), showing that this is an area of ongoing research. Thus, in order to obtain the most realistic estimation for the landslide volume, a total of five volume calculations, three post-event and two pre-event, were applied (Bichler et al. 2004, Jaboyedoff et al. 2020).

Considering all calculation results, V_{DoD} by far provides the smallest volume estimate. This could be expected in advance, as the calculation approach only considers the displaced mass in relation to the former ground surface (e.g. Bichler et al. 2004, de Bari et al. 2011). The remaining post-event volume calculations (V_d and V_{post}) are not restricted to surface changes and consider the entire slide mass (cf. chapter 4.6). Interestingly, both, V_d and

$V_{post,}$ show nearly identical results (Figure 7-16; chapter 4.6), even though Approach I (V_d) is a more generalized calculation and Approach III (V_{post}) uses a higher degree of detail (Cruden and Varnes 1996, de Bari et al. 2011). Based on these findings it seems reasonable to assume that even a simplified approach can produce a good approximation of the landslide volume in case of limited data availability (Jaboyedoff et al. 2020).

Comparing the V_{total} to the V_{pre} and further assuming that landslide volume calculated with geophysical information reflects best the real volume, the V_{total} value is only slightly smaller (approx. 4 %) than V_{pre}. Bichler et al. (2004) stated that landslide volume calculated with geophysical information achieves the best estimation of the real volume (Approach V, V_{pre}). Although geophysical methods provide a more precise determination of the slip surface and the subsurface conditions in general, they are still subject to uncertainty (e.g. Jongmans and Garambois 2007, Naudet et al. 2008, Perrone et al. 2008). A clear advantage of geophysical methods compared to e.g. drilling techniques is the possibility to cover larger areas instead of punctual measurements. However, the quantity and density of geophysical surveys is of great significance for the accuracy. Indeed, the extent of interpolation procedures controls the reliability of the outcome (e.g. Kalenchuk et al. 2009, Aguilar et al. 2005, Travelletti and Malet 2012, Jaboyedoff et al. 2020). Nevertheless, the present study demonstrates that V_{total} is capable of achieving results comparable to V_{pre} and thus, exhibits a great potential for the application of statistical analyses in combination with DoDs.

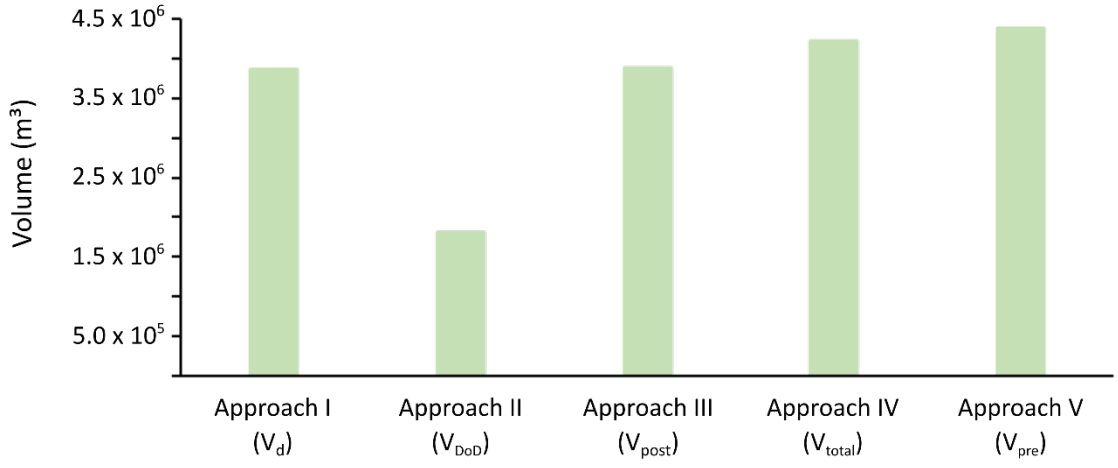

Figure 7-16. Resulting volumes of the different calculation approaches (cf. chapter 4.6). Source: Own illustration.

In summary, it is obvious that the applied volume calculation methods differ in their assumptions and their data requirements, however, all of them seem suitable as they are in a comparable range. V_{DoD} represents the only exception as this approach does not consider the overall volume (de Bari et al. 2011). It can be noted that for the Capulín landslide V_{pre} (Approach V) provides the most precise calculation.

7.2 Regional landslide susceptibility assessment

A main objective of this study is the creation of a susceptibility map for the Chiconquiaco Mountain Range area. This regional assessment consists of two steps, the first is the generation and validation of the geotechnical input data and the second the susceptibility modeling for the study area. The following chapters focus on the discussion of the applied methods and the results of this regional approach.

7.2.1 Input data generation

The application of slope stability models for large areas (e.g. at scales of 1 : 10.000 to 1 : 50.000) is challenging, since it requires a comprehensive basis of geomorphological and geotechnical data (e.g. Neuhäuser 2014, Raia et al. 2014, Zieher et al. 2017a). Even though sufficient geomorphological data are usually accessible (e.g. DEMs are commonly obtainable), geotechnical data sets often have spatially limited availability or sometimes are not available at all (e.g. Smith and Pain 2009, Raia et al. 2014). This poses a problem as the geotechnical properties of the slope material are critical for landslide susceptibility modeling (e.g. Van Westen et al. 2008). Generally, field- and laboratory analyses provide information on the geotechnical properties of the material (e.g. Michel et al. 2014, Mathew et al. 2016) and in some cases, modeling also relies on data sets from previous investigations (e.g. Lepore et al. 2013, Neuhäuser 2014, Jeong et al. 2018). While a few studies on landslides near the study area exist (e.g. Capra et al. 2003, Legorreta Paulín et al. 2014b), a transfer of their data to the Chiconquiaco Mountain Range area would not have been suitable. For example, Capra et al. (2003) analyzed mass movements (soil slide / debris flows) in volcanic terrains in Teziutlán (in the Sierra Norte of Puebla State, Mexico) located approx. 70 km west of the study area. Although their investigations show similarities to the present study, they differ in significant components, such as process

type, slip surface depth and sediment characteristics, and therefore, their geotechnical data are not transferable to the study area.

Thus, the lack of data for the Chiconquiaco Mountain Range area, motivated developing an approach, which generates necessary geotechnical parameters mainly based on geomorphological information and using data from own local analyses for validation. Here, the implementation of the case study (Capulín landslide) plays a crucial role as it allowed for obtaining a data set, which functioned as initial and validation values (chapter 3.3.1). This approach is as of yet rarely used in the field of stability analysis (Zieher et al. 2017a). However, the main advantage is that this calculation process of the geotechnical parameter requires geomorphological parameters as input data, which in most cases are clearly easier to obtain, since they mainly base on DEMs (Smith and Pain 2009). Overall, this input parameter generation process deviates from other approaches. For example, Iñeguez (2016) combined a finite elements method (FEM) and optimization algorithms to analyze the deviation of measured and predicted data. Furthermore, Raia et al. (2014) used a probability distribution in order to determine input parameters, therefore, modifying the model TRIGRS. However, since this model is designed for shallow landslides (Raia et al. 2014), this approach is unsuited for the present study.

The laboratory results from the case study, which are the base for the validation, show an overall good agreement with the calculated input parameters (Table 7-4). The calculated density value (1.7 g/cm³) lies within the expected range, differing only slightly from the mean value of the laboratory results (1.8 g/cm³, Table 7-4). Furthermore, the calculated friction angle (22°) exceeds the mean value of the laboratory results (19°) while remaining in the initial range (cf. Table 7-4, chapter 6.1). Owing to the fact that the indicated range acts as 'initial values' and does not restrict the value, the calculated cohesion values do in fact exceed their range, the latter being determined by the minimum and maximum values from the analyzed sediments. The cohesion values represent derivatives from other laboratory methods, namely classified grain-size and limits of consistency, and herein, the value of the effective cohesion (c'), representing the consolidate soil, is applied (chapter 3.2.2, cf. Terhorst and Damm 2009, Damm and Terhorst 2010, Damm et al. 2013). However, considering the calculated value (0.037 MPa) it turns out that the cohesion values corresponding to unconsolidated soils (c_u), with 0.028 MPa (mean c_u value of the analyzed samples, Appendix G) are a better match. As the Capulín landslide most probably represents a reactivated processes, it seems plausible, that the cohesion values

Table 7-4. Overview of sediment analyses results and generated input parameters.

Parameter	Lab. results (value range)	Lab. results (mean value)	Calculated value (Capulín landslide)	Calculated value (landslide no. 2)
cohesion [MPa]	0 - 0.010	0.003	0.037	0.039
friction angle [°]	15 - 30	19	22	22
density [g/cm³]	1.4 - 2.0	1.8	1.7	1.8

correspond to the values for unconsolidated soils (DIN 1055 1976, Zêzere et al. 1999). Consequently, the calculation results shows that in case of the present study, the c_u is more fitting, even though the cohesion for consolidated soils seems appropriate in other studies (e.g. Terhorst and Damm 2009, Damm and Terhorst 2010, Damm et al. 2013).

A second input data generation, based on the characteristics of landslide no. 2 allowed to further analyze the performance of the calculation approach (chapter 6.1). The results are very similar to the ones from the Capulín landslide (Table 7-4). However, this may also be due to the fact that the initial geotechnical values remained unchanged and only the geomorphological input data was adjusted to the specific characteristics of landslide no. 2 (Table 6-3, chapter 6.1). Therefore, more case studies would help to reliably validate the results.

Furthermore, the implementation of the generated geotechnical input data into a second slope stability model, which estimates slope stability based on the method of slices, allowed for an additional validation. The comparison of models with different theoretical backgrounds is common practice in landslide research and small deviations between the resulting Factors of Safety (FoS) are to be expected (e.g. Zizioli et al. 2013, Duncan et al. 2014). However, the constant deviation shows that the calculated geotechnical values produce viable results for stability modeling of the Capulín landslide and therefore, this supports the suitability of the input data generation process.

7.2.2 Landslide susceptibility assessment

The goal to assess the landslide susceptibility in the Chiconquiaco Mountain range area is achieved by creating landslide susceptibility maps. There already exists a map for this region, however, it has a small scale (1 : 700,000), which results in the map being very

generalized (Rodríguez Elizarrarás and Morales Barrera 2011). Even more generalization occurs in the landslide susceptibility map for Mexico, which classifies most of the study area as 'low susceptible' (Figure 7-17, Gobierno de México 2020). This map illustrates that the areas classified as highly susceptible correspond to the steep slopes surrounding the study area and in contrast, the less inclined areas in the center mainly record low susceptibility with smaller parts corresponding to the classes very low and intermediate (Figure 7-17). Considering the mapped landslides, which are mainly located in the central part of the study area (chapter 4.3), it reveals that this map would not accurately represent the landslide occurrence in this area (Figure 7-17), which highlights the importance of incorporating site-specific characteristics into the modeling process (e.g. Zizioli et al. 2013, Neuhäuser 2014). Thus, the focus in the present study lied on integrating the site-specific characteristics into the modeling approach, which enabled to obtain a detailed assessment of the landslide susceptibility in the Chiconquiaco Mountain Range area.

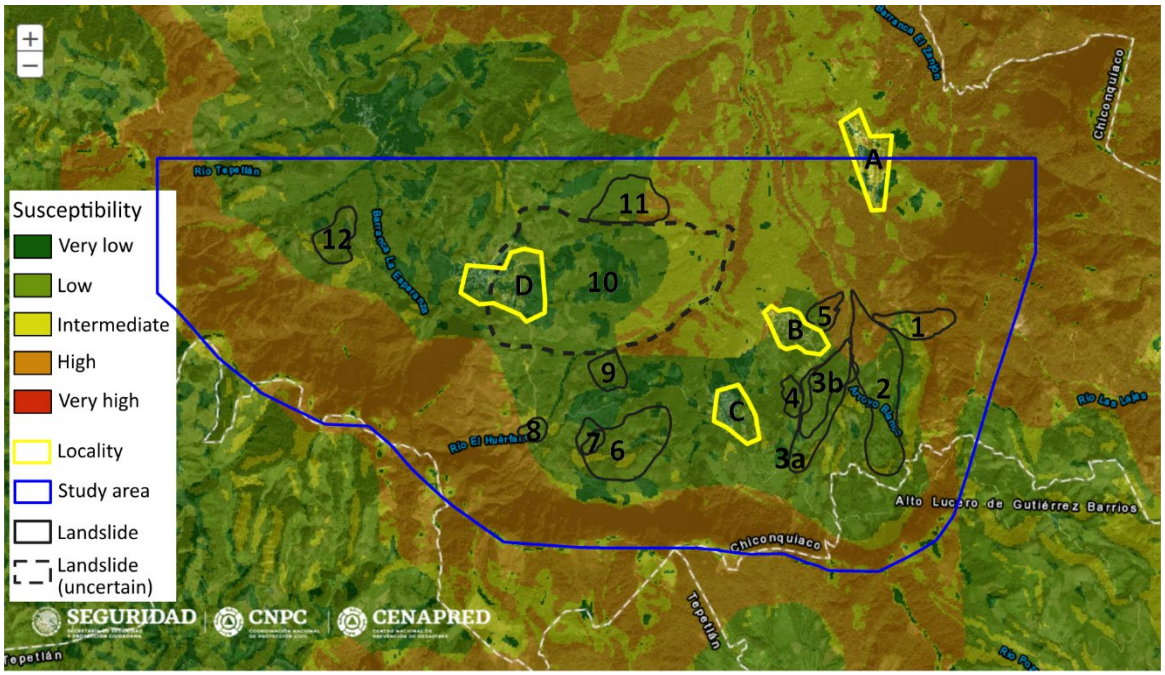

Figure 7-17. Landslide susceptibility map of the study area. Source: Modified after Gobierno de México (2020).

Methodological approach

The modeling approach includes the calculation of the slope stability for the Chiconquiaco Mountain Range based on two different models (SAFETYFACTOR and Scoops3D). The SAFETYFACTOR program uses the infinite slope approach and the Scoops3D program

the method of slices (cf. chapter 3.3, Sharma 2002, Reid et al. 2000, 2015, Teixeira et al. 2015, Martins et al. 2017). Since each model has a different theoretical background the goal was to evaluate their suitability for the present study (Zizioli et al. 2013, Duncan et al. 2014).

Considering the programs based on the infinite slope method, SAFETFACTOR is the most suitable in this case as it does not specialize in shallow landslides unlike the programs SINMAP and SHALSTAB (e.g. Selby 1982, Dietrich and Montgomery 1998, Pack et al. 1998, Sharma 2002, Teixeira et al. 2015, Martins et al. 2017). Although most studies that apply the infinite slope approach focus on shallow landslides, this method is also applicable for deep-seated landslides with a slip surface parallel to the slope, when the slip surface depth is relatively small in comparison to the lateral slope dimension (e.g. Legorreta Paulín et al. 2010, Duncan et al. 2014).

Scoops3D, originally developed to model stability of volcanic edifices, analyzes slope stability by applying the three-dimensional limit equilibrium method of slices (Reid et al. 2000, 2015). The advantage of this program is its ability to simulate slope stability over large areas. The application of Scoops3D for the calculation of landslide susceptibility increased in the last years, indicating its potential for the subject of this study (e.g. Weidner et al. 2019, Chiang and Kuo 2020, Palazzolo et al. 2020). Zhang and Wang (2019) and He et al. (2021) showed that Scoops3D produces good results for shallow landslides as well. This is an important information, as shallow landslides tend to be translational movements, which was not the originally targeted movement type of Scoops3D (Reid et al. 2000, 2015).

Besides the selection of slope stability models, the focus lied on determining the spatial distribution of the input parameters. This is an especially critical process as in the present work, the data basis is very small. However, different studies have proven that a small data set is able to produce reliable results (e.g. Morelli et al. 2017, Ramírez-Herrera and Gaidzik 2017). For the SAFETYFACTOR method, the spatial distribution of the data includes the creation of process regions (cf. chapter 3.3.3), which allow for assigning geotechnical values to specific regions throughout the study area. This approach is highly flexible as these areas do not have to be connected and geotechnical input parameters can differ in their spatial distribution (e.g. Terhorst and Kreja 2009, Neuhäuser 2014). The Scoops3D model has a similar approach for the determination of the geotechnical values, defining various layers with different geotechnical values and varying depth (Reid et al. 2015).

The goal of the geotechnical parameter input was to incorporate the input data from Step I (chapter 6.1) into the susceptibility models. These values were assigned to Region 3 in the SAFETYFACTOR approach and to Layer 1 in the Scoops3D model. The remaining areas correspond to data based on literature values (Table 6-3, 6-4, chapters 6.3.1, 6.4.1). Applying literature values is common, even though geotechnical data collected in the study area improves the model performance significantly (e.g. Fall et al. 2006, Neuhäuser 2014, Zieher et al. 2017, Weidner et al. 2019). In this study, however, the areas corresponding to the literature values play only a minor role and their impact is therefore limited.

Another important value to transfer from the local to the regional approach is the layer thickness. In the present work, calculation of the layer thickness is based on the Capulín case study, namely the thickness of the slide and its corresponding slope angle (cf. chapter 3.3.3). Soil or layer depth determination still poses a huge challenge and many different approaches exist (e.g. Wilford and Thomas 2013, van Westen et al. 2008, Cascini et al. 2017, Devkota et al. 2018). For example, Kuriakose et al. (2009) predicted regolith depth based on empirico-statistical and geostatistical methods, whereas Dietrich et al. (1995) modeled the soil depth based on finite difference models and integrated the resulting soil depths into shallow landslide modeling.

Beside the geotechnical parameters and thickness, slope stability analyses rely on the specification of hydrological conditions. In this approach, the lack of hydrological data for the study area necessitated estimating the hydrological conditions (cf. chapter 3.3.3 and 3.3.4). In case detailed information on hydrological parameters is available, these data sets can be used in modeling the hydrological conditions to then incorporate these findings into slope stability models (e.g. Klose et al. 2012, Formetta et al. 2014, Neuhäuser 2014). Especially the combination of the TRIGRS model, which simulates the dynamic hydraulic conditions of a slope with slope stability models, seems to achieve good results (e.g. Baum et al. 2008, Jeong et al. 2018, Tran et al. 2018).

Susceptibility maps

A closer look at the resulting maps (Scoops3D map - Figure 7-18a, SAFETYFACTOR map - Figure 7-18b) reveal that the areas considered as highly unstable predominantly correspond to regions with slope gradients less than 30°. In contrast, steeper slopes (> 30°),

especially the ones surrounding the study area in an almost U-shaped form, mainly classify as stable (chapter 6.3, 6.4). The reason for this stability class distribution is that these maps and their calculations only incorporate the susceptibility to sliding processes and disregard other mass movement types, such as falls. This follows the recommendation to analyze single landslide types individually, instead of combining several in one approach (e.g. Corominas et al. 2014). Furthermore, it is noticeable that the obtained results (Figure 7-18) represent the opposite of the result shown in Figure 7-17. A possible explanation for this deviation is the fact that the existing susceptibility map of Mexico includes falls and slides and does not further differentiate between the processes (Corominas et al. 2014, Gobierno de México 2020). However, the distribution of the high susceptibility classes in this map further indicate a close correlation to the geological unit of basalts and andesites (cf. Figure 7-1). In contrast, the high susceptibility classes of the Scoops3D and SAFETYFACTOR maps coincide with areas identified as slope deposits (Figure 7-1, 7-18). The fact that latter maps do reflect the reality more accurately becomes obvious when considering the resulting maps in relation to the mapped landslides (Figure 7-17, 7-18).

Overall, most of the identified landslides primarily classify as unstable in both the Scoop3D map as well as in the SAFETYFACTOR map (Figure 7-18, chapter 6.3, 6.4). For example, landslide no. 9 (Escalanar landslide) mainly corresponds to the 'highly unstable' and 'unstable' classes and thus, the assessment for this landslide area was successful. Upon closer inspection, the maps indicate that a further extension would be concentrated in the southwestern part of the Escalanar landslide (Figure 7-18).

The most noticeable exceptions, where the classification did not work well, are landslides nos. 5, 8, and 12. Especially nos. 8 and 12 show poor classification as they encompass mainly 'stable' and 'moderate' and almost no 'unstable' areas (Figure 7-18). At least the central parts of landslide no. 5 corresponds to 'unstable' and a smaller reactivation within the mapped landslide seems plausible considering the occurrence of reactivation processes in these areas. The occurrence of reactivation processes is highly probable as well for landslide no. 10 (Figure 7-18). Due to surficial processes of erosion and weathering, it is not possible to clearly determine the extent of this landslide, which is the reason why it is marked as 'uncertain' (Figure 7-18). The Scoops3D and SAFETYFACTOR maps classify larger proportions of this uncertain landslide as 'unstable' and with regard to the Capulín landslide, where the former landslide area was only partially reactivated,

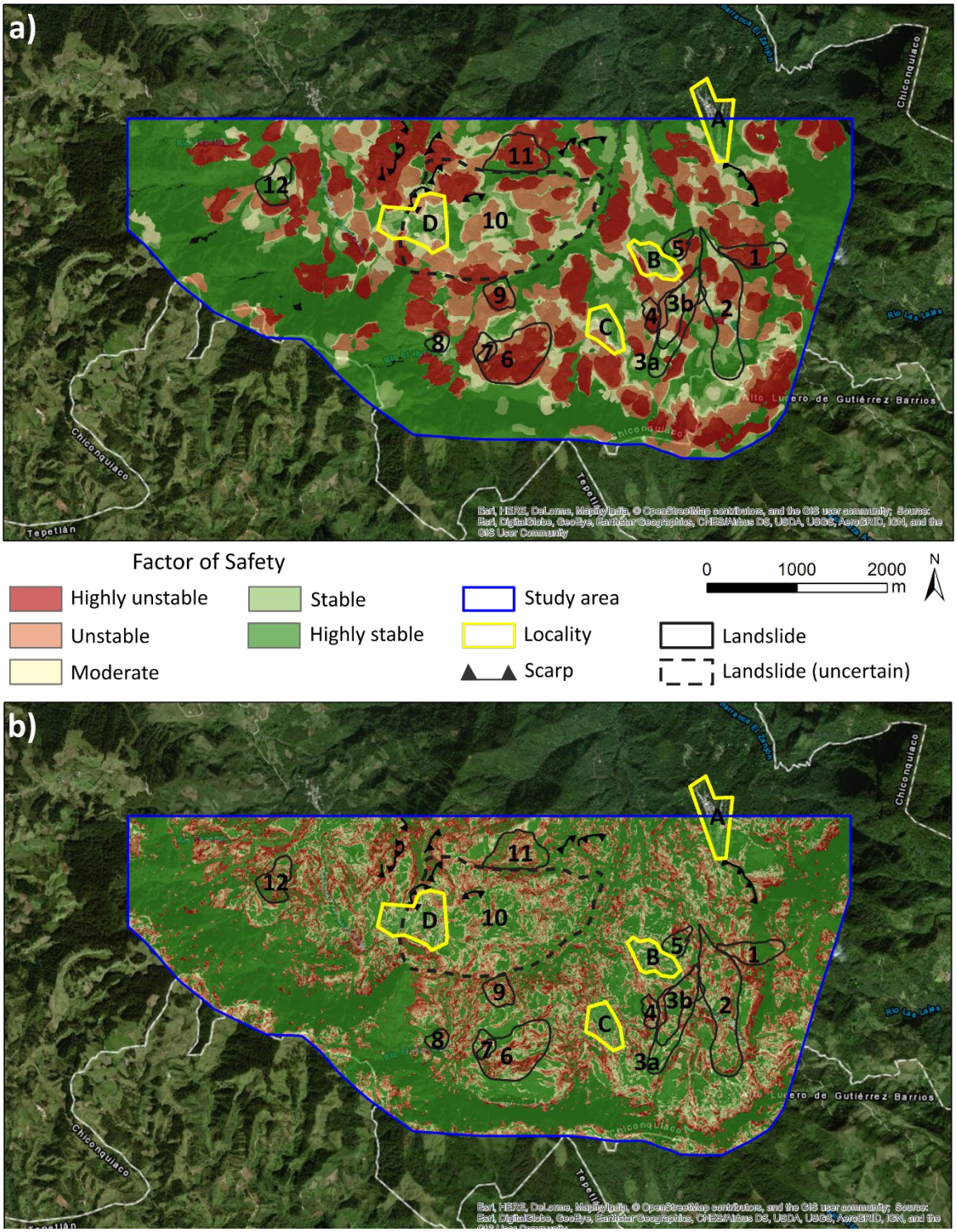

Figure 7-18. a) Factor of Safety map calculated with Scoops3D. b) Factor of Safety map calculated with SAFETYFACTOR. Source of background map: Esri World Imagery (2019).

smaller reactivations are more likely than a large reactivation encompassing the entire area, which supports the modeling result.

A similar pattern, where only parts of the mapped landslide record unstable classes, are landslides no. 1, 2, and 3a (Figure 7-18). A closer look at the landslide no. 3a (also referred

to as former landslide) shows that the area above the recent Capulín landslide (no. 3b) classifies as 'highly stable' to 'moderate' and the same is true for some areas in the center of the slide. Nevertheless, considering the Capulín landslide as a reactivation it becomes apparent that the areas, which were unaffected by the reactivation process mainly classify as stable. Therefore, even with the 'misclassification' in these areas, this can be considered as a good assessment of the process. This is particularly interesting regarding landslide no. 1 and especially no. 5, whose slide body and scarp have similar shapes (although slightly taller) as the Capulín landslide (Figure 7-18). Considering the FoS classification, a distribution similar to the landslide no. 3a is possible to observe, with the scarp area classified as 'highly stable' to 'stable' and the remaining areas as 'moderate' to 'highly unstable'. This leads to the conclusion that there is a high potential for the occurrence of reactivation processes and could lead to similar processes as the Capulín landslide.

In general, landslide mapping plays a key role in susceptibility modeling, on the one side as validation parameters and on the other side as input parameters, especially in statistical modeling (e.g. Cascini et al. 2005, Guzzetti et al. 2012, Weidner et al. 2019). In this study, the main focus for the generation of the landslide inventory lied on evaluating the resulting maps from the modeling approach, which has proven to be a valuable tool as shown above.

Furthermore, analyzing landslide stability within the settlements is particularly important. Four villages are located inside the study area and Las Sombra (locality A) is the only village that does not contain any unstable areas (Figure 7-18). The village El Capulín (locality B) mostly records stable areas as well, although the southern border (at a slope facing southwest) coincides with areas classified as 'highly unstable' (Figure 7-18). This gives reasonable cause for concern as retrogressive processes could affect the village. A similar situation appears at the locality El Escalanar (locality C), where the majority of the area corresponds to the classes 'highly stable' to 'moderate', except for the southern region where the slopes classify as 'unstable'. El Huerfano (locality D) shows the most cause for concern. This location mostly corresponds to the 'moderate' class, however, records 'unstable' and 'highly unstable' classes as well (Figure 7-18). In addition, the village is situated within the area mapped as landslide no. 10 and close to three scarp areas (Figure 7-18). Therefore, in case of reactivation processes within the old landslide, El Huerfano could be seriously affected. The western border of the village, at the other side

of the ridge, coincides with another highly unstable area, posing yet another potential threat (Figure 7-18).

In summary, three out of four villages located in the study area lie in the immediate vicinity of, or even include, unstable areas. These susceptibility maps are therefore important sources of information regarding the landslide situation for each of these settlements and their potential future extensions.

Comparison of the resulting maps

An important step to further examine the performance of susceptibility modeling is to compare the map results (chapter 6.5). The comparison of different models is a widely applied approach and a helpful tool for analyzing the performance of the models (e.g. Teixeira et al. 2015, Pradhan and Kim 2015, Zieher et al. 2017b, Xiao et al. 2020, Fleuchaus et al. 2021).

- **Simple SAFETYFACTOR map vs. filtered SAFETYFACTOR map:** The comparison of the two SAFETYFACTOR maps shows that using a filter considerably improves the modeling results (cf. chapter 6.5.1). With filtering, the percentage of the 'highly stable' class increases from 43 to 55 % and at the same time facilitates the interpretation of the map as this method eliminates isolated pixels. However, the use of the filter should be limited to a single or few applications, since excessive filtering leads to considerable loss of information (e.g. Kim 1996, Claessens et al. 2005, Legorreta Paulín et al. 2010).

- **Filtered SAFETYFACTOR map vs. classified slope map**: The slope gradient is one of the most influential disposition factors related to landslides and therefore, dominates many susceptibility maps. For example, this is visible in the susceptibility map for Mexico (Figure 7-17), where areas classified as highly susceptible to landslides mainly correspond to steep inclined slopes. However, as shown above, the landslides in the Chiconquiaco Mountain Range do not occur in these areas (Figure 7-17, 7-18). This kind of overestimation of one factor and the insufficient consideration of other factors is a common phenomenon in susceptibility modeling (e.g. Xiao et al. 2020). Therefore, it is critical to assess the influence of slope gradient to the modeling results. Here, the comparison of the susceptibility map with a classified slope map enables to evaluate

whether the slope dominates the computed map. The classifications of the filtered SAFETYFACTOR map and the classified slope map coincide for almost 40 % of the area, yet the best agreements are in the stable areas. Consequently, classifications of unstable areas differ substantially, limiting the usefulness of susceptibility maps mainly based on slope gradient. This is an essential result as it emphasizes the importance to consider site-specific characteristics and simultaneously demonstrates that simplified approaches often are not capable of adapting to the specific conditions. This issue often occurs in large study areas and when data availability is limited (e.g. He and Beighley 2008, Neuhäuser 2014, Xiao et al. 2020).

- **Filtered SAFETYFACTOR map vs. literature-value SAFETYFACTOR map:** Another interesting aspect in landslide susceptibility modeling is the use of literature values. It is a common approach and often applied when the data basis is scarce or insufficient (e.g. Arrone et al. 2009). A comparison of the computed map with a literature value map reveals whether slope stability based solely on literature values would provide realistic results for the study area.

  The filtered SAFETYFACTOR map already incorporates literature values in the process regions 1 and 2, however, these regions account for only 27 % of the study area (chapter 6.4, 6.5.3). Thus, the main difference in this comparison is the input data for process region 3, where the filtered SAFETYFACTOR map uses the data calculated in Step I (chapter 6.1), and the 'literature-value SAFETYFACTOR map' applies the same literature values as Region 2 (chapter 6.5.3). The comparison yields the same classification in both maps for approx. 60 % of the area. While the steep areas mainly correspond to the same classes, the less inclined slopes in the center of the study area typically differ by one or two classes (cf. Figure 6-20, chapter 6.5.3). In view of the other comparisons, the agreement of the maps is rather high, and hence, the maps seem similar at first glance. However, a closer look reveals that the values within the classes differ between the maps. The range for the filtered SAFETYFACTOR map is from 0.75 to 1.5 (Figure 6-8) and the range of the literature-value SAFETYFACTOR map is between 3.3 and 8.9 (Figure 6-19). Latter FoS values exceed the range, which would normally be considered as 'unstable' (e.g. Selby 1982, Abramson et al. 2002). Consequently, susceptibility modeling based solely on literature values would not be feasible in the present work.

- **Scoops3D map vs. filtered SAFETYFACTOR map:** The application and comparison of two models based on different theoretical assumptions helps to understand their strength and weaknesses as well as their applicability to a particular study area and its specific characteristics (e.g. Zizioli et al. 2013, Pradhan and Kim 2015, Teixeira et al. 2015, Xiao et al. 2020).

  The difference model of the 'Scoops3D map' and the 'filtered SAFETYFACTOR map' shows that the two maps correspond to the same classes in more than 40 % of the study area (chapter 6.5.4). The main reason for this relatively low agreement is that the SAFETYFACTOR model results are grid-based, which results in a discontinuous distribution of the FoS classes, while at the same time making the map more difficult to interpret. In contrast, Scoops3D produces maps with continuous areas. Consequently, the direct comparison of the two approaches, subtracting one map from the other, leads to relatively low accordance (chapter 6.5.4). The Scoops3D map classifies 61 % of the area as 'highly stable' to 'moderate' (classes 3 - 5). The filtered SAFTEYFACTOR map records 70 % of the area in the same categories and in turn only classifies 30 % as 'unstable' to 'highly unstable' (classes 1 - 2). This difference mainly traces back to the incoherent distribution in the SAFETYFACTOR map rather than increased predictive power. Thus, the Scoops3D map has a clear advantage over the SAFETYFACTOR map, since it is essentially more intuitive. For example, Figure 7-19 shows that both maps record similar classes for landslide no. 9 (Escalanar). Here, the Scoops3D map illustrates the classes as continuous areas (polygons) and the SAFETYFACTOR map exhibits interruptions (Figure 7-19). Therefore, at a first glance it is easier to identify the landslide area as highly susceptible in the Scoops3D map (Figure 7-19a) and less clear in the SAFETYFACTOR map (Figure 7-19b) as latter

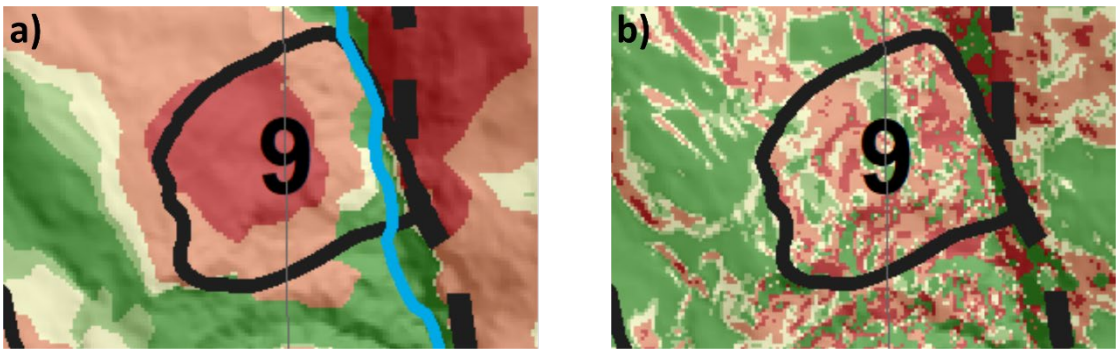

Figure 7-19. Section of the Scoops3D map (a) and the filtered SAFETYFACTOR map (b) showing the Escalanar landslide (no. 9). Source: Own illustration.

contains classes of low susceptibility as well. In order to avoid this, a possibility is to reduce the resolution of the DEM, which would lead to a generalization and thus to a more homogenous result. However, generalization usually leads to information loss and the pixel size should not exceed 30 m, otherwise some landslides may not be captured correctly (Claessens et al. 2005, Legorreta Paulín et al. 2010). A visual interpretation of the two maps, however, shows a good agreement between them. The areas with the lowest and highest susceptibility classes generally have the same distributions and both record good correspondences with the mapped landslides (Figure 7-18).

It is noteworthy that these maps achieved good results, even though one model primarily targets translational processes (SAFETYFACTOR), while the other (Scoops3D) is designed for rotational landslides (Duncan et al. 2014, Reid et al. 2015). This is of particular importance as the results of the site-specific approach show that the Capulín landslide is a complex mass movement and since the Capulín landslide and the mapped landslides have many common characteristics, it is reasonable to assume that their processes are also very similar. This means that the dominant process in this area is most likely a complex process. Consequently, the results reveal that these models are appropriate to assess complex landslides as well. This is in good agreement with other studies that made similar observations, showing that models work well for processes that deviate from the original intent of the model (e.g. Legorreta-Paulin et al. 2010, Neuhäuser 2014, Qiao et al. 2019, Palazollo et al. 2020).

8. Conclusion

The present study provides important contributions to the assessment of the landslide susceptibility in the Chiconquiaco Mountain Range area. The combination of site-specific (local) and regional approaches allowed for a comprehensive analysis of the landslide situation in the study area.

The analysis of the disposition factors of the study area demonstrates a close correlation between the landslide occurrences and moderate slopes (< 35°), which are covered by slope deposits. Additionally, the close proximity to streams plays an important role, since water level rise can lead to erosional processes at the foot of the slope. Another highly relevant outcome lies on the fact that the Capulín landslide represents a large reactivation process indicating that recent processes are closely linked to former landslides.

The analyses further reveal that extreme and long-lasting rainfalls are the main triggering factor leading to oversaturation of the slope material and an increase of discharge at the adjacent stream. The fact that extreme events like in the year 2013 triggered the Capulín landslide and many others in this area highlights the importance to further investigate this aspect, since the occurrence of such events can increase due to climate change.

Geomorphological and sedimentological analyses reveal that the Capulín landslide is a complex mass movement comprising different sliding and flow processes. The complete classification according to Cruden and Varnes (1996), is a *reactivated, rapid to very rapid, wet, compound debris slide-very wet earth flow*. This complex type of landslide is particularly susceptible to reactivation and therefore, requires monitoring, especially in case of anthropogenic activities (e.g. road cuts through the landslide) further influencing the overall stability.

The methodological approach implements multiple flexible, cost- and time-effective methods, which allowed for a comprehensive assessment of the Capulín landslide. Furthermore, detailed analyses of these methods enabled to identify their strength and weaknesses.

The results of the DEM analyses show that the generation of DEMs based on data collected by UAVs contribute strongly to geomorphological analyses. The results, especially of the digital terrain models (DTMs), prove that this approach is still subject to some

uncertainties as it is sensitive to suboptimal field conditions. However, with regard to the intended use in the present study these uncertainties and errors remain in an acceptable range. Furthermore, their clear advantage in comparison to further methods (e.g. LIDAR) is that the application is flexible and cost-effective, enabling the generation of DEMs even in remote areas with little or no access.

DoDs based on pre-and post-event DEMs represent a valuable tool for landslide characterization. They allow for identifying the spatial distribution of eroded and accumulated areas and form the base for volume calculation of the slide mass. In the case that post-event DEMs of different time periods are available, DoDs even enable to track how the slide mass changes over time. This possibility makes DoDs a valuable asset for landslide monitoring, which will most likely experience a further increased application in this field as it offers reliable, yet flexible and cost-effective solutions.

In general, when investigating landslides it is always crucial to gather information on the slip surface as it represents an essential feature and helps for a better understanding of the landslide process. The present results were able to show that a combined approach of various methods can lead to a reliable detection of the slip surface. The determination of the slip surface location contributes to the identification of the process type and provides valuable information for the calculation of the landslide volume as well. In this context, the combination of geophysical analyses, slip surface calculation, and DoD analyses proves to be the most reliable approach to determine the landslide volume.

The sediment analyses provide major datasets for the site-specific as well as for the regional approach. For the site-specific approach, the results gave valuable information on the sediments involved in the landslide process. In this context, it was possible to identify an underlying layer below the slope deposits consisting of shale. In general, the contact between sedimentary rocks like shales and slope deposits is highly prone to landslides, which supports the assumption that the sliding occurred at the contact between the two layers. The geological information, which is available for this area does not record the presence of sedimentary rocks. Consequently, the characterization of the sediments definitely leads to a better understanding of the causal factors and processes present in the Chiconquiaco Mountain Range area.

For the regional approach, the goal was to gain independence from comprehensive data sets by calculating input parameters and subsequently validating the results with in-situ

data. The validation process proves that this approach is a suitable alternative, which offers the possibility to enhance the data availability over larger areas.

Furthermore, the application of two slope stability models with different theoretical backgrounds allowed for an integrated landslide susceptibility assessment in the study area. The results demonstrate the suitability of both approaches, even though the SAFETYFACTOR map is less intuitive and therefore, more difficult to apply, especially for nonprofessionals. In this case, the Scoops3D map would be the better choice, since it is easier to interpret.

The resulting susceptibility maps display the relevance of the slope deposits and furthermore that steep slopes (> 45°) play a subordinate role. This is by far an important fact, since the existing susceptibility map (Gobierno de México 2020) identified steep slopes of basalt and andesites as highly susceptible to landslides and disregarded moderate slopes covered by slope deposits. Thus, the new susceptibility map represents an improvement towards the landslide assessment in the study area.

Generally, the comparison of the different susceptibility maps underlines the importance of integrating site-specific characteristics to the models. For future work, it can be essential to include further data in order to contribute to the verification and improvement of the methods and approaches established in the present work. On the one side, forthcoming research can expand the landslide investigations in the Chiconquiaco Mountain Range area, e.g. by further developing the susceptibility approach towards a hazard or even risk assessment. On the other side, the methodological approach can be refined by improving the overall design and by testing the transferability of the developed approach to other study areas.

References

Abramson, L. W., Lee, T. S., Sharma, S., Boyce, G. M. (2002): Slope stability and stabilization methods. John Wiley & Sons, Inc., New York, 712 pp.

Ad-hoc-AG Boden (2005): Bodenkundliche Kartieranleitung, 5. edition, Schweizerbart, Stuttgart, 438 pp.

Agisoft PhotoScan (2016): Agisoft PhotoScan professional edition version 1.2.6.2834. Available online. URL: https://www.agisoft.com/. Latest access: September 2020.

Agisoft LLC (2016): Agisoft PhotoScan User Manual. Professional edition, Version 1.2. URL: https://www.agisoft.com/pdf/photoscan-pro_1_2_en.pdf. Latest access: September 2020.

Agisoft LLC (2019): Agisoft Metashape User Manual: Professional edition, Version 1.5. URL: https://www.agisoft.com/pdf/metashape-pro_1_5_en.pdf. Last access: Latest access: September 2020.

Aguilar, F. J., Agüera, F., Aguilar, M. A., Carvajal (2005): Effects of Terrain Morphology, Sampling Density, and Interpolation Methods on Grid DEM Accuracy. Photogrammetric Engineering & Remote Sensing 71: 805-816.

Aguilar, M. A., Aguilar, F. J., Fernández, I., Mills, J. P. (2013): Accuracy Assessment of Commercial Self-Calibrating Bundle Adjustment Routines Applied to Archival Aerial Photography. The Photogrammetric Record 28 (141): 96-114.

Albrecht, J. (2007): Key concepts & techniques in GIS. SAGE Publications, Los Angeles, 116 pp.

Alcántara-Ayala, I. (2004): Hazard assessment of rainfall-induced landsliding in Mexico. Geomorphology 61: 19-40.

Alcántara-Ayala, I. (2008): On the historical account of disastrous landslides in Mexico: the challenge of risk management and disaster prevention. Advances in Geosciences 14: 159-164.

Alcántara-Ayala, I., Esteban-Chávez, O., Parrot, J. F. (2006): Landsliding related to land-cover change: A diachronic analysis of hillslope instability distribution in the Sierra Norte, Puebla, Mexico. Catena 65: 152-165.

Alcántara-Ayala, I., Dykes, A. P. (2010): Introduction - Land use change in the tropics: Causes, consequences and monitoring in Mexico. Singapore Journal of Tropical Geography 31: 143-151.

Aleotti, P., Chowdhury, R. (1999): Landslide hazard assessment: summary review and new perspectives. Bulletin of Engineering Geology and the Environment 58: 21-44.

Altmann, M., Piermattei, L., Haas, F., Heckmann, T., Fleischer, F., Rom, J., Betz-Nutz, S., Knoflach, B., Müller, S., Ramskogler, K., Pfeier, M., Hofmeister, F., Ressl, C., Becht, M. (2020): Long-Term Changes of Morphodynamics on Little Ice Age Lateral Moraines and the Resulting Sediment Transfer into Mountain Streams in the Upper Kauner Valley, Austria. Water 12: 3375. DOI: 10.3390/w12123375.

Amelung, W., Blume, H.-P., Fleige, H., Horn, R., Kandeler, E., Kögel-Knabner, I., Kretzschmar, R., Stahr, K., Wilke, B.-M. (2018): Scheffer/Schachtschabel. Lehrbuch der Bodenkunde. 17. edition, Springer Spektrum, Berlin, 749 pp.

Anders, N., Valente, J., Masselink, R., Keesstra, S. (2019): Comparing Filtering Techniques for Removing Vegetation from UAV-Based Photogrammetric Point Clouds. Drones 3 (61): 1-14.

Arrone, E., Noto, L. V., Lepore, C., Bras, R. L. (2009): Physically-based and distributed approach to analyze rainfall-triggered landslides at watershed scale. Geomorphology 133: 121-131.

Aryal, A., Brooks, B. A., Reid, M. E. (2015): Landslide subsurface slip geometry inferred from 3-D surface displacement fields. Geophysical Research Letters 42 (5): 1411-1417.

Asniar, N., Purwana, Y. M., Surjandari, N. S. (2019): Tuff as rock and soil: Review of the literature on tuff geotechnical, chemical and mineralogical properties around the world and in Indonesia. AIP Conference Proceedings 2114 (050022): 1-9. DOI: 10.1063/1.5112466.

ASTM (2006): D2487-06, Standard Practice for Classification of Soils for Engineering Purposes (Unified Soil Classification System), ASTM International, West Conshohocken, PA, 12 pp.

Ausilio, E., Zimmaro, P. (2017): Landslide characterization using a multidisciplinary approach. Measurement 104: 294-301.

Bakker, M., Lane, S. N. (2017): Archival photogrammetric analysis of river-floodplain systems using Structure from Motion (SfM) methods. Earth Surface Processes and Landforms 42: 1274-1286.

Bangen, S. G., Wheaton, J. M., Bouwes, N., Bouwesm, B., Jordan, C. (2014): A methodological intercomparison of topographic survey techniques for characterizing wadeable streams and rivers. Geomorphology 206: 343-361.

Baum, R. L., Savage, W. Z., Godt, J. W. (2008): TRIGRS - A fortran program for transient rainfall infiltration and grid - based regional slope-stability analysis, Version 2.0. USGS Open File Report 08-1159, U.S. Geological Survey, 75 pp.

Bentivenga, M., Giocoli, A., Palladino, G., Perrone, A., Piscitelli, S. (2019): Geological and geophysical characterization of the Brindisi di Montagna Scalo landslide (Basilicata, Southern Italy). Geomatics, Natural Hazards and Risk 10 (1): 1367-1388.

Bichler, A., Bobrowsky, P., Best, M., Douma, M., Hunter, J., Calvert, T., Burns, R. (2004): Three-dimensional mapping of a landslide using a multi-geophysical approach: the Quesnel Forks landslide. Landslides 1: 29-40.

Bishop, A. W. (1955): The use of the slip circle for the stability analysis of slopes. Géotechnique 5 (1): 7-17.

Bishop, K. M. (1999): Determination of translational landslide slip surface depth using balanced cross sections. Environmental & Engineering Geoscience 5 (2): 147-156.

Blake, E. S. (2014): 2013 Atlantic Hurricane Season. National Hurricane Center Annual Summary. 2013 Atlantic Hurricane Season. Online document of the National Hurricane Center. URL: https://www.nhc.noaa.gov/data/tcr/summary_ atlc_2013.pdf. Last access: October 2020.

Blott, S. J., Pye, K. (2012): Particle size scales and classification of sediment types based on particle size distributions: Review and recommended procedures. Sedimentology 59: 2071-2096.

Blume, H.-P., Stahr, K., Leinweber, P. (2011): Bodenkundliches Praktikum. 3. edition, Spektrum Akademischer Verlag, Heidelberg, 255 pp.

Borja-Baeza, R. C., Esteban-Chávez, O., Marcos-López, J., Peña-Garnica, R. J., Alcántara-Ayala, I. (2006): Slope Instability on Pyroclastic Deposits: Landslide Distribution and Risk Mapping in Zacapoaxtla, Sierra Norte De Puebla, Mexico. Journal of Mountain science 3 (1): 1-19.

Bossi, G., Cavalli, M., Crema, S., Frigerio, S., Quan Luna, B., Mantovani, M., Marcato, G., Schenato, L., Pasuto, A. (2015): Multi-temporal LiDAR-DTMs as a tool for modelling a complex landslide: a case study in the Rotolon catchment (eastern Italian Alps). Natural Hazards and Earth System Sciences 15: 715-722.

Brabb, E. E. (1991): The world landslide problem. Episodes 14 (1): 52-61.

Brardinoni, F., Church, M. (2004): Representing the landslide magnitude-frequency relation: capilano river basin, British Columbia. Earth Surface Processes and Landforms 29: 115-124.

Brückl, E., Brunner, F. K., Kraus, K. (2006): Kinematics of a deep-seated landslide derived from photogrammetric, GPS and geophysical data. Engineering Geology 88: 149-159.

Brus, D. J., de Gruijter, J. J., Marsma, B. A., Visschers, R., Bregt, A. K., Breeuwsma, A. (1996): The performance of spatial interpolation methods and choropleth maps to estimate properties at points: a soil survey case study. Environmetrics 7: 1-16.

Bruster-Flores, J. L., Ortiz-Gómez, R., Ferriño-Fierro, A. L., Guerra-Cobián, V. H., Burgos-Flores, D., Lizárraga-Mendiola, L. G. (2019): Evaluation of Precipitation Estimates CMORPH-CRT on Regions of Mexico with Different Climates. Water 11 (8): 1722. DOI: 10.3390/w11081722.

Bunn, M. D., Leshchinsky, B. A., Olsen, M. J., Booth, A. (2019): A Simplified, Object-Based Framework for Efficient Landslide Inventorying Using LIDAR Digital Elevation Model Derivatives. Remote Sensing 11 (3): 303. DOI: 10.3390/rs11030303.

Buša, J., Rusnák, M., Kušnirák, D., Greif, V., Bednarik, M., Putiška, R., Dostál, I., Sládek, J., Rusnáková, D. (2020): Urban landslide monitoring by combined use of multiple methodologies - a case study on Sv. Anton town, Slovakia. Physical Geography 41 (2): 169-194.

Caballero, L., Macías, J. L., García-Palomo, A., Saucedo, G. R., Borselli, L., Sarocchi, D., Sánchez, J. M. (2006): The September 8–9, 1998 Rain-Triggered Flood Events at Motozintla, Chiapas, Mexico. Natural Hazards 39: 103-126.

Capra, L., Lugo-Hubp, J., Dávila-Hernández, N. (2003): Fenómenos de remoción en masa en el poblado de Zapotitlán de Méndez, Puebla: relación entre litología y tipo de movimiento. Revista Mexicana de Ciencias Geológicas 20 (2): 95-106.

Capra, L., Lugo-Hubp, J., Borselli, L. (2007): Mass movements in tropical volcanic terrains: the case of Teziutlán (México). Engineering Geology 69: 359-379.

Carrara, A., Cardinali, M., Guzzetti, F., Reichenbach, P. (1995): GIS Technology in Mapping Landslide Hazard. In: Carrara, A., Guzzetti, F. (Eds.), Geographical Information Systems in Assessing Natural Hazards. Volume 5, Springer Netherlands, Dordrecht, pp. 35-175.

Carrara, A., Bitelli, G., Carla, R. (1997): Comparison of techniques for generating digital terrain models from contour lines. International Journal of Geographical Information Science 11 (5): 451-473.

Carter, M., Bentley, S. P. (1985): The geometry of slip surfaces beneath landslides: predictions from surface measurements. Canadian Geotechnical Journal 22 (2): 234-238.

Casagli, N., Frodella, W., Morelli, S., Tofani, V., Ciampalini, A., Intrieri, E., Raspini, F., Rossi, G., Tanteri, L., Lu, P. (2017): Spaceborne, UAV and ground-based remote

sensing techniques for landslide mapping, monitoring and early warning. Geoenvironmental Disasters 4 (9): 1-23.

Cascini, L., Bonnard, C., Corominas, J., Jibson, R., Montero-Olarte, J. (2005): Landslide hazard and risk zoning for urban planning and development. In: Hungr, O., Fell, R., Couture, R., Eberhardt, E. (Eds.), Landslide Risk Management, Proceeding of the International Conference on Landslide Risk Management, Vancouver, Canada. Taylor & Francis Group, London, pp. 199-235.

Cascini, L., Ciurleo, M., Di NOcera, S. (2017): Soil depth reconstruction for the assessment of the susceptibility to shallow landslides in fine-grained slopes. Landslides 14: 459-471.

Chalupa, V., Pánek, T., Táborík, P., Klimeš, J., Hartvich, F., Grygar, R. (2018): Deep-seated gravitational slope deformations controlled by the structure of flysch nappe outliers: Insights from large-scale electrical resistivity tomography survey and LiDAR mapping. Geomorphology 321: 174-187.

Chelli, A., Mandrone, G., Truffelli, G. (2006): Field investigations and monitoring as tools for modelling the Rossena castle landslide (Northern Appennines, Italy). Landslides 3: 252-259.

Chen, R.-F., Chang, K.-J., Angelier, J., Chan, Y.-C., Deffontaines, B., Lee, C.-T., Lin, M.-L. (2006): Topographical changes revealed by high-resolution airborne LiDAR data: The 1999 Tsaoling landslide induced by the Chi–Chi earthquake. Engineering Geology 88: 160-172.

Chen, S. C., Chen, C. Y., Huang, W. Y. (2019): Exploring landslide erosion volume-area scaling relationships by slip depth using changes in DTMs for basin sediment volume estimation. Journal of Mountain Science 16 (3): 581-594.

Chiang, J.-L., Kuo, C.-M. (2020): Evaluation of rainfall-induced large-scale landslide potential using Scoops3D. EGU General Assembly 2020, EGU2020-6397. DOI: 10.5194/egusphere-egu2020-6397.

Chowdhury, R., Flentje, P., Bhattacharya, G. (2010): Geotechnical Slope Analysis. Taylor & Francis Group, Boca Raton, 774 pp.

Cignetti, M., Godone, D., Wrzesniak, A., Giordan, D. (2019): Structure from Motion Multisource Application for Landslide Characterization and Monitoring: The Champlas du Col Case Study, Sestriere, North-Western Italy. Sensors 19 (2364): 1-23.

Claessens, L., Heuvelink, G. B. M., Schoorl, J. M., Veldkamp, A. (2005): DEM resolution effects on shallow landslide hazard and soil redistribution modeling. Earth Surface Processes and Landforms 30: 461-477.

Clapuyt, F., Vanacker, V., Van Oost, K. (2016): Reproducibility of UAV-based earth topography reconstructions based on Structure-from-Motion algorithms. Geomorphology 260: 4-15.

Claude, A., Ivy-Ochs, S., Kober, F., Antognini, M., Salcher, B., Kubik, P. W. (2014): The Chironico landslide (Valle Leventina, southern Swiss Alps): age and evolution. Swiss Journal of Geosciences 107: 273-291.

Clayton, R. W., Trampert, J., Rebollar, C., Ritsema, J., Persaud, P., Paulssen, H., Pérez-Campos, X., van Wettum, A., Pérez-Vertti, A., DiLuccio, F. (2004): The NARS-Baja Seismic Array in the Gulf of California Rift Zone. Margins Newsletter 13: 1-4.

Concha-Dimas, A., Cerca, M., Rodríguez, S. R., Watters, R. J. (2005): Geomorphological evidence of the influence of pre-volcanic basement structure on emplacement and deformation of volcanic edifices at the Cofre de Perote - Pico de Orizaba chain and implications for avalanche generation. Geomorphology 72: 19-39.

Conrad, O., Bechtel, B., Bock, M., Dietrich, H., Fischer, E., Gerlitz, L., Wehberg, J., Wichmann, V., Böhner, J. (2015): System for Automated Geoscientific Analyses (SAGA) v. 2.1.4. Geoscientific Model Development 8: 1991-2007.

Cook, K. L. (2017): An evaluation of the effectiveness of low-cost UAVs and structure from motion for geomorphic change detection. Geomorphology 278: 195-208.

Corominas, J., van Westen, C., Frattini, P., Cascini, L., Malet J.-P., Fotopoulouet, S., Catani, F., Van Den Eeckhaut, M., Mavrouli, O., Agliardi, F., Pitilakis, K., Winter, M. G., Pastor, M., Ferlisi, S., Tofani, V., Hervás, J., Smith, J. T. (2014): Recommendations for the quantitative analysis of landslide risk. Bulletin of Engineering Geology and the Environment 73: 209-263.

Corsini, A., Borgatti, L., Cervi, F., Dahne, A., Ronchetti, F., Sterzai, P. (2009): Estimating mass-wasting processes in active earth slides – earth flows with time-series of High-Resolution DEMs from photogrammetry and airborne LiDAR. Natural Hazards and Earth System Sciences 9: 433-439.

Cressie, N. (1990): The Origins of Kriging. Mathematical Geology 22 (3): 239-252.

Cruden, D. M., Varnes, D. J. (1996): Landslide Types and Processes. In: Turner, A. K., Schuster, R. L. (Eds.), Landslides: Investigation and Mitigation. Transportation Research Board Special Report 247. National Academy Press, Washington DC, pp. 36-75.

Dachroth, W. (2017): Handbuch der Baugeologie und Geotechnik. 4. edition, Springer Berlin Heidelberg, Berlin Heidelberg, 747 pp.

Dai, F. C., Lee, C. F. (2001): Frequency - volume relation and prediction of rainfall induced landslides. Engineering Geology 59: 253-266.

Damm, B., Terhorst, B. (2010): A model of slope formation related to landslide activity in the Eastern Prealps, Austria. Geomorphology 122 (3-4): 338-350.

Damm, B., Terhorst, B., Ottner, F. (2013): Geotechnical properties of periglacial cover beds (Chapter 5). In: Kleber, A., Terhorst, B. (Eds.), Mid-Latitude Slope Deposits (Cover Beds), Developments in Sedimentology 66. Elsevier, Amsterdam/Boston/ Heidelberg/London/New York/Oxford, pp. 153-170.

de Bari, C., Lapenna, V., Perrone, A., Puglisi, C., Sdao, F. (2011): Digital photogrammetric analysis and electrical resistivity tomography for investigating the Picerno landslide (Basilicata region, southern Italy). Geomorphology 133: 34-46.

Del Carmen Velázquez Simental, L. (2014): Atlas del Agua en México 2014. Secretaría de Medio Ambiente y Recursos Naturales, Mexico City, 138 pp.

Delgadillo, C. M., Villaseñor Ríos, J. L., Dávila Aranda, P. (2003): Endemism in the Mexican Flora: A Comparative Study in Three Plant Groups. Annals of the Missouri Botanical Garden 90: 25-34.

Demoulin, A. (2006): Monitoring and mapping landslide displacements: a combined DGPS-stereophotogrammetric approach for detailed short- and long-term rate estimates. Terra Nova 18 (4): 290-298.

Deng, H., Wu, L. Z., Huang, R. Q., Guo, X. G., He, Q. (2017): Formation of the Siwanli ancient landslide in the Dadu River, China. Landslides 14: 385-394.

Desmet, P. J. (1997): Effects of interpolation errors on the analysis of DEMs. Earth Surface Processes and Landforms 22: 563-580.

Deutsches Institut für Normung (1976): DIN 1055: Design loads for buildings: soil properties: unit weight, angle of friction, cohesion, wall friction. Beuth Verlag GmbH, Berlin, 11 pp.

Deutsches Institut für Normung (1996a): DIN 18123-1: Soil, Investigation and testing - Determination of grain-size distribution. Beuth Verlag GmbH, Berlin, 12 pp.

Deutsches Institut für Normung (1996b): DIN 18129: Soil, Investigation and testing - Determination of lime content. Beuth Verlag GmbH, Berlin, 4 pp.

Deutsches Institut für Normung (1996c): DIN ISO 10694: Determination of organic and total carbon after dry combustion (elementary analysis). Beuth Verlag GmbH, Berlin, 5 pp.

Deutsches Institut für Normung (1997): DIN 18122-1: Soil, Investigation and testing - consistency limits. Part 1: Determination of liquid limit and plastic limit. Beuth Verlag GmbH, Berlin, 7 pp.

Deutsches Institut für Normung (1998a): DIN 18130-1: Soil, investigation and testing - Determination of the coefficient of water permeability - Part 1: Laboratory tests. Beuth Verlag GmbH, Berlin, 20 pp.

Deutsches Institut für Normung (1998b): DIN 19683-9: Methods of soil investigations for agricultural engineering - Physical laboratory tests - Part 9: Determination of the saturated hydraulic water conductivity in the cylindrical core-cutter. Beuth Verlag GmbH, Berlin, 7 pp.

Deutsches Institut für Normung (2001): DIN ISO 11272: Soil quality - Determination of dry bulk density. Beuth Verlag GmbH, Berlin, 10 pp.

Deutsches Institut für Normung (2002): DIN ISO 11277: Soil quality - Determination of particle size distribution in mineral soil material - Method by sieving and sedimentation. Beuth Verlag GmbH, Berlin, 38 pp.

Deutsches Institut für Normung (2005): DIN ISO 10390: Soil quality - Determination of pH. Beuth Verlag GmbH, Berlin, 9 pp.

Deutsches Institut für Normung (2008): DIN 4220: Bodenkundliche Standortbeurteilung - Kennzeichnung, Klassifizierung und Ableitung von Bodenkennwerten (normative und nominale Skalierungen). Beuth Verlag GmbH, Berlin, 24 pp.

Deutsches Institut für Normung (2011): DIN 18196: Earthworks and foundations - Soil classification for civil engineering purposes. Beuth Verlag GmbH, Berlin, 13 pp.

Devkota, S., Shakya, N., Sudmeier, K., McAdoo, B., Jaboyedoff, M. (2018): Predicting soil depth to bedrock in an anthropogenic landscape: a case study of Phewa Watershed in Panchase region of Central-Western Hills, Nepal. Journal of Nepal Geological Society 55 (1): 173-182.

Devoli, G., Tiranti, D., Cremonini, R., Sund, M., Boje, S. (2018): Comparison of landslide forecasting services in Piedmont (Italy) and Norway, illustrated by events in late spring 2013. Natural Hazards and Earth System Sciences 18: 1351-1372.

Díaz, J. D. G., Monterroso, A. I., Ruiz, P., Lechuga, L. M., Álvarez, A. C. C., Asensio, C. (2019): Soil moisture regimes in Mexico in a global 1.5°C warming scenario. International Journal of Climate Change Strategies and Management 11: 465-482.

Díaz, S. R., Cadena, E., Adame, S., Dávila, N. (2020): Landslides in Mexico: their occurrence and social impact since 1935. Landslides 17: 379-394.

Dietrich, W. E., Reiss, R., Hsu, M. L., Montgomery, D. R. (1995): A process-based model for colluvial soil depth and shallow landsliding using digital elevation data. Hydrological Processes 9 (3-4): 383-400.

Dietrich, W. E., Montgomery, D. R. (1998): SHALSTAB: a digital terrain model for mapping shallow landslide potential. National Council of the Paper Industry for Air and Stream Improvement (NCASI) Technical Report, 26 pp.

Dixon, J. C. (2015): Soil morphology in the critical zone: The role of climate, geology, and vegetation in soil formation in the critical zone. Developments in Earth Surface Processes 19: 147-172.

DJI (2019): Phantom 3 Professional. URL: https://www.dji.com/de/phantom-3-pro. Latest access: September 2020.

Domínguez Morales, L., Castañeda Martínez, A., Gonzáles Huesca, A. E. (2016): Análisis de umbrales de lluvia que detonan deslizamientos y sus posibles aplicaciones en unsistemas de alerta temprana por inestabilidad de laderas. Subdirección de Dinámica de Suelos y Procesos Gravitacionales CENAPRED, 28 pp. https://www1.cenapred.unam.mx/COORDINACION_ADMINISTRATIVA/SRM/FRACCION_XLI_A/23.pdf.

Dou, J., Paudel, U., Oguchi, T., Uchiyama, S., Hayakawa, Y. S. (2015): Shallow and Deep-Seated Landslide Differentiation Using Support Vector Machines: A Case Study of the Chuetsu Area, Japan. Terrestrial, Atmospheric and Oceanic Sciences 26 (2): 227-239.

Duncan, J. M., Wright, S. G., Brandon, T. L. (2014): Soil strength and slope stability. 2. edition, John Wiley & Sons, Inc., Hoboken New Jersey, 317 pp.

Ehrlich, M., Pereira da Costa, D., Cerqueira Silva, R. (2021): Long-term monitoring of the behavior of a talus-colluvium deposit. Landslides 18: 2225-2245.

Eker, R., Aydin, A., Hübl, J. (2018): Unmanned aerial vehicle (UAV)-based monitoring of a landslide: Gallenzerkogel landslide (Ybbs-Lower Austria) case study. Environmental Monitoring Assessment 190 (28): 1-14.

Eltner, A., Kaiser, A., Castillo, C., Rock, G., Neugirg, F., Abellán, A. (2016): Image-based surface reconstruction in geomorphometry – merits, limits and developments. Earth Surface Dynamics 4: 359-389.

Eltner, A., Kaiser, A., Abellan, A., Schindewolf, M. (2017): Time lapse structure-from-motion photogrammetry for continuous geomorphic monitoring. Earth Surface Processes and Landforms 42 (14): 2240-2253.

Emberson, R., Kirschbaum, D., Stanley, T. (2020): New global characterisation of landslide exposure. Natural Hazards and Earth System Sciences 20: 3413-3424.

Erginal, A. E., Öztürk, B., Ekinci, Y. L., Demirci, A. (2009): Investigation of the nature of slip surface using geochemical analyses and 2-D electrical resistivity tomography: a case study from Lapseki area, NW Turkey. Environmental Geology 58 (6): 1167-1175.

Esri World Imagery (2019): World Imagery [basemap]. URL: https://www.arcgis.com/home/item. html?id=10df2279f9684e4a9f6a7f08febac2a9. Latest access: December 2019.

Estrada-Contreras, I., Equihua, M., Castillo-Campos, G., Soto, O. R. (2015): Climate change and effects on vegetation in Veracruz, Mexico: An Approach using ecological niche modelling. Acta Botanica Mexicana 112: 73-93.

Fall, M., Azzam, R., Noubactep, C. (2006): A multi-method approach to study the stability of natural slopes and landslide susceptibility mapping. Engineering Geology 82: 241-263.

Fazio, N. L., Perrotti, M., Andriani, G. F., Mancini, F., Rossi, P., Castagnetti, C., Lollino, P. (2019): A new methodological approach to assess the stability of discontinuous rocky cliffs using in-situ surveys supported by UAV-based techniques and 3-D finite element model: a case study. Engineering Geology 260: 105205. DOI: 10.1016/j.enggeo.2019.105205.

Federici, P. R., Puccinelli, A., Cantarelli, E., Casarosa, N., D'Amato Avanzi, G., Falaschi, F., Giannecchin, R., Pochin, A., Ribolin, A., Bottai, M., Salvati, N., Testi, C. (2007): Multidisciplinary investigations in evaluating landslide susceptibility-An example in the Serchio River valley (Italy). Quaternary International 171-172: 52-63.

Ferrari, L., Orozco-Esquivel, T., Manea, V., Manea, M. (2012): The dynamic history of the Trans-Mexican Volcanic Belt and the Mexico subduction zone. Tectonophysics 522-523: 122-149.

Fleuchaus, P., Blum, P., Wilde, M., Terhorst, B., Butscher, C. (2021): Retrospective evaluation of landslide susceptibility maps and review of validation practice. Environmental Earth Sciences 80: 485. DOI: 10.1007/s12665-021-09770-9.

Flores, P., Alcántara-Ayala, I. (2012) Susceptibility to shallow landslides of soil in the municipality of Temoaya, Mexico: multicriteria analysis. Investigaciones Geográficas, Boletín del Instituto de Geografía, UNAM 77: 31-47.

Formetta, G., Rago, V., Capparelli, G., Rigon, R., Muto, F., Versace, P. (2014): Integrated Physically based system for modeling landslide susceptibility. Procedia Earth and Planetary Science 9: 74 82.

Froude, M. J., Petley, D. N. (2018): Global fatal landslide occurrence from 2004 to 2016. Natural Hazards and Earth System Sciences 18: 2161-2181.

Füssl, M. L. (2020): Ableitung hydrologischer Parameter aus sedimentologischen Eigenschaften und deren Bewertung. Bachelor thesis, unpublished, 58 pp.

Furuya, T., Jiang, J.-C. (2015): Determination of slip surfaces in fracture zone landslides using oriented borehole core samples. International Journal of GEOMATE 8 (1): 1151-1158.

García-Aguirre, M. C., Álvarez, R., Dirzo, R., Ortiz, M. A., Eng, M. M. (2010): Delineation of biogeomorphic land units across a tropical natural and humanized terrain in Los Tuxtlas, Veracruz, México. Geomorphology 121: 245-256.

Gariano, S. F., Guzzetti, F. (2016): Landslides in a changing climate. Earth-Science Reviews 162: 227 252.

Geertsema, M., Pojar, J. J. (2007): Influence of landslides on biophysical diversity — A perspective from British Columbia. Geomorphology 89: 55-69.

Gerez-Fernández, P., del Rosario Pineda-López, M. (2011): The forests of Veracruz in the context of a rEDD+ state strategy. Madera y Bosques 17 (3): 7-27.

Geo-Slope International (2018): Stability modeling with GeoStudio. GEOSLOPE International Ltd., Calgary, 244 pp.

Giddings, M. S., Rutherford, B. M., Maarouf, A. (2005): Standardized Precipitation Index Zones for México. Atmósfera 18: 33-56.

Glendell, M., McShane, G., Farrow, L., James, M. R., Quinton, J., Anderson, K., Evans, M., Benaud, P., Rawlins, B., Morgan, D., Jones, L., Kirkham, M., DeBell, L., Quine, T. A., Lark, M., Rickson, J., Brazier, R. E. (2017): Testing the utility of structure-from-motion photogrammetry reconstructions using small unmanned aerial vehicles and ground photography to estimate the extent of upland soil erosion. Earth Surface Processes and Landforms 42 (12): 1860-1871.

Gobierno de México (2020): Mapa Nacional de Susceptibilidad por Inestabilidad de Laderas. URL: http://www.atlasnacionalderiesgos.gob.mx/archivo/inestabilidad-laderas.html. Latest access: September 2020.

Gómez-Díaz, J. A., Brast, K., Degener, J., Krömer, T., Ellis, E., Heitkamp, F., Gerold, G. (2018): Long-Term Changes in Forest Cover in Central Veracruz, Mexico (1993-2014). Tropical Conservation Science 11: 1-12.

Gómez-Tuena, A., LaGatta, A. B., Langmuir, C. H., Goldstein, S. L., Ortega-Gutierrez, F. (2003): Temporal control of subduction magmatism in the eastern Trans-Mexican

Volcanic Belt: Mantle sources, slab contributions, and crustal contamination. Geochemistry, Geophysics, Geosystems 4. DOI: 10.1029/2003GC000524.

Gómez-Tuena, A., Orozco-Esquivel, Ma. T., Ferrari, L. (2007): Igneous petrogenesis of the Trans-Mexican Volcanic Belt. In: Alaniz-Álvarez, S. A., Nieto-Samaniego, Á. F. (Eds.), Geology of México: Celebrating the Centenary of the Geological Society of México. Geological Society of America, Boulder (U.S.A), pp. 129-181.

Google Earth (2021): El Capulín, Veracruz, Mexico. Imagery date 2010. 19° 44′ 12.62″ N, 96° 43′ 14.66″ W, eye alt 1.64 km. Image © 2021 Maxar Technologies. Latest access: January 2021.

Grotzinger, J., Jordan, T. (2017): Allgemeine Geologie. 7. edition, Springer Spektrum, New York, 769 pp.

Gupta, V., Nautiyal, H., Kumar, V., Jamir, I., Tandon, R. S. (2016): Landslide hazards around Uttarkashi township, Garhwal Himalaya, after the tragic flash flood in June 2013. Natural Hazards 80: 1689-1707.

Guthrie, R. H., Friele, P., Allstadt, K., Roberts, N., Evans, S. G., Delaney, K. B., Roche, D., Clague, J. J., Jakob, M. (2012): The 6 August 2010 Mount Meager rock slide-debris flow, Coast Mountains, British Columbia: characteristics, dynamics, and implications for hazard and risk assessment. Natural Hazards and Earth System Sciences 12: 1-18.

Guzmán Lagunes, N. Z., Morales Barrera, W. V. (2014): La Gestión del riesgo por deslizamientos de laderas en el Estado de Veracruz, durante el 2013. Gobierno del estado de Veracruz, Secretaría de Protección Civil, Xalapa, Veracruz, 114 pp.

Guzzetti, F., Carrara, A., Cardinali, M., Reichenbach, P. (1999): Landslide hazard evaluation: a review of current techniques and their application in a multi-scale study, Central Italy. Geomorphology 31: 181-216.

Guzzetti, F., Ardizzone, F., Cardinali, M., Rossi, M., Valigi, D. (2009): Landslide volumes and landslide mobilization rates in Umbria, central Italy. Earth and Planetary Science Letters 279: 222-229.

Guzzetti, F., Mondini, A. C., Cardinali, M., Fiorucci, F., Santangelo, M., Chang, K.-T. (2012): Landslide inventory maps: New tools for an old problem. Earth-Science Reviews 112: 42-66.

Hack, R. (2000): Geophysics for slope stability. Surveys in Geophysics 21: 423-448.

Hackney, C., Clayton, A. I. (2015): Unmanned Aerial Vehicles (UAVs) and their application in geomorphic mapping. In: Clarke, L. E., Nield, J. M. (Eds.),

Geomorphological techniques, chapter 2.17. Online edition, British Society for Geomorphology, London, pp. 1-12.

Haneberg, W. C., Cole, W. F., Kasali, G. (2009): High-resolution lidar-based landslide hazard mapping and modeling, UCSF Parnassus Campus, San Francisco, USA. Bulletin of Engineering Geology and the Environment 68: 263-276.

Harwin, S., Lucieer, A. (2012): Assessing the Accuracy of Georeferenced Point Clouds Produced via Multi-View Stereopsis from Unmanned Aerial Vehicle (UAV) Imagery. Remote Sensing 4 (6): 1573-1599.

Hashemi-Beni, L., Jones, J., Thompson, G., Johnson, C., Gebrehiwot, A. (2018): Challenges and Opportunities for UAV-Based Digital Elevation Model Generation for Flood-Risk Management: A Case of Princeville, North Carolina. Sensors 18: 3843. DOI: 10.3390/s18113843.

He, Y., Beighley, R. E. (2008): GIS-based regional landslide susceptibility mapping: a case study in southern California. Earth Surface Processes and Landforms 33: 380-393.

He, J., Qiu, H., Qu, F., Hu, S., Yang, D., Shen, Y., Zhang, Y., Sun, H., Cao, M. (2021): Prediction of spatiotemporal stability and rainfall threshold of shallow landslides using the TRIGRS and Scoops3D models. Catena 197: 104999. DOI: 10.1016/j.catena.2020.104999.

Heckmann, T., Vericat, D. (2018): Computing spatially distributed sediment delivery ratios: inferring functional sediment connectivity from repeat high-resolution digital elevation models. Earth Surface Processes and Landforms 43: 1547-1554.

Heidari, A., Raheb, A. (2020): Geochemical indices of soil development on basalt rocks in arid to sub-humid climosequence of Central Iran. Journal of Mountain Science 17: 1652-1669.

Heine, K. (1994): Present and Past Geocryogenic Processes in Mexico. Permafrost and Periglacial Processes 5: 1-12.

Hernández-Madrigal, V., Mora-Chaparro, J., Garduño-Monroy, V. (2011): Large block slide at San Juan Grijalva, Northwest Chiapas, Mexico. Landslides 8: 109-115.

Hernández-Santana, J. R., Méndez-Linares, A. P., López-Portillo, J. A., Preciado-López, J. C. (2016): Coastal geomorphological cartography of Veracruz State, Mexico. Journal of Maps 12 (2): 316-323.

Hibert, C., Grandjean, G., Bitri, A., Travelletti, J., Malet, J.-P. (2012): Characterizing landslides through geophysical data fusion: Example of the La Valette landslide (France). Engineering Geology 128: 23-29.

Highland, L. M., Bobrowsky, P. (2008): The landslide handbook - A guide to understand landslides. U.S. Geological Survey Circular, Reston, Virginia, 129 pp.

Hinojosa-Corona, A., Rodríguez-Moreno, V. M., Munguía-Orozco, L., Meillón-Menchaca, O. (2011): El deslizamiento de ladera de noviembre 2007 y generación de una presa natural en el río Grijalva, Chiapas, México. Boletín de la Sociedad Geológica Mexicana 63 (1): 15-38.

Hölbling, D., Eisank, C., Albrecht, F., Vecchiotti, F., Friedl, B., Weinke, E., Kociu, A. (2017): Comparing Manual and Semi-Automated Landslide Mapping Based on Optical Satellite Images from Different Sensors. Geosciences 7: 37. DOI: 10.3390/geosciences7020037.

Hsieh, Y.-C., Chan, Y.-C., Hu, J.-C. (2016): Digital Elevation Model Differencing and Error Estimation from Multiple Sources: A Case Study from the Meiyuan Shan Landslide in Taiwan. Remote Sensing 8 (199): 1-20.

Hubbard, B. E., Sheridan, M. F., Carrasco- Núñez, G., Díaz-Castellón, R., Rodríguez, S. R. (2007): Comparative lahar hazard mapping at Volcan Citlaltépetl, Mexico using SRTM, ASTER and DTED-1 digital topographic data. Journal of Volcanology and Geothermal Research 160: 99-124.

Hugenholtz, C. H., Whitehead, K., Brown, O. W., Barchyn, T. E., Moorman, B. J., LeClair, A., Riddell, K., Hamilton, T. (2013): Geomorphological mapping with a small unmanned aircraft system (sUAS): Feature detection and accuracy assessment of a photogrammetrically-derived digital terrain model. Geomorphology 194: 16-24.

Hungr, O., Evans, S. G. (2004): Entrainment of debris in rock avalanches: An analysis of a long run-out mechanism. Geological Society of America Bulletin 116 (9/10): 1240-1252.

Hungr, O., Leroueil, S., Picarelli, L. (2014): The Varnes classification of landslide types, an update. Landslides 11: 167-194.

INEGI (2019): Modelos Digitales de Elevación. Xalapa. 1 : 50 000. URL: https://www.inegi.org.mx/app/biblioteca/ficha.html?upc=702825733100. Latest access: January 2019.

INEGI (2020a): Conjunto de datos vectoriales de la carta topográfica. Xalapa. 1 : 50 000. URL: https://www.inegi.org.mx/app/biblioteca/ficha.html?upc=702825638030. Latest access: January 2020.

INEGI (2020b): Red hidrográfica. Escala 1:50 000. Edición 2.0. Subcuenca hidrográfica RH27Ac R. Yachite. Cuenca R. Nautla y Otros. RH Tuxpan - Nautla.

https://www.inegi.org.mx/app/biblioteca/ficha.html?upc=889463130567. Latest access: February 2020.

INEGI (2020c): Servicio de Mapas Web. URL: https://www.inegi.org.mx/servicios/wsinfogeo/default.html. Latest access: February 2020.

Iñeguez, J. B. (2016): Back-Analysis of Slope Failures by Numerical Techniques. Electronic Journal of Geotechnical Engineering 21 (2): 615-625.

IUSS Working Group (2014): World reference base for soil resources 2014, update 2015: International soil classification system for naming soils and creating legends for soil maps. World Soil Resources Reports 106. FAO, Rome, 192 pp.

Jaboyedoff, M., Oppikofer, T., Abellán, A., Derron, M.-H., Loye, A., Metzger, R., Pedrazzini, A. (2012): Use of LIDAR in landslide investigations: a review. Natural Hazards 61: 5-28.

Jaboyedoff, M., Carrea, D., Derron, M.-H., Oppikofer, T., Penna, I. M., Rudaz, B. (2020): A review of methods used to estimate initial landslide failure surface depths and volumes. Engineering Geology 267: 105478. DOI: 10.1016/j.enggeo.2020.105478.

Jäger, D., Sandmeier, C., Schwindt, D., Terhorst, B. (2013): Geomorphological and geophysical analyses in a landslide area near Ebermannstadt, Northern Bavaria. E & G Quaternary Science Journal 62 (2): 150-161.

Jäger, D., Menzies, J., Terhorst, B. (2014): Micromorphology in landslide sediments – a different approach for investigating mass movement deposits. Proceedings of the International Conference on Analysis and Management of Changing Risks for Natural Hazards, 18-19th November 2014, Padua, Italy. AP17, 10 pp.

James, M. R., Robson, S. (2012): Straightforward reconstruction of 3D surfaces and topography with a camera: Accuracy and geoscience application. Journal of Geophysical Research 117 (F03017): 1-17.

James, M. R., Robson, S., d'Oleire-Oltmanns, S., Niethammer, U. (2017a): Optimising UAV topographic surveys processed with structure-from-motion: Ground control quality, quantity and bundle adjustment. Geomorphology 280: 51-66.

James, M. R., Robson, S., Smith, M. W. (2017b): 3-D uncertainty-based topographic change detection with structure-from-motion photogrammetry: precision maps for ground control and directly georeferenced surveys. Earth Surface Processes and Landforms 42: 1769-1788.

James, M. R., Chandler, J. H., Eltner, A., Fraser, C., Miller, P. E., Mills, J. P., Noble, T., Robson, S., Lane, S. N. (2019): Guidelines on the use of structure-from-motion

photogrammetry in geomorphic research. Earth Surface Processes and Landforms 44: 2081-2084.

Jáuregui, E. (2003): Climatology of landfalling hurricanes and tropical storms in Mexico. Atmósfera 16 (4): 193-204.

Jeong, S., Kassim, A., Hong, M., Saadatkhah, N. (2018): Susceptibility Assessments of Landslides in Hulu Kelang Area Using a Geographic Information System-Based Prediction Model. Sustainability 10: 2941. DOI: 10.3390/su10082941.

Jiménez-Jiménez, S. I., Ojeda-Bustamante, W., de Jesús Marcial-Pablo, M., Enciso, J. (2021): Digital Terrain Models Generated with Low-Cost UAV Photogrammetry: Methodology and Accuracy. International Journal of Geo-Information 10 (5): 285. DOI: 10.3390/ijgi10050285.

Jiménez Sánchez, M. (2002): Slope deposits in the Upper Nalón River Basin (NW Spain): an approach to a quantitative comparison. Geomorphology 43: 165-178.

Jongmans, D., Garambois, S. (2007): Geophysical investigation of landslides: a review. Bulletin of the Geological Society of France 178: 101-112.

Jongmans, D., Bièvre, G., Renalier, F., Schwartz, S., Beaurez, N., Orengo, Y. (2009): Geophysical investigation of a large landslide in glaciolacustrine clays in the Trièves area (French Alps). Engineering Geology 109: 45-56.

Kalenchuk, K. S., Hutchinson, D. J., Diederichs, M. S. (2009): Application of spatial prediction techniques to defining three-dimensional landslide shear surface geometry. Landslides 6: 321-333.

Kalenchuk, K. S., Diederichs, M. S., Hutchinson, D. J. (2012): Three-dimensional numerical simulations of the Downie Slide to test the influence of shear surface geometry and heterogeneous shear zone stiffness. Computers & Geosciences 26: 21-38.

Kamp, U., Growley, B. J., Khattak, G. A., Owen, L. A. (2008): GIS-based landslide susceptibility mapping for the 2005 Kashmir earthquake region. Geomorphology 101: 631-642.

Kaunda, R. B. (2010): A linear regression framework for predicting subsurface geometries and displacement rates in deep-seated, slow-moving landslides. Engineering Geology 114: 1-9.

Keefer, D. K., Larsen, M. C. (2009): Assessing landslide hazards. Science 316 (5828): 1136-1138.

Kim, K. E. (1996): Adaptive majority filtering for contextual classification of remote sensing data, International Journal of Remote Sensing 17 (5): 1083-1087.

Kjekstad, O., Highland, L. (2009): Economic and Social Impacts of Landslides. In: Sassa, K., Canuti, P. (Eds.), Landslides - Disaster Risk Reduction. Springer, Berlin, pp. 573-587.

Klose, M., Damm, B., Gerold, G. (2012): Analysis of Landslide Activity and Soil Moisture in Hillslope Sediments Using Landslide Database and Soil Water Balance Model. GEOÖKO XXXIII: 204-231.

Klose, M., Highland, L., Damm, B., Terhorst, B. (2014): Estimation of direct landslide costs in industrialized countries: Challenges, concepts, and case study. In: Sassa, K., Canuti, P., Yin, Y. (Eds.), Landslide Science for a Safer Geoenvironment, Vol. 2: Methods of Landslide Studies. Springer, Berlin, pp. 661-667.

Knapen, A., Kitutu, M. G., Poesen, J., Breugelmans, W., Deckers, J., Muwanga, A. (2006): Landslides in a densely populated county at the footslopes of Mount Elgon (Uganda): Characteristics and causal factors. Geomorphology 73: 149-165.

Koca, T. K., Koca, M. Y. (2019): Volume estimation and evaluation of rotational landslides using multi-temporal aerial photographs in Çağlayan dam reservoir area, Turkey. Arabian Journal of Geosciences 12 (140): 1-19.

Korup, O. (2006): Effects of large deep-seated landslides on hillslope morphology, western Southern Alps, New Zealand. Journal of Geophysical Research 111: F01018. DOI: 10.1029/2004JF000242.

Krahn, J. (2003): The 2001 R.M. Hardy Lecture: The limits of limit equilibrium analyses. Canadian geotechnical Journal 40: 643-660.

Krasilnikov, P., del Carmen Gutiérrez-Castorena, M., Ahrens, R. J., Cruz-Gaistardo, C.O., Sedov, S., Solleiro-Rebolledo, E. (2013): The soils of Mexico. Springer, New York, 181 pp.

Kreuzer, T. Damm, B. (2020): Automated digital data acquisition for landslide inventories. Landslides 17: 2205-2215.

Kuriakose, S., van Beek, L. P. H., van Westen, C. J. (2009): Parameterizing a physically based shallow landslide model in a data poor region. Earth Surface Processes and Landforms 34: 867-881.

Laberg, J. S., Vorren, T. O. (2000): The Trænadjupet Slide, offshore Norway Ð morphology, evacuation and triggering mechanisms. Marine Geology 171: 95-114.

Lague, D., Brodu, N., Leroux, J. (2015): Accurate 3D comparison of complex topography with terrestrial laser scanner: Application to the Rangitikei canyon (N-Z). ISPRS Journal of Photogrammetry and Remote Sensing 82: 10-26.

Lam, N. S. (1983): Spatial interpolation methods: A review. The American Cartographer 10 (2): 129-149.

Lane, S. N., Westaway, R. M., Hicks, M. D. (2003): Estimation of erosion and deposition volumes in a large, gravel-bed, braided ricer using synoptic remote sensing. Earth Surface Processes and Landforms 28: 249-271.

Larsen, I. J., Montgomery, D. R., Korup, O. (2010): Landslide erosion controlled by hillslope material. Nature Geoscience 3: 247-251.

Lascurain-Rangel, M., Avendaño-Reyes, S., Cházaro-Basañez, M., Geissert-Kientz, D., Villegas-Patraca, R., Gallo-Gómez, C. A., Gutiérrez-Báez, C. (2017): Floristic, vegetational and geographic characteristics of the Sierra de Chiconquiaco, Veracruz, Mexico. Botanical Sciences 95: 610-659.

Legorreta Paulín, G., Bursik, M., Lugo-Hubp, J., Zamorano Orozco, J. J. (2010): Effect of pixel size on cartographic representation of shallow and deep-seated landslide, and its collateral effects on the forecasting of landslides by SINMAP and Multiple Logistic Regression landslide models. Physics and Chemistry of the Earth 35: 137-148.

Legorreta Paulín, G., Lugo Hubp, J. (2013): Zonación de peligros por procesos gravitacionales en el flanco suroccidental del volcán Pico de Orizaba, México. Investigaciones Geográficas, Boletín 84: 20-31.

Legorreta Paulín, G., Bursik, M., Solene, P., Serdar, C., Lugo Hubp, J. (2014a): Mapping landforms for landslide hazards assessment on the SW flank of Pico de Orizaba volcano, Puebla-Veracruz, Mexico. Zeitschrift für Geomorphologie 58 (1): 81-93.

Legorreta Paulín, G., Bursik, M., Solene, P., Lugo Hubp, J., Paredes Mejía, L. M., Aceves Quesada, F. (2014b): Inventario multitemporal, análisis de susceptibilidad y estimación de volumen de deslizamientos en el flanco SW del volcán Pico de Orizaba, Puebla-Veracruz. Boletín de la Sociedad Geológica Mexicana 66 (2): 343-354.

Legorreta Paulín, G., Bursik, M., Zamorano Orózco, J. J., Figueroa García, J. E. (2015): Landslide susceptibility of volcanic landforms in the Río El Estado watershed, Pico de Orizaba volcano, Mexico. Natural Hazards 77: 559-674.

Lenz, A. (2019): Die Eigenschaften von Rutschhängen im Chiconquiaco-Gebirge im Transmexikanischen Vulkangürtel (Veracruz). Master thesis, Julius Maximilians University of Würzburg, unpublished, 78 pp.

Lepore, C., Arnone, E., Noto, L. V., Sivandran, G., Bras, R. L. (2013): Physically based modeling of rainfall-triggered landslides: a case study in the Luquillo forest, Puerto Rico. Hydrology and Erath System Sciences 17: 3371-3387.

Leser, H., Stäblein, G., Göbel, P. (1975): Geomorphologische Kartierung. Richtlinien zur Herstellung geomorphologischer Karten 1 : 25000. GMK-Schwerpunktprogramm. Berliner geographische Abhandlungen, Sonderheft. 2. edition, Institut für Physische Geographie der Freien Universität Berlin, Berlin, 39 pp.

Lindner, G., Schraml, K., Mansberger, R., Hübl, J. (2016): UAV monitoring and documentation of a large landslide. Applied Geomatics 8: 1-11.

Ling, C., Xu, Q., Zhang, Q., Ran, J., Lv, H. (2016): Application of electrical resistivity tomography for investigating the internal structure of a translational landslide and characterizing its groundwater circulation (Kualiangzi landslide, Southwest China). Journal of Applied Geophysics 131: 154-162.

Link, M. (1997): Die Rutschungen im Deggenhausertal – Geomorphologie, Alter und ein Vorwarnmodell. Berichte der Naturforschenden Gesellschaft zu Freiburg im Breisgau 86/87: 21-42.

Liu, Z., Qiu, H., Ma, S., Yang, D., Pei, Y., Du, C., Sun, H., Hu, S., Zhu, Y. (2021): Surface displacement and topographic change analysis of the Changhe landslide on September 14, 2019, China. Landslides 18: 1471-1483.

López-García, J., Alcántara-Ayala, I. (2012): Land-use change and hillslope instability in the Monarch Butterfly Biosphere Reserve, Central Mexico. Land Degradation & Development 23: 384-397.

Lopez-Infanzon, M. (1991): Petrologic study of the volcanic rocks in the Chiconquiaco-Palma Sola area, Central Veracruz, Mexico. Master of Science Thesis, Tulane University, New Orleans, 138 pp.

Lu, N., Godt, J. W. (2013): Hillslope Hydrology and Stability. Cambridge University Press, New York, 437 pp.

Lucieer, A., de Jong, S. M., Turner, D. (2014a): Mapping landslide displacements using Structure from Motion (SfM) and image correlation of multi-temporal UAV photography. Progress in Physical Geography 38 (1): 97-116.

Lucieer, A., Turner, D., King, D. H., Robinson, S. A. (2014b): Using an Unmanned Aerial Vehicle (UAV) to capture micro-topography of Antarctic moss beds. International Journal of Applied Earth Observation and Geoinformation 27: 53-62.

Lugo Hubp, J., Córdova, C. (1991): Regionalización geomorfológica de la república mexicana. Investigaciones geográficas 25: 25-63.

Malamud, B. D., Turcotte, D. L., Guzzetti, F., Reichenbach, P. (2004): Landslide inventories and their statistical properties. Earth Surface Processes and Landforms 29: 687-711.

Mancini, F., Castagnetti, C., Rossi, P., Dubbini, M., Fazio, N. L., Perrotti, M., Lollino, P. (2017): An Integrated Procedure to Assess the Stability of Coastal Rocky Cliffs: From UAV Close-Range Photogrammetry to Geomechanical Finite Element Modeling. Remote sensing 9: 1235. DOI: 10.3390/rs9121235.

Marchesini, I., Cencetti, C., De Rosa, P. (2009): A preliminary method for the evaluation of the landslides volume at a regional scale. Geoinformatica 13: 277-289.

Martins, T. D., Vieira, B. C., Fernandes, N. F., Oka-Fiori, C., Montgomery, D. R. (2017): Application of the SHALSTAB model for the identification of areas susceptible to landslides: Brazilian case studies. Revista de Geomofologie 19: 136-144.

Mathew, J., Kundu, S., Vinod Kumar, K., Pant, C. C. (2016): Hydrologically complemented deterministic slope stability analysis in part of Indian Lesser Himalaya. Geomatics, Natural Hazards and Risk 7 (5): 1557-1576.

Mendoza-Rosas, A. T., De la Cruz-Reyna, S. (2010): Hazard estimates for El Chichón volcano, Chiapas, México: a statistical approach for complex eruptive histories. Natural Hazards and Earth System Sciences 10: 1159-1170.

Michel, G. P., Kobiyama, M., Goerl, F. (2014): Comparative analysis of SHALSTAB and SINMAP for landslide susceptibility mapping in the Cunha River basin, southern Brazil. Journal of Soils and Sediments 14: 1266-1277.

Micheletti, N., Chandler, J. H., Lane, S. N. (2015): Section 2.2.2: Structure from Motion (SfM) Photogrammetry. In: Clarke, L. E., Nield, J. M. (Eds.), Geomorphological techniques, chapter 2 2.2. Online edition, British Society for Geomorphology, London, pp. 1-12.

Miller, B. G. N., Cruden, D. M. (2002): The Eureka River landslide and dam, Peace River Lowlands, Alberta. Canadian Geotechnical Journal 39: 863-878.

Mora, O. E., Lenzano, M. G., Toth, C. K., Grejner-Brzezinska, D. A., Fayne, J. V. (2018): Landslide Change Detection Based on Multi-Temporal Airborne LiDAR-Derived DEMs. Geosciences 8 (1): 23. DOI: 10.3390/geosciences8010023.

Morelli, S., Pazzi, V., Garduño Monroy, V. H., Casagli, N. (2017): Residual Slope Stability in Low Order Streams of Angangueo Mining Area (Michoacán, Mexico) After the 2010 Debris Flows. In: Mikoš, M., Vilímek, V., Yin, Y., Sassa, K. (Eds), Advancing Culture of Living with Landslides. Volume 5 Landslides in Different Environments. Springer International Publishing, pp. 651-660.

Morgenstern, N. R., Price, V. E. (1965): The analysis of the stability of general slip surfaces, Géotechnique 15 (1): 79-93.

Mori, L., Gómez-Tuena, A., Cai, Y., Goldstein, S. L. (2007): Effects of prolonged flat subduction on the Miocene magmatic record of the central Trans-Mexican Volcanic Belt. Chemical Geology 244: 452-473.

Mreyen, A. S., Demoulin, A., Havenith, H. B. (2018): Seismotectonic activity in East Belgium: relevance of a major scarp and two associated landslides in the region of Malmedy. Geologica Belgica 21 (3-4): 101-110.

Müller, H.-W., Dohrmann, R., Klosa, D., Rehder, S., Eckelmann, W. (2009): Comparison of two procedures for particle-size analysis: Köhn pipette and X-ray granulometry. Journal of Plant Nutrition and Soil Science 172 (2): 172-179.

Mugagga, F., Kakembo, V., Buyinza, M. (2012): Land use changes on the slopes of Mount Elgon and the implications for the occurrence of landslides. Catena 90: 39-46.

Munsell Color Company (2010): Munsell Soil Color Charts: with genuine Munsell color chips. Munsell Color, Grand Rapids, MI.

Murthy, V. N. S. (2003): Geotechnical engineering: principles and practices of soil mechanics and foundations engineering. Marcel Dekker, Inc., New York, 465 pp.

Nanzyo, M., Yamasaki, S., Honna, T., Yamada, I., Shoji, S., Takahashi, T. (2007): Changes in element concentrations during Andosol formation on tephra in Japan. European Journal of Soil Science 58: 465-477.

National Water Commission (2016): Statistics on Water in Mexico, 2016 edition. Ministry of the Environment and Natural Resources, Mexico City, 276 pp.

Naudet, V., Lazzari, M., Perrone, A., Loperte, A., Piscitelli, S., Lapenna, V. (2008): Integrated geophysical and geomorphological approach to investigate the snowmelt-triggered landslide of Bosco Piccolo village (Basilicata, southern Italy). Engineering Geology 98: 156-167.

Nelson, A., Reuter, H. I., Gessler, P. (2009): DEM production methods and sources. In: Hengl, T., Reuter, H. I. (Eds.), Geomorphometry: Concepts, Software, and Applications. Elsevier, Amsterdam, pp. 65-85.

Neuhäuser, B., Damm, B., Terhorst, B. (2012a): GIS-based assessment of landslide susceptibility on the base of the Weights-of-Evidence model. Landslides 9: 511-528.

Neuhäuser, B., Terhorst, B., Damm, B. (2012b): Landslide Identification and Modelling in Flysch Areas of the European Alpine Foreland. Zeitschrift für Geomorphologie 56 (4): 115-146.

Neuhäuser, B. (2014): Landslide Susceptibility and Climate Change Scenarios in Flysch Areas of the Eastern Alps. Dissertation, Julius-Maximilians-Universität Würzburg, Würzburg, 208 pp.

Nichols, G. (2009): Sedimentology and Stratigraphy. 2. edition, Wiley-Blackwell, Chichester, West Sussex, UK, 419 pp.

Nicoletti, P. G., Parise, M. (1995): Geomorphology and kinematics of the Conturrana rockslide-debris flow (NW Sicily). Earth Surface Processes and Landforms 21: 875-892.

Niethammer, U., James, M. R., Rothmund, S., Travelletti, J., Joswig, M. (2012): UAV-based remote sensing of the Super-Sauze landslide: Evaluation and results. Engineering Geology 128: 2-11.

Nikolakopoulos, K., Kavoura, K., Depountis, N., Kyriou, A., Argyropoulos, N., Koukouvelas, I., Sabatakakis, N. (2017): Preliminary results from active landslide monitoring using multidisciplinary surveys. European Journal of Remote Sensing 50 (1): 280-299.

Nikolaeva, E., Walter, T. R., Shirzaei, M., Zschau, J. (2014): Landslide observation and volume estimation in central Georgia based on L-band InSAR. Natural Hazards and Earth System Sciences 14: 675-688.

Nyssen, J., Moeyersons, J., Poesen, J., Deckers, J., Haile, M. (2002): The environmental significance of the remobilisation of ancient mass movements in the Atbara–Tekeze headwaters, Northern Ethiopia. Geomorphology 49: 303-322.

Oniga, V.-E., Breaban, A.-I., Statescu, F. (2018): Determining the Optimum Number of Ground Control Points for Obtaining High Precision Results Based on UAS Images. Proceedings 2: 352. DOI: 10.3390/ecrs-2-05165.

Otto, J.-C., Smith, M. J. (2013): Geomorphological mapping. In: Clarke, L. E., Nield, J. M. (Eds.), Geomorphological techniques, chapter 2.6. Online edition, British Society for Geomorphology, London, pp. 1-10.

Pack, R. T., Tarboton, D. G., Goodwin, C. N. (1998): The SINMAP approach to terrain stability mapping. 8th congress of the international association of engineering geology, Vancouver, British Columbia, Canada, 8 pp.

Palazzolo, N., Peres, D. J., Bordoni, M., Meisina, C., Creaco, E., Cancelliere, A. (2020): Comparison of the performance of spatial landslide prediction with TRIGRS1D and SCOOPS3D models and parameter optimization: application to the Oltrepò Pavese. EGU General Assembly 2020, EGU2020-19584. DOI: 10.5194/egusphere-egu2020-19584.

Pánek, T., Březný, M., Kapustová, V., Lenart, J., Chalupa, V. (2019): Large landslides and deep-seated gravitational slope deformations in the Czech Flysch Carpathians: New LiDAR-based inventory. Geomorphology 346: 106852. DOI: 10.1016/j.geomorph.2019.106852.

Parise, M., Guzzi, R. (1992): Volume and Shape of the Active and Inactive Parts of the Slumgullion Landslide, Hinsdale County. Colorado, US Geological Survey, Open-File Report 92-216: 1-29.

Pazzi, V., Tanteri, L., Bicocchi, G., D'Ambrosio, M., Caselli, A. (2017): H/V measurements as an effective tool for the reliable detection of landslide slip surfaces: Case studies of Castagnola (La Spezia, Italy) and Roccalbegna (Grosseto, Italy). Physics and Chemistry of the Earth 98: 136-153.

Peduzzi, P. (2010): Landslides and vegetation cover in the 2005 North Pakistan earthquake: a GIS and statistical quantitative approach. Natural Hazards and Earth System Sciences 10: 623-640.

Perrone, A., Vassallo, R., Lapenna, V., Di Maio, C. (2008): Pore water pressures and slope stability: a joint geophysical and geotechnical analysis. Journal of Geophysics and Engineering 5: 323-337.

Perrone, A., Lapenna, V., Piscitelli, S. (2014): Electrical resistivity tomography technique for landslide investigation: A review. Earth-Science Reviews 135: 65-82.

Perrone, A., Canora, F., Calamita, G., Bellanova, J., Serlenga, V., Panebiano, S., Tragni, N., Piscitelli, S., Vignola, K., Doglioni, A., Simeone, V., Sdao, F., Lapenna, V. (2021): A multidisciplinary approach for landslide residual risk assessment: the Pomarico landslide (Basilicata Region, Southern Italy) case study. Landslides 18: 353-365.

Petley, D. (2012): Global patterns of loss of life from landslides. Geology 40: 927-930.

Pineda-Martínez, L. F., Carbajal, N. (2017): Climatic analysis linked to land vegetation cover of Mexico by applying multivariate statistical and clustering analysis. Atmósfera 30: 233-242.

Pix4Dcapture (2019): Android Manual. Pix4Dcapture. URL: https://support.pix4d.com/hc/en-us/articles/360019848872-Android-Pix4Dcapture-Manual-and-Settings. Latest access: May 2019.

Pradhan, A. M. S., Kim, Y.-T. (2015): Application and comparison of shallow landslide susceptibility models in weathered granite soil under extreme rainfall events. Environmental Earth Sciences 73: 5761-5771.

Pradhan, S. P., Vishal, V., Singh, T. N. (2019): Landslides: Theory, Practice and Modelling. Springer International Publishing AG, Cham, 313 pp.

Press, W. H., Teukolsky, S. A., Vetterling, W. T., Flannery, B. P. (2006): Numerical recipes in FORTRAN 77: the art of scientific computing. Cambridge University Press, Cambridge, 973 pp.

Prinz, H., Strauß, R. (2011): Ingenieurgeologie. 5. edition, Spektrum Akademischer Verlag, Heidelberg, 738 pp.

Prokešová, R., Kardoš, M., Medveďová, A. (2010): Landslide dynamics from high-resolution aerial photographs: A case study from the Western Carpathians, Slovakia. Geomorphology 115: 90-101.

Prokešová, R., Medveďová, A., Tábořík, P. Snopková, Z. (2013): Towards hydrological triggering mechanisms of large deep-seated landslides. Landslides 10: 239-254.

Qiao, S., Qin, S., Chen, J., Hu, X., Ma, Z. (2019): The Application of a Three-Dimensional Deterministic Model in the Study of Debris Flow Prediction Based on the Rainfall-Unstable Soil Coupling Mechanism. Processes 7: 99. DOI: 10.3390/pr7020099.

Quezadas, J. P., Silva, A. C., Inguaggiato, S., del Rocío Salas Ortega, M., Pérez, J. C., Heilweil, V. M. (2015): Meteoric isotopic gradient on the windward side of the Sierra Madre Oriental area, Veracruz - Mexico. Geofísica Internacional 54 (3): 267-276.

Raia, S., Alvioli, M., Rossi, M., Baum, R. L., Godt, J. W., Guzzetti, F. (2014): Improving predictive power of physically based rainfall-induced shallow landslide models: a probabilistic approach. Geoscientific Model Development 7: 495-514.

Rasmussen, C., Dahlgren, R. A., Southard, R. J. (2010): Basalt weathering and pedogenesis across an environmental gradient in the southern Cascade Range, California, USA. Geoderma 154: 473-485.

Ramírez, R. P. (2013): Reporte del Clima en México. Septiembre 2013, Ano 3, Número 9. Servicio Meterológico Nacional, Gerencia de Meterorología y Climatología, Subgerencia de Pronóstico a Mediano y Largo Plazo, Mexico City, 25 pp.

Ramírez-Herrera, M. T., Gaidzik, K. (2017): La Pintada landslide—A complex double-staged extreme event, Guerrero, Mexico. Cogent Geoscience 3. 1356012. DOI: 10.1080/23312041.2017.1356012.

Reid, M. E., Christian, S. B., Brien, D. L. (2000): Gravitational stability of three-dimensional stratovolcano edifices. Journal of Geophysical Research 105 (B3): 6043-6056.

Reid, M. E., Brien, D. L. (2006): Assessing massive flank collapse at stratovolcanoes using 3-D slope stability analysis. In: Evans, S. G., Scarascia Mugnozza, G., Strom, A., Hermanns, R. L. (Eds.), Landslides from Massive Rock Slope Failure. Nato Science Series IV (49). Springer Netherlands, Dordrecht, pp. 445-458.

Reid, M. E., Christian, S. B., Brien, D. L., Henderson, S. (2015): Scoops3D—Software to analyze three-dimensional slope stability throughout a digital landscape. U.S. Geological Survey Techniques and Methods 14-A1, 218 pp. DOI: 10.3133/tm14A1.

Renschler, C. S., Doyle, M. W., Thoms, M. (2007): Geomorphology and ecosystems: Challenges and keys for success in bridging disciplines. Geomorphology 89: 1-8.

Restrepo, C., Alvarez, N. (2006): Landslides and their contribution to land-cover change in the mountains of Mexico and Central America. Biotropica 38 (4): 446-457.

Rodríguez Elizarrarás, S., Morales Barrera, W. V. (2011): Peligros geológicos. In: Mora Gonzáles, I., Rodríguez Elizarrarás, S. (Eds.), Peligros geológicos e hidrometerológicos en el estado de Veracruz. Consejo Veracurzano de Investigación Científica y Desarrollo Tecnológico, Mexico, pp. 8-59.

Rossi, G., Tanteri, L., Tofani, V., Vannocci, P., Moretti, S., Casagli, N. (2018): Multitemporal UAV surveys for landslide mapping and characterization. Landslides 15: 1045-1052.

Rothe, P. (2015): Allgemeine Geologie. WBG, Darmstadt, 147 pp.

Samodra, G., Ramadhan, M. F., Sartohadi, J., Setiawan, M. A., Christanto, N., Sukmawijaya, A. (2020): Characterization of displacement and internal structure of landslides from multitemporal UAV and ERT imaging. Landslides 17: 2455-2468.

Sánchez-Núñez, J. M., Macías, J. L., Zamorano-Orozco, J. J., Saucedo, R., Torres, J. R., Novelo, D. (2012): Mass movement processes at the Motozintla Basin, Chiapas, Southern Mexico. Geofísica Internacional 51 (2): 169-186.

Santangelo, M., Marchesini, I., Bucci, F., Cardinali, M., Fiorucci, F., Guzzetti, F. (2015): An approach to reduce mapping errors in the production of landslide inventory maps. Natural Hazards and Earth System Sciences 15: 2111-2126.

Sanz-Ablanedo, E., Chandler, J., Rodríguez-Pérez, J., Ordóñez, C. (2018): Accuracy of Unmanned Aerial Vehicle (UAV) and SfM Photogrammetry Survey as a Function of the Number and Location of Ground Control Points Used. Remote Sensing 10 (10): 1606. DOI: 10.3390/rs10101606.

Schilirò, L., Poueme Djueyep, G., Esposito, C., Scarascia Mugnozza, G. (2019): The Role of Initial Soil Conditions in Shallow Landslide Triggering: Insights from Physically Based Approaches. Geofluids 2019: 1-14. DOI: 10.1155/2019/2453786.

Schroth, G., Laderach, P. Dempewolf, J., Philpott, S., Haggar, J., Eakin, H., Castillejos, T., Garcia Moreno, J., Soto Pinto, L., Hernandez, R., Eitzinger, A., Ramierez-Villegas, J. (2009): Towards a climate change adaptation strategy for coffee communities and ecosystems in the Sierra Madre de Chiapas, Mexico. Mitigation and Adaptation Strategies for Global Change 14: 605-625.

Schwindt, D., Sandmeier, C., Büdel, C., Jäger, D., Wilde, M., Terhorst, B. (2016): The inner structure of landslides and landslide-prone slopes in south German cuesta landscapes assessed by geophysical, geomorphological and sedimentological approaches. Geophysical Research Abstracts 18, EGU2016- 17007-1. EGU General Assembly, Vienna.

Sedlock, R. L., Ortega-Gutierrez, F., Speed, R. C. (1993): Tectonostratigraphic Terranes of México. In: Sedlock, R. L., Ortega-Gutierrez, F., Speed, R. C. (Eds.), Tectonostratigraphic Terranes and Tectonic Evolution of Mexico. Geological Society of America, Boulder (U.S.A), 155 pp.

Seier, G., Sulzer, W., Lindbichler, P., Gspurning, J., Hermann, S., Konrad, H. M., Irlinger, G., Adelwöhrer, R. (2018): Contribution of UAS to the monitoring at the Lärchberg-Galgenwald landslide (Austria). International Journal of Remote Sensing 39 (15-16): 5522-5549.

Selby, M. J. (1982): Hillslope materials and processes. Oxford University Press, Oxford, 264 pp.

Shano, L., Raghuvanshi, T. K., Meten, M. (2020): Landslide susceptibility evaluation and hazard zonation techniques – a review. Geoenvironmental Disasters 7: 18. DOI: 1 0.1186/s40677-020-00152-0.

Sharma, S. (2002): Slope stability concepts. In: Abramson, L. W., Lee, T. S., Sharma, S., Boyce, G. M. (Eds.), Slope stability and stabilization methods. John Wiley & Sons, Inc., New York, pp. 329-461.

Skempton, A. W., Hutchinson, J. N. (1969): Stability of natural slopes and embankment foundations. Seventh International Conference on Soil Mechanics and Foundation Engineering, Sociedad Mexicana de Mecäna de Suelos, Mexico City, State of the Art Volume: 291-340.

Smith, M. J., Pain, C. F. (2009): Applications of remote sensing in geomorphology. Progress in Physical Geography 33 (4): 568-582.

Smith, M. W., Carrivick, J. L., Quincey, D. J. (2016): Structure from motion photogrammetry in physical Geography. Progress in Physical Geography 40 (2): 247-275.

SMN (2020a): Climogramas 1981-2010. Servicio Metereológico Nacional, Comisión Nacional del Agua. https://smn.conagua.gob.mx/es/climatologia/informacion-climatologica/climogramas-1981-2010. Latest access: January 2020.

SMN (2020b): Cliamtología diaria – estacion Acatlán, Veracruz. Servicio Metereológico Nacional, Comisión Nacional del Agua. https://smn.conagua.gob.mx/tools/RESOURCES/Diarios/30338.txt. Latest access: January 2020.

Soeters, R., Van Westen, C. J. (1996): Slope stability recognition, analysis, and zonation: Application of geographical information system to landslide hazard zonation. In: Turner, A. K., Schuster, R. L. (Eds.), Landslides investigation and mitigation. Special Report 247, Transportation Research Board of the National Research Council, National Academy Press, Washington D.C., pp. 129-177.

Soto, J., galve, J. P., Palenzuela, J. A., Azañón, J. M., Tamay, J., Irigaray, C. (2017): A multi-method approach for the characterization of landslides in an intramontane basin in the Andes (Loja, Ecuador). Landslides 14: 1929-1947.

Stark, T. D., Choi, H. (2008): Slope inclinometers for landslides. Landslides 5: 339-350.

Sujatha, E. R, Rajamanickam, E. R., Kumaravel, G. V. (2012): Landslide susceptibility analysis using probabilistic certainty factor approach: A case study on Tevankarai stream watershed, India. Journal of Earth System Science 121: 1337-1350.

Suter, M., López Martinez, M., Quintero Legorreta, O., Martinez, M. C. (2001): Quaternary intra-arc extension in the central Trans-Mexican volcanic belt. Geological Society of America Bulletin 113: 693-703.

Tarboton, D. G. (1997): A new method for the determination of flow directions and upslope areas in grid digital elevation models. Water Resources Research 33 (2): 309-319.

Taylor, F. E., Malamud, B. D., Witt, A., Guzzetti, F. (2018): Landslide shape, ellipticity and length-to-width ratios. Earth Surface Processes and Landforms 43: 3164-3189.

Temme, A., Guzzetti, F., Samia, J., Mirus, B. B. (2020): The future of landslides' past—a framework for assessing consecutive landsliding systems. Landslides 17: 1519-1528.

Travelletti, J., Malet, J.-P. (2012): Characterization of the 3D geometry of flow-like landslides: A methodology based on the integration of heterogeneous multi-source data. Engineering Geology 128: 30-48.

Teixeira, M., Bateira, C., Marques, F., Vieira, B. (2015): Physically based shallow translational landslide susceptibility analysis in Tibo catchment, NW of Portugal. Landslides 12: 455-468.

Terhorst, B. (1997): Formenschatz, Alter und Ursachenkomplexe von Massenverlagerungen an der schwäbischen Juraschichtstufe unter besonderer Berücksichtigung von Boden- und Deckschichtenentwicklung. Tübinger

Geowissenschaftliche Arbeiten, Geographisches Institut der Universität Tübingen, Tübingen, 212 pp.

Terhorst, B. (2001): Mass movements of various ages on the Swabian Jurassic escarpment: geomorphologic processes and their causes. Zeitschrift für Geomorphologie N. F. (125): 105-127.

Terhorst, B., Damm, B. (2009): Slope Stability and Slope Formation in the Flysch Zone of the Vienna Forest (Austria). Journal of Geological Research 2009: 589037. DOI: 10.1155/2009/589037.

Terhorst, B., Kreja, R. (2009): Slope stability modelling with SINMAP in a settlement area of the Swabian Alb. Landslides 6: 309-319.

Thiery, Y., Reninger, P.-A., Lacquement, F., Raingeard, A., Lombard, M., Nachbaur, A. (2017): Analysis of Slope Sensitivity to Landslides by a Transdisciplinary Approach in the Framework of Future Development: The Case of La Trinité in Martinique (French West Indies). Geosciences 7 (4): 135. DOI: 10.3390/geosciences7040135.

Tofani, V., Raspini, F., Catani, F., Casagli, N. (2013): Persistent Scatterer Interferometry (PSI) Technique for Landslide Characterization and Monitoring. Remote Sensing 5: 1045-1065.

Tomás, R., Abellán, A., Cano, M., Riquelme, A., Tenza-Abril, A. J., Baeza-Brotons, R., Saval, J. M., Jaboyedoff, M. (2018): A multidisciplinary approach for the investigation of a rock spreading on an urban slope. Landslides 15: 199-217.

Tran, T. V., Alvioli, M., Lee, G., An, H. U. (2018): Three-dimensional, time-dependent modeling of rainfall-induced landslides over a digital landscape: a case study. Landslides 15: 1071-1084.

Tseng, C.-M., Lin, C.-W., Stark, C. P., Liu, J.-K., Fei, L.-Y., Hsieh, Y.-C. (2013): Application of a multi-temporal, LiDAR-derived, digital terrain model in a landslide-volume estimation. Earth Surface Processes and Landforms 38: 1587-1601.

Turner, A. K. (1996): Colluvium and Talus. In: Turner, A. K., Schuster, R. L. (Eds.), Landslides: Investigation and Mitigation. Transportation Research Board Special Report 247. National Academy Press, Washington DC, pp. 525-554.

Turner, D., Lucieer, A., Watson, C. (2012): An Automated Technique for Generating Georectified Mosaics from Ultra-High Resolution Unmanned Aerial Vehicle (UAV) Imagery, Based on Structure from Motion (SfM) Point Clouds. Remote Sensing 4: 1392-1410.

Turner, D., Lucieer, A., de Jong, S. M. (2015): Time Series Analysis of Landslide Dynamics Using an Unmanned Aerial Vehicle (UAV). Remote sensing 7: 1736-1757.

Vanacker, V., Vanderschaeghe, M., Govers, G., Willems, E., Poesen, J., Deckers, J., De Bievre, B. (2003): Linking hydrological, infinite slope stability and land-use change models through GIS for assessing the impact of deforestation on slope stability in high Andean watersheds. Geomorphology 52: 299-315.

Van Den Eeckhaut, M., Poesen, J., Dewitte, O., Demoulin, A., De Bo, H., Vanmaercke-Gottigny, M. C. (2007a): Reactivation of old landslides: lessons learned from a case-study in the Flemish Ardennes (Belgium). Soil Use and Management 23: 200-211.

Van Den Eeckhaut, M., Poesen, J., Verstraeten, G., Vanacker, V., Nyssen, J., Moeyersons, J., van Beek, L. P. H., Vandekerckhove, L. (2007b): Use of LIDAR-derived images for mapping old landslides under forest. Earth Surface Processes and Landforms 32: 754-769.

Van Den Eeckhaut, M., Kerle, N., Poesen, J., Hervás, J. (2012): Object-oriented identification of forested landslides with derivatives of single pulse LiDAR data. Geomorphology 173-174: 30-42.

Van Westen, C. J., Castellanos, E., Kuriakose, S. L. (2008): Spatial data for landslide susceptibility, hazard, and vulnerability assessment: An overview. Engineering Geology 102 (3-4): 112-131.

Varley, N. (2019): Volcanoes of Mexico. In: LaMoreaux, J. W. (Ed.), Environmental Geology. Sustainability Science and Technology. 2. edition, Springer Verlag, Heidelberg, pp. 439-462.

Varnes, D. J. (1978): Slope movements: types and processes. In: Schuster, R. L., Krizek, R. J. (Eds.), Landslide analysis and control, National Academy of Sciences, Transportation Research Board Special Report 176, Washington, pp. 11-33.

Verbovšek, T., Košir, A., Teran, M., Zajc, M., Popit, T. (2017): Volume determination of the Selo landslide complex (SW Slovenia): integrating field mapping, ground penetrating radar and GIS approaches. Landslides 14: 1265-1274.

Vericat, D., Wheaton, J. M., Brasington, J. (2017): Revisiting the Morphological Approach: Opportunities and Challenges with Repeat High-Resolution Topography. In: Tsutsumi, D., Laronne, J. B. (Eds.), Gravel-Bed Rivers: Processes and Disasters. John Wiley & Sons, Ltd., Chichester, pp. 121-158.

Villanueva, J. K. S., Blanco, A. C. (2019): Optimization of ground control point (GCP) configuration for unmanned aerial vehicle (UAV) survey using structure from motion (SfM). ISPRS - International Archives of the Photogrammetry, Remote Sensing and Spatial Information Sciences XLII-4 (W12): 167-174.

Vollgger, S. A., Cruden, A. R. (2016): Mapping folds and fractures in basement and cover rocks using UAV photogrammetry, Cape Liptrap and Cape Paterson, Victoria, Australia. Journal of Structural Geology 85: 168-187.

Voltz, M., Webster, R. (1990): A comparison of kriging, cubic splines and classification for predicting soil properties from sample information. Journal of Soil Science 41: 473-490.

Walsh, K. J. E., Camargo, S. J., Knutson, T. R., Kossin, J., Lee, T.-C., Murakami, H., Patricola, C. (2019): Tropical Cyclones and Climate Change. Tropical Cyclone Research Review 8: 240-250.

Wang, H., Sun, P., Zhang, S., Han, S., Li, X., Wang, T., Guo, Q., Xin, P. (2020): Rainfall-induced landslide in loess area, Northwest China: a case study of the Changhe landslide on September 14, 2019, in Gansu Province. Landslides 17: 2145-2160.

Weber, D. D., Englund, E. J. (1994): Evaluation and comparison of spatial interpolators II. Mathematical Geology 26 (5): 589-603.

Weidner, L., DePrekel, K., Oommen T., Vitton, S. (2019): Investigating large landslides along a river valley using combined physical, statistical, and hydrologic modeling. Engineering Geology 259: 105169. DOI: 10.1016/j.enggeo.2019.105169.

Westoby, M. J., Brasington, J., Glasser, N. F., Hambrey, M. J., Reynolds, J. M. (2012): 'Structure-from-Motion' photogrammetry: A low-cost, effective tool for geoscience applications. Geomorphology 179: 300-314.

Wheaton, J. M., Brasington, J., Darby, S. E., Sear, D. A. (2010): Accounting for uncertainty in DEMs from repeat topographic surveys: improved sediment budgets. Earth Surface Processes and Landforms 25: 136-156.

Wieczorek, G. F. (1996): Landslide triggering mechanisms. In: Turner, A. K., Schuster, R. L. (Eds.), Landslides: Investigation and Mitigation. Transportation Research Board Special Report 247. National Academy Press, Washington DC, pp. 76-90.

Wilde, M., Morales Barrera, W. V., Schwindt, D., Bücker, M., Solis Castillo, B., Terhorst, B., Rodríguez Elizarrarás, S. R. (2017a): Multi-methodological Studies on the Large El Capulín Landslide in the State of Veracruz (Mexico In: Mikoš, M., Vilímek, V., Yin, Y., Sassa, K. (Eds), Advancing Culture of Living with Landslides. Volume 5 Landslides in Different Environments. Springer International Publishing, pp. 173-181.

Wilde, M., Rodríguez Elizarrarás, S. R., Morales Barrera, W. V., Schwindt, D., Bücker, Flores Orozco, A., García García, E., Pita de la Paz, C., Terhorst, B. (2017b): Multidisciplinary approach for the characterization of landslides in volcanic areas -

a case study from the Palma Sola-Chiconquiaco Mountain Range, Mexico. Geophysical Research Abstracts 19, EGU2017-16475-1. EGU General Assembly, Vienna.

Wilford, J., Thomas, M. (2013): Predicting regolith thickness in the complex weathering setting of the central Mt Lofty Ranges, South Australia. Geoderma 206: 1-13.

Williams, R. D. (2012): DEMs of difference. In: Clarke, L. E., Nield, J. M. (Eds.), Geomorphological techniques, chapter 2.3.2. Online edition, British Society for Geomorphology, London, pp. 1-17.

Wilson, J. P. (2012): Digital terrain modeling. Geomorphology 137: 107-121.

Wood, J., Fisher, P. (1993): Assessing interpolation accuracy in elevation models. Computer Graphics & Applications 13: 48-56.

WP/WLI - International Geotechnical Society's UNESCO Working Party on World Landslide Inventory (1990): A suggested method for reporting a landslide. Bulletin of the International Association of Engineering Geology 41: 5-12.

WP/WLI - International Geotechnical Society's UNESCO Working Party on World Landslide Inventory (1993): A multi-lingual landslide glossary. Bitech Publishers, Vancouver, 59 pp.

Xiao, T., Segoni, S., Chen, L., Yin, K., Casagli, N. (2020): A step beyond landslide susceptibility maps: a simple method to investigate and explain the different outcomes obtained by different approaches. Landslides 17: 627-640.

Zech, W., Hintermaier-Erhard, G. (2002): Böden der Welt. Ein Bildatlas. Spektrum Akademischer Verlag, Heidelberg, 120 pp.

Zêzere, J. L., de Brum Ferreira, A., Rodrigues, M. L. (1999): The role of conditioning and triggering factors in the occurrence of landslides: a case study in the area north of Lisbon (Portugal). Geomorphology 30: 133-146.

Zhang, S., Wang, F. (2019): Three-dimensional seismic slope stability assessment with the application of Scoops3D and GIS: a case study in Atsuma, Hokkaido. Geoenvironmental Disasters 6: 9. DOI: 10.1186/s40677-019-0125-9.

Zieher, T., Rutzinger, M., Schneider-Muntau, B., Perzl, F., Leidinger, D., Formayer, H., Geitner, C. (2017a): Sensitivity analysis and calibration of a dynamic physically based slope stability model. Natural Hazards and Earth System Sciences 17: 971-992.

Zieher, T., Schneider-Muntau, B., Mergili, M. (2017b): Are real-world shallow landslides reproducible by physically-based models? Four test cases in the Laternser valley, Vorarlberg (Austria). Landslides 14: 2009-2023.

Zizioli, D., Meisina, C., Valentino, R., Montrasio, L. (2013): Comparison between different approaches to modeling shallow landslide susceptibility: a case history in Oltrepo Pavese, Northern Italy. Natural Hazards and Earth System Sciences 13: 559-573.

List of Figures

Figure 1-1. Schematic of a rotational slide showing the main features of a landslide …….2
Figure 1-2. Schematic of a translational slide showing the main features of a landslide …3
Figure 1-3. Landslide distribution in Mexico ……6
Figure 1-4. Summary of the goals and working steps of this study …….....7
Figure 2-1. Position of the study area within Chiconquiaco, Veracruz (Mexico) ……...11
Figure 2-2. Litho- and chronostratigraphic map of the Trans-Mexican Volcanic Belt ……13
Figure 2-3. Characteristic occurrences of mafic volcanic rocks in the study area ……13
Figure 2-4. Basaltic dominated talus below a plateau basalt outcrop, East of El Capulín ...14
Figure 2-5 Mean monthly temperature and precipitation at Acatlán ……...15
Figure 2-6. Tracks of storms during the 2013 Atlantic Ocean hurricane season ……..16
Figure 2-7. Mean precipitation in Mexico ……..17
Figure 2-8. The three major soil zones of Mexico ……18
Figure 2-9. Andosol from Tlaxcala state ……20
Figure 2-10. Slope gradient in the Chiconquiaco Mountain Range…..……..21
Figure 2-11. Hydrological drainage basin for the Juchique River ……23
Figure 2-12. Current vegetation types and land use in Mexico ……...24
Figure 3-1. Ground control points in the Capulín landslide ……..28
Figure 3-2. Photogrammetric processing workflow in Agisoft for the present study …….29
Figure 3-3. Ground point classification of the dense cloud (2013 data) ……33
Figure 3-4. Hillshades of the study area with different azimuth angles ……35
Figure 3-5. Location of the geophysical transects in the Capulín landslide …..…….39
Figure 3-6. Schematic illustration of the components for the calculation of V_{total} ……..42
Figure 3-7. Process description of the developed slope stability approach ……..47
Figure 3-8. Cross section of pre-event surface and slip surface of the Capulín slide ……51
Figure 3-9. Schematic representation of a sliding mass with circular slip surface ……...53
Figure 3-10. Slope surface topography and cross section of the slip surface ……55
Figure 3-11. Process regions of the study area ……..58
Figure 4-1. Geomorphological map of the Capulín landslide ……64
Figure 4-2. Hillshade and orthomosaic acquired from the 2016 UAV data ……...67
Figure 4-3. Cross section extract along the Capulín slide comparing DSM and DTM ……68

Figure 4-4. Classified dense cloud (2016 data) derived from Agisoft ……69
Figure 4-5. Hillshades and orthomosaics derived from the DEM 2016 ……70
Figure 4-6. Elevation difference between the stable areas of DEM 2011 and DEM 2016 …71
Figure 4-7. Hillshade and orthomosaic acquired from the 2013 data ……72
Figure 4-8. Classified dense cloud (2013 data) derived from Agisoft ……73
Figure 4-9. Hillshade (based on DEM 2013) and photographs of the Capulín landslide …74
Figure 4-10. Simple linear regression of the DEM 2013 against DEM 2011 ……..75
Figure 4-11. Slope gradient map of the study area ……...76
Figure 4-12. Proportion of each landslide in relation to the total landslide area ……77
Figure 4-13. Comparison of raw and thresholded DoDs of 2013 ……79
Figure 4-14. Differences between the DEMs from 2013 and 2011 ……..80
Figure 4-15. Comparison of raw and thresholded DoDs of 2016 ……..……82
Figure 4-16. Differences between the DEMs from 2016 and 2011 ……...83
Figure 4-17. Thresholded DoD from the 2013 and 2016 data ……84
Figure 4-18. Results of the thresholded DoDs of 2013 and 2016 ……86
Figure 4-19. Geophysical transect locations with interpolation- and validation points ….87
Figure 4-20. Cross section of the pre- and post-event surface of the Capulín landslide ….89
Figure 4-21. 3D illustration of the interpolated slip surfaces ……90
Figure 4-22. Cross section of pre-, post-event surfaces, and interpolated slip surface ……91
Figure 5-1. Sample locations ……...95
Figure 5-2. Sample locations in the Capulín landslide and the surrounding areas ....……...96
Figure 5-3. Location of the scarp samples (Capulín landslide) ……..97
Figure 5-4. Sample location S 4 ……98
Figure 5-5. Grain size contents of the Capulín scarp ……99
Figure 5-6. Limits of consistency analysis for the samples of the Capulín landslide …….100
Figure 5-7. Photos of the sample locations of the eastern flank (Capulín landslide)…….103
Figure 5-8. Grain size contents of the eastern flank (Capulín landslide) ……105
Figure 5-9. Sample locations of the western flank ……..106
Figure 5-10. Grain size contents of the Capulín landslide's western flank ……..108
Figure 5-11. Sample locations of the slide mass ……..111
Figure 5-12. Grain size content of the Capulín slide mass ……112
Figure 5-13. Profile and laboratory results of M 6 …….....114

Figure 5-14. Study site and sampling locations SA 1 and SA 10 ……117
Figure 5-15. Grain size content of the sample locations SA 1 and SA 10 ……118
Figure 5-16. Limits of consistency results for the surrounding areas (Capulín slide) ……119
Figure 5-17. Sample locations of the surrounding areas of the Capulín landslide …….120
Figure 5-18. Grain size content of the sample locations SA 2 to SA 9 ……122
Figure 5-19. Profile and laboratory results of SA 2 ……123
Figure 5-20. Locations of the samples of the Escalanar landslide ……124
Figure 5-21. Limits of consistency analysis for the samples of the Escalanar landslide ….125
Figure 5-22. Study site and sampling locations at the eastern flank (Escalanar slide) …...126
Figure 5-23. Grain size content of the eastern flank of the Escalanar landslide ……..126
Figure 5-24. Study site and sampling locations in the slide mass of the Escalanar slide …127
Figure 5-25. Grain size distribution of the Escalanar slide mass ……..128
Figure 5-26. Study site and sample location at the western flank of the Escalanar slide …129
Figure 5-27. Grain size content of Escalanar's western flank ……130
Figure 6-1. Geotechnical model designed in Slope/W ……..133
Figure 6-2. Comparison of the different limit equilibrium methods representing the FoS, calculated for three different levels of saturation ……...133
Figure 6-3. Comparison of the limit equilibrium methods representing the computed FoS, utilizing eight geotechnical parameter sets as input ……134
Figure 6-4. Input parameter for SAFETYFACTOR ……136
Figure 6-5. Distribution of the water saturation in the study area ……138
Figure 6-6. Proportion of the stability classes for the simple SAFETYFACTOR map ……139
Figure 6-7. FoS map for the study area modeled with the infinite slope method …….140
Figure 6-8. Filtered SAFETYFACTOR map for the study area (infinite slope method) ….142
Figure 6-9. Proportion of the stability classes for the filtered SAFETYFACTOR map ….143
Figure 6-10. Input parameters as specified for modeling in Scoops3D ……144
Figure 6-11. FoS map for the study area modeled with the method of slices ……146
Figure 6-12. Proportion of the stability classes for the Scoops3D map ……147
Figure 6-13. Pixel-based difference model of the SAFETYFACTOR maps ……148
Figure 6-14. Comparison of FoS classes - simple and filtered SAFETYFACTOR map ….149
Figure 6-15. Proportion of the FoS classes within the process regions, comparing the simple SAFETYFACTOR map and the filtered SAFETYFACTOR map ……150

Figure 6-16. Classified slope map, calculated based on the DEM 2011 ……151
Figure 6-17. Difference model - filtered SAFETYFACTOR- and classified slope map …152
Figure 6-18. Proportion of slope classes in relation to the study area ……153
Figure 6-19. FoS map calculated exclusively using literature values ……154
Figure 6-20. Difference model of filtered- and literature-value SAFETYFACTOR map ...155
Figure 6-21. FoS comparison of filtered- and literature-value SAFETYFACTOR map ….156
Figure 6-22. Proportion of the FoS classes within the process regions, comparing the filtered SAFETYFACTOR map and the literature-value SAFETYFACTOR map ……157
Figure 6-23. FoS classes comparison of Scoops3D and filtered SAFETYFACTOR map …158
Figure 6-24. Proportion of the FoS classes within the process regions, comparing the filtered SAFETYFACTOR map and the Scoops3D map ……158
Figure 6-25. Difference model between Bishop's simplified and infinite slope method ...159
Figure 7-1. Classified slope map of the study area, including the registered landslides ...163
Figure 7-2. Exemplary sample locations from each sedimentary group ……165
Figure 7-3. Satellite image from 2010 and outline of the present Capulín landslide …….168
Figure 7-4. Accumulated monthly precipitation at Acatlán ……170
Figure 7-5. Daily precipitation at Acatlán, for the year of 2013 ……170
Figure 7-6. Extension of the former landslide including significant features ……172
Figure 7-7. Photographs of the western flank of the Capulín landslide ……175
Figure 7-8. Photographs of the scarp and slide mass of the Capulín landslide ……176
Figure 7-9. Stream cutting through the Capulín landslide at the foot area ……178
Figure 7-10. Cross sections of the DEMs from 2013 and 2016 showing the toe area ……178
Figure 7-11. Geomorphological map and process regions of the Capulín landslide ……180
Figure 7-12. Area of high distortion between two slide blocks of the Capulín landslide ..181
Figure 7-13. Photograph and satellite image of the primary and secondary landslide ….182
Figure 7-14. Overview of applied methods and their relation to the aims of the study ….184
Figure 7-15. Exemplary excerpt of the hillshades from the Capulín landslide ……186
Figure 7-16. Resulting volumes of the different calculation approaches ……192
Figure 7-17. Landslide susceptibility map of the study area ……196
Figure 7-18. FoS map calculated with Scoops3D and SAFETYFACTOR ……200
Figure 7-19. Section of the Scoops3D map and filtered SAFETYFACTOR map ……204

List of Tables

Table 3-1. Technical details of the DJI Phantom 3 Professional and the camera ……27
Table 3-2. Properties of the alignment setting (DEM 2016) ……29
Table 3-3. Properties of the alignment setting (DEM 2013) ……32
Table 4-1. Main acquisition parameters of the 2016 and 2013 surveys ……66
Table 4-2. Ground Control Point accuracy for the 2016 data ……68
Table 4-3. Ground Control Point accuracy for the 2013 data ……72
Table 4-4. Areal and volumetric values of raw and thresholded 2013 DoDs ……..79
Table 4-5. Areal and volumetric values of raw and thresholded 2016 DoDs ……81
Table 4-6. RMSE results of the different interpolations algorithms ……...88
Table 4-7. Results of the landslide volume calculation ……92
Table 4-8. Volume calculation for the areas of erosion and accumulation ……92
Table 4-9. Results of the different DoDs ……93
Table 5-1. Results of the pH and total carbon analyses (Capulín slide - scarp area) ……101
Table 5-2. Bulk density, hydraulic conductivity analyses results (Capulín - scarp area) ..102
Table 5-3. Results of pH, TC, and carbonate analyses (Capulín slide - eastern flank) ….104
Table 5-4. Bulk density and hydraulic conductivity results (Capulín - eastern flank) …..104
Table 5-5. Results of the geotechnical analyses (Capulín landslide - western flank) …….107
Table 5-6. Bulk density, hydraulic conductivity, carbonate analyses (western flank) ….109
Table 5-7. Results of the pH and TC analyses (Capulín landslide - western flank) …….110
Table 5-8. Results of pH, TC, dry bulk density analyses (Capulín slide mass) ……..….113
Table 5-9. Results of pH, TC, carbonates, bulk density analyses (SA 1, SA 10) ……118
Table 5-10. Results of pH, TC, carbonates, and bulk density analyses (SA 2 - SA 7) ……121
Table 5-11. Results of pH and TC analyses (Escalanar landslide - eastern flank) ……..….126
Table 5-12. Results of the pH and TC analyses (Escalanar landslide - slide mass) ……....128
Table 5-13. TC, pH, hydraulic conductivity analyses (Escalanar slide - western flank) …130
Table 6-1. Input parameters for the root-finding equation ……131
Table 6-2. Calculation results for the geotechnical parameters for the Capulín slide ……131
Table 6-3. Input parameters of the landslides no. 2 for the root-finding equation ……132
Table 6-4. Calculation results for the geotechnical parameters for landslide no. 2 ……132
Table 6-5. Geotechnical input parameters for SAFETYFACTOR ……137

Table 6-6. Input parameters for Scoops3D ……145
Table 6-7. Geotechnical input data for the literature-value SAFETYFACTOR map …….156
Table 7-1. Characteristics of the landslides mapped in the study area ……162
Table 7-2. Subdivision of the sediment analyses results into three main groups ……..166
Table 7-3. Overview of the individual properties of the Capulín landslide ……183
Table 7-4. Overview of sediment analyses results and generated input parameters …….195

Appendix

Appendix A: Program code of the program ABIFR (Root finding back analysis), which calculates geotechnical parameters with the multidimensional Newton-Raphson method. Program written by Thomas Kreuzer (2019, University of Würzburg).

```
#########################################################################
###
Model: Root finding back analysis (ABIFR)
Author: Thomas Kreuzer
#########################################################################
####

import numpy as np
import sys

from numba import njit

grav = 9.81

class properties:
    def __init__(self, name):
        #global args, bounds, num, fs
        with open(name) as f:
            lines = []
            for line in f:
                s = line.strip()
                if not s or s.startswith("#"):
                    continue
                lines.append(s)
            assert len(lines) > 5
            self.num = int(lines[0])
            self.fs = float(lines[1])
            args = [float(n) for n in lines[2:5]]
            args[0] = np.radians(args[0])
            self.args = tuple(args)
            self.bounds = [
                tuple([float(n) for n in lines[5].split()]),
                tuple([float(n) for n in lines[6].split()]),
                tuple([float(n) for n in lines[7].split()]),
            ]

# a => slope
# b => thickness
# c => saturation
# d => friction
# e => density
# f => cohesion
@njit
def grad(x, a, b, c) -> np.array:
    d = x[0] / 57.2958
    e = x[1]
    f = x[2]
    sec2 = np.square(1.0 / np.cos(d))
```

```
    return np.array(
        [
            (np.cos(a) * sec2 * (e * grav - c * grav)) / (np.sin(a)
* e * grav),
            (np.cos(a) * np.tan(d)) / (np.sin(a) * e)
            - (
                np.square(np.cos(a)) * b * np.tan(d) * (e * grav - c
* grav)
                + 1000.0 * f
            )
            / (np.cos(a) * np.sin(a) * b * np.square(e) * grav),
            1000.0 / (np.cos(a) * np.sin(a) * b * e * grav),
        ]
    )


@njit
def g(x, a, b, c) -> float:
    d = x[0] / 57.2958
    e = x[1]
    f = x[2]
    return (
        (f * 1000.0)
        + (((e * grav) - (c * grav)) * (((b * np.square(np.cos(a)) *
np.tan(d)))))
    ) / ((e * grav) * b * np.sin(a) * np.cos(a))


def newt(x0, fs, tol=1e-6, maxit=10000) -> np.array:
    x = x0
    for n in range(maxit):
        f = g(x, *args) - fs
        if np.abs(f) < tol:
            break
        fderiv = grad(x, *args)
        x = x - fderiv * f / np.square(np.linalg.norm(fderiv))
    return x


def parse(f):
    lines = []
    for line in f:
        s = line.strip()
        if not s or s.startswith("#"):
            continue
        lines.append(s)
    assert len(lines) > 5
    global args, bounds, num, fs
    num = int(lines[0])
    fs = float(lines[1])
    args = [float(n) for n in lines[2:5]]
    args[0] = np.radians(args[0])
    args = tuple(args)
    bounds = [
        tuple([float(n) for n in lines[5].split()]),
        tuple([float(n) for n in lines[6].split()]),
        tuple([float(n) for n in lines[7].split()]),
    ]
```

```
def main():
    m = len(bounds)

    if len(sys.argv) > 1 and sys.argv[1] == "-s":
        xs = np.array([bounds[0][0], bounds[1][0], bounds[2][0]])
        print(f"FOS: {g(xs, *args):.3f}")
        return 0

    x0 = np.zeros(m)
    x = np.zeros(m)
    for j in range(num):
        for i in range(m):
            x0[i] = np.random.default_rng().uniform(bounds[i][0],
bounds[i][1])
        x += newt(x0, fs)
    x /= num
    print(f"phi: {x[0]:.1f}Â°, rho: {x[1]:.2f}, c: {x[2]*1000.0:.2f}
KPa")
    print(f"FS: {g(x, *args):.2f}")
    return 0


if __name__ == "__main__":
    sys.tracebacklimit = 0
    # assert len(sys.argv) == 2
    with open("example.txt") as f:
        parse(f)
    sys.exit(main())
##############################################################################
###
```

Appendix B: In histogram a) the elevation difference between the stable areas of DEM 2016 and DEM 2013 are shown. b) Simple linear regression of the DEM 2013 against DEM 2016. c) Volumetric elevation change distribution from the thresholded DoD, where LoD_{min} (the 2.89 m) was applied. The red color represents the eroded areas, blue the accumulated and gray represents the areas which were beneath the threshold and therefore not considered in the thresholded DoD. Source: Own illustration.

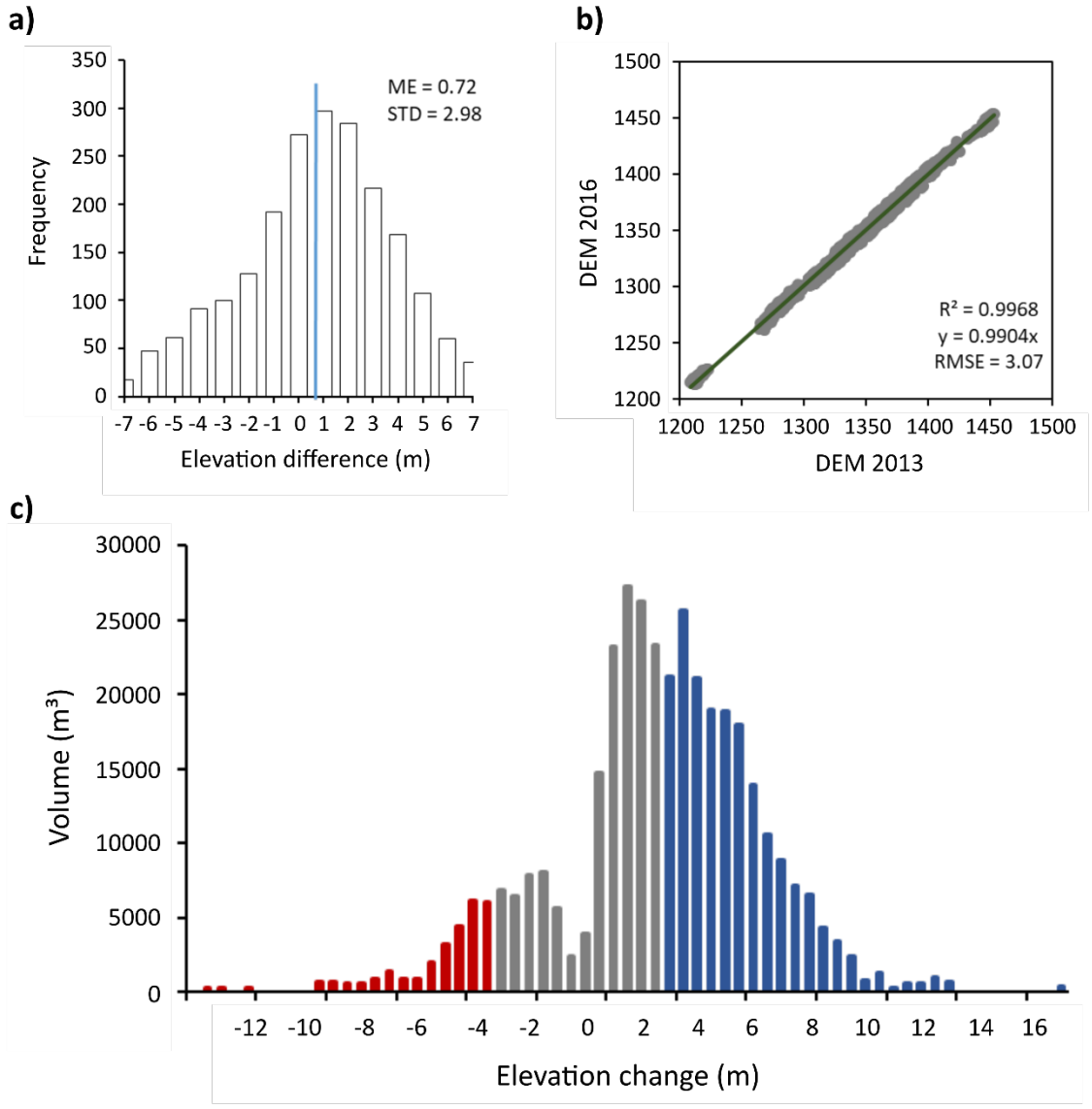

Appendix C: Subsurface models derived from combined ERT and SRT surveys. Exact transect locations are shown in Figure 3-5. Source: Modified after Wilde et al. (2017a, b).

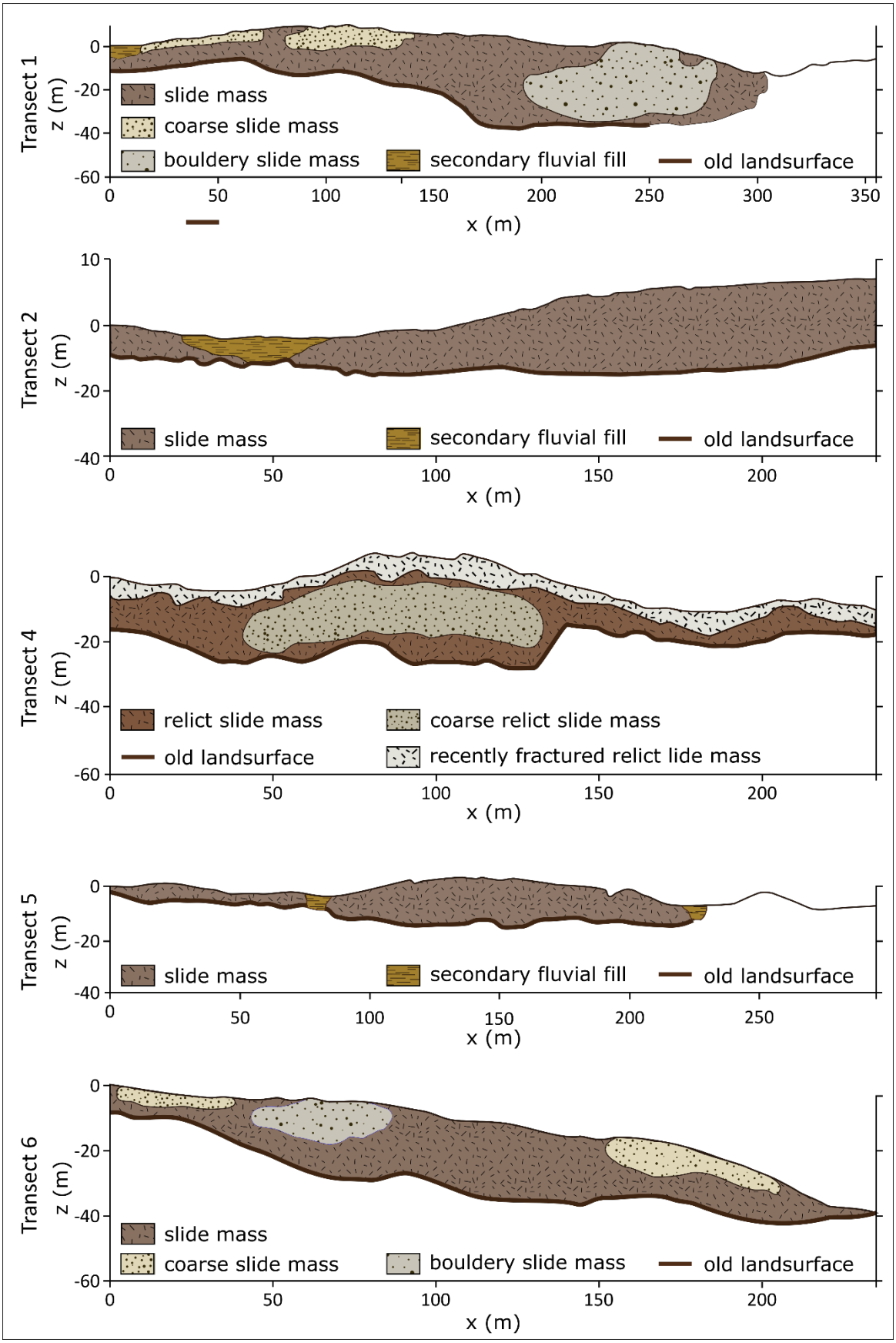

Appendix D: Sample location and depth (1/2).

Name	X-coordinate	Y-coordinate	Depth (m)
S 1	738985	2182986	19.4
S 2	738947	2183018	15.4
S 3-1	738962	2183084	20.0
S 3-2	738962	2183084	20.5
S 3-3	738962	2183084	22.0
S 4-1	738955	2183148	0.2
S 4-2	738955	2183148	0.5
S 4-3	738955	2183148	1.0
S 4-4	738955	2183148	1.2
S 4-5	738955	2183148	3.0
S 4-6	738955	2183148	5.0
S 4-7	738955	2183148	5.2
S 4-8	738955	2183148	6.7
S 4-9	738955	2183148	8.9
S 4-10	738955	2183148	9.2
S 4-11	738955	2183148	9.2
S 4-12	738955	2183148	10.7
S 4-13	738955	2183148	11.7
S 4-14	738955	2183148	11.2
S 4-15	738955	2183148	11.4
S 4-16	738955	2183148	19.4
S 4-17	738955	2183148	19.1
S 4-18	738955	2183148	19.5
S 4-19	738955	2183148	19.7
FW 1	738982	2183172	13.0
FW 2-1	739005	2183181	13.0
FW 2-2	739005	2183181	12.5
FW 2-3	739005	2183181	12.0
FW 3-1	739012	2183195	5.2
FW 3-2	739012	2183195	5.3
FW 3-3	739012	2183195	5.5
FW 3-4	739012	2183195	5.4
FW 3-5	739012	2183195	5.5
FW 3-6	739012	2183195	5.7
FW 3-7	739012	2183195	5.8
FW 3-8	739012	2183195	5.7
FW 3-9	739012	2183195	5.7
FW 3-10	739012	2183195	5.9
FW 3-11	739012	2183195	5.9
FW 3-12	739012	2183195	6.2
FW 3-13	739012	2183195	6.4
FW 4-1	739013	2183197	4.2
FW 4-2	739013	2183197	4.2
FW 4-3	739013	2183197	4.3
FW 4-4	739013	2183197	4.5
FW 4-5	739013	2183197	4.6
FW 4-6	739013	2183197	4.7
FW 4-7	739013	2183197	4.7
FW 4-8	739013	2183197	4.8
FW 4-9	739013	2183197	5.0
FW 4-10	739013	2183197	5.1
FW 4-11	739013	2183197	5.3
FW 4-12	739013	2183197	5.3
FW 4-13	739013	2183197	5.3
FW 5-1	739034	2183215	5.0
FW 5-2	739034	2183215	5.7
FW 5-3	739034	2183215	6.0
FW 5-4	739034	2183215	6.4
FE 1-1	739173	2183267	0.2
FE 1-2	739173	2183267	0.5
FE 1-3	739173	2183267	0.7
FE 1-4	739173	2183267	0.8
FE 1-5	739173	2183267	1.5
FE 1-6	739173	2183267	1.9
FE 1-7	739173	2183267	2.2
FE 1-8	739173	2183267	3.1
FE 1-9	739173	2183267	3.6
FE 1-10	739173	2183267	4.7
FE 1-11	739173	2183267	6.0
FE 1-12	739173	2183267	6.0
FE 1-13	739173	2183267	6.1
FE 2-1	739179	2183275	0.5
FE 2-2	739179	2183275	1.0
FE 2-3	739179	2183275	1.2
FE 2-4	739179	2183275	2.1
FE 2-5	739179	2183275	2.6
FE 2-6	739179	2183275	1.9
FE 2-7	739179	2183275	3.4
FE 2-8	739179	2183275	4.0
FE 2-9	739179	2183275	4.5
FE 2-10	739179	2183275	4.9
FE 2-11	739179	2183275	5.0
FE 3	739251	2183391	2.5
M 1	739006	2183086	0.2

Appendix D: Sample location and depth (2/2).

Name	X-coordinate	Y-coordinate	Depth (m)
M 2-1	739075	2183151	2.1
M 2-2	739075	2183151	2.9
M 3-1	739144	2183287	0.2
M 3-2	739144	2183287	0.8
M 4-1	739163	2183306	1.1
M 4-2	739163	2183306	1.2
M 4-3	739163	2183306	1.3
M 4-4	739163	2183306	1.3
M 4-5	739163	2183306	1.4
M 4-6	739163	2183306	1.6
M 4-7	739163	2183306	1.7
M 5	739110	2183431	0.2
M 6-1	739155	2183448	0.1
M 6-2	739155	2183448	0.2
M 6-3	739155	2183448	0.4
M 6-4	739155	2183448	0.5
M 6-5	739155	2183448	0.6
M 6-6	739155	2183448	0.8
M 6-7	739155	2183448	1.0
M 7-1	739086	2183522	0.2
M 7-2	739086	2183522	0.1
M 8	739231	2183508	0.8
SA 1-1	739491	2183362	4.0
SA 1-2	739491	2183362	4.2
SA 2-1	738982	2182940	0.2
SA 2-2	738982	2182940	0.3
SA 2-3	738982	2182940	0.5
SA 2-4	738982	2182940	0.8
SA 2-5	738982	2182940	1.1
SA 3	738986	2182958	0.3
SA 4-1	738948	2183160	0.3
SA 4-2	738948	2183160	0.9
SA 4-3	738948	2183160	1.5
SA 5-1	738999	2183200	0.1
SA 5-2	738999	2183200	0.3
SA 6-1	739018	2183370	0.1
SA 6-2	739018	2183370	1.0
SA 7	739057	2183550	0.4
SA 8	739075	2183630	0.5
SA 9-1	739128	2183710	0.4
SA 9-2	739128	2183710	0.7
SA 9-3	739128	2183710	1.2
SA 9-4	739128	2183710	1.6
SA 10-1	738709	2183898	2.0
SA 10-2	738709	2183898	2.4
EFE 1-1	737317	2183444	13.0
EFE 1-2	737317	2183444	13.5
EFE 1-3	737317	2183444	14.0
EFW 1-1	737099	2183481	0.1
EFW 1-2	737099	2183481	0.2
EFW 1-3	737099	2183481	0.3
EFW 1-4	737099	2183481	0.5
EFW 1-5	737099	2183481	0.7
EFW 1-6	737099	2183481	0.9
EFW 1-7	737099	2183481	1.0
EFW 1-8	737099	2183481	1.1
EFW 1-9	737099	2183481	1.7
EFW 1-10	737099	2183481	1.9
EM 1-1	737170	2183481	0.0
EM 1-2	737170	2183481	0.1
EM 1-3	737170	2183481	0.2
EM 1-4	737170	2183481	0.2
EM 1-5	737170	2183481	0.3
EM 1-6	737170	2183481	0.3
EM 1-7	737170	2183481	0.4
EM 1-8	737170	2183481	0.5
EM 1-9	737170	2183481	0.5
EM 1-10	737170	2183481	0.6
EM 1-11	737170	2183481	0.8
EM 1-12	737170	2183481	0.9

Appendix E: Laboratory results (1/4).

Name	Dry bulk density (g/cm³)	Variable hydraulic conductivity (cm/h)	Constant hydraulic conductivity (cm/h)	Carbonates (%)	pH ($CaCl_2$)	Total carbon (%)
S 1	1.22	-	-	-	7.5	-
S 2	1.16	-	-	-	6.7	-
S 3-1	-	-	-	-	-	-
S 3-2	-	-	-	-	-	-
S 3-3	0.96	-	4.00	-	6.9	-
S 4-1[1]	-	-	-	-	4.9	6.36
S 4-2[1]	-	-	-	-	5.1	3.21
S 4-3	-	-	-	-	5.2	2.05
S 4-4	-	-	-	-	5.1	0.82
S 4-5[1]	-	-	-	-	4.5	0.08
S 4-6[1]	-	-	-	-	4.6	0.70
S 4-7[1]	-	-	-	-	4.7	0.29
S 4-8[2]	-	-	-	0.33	4.8	0.16
S 4-9[1]	-	-	-	-	5.0	0.46
S 4-10	-	-	-	-	4.9	0.41
S 4-11	-	-	-	-	5.3	0.20
S 4-12	0.59	0.05	0.03	-	5.0	0.29
S 4-13	0.61	0.07	0.04	-	5.5	0.62
S 4-14	0.52	0.24	0.21	-	6.4	0.29
S 4-15	0.49	0.02	0.03	-	5.2	0.23
S 4-16	-	-	-	-	5.0	0.20
S 4-17	-	-	-	-	5.1	0.22
S 4-18	0.82	0.12	0.07	-	5.4	0.24
S 4-19	0.98	0.01	0.01	-	6.0	0.32
FW 1	-	-	-	-	-	-
FW 2-1	-	-	-	-	5.6	0.08
FW 2-2	-	-	-	-	6.0	0.03
FW 2-3	-	-	-	-	-	-
FW 3-1	-	-	-	-	6.9	0.04
FW 3-2[2]	-	-	-	0.22	5.8	0.05
FW 3-3[2]	-	-	-	-	5.7	0.02
FW 3-4[2]	-	-	-	-	7.0	0.02
FW 3-5[2]	-	-	-	-	5.7	0.02
FW 3-6[2]	-	-	-	-	6.6	0.02
FW 3-7[2]	-	-	-	-	6.0	0.03
FW 3-8[2]	-	-	-	-	6.7	0.03
FW 3-9[2]	-	-	-	-	5.8	0.03
FW 3-10[2]	-	-	-	-	5.9	0.05
FW 3-11[2]	-	-	-	-	5.9	0.04
FW 3-12[2]	-	-	-	-	5.8	0.03

[1] = Füssl (2020); [2] = Lenz (2019); '-' = method not applied.

Appendix E: Laboratory results (2/4).

Name	Dry bulk density (g/cm³)	Variable hydraulic conductivity (cm/h)	Constant hydraulic conductivity (cm/h)	Carbonates (%)	pH ($CaCl_2$)	Total carbon (%)
FW 3-13[2]	-	-	-	-	6.0	0.03
FW 4-1[1, 2]	0.97	-	-	0.10	5.8	0.02
FW 4-2[1,2]	1.49	0.71	0.27	0.26	5.7	0.02
FW 4-3[2]	-	-	-	0.08	6.6	0.02
FW 4-4[2]	-	-	-	0.80	5.8	0.03
FW 4-5[1,2]	1.35	0.71	0.55	0.04	5.6	0.02
FW 4-6[1]	1.37	0.10	0.06	-	6.7	0.02
FW 4-7[2]	-	-	-	0.42	6.4	0.02
FW 4-8	-	-	-	-	6.7	0.02
FW 4-9[1]	0.99	0.07	0.07	-	5.3	0.03
FW 4-10[1]	1.01	0.24	0.38	-	5.7	0.03
FW 4-11[1,2]	1.37	0.40	0.35	0.32	4.9	0.04
FW 4-12	0.00	0.04	0.06	-	6.5	0.06
FW 4-13[2]	-	-	-	0.32	5.7	0.04
FW 5-1	-	-	-	-	6.0	0.06
FW 5-2	-	-	-	-	6.0	0.09
FW 5-3	-	-	-	-	5.8	0.10
FW 5-4	-	-	-	-	5.9	0.08
FE 1-1[1,2]	1.36	0.07	0.06	-	7.4	0.29
FE 1-2[1,2]	2.94	0.02	0.01	1.88	7.1	0.17
FE 1-3[2]	-	-	-	2.92	7.3	0.18
FE 1-4[2]	-	-	-	1.00	7.4	0.09
FE 1-5[1,2]	1.79	0.05	-	38.09	7.5	4.49
FE 1-6[1,2]	1.90	-	-	36.71	7.1	4.12
FE 1-7[2]	-	-	-	25.29	7.5	4.31
FE 1-8[1,2]	1.85	0.00	-	38.92	7.4	4.86
FE 1-9[1,2]	1.76	0.02	-	37.89	7.3	4.81
FE 1-10[2]	1.81	0.48	0.16	38.41	7.2	4.88
FE 1-11[1,2]	1.75	0.39	1.09	36.94	7.1	4.48
FE 1-12[1,2]	1.77	4.13	3.78	37.69	7.2	4.39
FE 1-13[2]	-	-	-	35.34	7.3	4.33
FE 2-1[2]	-	-	-	2.53	7.5	0.19
FE 2-2[2]	-	-	-	9.85	7.6	1.13
FE 2-3[2]	-	-	-	1.20	7.5	0.17
FE 2-4[2]	-	-	-	5.28	7.6	0.49
FE 2-5	-	-	-	-	7.3	0.07
FE 2-6[2]	-	-	-	11.32	7.2	1.15
FE 2-7[2]	-	-	-	6.55	7.2	0.40
FE 2-8[2]	-	-	-	5.97	7.2	0.77

[1] = Füssl (2020); [2] = Lenz (2019); '-' = method not applied.

Appendix E: Laboratory results (3/4).

Name	Dry bulk density (g/cm³)	Variable hydraulic conductivity (cm/h)	Constant hydraulic conductivity (cm/h)	Carbonates (%)	pH ($CaCl_2$)	Total carbon (%)
FE 2-9	-	-	-	-	7.0	0.09
FE 2-10[2]	-	-	-	1.12	7.2	0.10
FE 2-11[2]	-	-	-	35.48	7.2	4.02
FE 3	1.18	-	4.54	-	7.2	-
M 1	1.33	-	17.44	-	6.6	-
M 2-1	0.88	-	-	-	7.5	-
M 2-2	0.99	-	-	-	7.1	-
M 3-1	-	-	-	-	5.4	0.06
M 3-2	-	-	-	-	5.2	0.57
M 4-1	-	-	-	-	5.7	0.06
M 4-2	6.25	-	-	-	5.6	0.06
M 4-3	-	-	-	-	5.7	0.06
M 4-4	-	-	-	-	5.6	0.04
M 4-5	-	-	-	-	5.6	-
M 4-6	-	-	-	-	5.7	0.04
M 4-7	-	-	-	-	5.6	0.04
M 5	1.40	-	-	-	7.4	-
M 6-1	-	-	-	-	4.9	7.5
M 6-2	-	-	-	-	5.7	3.2
M 6-3	-	-	-	-	5.7	1.7
M 6-4	-	-	-	-	5.4	1.2
M 6-5	-	-	-	-	5.3	1.0
M 6-6	-	-	-	-	5.3	1.0
M 6-7	-	-	-	-	5.3	1.2
M 7-1	-	-	-	-	-	-
M 7-2	-	-	-	-	-	-
M 8	1.02	-	1.65	-	6.7	-
SA 1-1[1,2]	2.00	0.23	0.17	35.33	7.4	4.44
SA 1-2[1,2]	1.80	0.48	0.44	18.66	7.6	2.34
SA 2-1	-	-	-	-	4.9	2.81
SA 2-2	-	-	-	-	5.4	1.65
SA 2-3	-	-	-	-	5.3	1.66
SA 2-4	-	-	-	-	5.0	1.34
SA 2-5	-	-	-	-	5.0	0.88
SA 3	0.97	-	16.82	-	6.0	-
SA 4-1	0.52	-	-	-	4.7	0.72
SA 4-2	0.73	-	-	-	4.3	0.51
SA 4-3	0.93	-	-	-	4.1	0.25
SA 5-1	1.19	-	-	-	4.3	1.57

[1] = Füssl (2020); [2] = Lenz (2019); '-' = method not applied.

Appendix E: Laboratory results (4/4).

Name	Dry bulk density (g/cm³)	Variable hydraulic conductivity (cm/h)	Constant hydraulic conductivity (cm/h)	Carbonates (%)	pH ($CaCl_2$)	Total carbon (%)
SA 5-2	1.53	-	-	-	5.4	0.17
SA 6-1	1.25	-	-	-	4.4	0.27
SA 6-2	1.23	-	-	-	5.1	0.07
SA 7	1.24	-	-	-	5.6	0.46
SA 8	1.38	-	-	-	4.8	0.46
SA 9-1	1.01	-	-	-	4.9	2.04
SA 9-2	1.32	-	-	-	5.2	0.94
SA 9-3	1.33	-	-	-	5.2	0.56
SA 9-4	1.23	-	-	-	5.2	0.34
SA 10-1[2]	-	-	-	38.23	7.6	4.60
SA 10-2[2]	-	-	-	40.28	7.6	4.83
EFE 1-1	-	-	-	-	6.2	0.08
EFE 1-2	-	-	-	-	6.3	0.05
EFE 1-3	-	-	-	-	6.3	0.05
EFW 1-1[1,2]	0.95	4.28	5.32	0.05	5.3	2.82
EFW 1-2[1,2]	0.88	17.61	8.04	-	5.4	2.42
EFW 1-3[1,2]	1.15	5.71	10.70	-	5.7	0.60
EFW 1-4[1,2]	1.14	0.44	0.30	-	5.7	0.53
EFW 1-5[1,2]	1.20	3.82	2.87	0.20	6.3	0.26
EFW 1-6[1,2]	1.29	1.11	0.86	-	5.6	0.32
EFW 1-7[1,2]	1.26	8.96	10.20	-	6.4	0.30
EFW 1-8[2]	-	44.02	-	-	5.8	0.34
EFW 1-9[2]	-	-	-	-	6.6	0.31
EFW 1-10[2]	-	-	-	-	6.0	0.04
EM 1-1[2]	-	-	-	-	4.4	4.77
EM 1-2[2]	-	-	-	-	4.5	2.59
EM 1-3[2]	-	-	-	-	4.7	2.94
EM 1-4[2]	-	-	-	-	5.4	2.39
EM 1-5[2]	-	-	-	-	5.6	0.80
EM 1-6[2]	-	-	-	-	5.5	0.60
EM 1-7[2]	-	-	-	-	5.4	1.34
EM 1-8[2]	-	-	-	-	5.5	1.82
EM 1-9[2]	-	-	-	-	5.1	0.54
EM 1-10[2]	-	-	-	-	5.1	1.12
EM 1-11[2]	-	-	-	-	6.0	0.08
EM 1-12[2]	-	-	-	-	4.8	0.15

[1] = Füssl (2020); [2] = Lenz (2019); '-' = method not applied.

Appendix F: Results of the grain size analyses (w.-%). Medium gravel (> 8 mm); fine gravel (4-8 mm); very fine gravel (2-4 mm); coarse sand (0.63-2.0 mm); medium sand (0.2-0.63 mm); fine sand (0.063-0.2 mm); coarse silt (0.02-0.063 mm); medium silt (0.0063-0.02 mm); fine silt (0.002-0.00063 mm); clay (< 0.002 mm) (1/5).

Name	Med. gravel	Fine gravel	Very fine gravel	Coarse sand	Med. sand	Fine sand	Coarse silt	Med. silt	Fine silt	Clay
S 1	0.0	0.0	0.0	7.8	8.6	7.6	15.8	22.6	18.7	18.9
S 2	0.0	0.0	0.0	5.2	1.3	1.7	32.2	33.8	11.3	14.5
S 3-1	0.0	0.0	0.0	0.1	2.0	2.5	14.4	17.6	15.9	47.5
S 3-2	0.0	0.0	0.0	0.0	0.1	0.5	3.8	12.9	16.2	66.3
S 3-3	0.0	0.0	0.0	0.0	1.1	2.7	9.7	25.7	24.5	36.2
S 4-1[1]	0.0	0.0	0.0	1.6	2.9	8.0	28.4	25.7	15.6	17.7
S 4-2[1]	0.0	0.0	0.0	0.3	2.1	6.7	36.9	25.1	13.9	15.0
S 4-3	0.0	0.0	0.0	0.5	4.3	10.4	31.5	21.2	11.9	20.2
S 4-4	0.0	1.1	0.0	0.7	2.2	8.3	24.3	29.0	15.7	18.9
S 4-5[1]	0.0	0.0	0.0	0.0	0.1	0.2	5.1	28.2	30.9	35.4
S 4-6[1]	0.0	0.0	0.0	0.0	1.3	2.5	2.9	12.5	10.1	70.6
S 4-7[1]	0.0	0.0	0.0	0.1	1.8	2.6	6.0	15.8	15.5	58.2
S 4-8	0.0	0.0	0.0	1.0	4.2	5.6	14.3	21.4	19.2	34.3
S 4-9[1]	0.0	0.0	0.0	0.2	2.2	8.0	25.1	19.2	13.2	32.0
S 4-10	0.0	0.0	0.0	0.0	3.3	11.8	13.1	21.0	14.3	36.5
S 4-11	11.2	15.8	8.9	7.6	5.5	8.5	15.2	9.4	5.1	12.8
S 4-12	0.0	0.0	0.0	0.7	1.3	3.0	10.7	17.7	19.4	47.1
S 4-13	0.0	0.0	0.0	0.1	1.2	2.0	29.1	16.5	9.0	42.1
S 4-14	0.0	0.0	0.0	0.6	2.8	10.5	19.6	16.4	14.3	35.8
S 4-15	0.0	0.0	0.0	1.2	3.3	2.4	23.0	30.1	13.9	26.2
S 4-16	0.0	0.0	10.4	3.3	3.8	6.2	19.2	15.6	10.5	31.0
S 4-17	0.0	0.0	0.0	0.6	2.4	4.6	16.0	17.4	14.5	44.4
S 4-18	0.0	0.0	0.0	0.1	1.2	2.6	9.8	19.2	15.5	51.6
S 4-19	0.0	0.0	0.0	0.1	1.3	3.6	13.5	21.6	16.2	43.6
FW 1	0.0	0.0	0.0	10.1	12.3	19.5	18.0	18.7	12.6	8.7
FW 2-1	0.0	1.1	0.7	6.1	12.4	17.4	10.6	18.3	16.1	17.3
FW 2-2	0.0	0.2	0.1	1.6	7.8	17.3	26.4	15.6	20.1	10.8
FW 2-3	0.0	0.0	0.0	3.6	7.9	10.1	22.1	27.6	15.3	13.4
FW 3-1[2]	29.1	15.0	10.5	16.8	9.8	4.8	4.0	4.6	2.9	2.5
FW 3-2[2]	16.5	9.7	10.7	20.7	13.6	6.8	6.1	5.9	3.4	6.6
FW 3-3[2]	8.9	5.0	11.6	14.7	12.2	9.8	8.5	11.3	8.9	9.1
FW 3-4[2]	2.5	4.7	9.1	16.9	17.1	14.2	6.5	13.9	7.9	7.2
FW 3-5[2]	0.0	3.9	6.5	14.8	15.6	14.9	10.2	14.9	7.0	12.3
FW 3-6[2]	0.0	3.6	4.1	6.7	11.0	11.3	16.1	19.8	12.1	15.2
FW 3-7[2]	0.0	0.0	0.0	0.1	1.8	14.0	21.2	20.7	15.2	26.9
FW 3-8[2]	3.0	2.4	3.1	7.8	10.9	10.4	13.3	18.4	12.2	18.6

[1] = Füssl (2020); [2] = Lenz (2019)

Appendix F: Results of the grain size analyses (w.-%). Medium gravel (> 8 mm); fine gravel (4-8 mm); very fine gravel (2-4 mm); coarse sand (0.63-2.0 mm); medium sand (0.2-0.63 mm); fine sand (0.063-0.2 mm); coarse silt (0.02-0.063 mm); medium silt (0.0063-0.02 mm); fine silt (0.002-0.00063 mm); clay (< 0.002 mm) (2/5).

Name	Med. gravel	Fine gravel	Very fine gravel	Coarse sand	Med. sand	Fine sand	Coarse silt	Med. silt	Fine silt	Clay
FW 3-9[2]	0.0	34.6	11.1	5.5	2.7	2.3	11.6	11.6	8.4	12.3
FW 3-10[2]	0.0	0.0	0.0	0.2	0.8	3.0	24.4	23.2	14.3	34.1
FW 3-11[2]	0.0	0.0	0.0	5.3	15.9	16.2	22.7	15.4	9.1	15.4
FW 3-12[2]	0.0	0.0	0.0	0.1	1.1	2.3	28.3	24.5	9.6	34.0
FW 3-13[2]	0.0	0.0	0.0	0.2	1.7	17.7	35.4	19.3	4.6	21.1
FW 4-1[1]	0.0	0.0	0.5	2.0	6.1	10.7	29.4	28.2	11.0	12.1
FW 4-2[1]	0.0	0.3	2.9	5.9	13.6	10.9	24.3	23.4	10.5	8.2
FW 4-3	0.0	0.0	1.6	6.6	15.2	16.3	20.0	22.0	8.6	9.6
FW 4-4	0.0	0.7	6.1	18.6	17.2	7.9	15.3	14.5	8.6	11.2
FW 4-5[1]	0.8	1.7	1.5	3.1	8.0	11.5	28.5	26.1	8.1	10.7
FW 4-6[1]	0.0	0.0	0.2	16.1	26.0	18.5	14.2	13.8	4.8	6.4
FW 4-7	0.0	0.0	0.4	5.5	10.6	15.9	22.4	25.3	10.0	9.9
FW 4-8	0.0	2.9	4.1	18.0	15.2	9.4	14.2	15.0	8.5	12.7
FW 4-9[1]	14.2	3.2	3.4	8.2	14.9	18.1	6.0	10.7	8.9	12.2
FW 4-10[1]	3.6	1.7	3.5	10.4	23.9	13.7	8.4	13.1	13.7	8.0
FW 4-11[1]	0.0	3.0	4.0	8.6	12.5	16.6	11.4	18.2	9.2	16.5
FW 4-12	0.0	0.1	0.9	2.5	7.3	8.5	24.2	34.1	13.7	8.6
FW 4-13	3.9	1.3	2.6	8.9	11.0	7.7	20.1	18.2	11.1	15.2
FW 5-1	0.0	0.0	0.0	10.8	16.0	14.5	14.2	18.6	12.7	13.2
FW 5-2	0.0	0.6	0.6	6.2	8.0	14.2	16.7	22.2	18.4	13.1
FW 5-3	0.0	3.1	0.0	7.4	12.6	18.4	11.1	18.8	15.9	12.6
FW 5-4	8.2	6.6	0.6	4.3	10.7	20.9	10.9	14.5	12.6	10.8
FE 1-1[1,2]	9.2	6.2	6.1	12.2	9.9	5.2	8.6	18.7	8.3	15.5
FE 1-2[1,2]	13.9	4.1	5.8	9.4	9.5	7.9	9.2	12.8	8.0	19.4
FE 1-3[2]	43.6	5.3	2.0	6.6	6.9	4.8	7.7	7.5	4.5	11.2
FE 1-4[2]	9.4	4.9	4.6	8.7	7.2	6.2	15.8	16.4	11.5	15.3
FE 1-5[1,2]	0.0	0.5	0.9	0.4	1.5	9.5	13.8	19.8	15.8	37.8
FE 1-6[1,2]	0.0	0.0	0.3	0.4	0.8	5.4	16.2	20.6	17.4	38.8
FE 1-7[2]	0.0	0.3	0.7	1.1	1.1	5.8	17.4	18.7	17.1	37.8
FE 1-8[1,2]	0.0	0.7	0.2	0.3	0.4	3.7	18.6	19.8	19.5	36.8
FE 1-9[1,2]	0.0	0.5	0.0	0.2	1.2	4.6	15.9	21.3	20.8	35.6
FE 1-10[2]	0.0	0.6	0.2	0.4	0.7	5.4	19.1	19.4	19.5	34.8
FE 1-11[1,2]	0.0	0.2	0.3	1.0	2.1	5.1	18.5	17.4	18.2	37.1
FE 1-12[1,2]	6.6	0.0	1.1	1.4	1.9	5.9	14.8	20.1	14.7	33.4
FE 1-13[2]	0.0	0.2	0.5	1.1	1.9	6.4	16.7	19.7	17.2	36.4
FE 2-1	2.8	3.8	5.0	6.1	13.6	11.2	14.6	16.3	9.7	16.9

[1] = Füssl (2020); [2] = Lenz (2019)

Appendix F: Results of the grain size analyses (w.-%). Medium gravel (> 8 mm); fine gravel (4-8 mm); very fine gravel (2-4 mm); coarse sand (0.63-2.0 mm); medium sand (0.2-0.63 mm); fine sand (0.063-0.2 mm); coarse silt (0.02-0.063 mm); medium silt (0.0063-0.02 mm); fine silt (0.002-0.00063 mm); clay (< 0.002 mm) (3/5).

Name	Med. gravel	Fine gravel	Very fine gravel	Coarse sand	Med. sand	Fine sand	Coarse silt	Med. silt	Fine silt	Clay
FE 2-2	0.0	0.0	7.4	23.7	12.7	11.3	14.2	12.1	6.5	12.0
FE 2-3	2.2	6.6	17.8	4.1	15.1	7.2	15.4	11.9	6.5	13.2
FE 2-4	0.0	0.3	8.3	3.1	7.9	12.6	18.2	17.0	10.0	22.7
FE 2-5	4.7	1.2	1.6	1.7	10.3	6.9	22.3	16.1	11.2	23.9
FE 2-6	0.0	2.7	0.0	0.8	1.4	3.8	17.2	21.5	18.3	34.2
FE 2-7	1.7	3.8	14.4	10.1	12.2	5.4	15.4	13.4	9.2	14.4
FE 2-8	3.2	1.3	7.1	3.5	7.8	4.8	19.6	17.0	11.2	24.4
FE 2-9	0.0	15.3	5.3	5.2	6.5	5.5	21.7	12.1	8.2	20.2
FE 2-10	25.5	10.2	8.4	8.9	8.0	8.7	10.5	7.1	3.9	8.8
FE 2-11	8.3	0.1	0.0	0.5	1.0	6.4	11.1	17.5	16.8	38.3
FE 3	0.0	0.0	0.0	15.9	14.7	9.4	18.8	18.8	9.8	12.6
M 1	0.0	0.0	0.0	15.1	8.2	6.5	16.7	24.0	15.1	14.4
M 2-1	0.0	0.0	0.0	1.2	0.6	0.3	27.3	27.9	14.1	28.5
M 2-2	0.0	0.0	0.0	2.4	1.5	2.4	22.1	28.5	17.9	25.2
M 3-1	5.3	4.9	8.5	2.5	7.6	5.2	14.6	23.0	16.4	12.0
M 3-2	0.0	6.7	11.5	4.9	7.4	9.4	11.0	18.5	11.6	19.2
M 4-1	0.0	2.6	5.0	1.7	2.0	4.3	18.5	22.4	19.5	23.9
M 4-2	0.0	0.0	0.0	5.4	3.1	5.6	29.0	28.2	12.5	16.3
M 4-3	0.0	0.0	0.0	0.3	3.1	8.8	16.4	30.7	26.3	14.4
M 4-4	0.0	0.0	0.0	2.9	4.9	7.6	11.1	32.0	25.7	15.8
M 4-5	0.0	0.0	0.0	0.5	1.2	3.8	28.9	30.3	16.0	19.3
M 4-6	0.0	0.0	0.0	2.0	4.4	8.2	12.0	29.7	26.9	16.9
M 4-7	0.0	0.0	0.2	1.3	2.0	7.4	18.0	36.1	24.4	10.5
M5	0.0	0.0	0.0	11.5	18.1	14.9	12.1	19.6	18.2	5.5
M 6-1	0.0	0.0	0.0	1.2	3.2	4.3	21.0	35.4	17.7	17.2
M 6-2	0.0	0.0	0.0	0.1	1.3	4.2	34.4	29.9	15.6	14.3
M 6-3	0.0	0.0	0.0	0.3	1.1	3.9	34.4	25.8	16.0	18.5
M 6-4	0.0	0.0	0.0	0.2	1.3	2.5	35.7	25.8	12.9	21.5
M 6-5	0.0	0.0	0.0	0.1	0.9	2.4	27.1	24.9	13.8	30.9
M 6-6	0.0	0.0	0.0	1.0	2.5	4.7	26.3	25.6	16.3	23.6
M 6-7	0.0	0.0	0.0	0.2	2.0	4.7	32.1	20.5	13.7	26.6
M 7-1	0.0	0.0	0.0	0.4	1.2	1.8	21.2	26.5	18.4	30.5
M 7-2	0.0	0.0	0.0	16.1	4.6	4.6	24.4	18.8	14.9	16.5
M 8	0.0	0.0	0.0	0.6	2.9	3.8	15.2	22.8	19.4	35.3
SA 1-1[1]	0.0	0.6	0.2	0.0	0.3	2.8	20.4	21.4	19.2	34.9
SA 1-2[1]	7.4	1.2	0.0	5.3	6.9	3.3	14.0	15.0	14.7	32.2
SA 2-1	0.0	0.0	0.0	0.3	1.4	3.7	18.7	25.9	19.9	30.1
SA 2-2	0.0	0.0	0.0	0.2	1.7	4.8	31.5	26.0	16.9	18.8

[1] = Füssl (2020); [2] = Lenz (2019)

Appendix F: Results of the grain size analyses (w.-%). Medium gravel (> 8 mm); fine gravel (4-8 mm); very fine gravel (2-4 mm); coarse sand (0.63-2.0 mm); medium sand (0.2-0.63 mm); fine sand (0.063-0.2 mm); coarse silt (0.02-0.063 mm); medium silt (0.0063-0.02 mm); fine silt (0.002-0.00063 mm); clay (< 0.002 mm) (4/5).

Name	Med. gravel	Fine gravel	Very fine gravel	Coarse sand	Med. sand	Fine sand	Coarse silt	Med. silt	Fine silt	Clay
SA 2-3	0.0	0.0	0.0	0.1	1.7	6.4	35.8	25.9	12.9	17.2
SA 2-4	0.0	0.0	0.0	0.2	1.5	4.0	26.6	31.2	21.1	15.5
SA 2-5	0.0	0.0	0.0	0.4	1.4	3.1	24.5	28.4	20.3	21.8
SA 3	0.0	0.0	0.0	0.5	2.7	4.8	25.3	31.9	17.7	17.1
SA 4-1	0.0	0.0	0.0	0.2	3.7	13.8	40.2	14.5	9.4	18.3
SA 4-2	0.0	0.0	0.0	0.1	0.6	1.7	15.6	17.3	15.6	49.2
SA 4-3	0.0	0.0	0.0	0.0	0.6	1.6	7.9	13.2	16.8	59.9
SA 5-1	0.0	0.0	0.0	6.2	11.5	9.7	14.2	24.1	17.0	17.3
SA 5-2	0.0	0.0	0.0	1.5	6.9	10.3	14.1	31.6	22.0	13.6
SA 6-1	0.0	0.0	0.0	0.0	0.1	0.8	28.4	26.1	12.5	32.1
SA 6-2	0.0	0.0	0.0	0.0	1.3	18.4	30.2	28.8	6.0	15.4
SA 7	0.0	0.0	0.0	0.0	1.4	4.4	23.1	26.2	15.3	29.6
SA 8	0.0	0.0	0.0	2.7	6.0	9.6	20.6	23.3	12.7	25.1
SA 9-1	0.0	0.0	0.0	1.0	2.6	2.9	18.0	20.8	25.0	29.6
SA 9-2	0.0	0.0	0.0	2.3	4.3	5.1	16.5	20.9	19.6	31.4
SA 9-3	0.0	0.0	0.0	2.5	6.6	7.6	15.9	18.9	17.4	31.1
SA 9-4	0.0	0.0	0.0	0.6	1.6	3.0	12.6	25.5	21.9	34.7
SA 10-1	0.0	4.5	1.3	1.0	0.2	4.9	21.6	23.9	22.3	20.2
SA 10-2	0.0	0.0	0.2	1.0	1.3	7.2	21.1	28.0	22.4	18.9
EFE 1-1	0.0	8.6	10.8	11.0	7.6	5.8	19.0	26.9	5.1	5.1
EFE 1-2	0.0	31.7	9.5	9.1	5.8	5.0	13.5	12.4	5.5	7.4
EFE 1-3	10.5	2.9	7.2	13.7	13.0	10.3	12.9	13.6	6.8	9.3
EFW 1-1[1,2]	9.0	1.1	2.8	5.9	3.8	3.3	11.8	21.4	15.6	25.3
EFW 1-2[1,2]	0.0	6.7	6.0	4.1	3.8	2.9	17.7	20.8	14.8	23.1
EFW 1-3[1,2]	20.3	10.6	3.4	13.5	4.5	4.0	10.7	10.3	6.5	16.2
EFW 1-4[1,2]	22.5	6.6	5.2	16.9	8.1	4.2	8.5	9.9	5.6	12.5
EFW 1-5[1,2]	0.0	0.0	2.1	6.0	4.5	3.8	17.5	21.8	12.3	32.0
EFW 1-6[1,2]	6.3	2.2	3.8	5.9	4.0	3.5	18.4	19.2	11.3	25.4
EFW 1-7[1,2]	59.7	6.8	1.4	6.0	2.7	2.1	5.0	5.8	3.4	7.1
EFW 1-8[2]	56.1	7.2	2.9	6.7	2.0	1.2	6.4	6.5	4.2	6.7
EFW 1-9[2]	41.4	10.0	4.1	8.5	2.8	2.5	5.7	8.2	5.1	11.6
EFW 1-10[2]	0.0	3.1	4.1	7.8	7.5	10.3	16.2	25.0	10.3	15.6
EM 1-1[2]	0.0	0.0	0.0	0.3	5.1	6.4	15.4	31.9	21.9	18.9
EM 1-2[2]	0.0	3.0	0.6	1.1	5.1	8.4	12.1	30.1	22.1	17.4
EM 1-3[2]	0.0	0.0	0.4	0.2	4.6	6.7	13.0	28.3	22.1	24.8
EM 1-4[2]	0.0	1.5	2.8	0.8	6.1	8.9	12.6	24.6	20.8	21.8

[1] = Füssl (2020); [2] = Lenz (2019)

Appendix F: Results of the grain size analyses (w.-%). Medium gravel (> 8 mm); fine gravel (4-8 mm); very fine gravel (2-4 mm); coarse sand (0.63-2.0 mm); medium sand (0.2-0.63 mm); fine sand (0.063-0.2 mm); coarse silt (0.02-0.063 mm); medium silt (0.0063-0.02 mm); fine silt (0.002-0.00063 mm); clay (< 0.002 mm) (5/5).

Name	Med. gravel	Fine gravel	Very fine gravel	Coarse sand	Med. sand	Fine sand	Coarse silt	Med. silt	Fine silt	Clay
EM 1-5[2]	5.1	2.8	3.5	0.2	7.5	10.0	14.3	24.6	14.0	18.0
EM 1-6[2]	1.3	3.9	2.7	1.8	10.7	11.6	12.5	24.6	14.8	16.1
EM 1-7[2]	0.0	0.0	3.2	0.5	5.3	8.5	16.9	25.7	19.6	20.3
EM 1-8[2]	30.8	1.4	0.1	0.3	1.6	2.7	11.8	20.2	13.4	17.7
EM 1-9[2]	0.0	1.5	0.6	1.0	4.6	6.6	8.2	21.7	22.9	33.0
EM 1-10[2]	16.7	0.0	0.0	0.3	2.0	4.5	11.1	19.1	19.0	27.3
EM 1-11[2]	0.0	1.2	0.9	0.7	8.9	7.8	12.3	35.1	19.0	14.2
EM 1-12[2]	2.2	1.8	2.3	1.3	7.5	7.3	14.5	28.9	17.0	17.2

[1] = Füssl (2020); [2] = Lenz (2019)

Appendix G: Geotechnical values.

Name	Short symbol (ASTM 2006)	Soil-mechanical specification (ASTM 2006)	Compactness, consistence (DIN 18121, 18122)	Unit weight (kN/m^3)	Friction angle (°)	Cohesion c' (kN/m^2)	Cohesion c_u (kN/m^2)
S 3-2	MH	elastic silt	soft	14.0	15.0	0.0	10.0
S 3-3	ML	silt	stiff	19.5	22.5	5.0	25.0
S 4-5	MH	elastic silt	stiff	17.0	15.0	0.0	20.0
S 4-8	MH	elastic silt	stiff	17.0	15.0	0.0	20.0
S 4-12	MH	elastic silt	stiff	17.0	15.0	0.0	20.0
S 4-17	MH	elastic silt	stiff	17.0	15.0	0.0	20.0
S 4-19	MH	elastic silt	stiff	17.0	15.0	0.0	20.0
FE 1-7	CL	lean clay	solid	20.5	22.5	10.0	60.0
FE 1-9	CL	lean clay	solid	20.5	22.5	10.0	60.0
FE 1-11	CL	lean clay	solid	20.5	22.5	10.0	60.0
FE 2-11	CL	lean clay with gravel	soft	19.0	22.5	0.0	5.0
FW 2-2	ML	sandy silt	solid	21.0	27.5	5.0	40.0
FW 3-10	MH	elastic silt	stiff	17.0	15.0	0.0	20.0
FW 4-1	ML	silt w. sand	stiff	19.5	22.5	5.0	25.0
FW 4-5	ML	silt w. sand	soft	19.0	22.5	0.0	5.0
FW 4-9	MH	sandy elastic silt w. gravel	stiff	17.0	15.0	0.0	20.0
FW 4-12	ML	silt w. sand	soft	19.0	22.5	0.0	5.0
FW 5-1	ML	sandy silt	solid	21.0	27.5	5.0	40.0
FW 5-3	ML	sandy silt	solid	21.0	27.5	5.0	40.0
M 2-1	MH	elastic silt	soft	14.0	15.0	0.0	10.0
M 8	MH	elastic silt	soft	14.0	15.0	0.0	10.0
SA 1-1	CL	lean clay	solid	20.5	22.5	10.0	60.0
SA 10-1	CL	lean clay	solid	21.0	27.5	5.0	40.0
SA 10-2	CL	lean clay	solid	21.0	27.5	5.0	40.0
EFE 1-3	CL	sandy lean clay w gravel	solid	21.0	27.5	5.0	40.0
EFW 1-5	MH	elastic silt w sand	stiff	17.0	15.0	0.0	20.0
EM 1-1	MH	elastic silt	stiff	17.0	15.0	0.0	20.0
EM 1-2	MH	elastic silt with sand	stiff	17.0	15.0	0.0	20.0
EM 1-3	MH	elastic silt	stiff	17.0	15.0	0.0	20.0
EM 1-4	MH	elastic silt with sand	stiff	17.0	15.0	0.0	20.0
EM 1-5	ML	silt w. sand	solid	20.5	22.5	10.0	60.0
EM 1-9	MH	elastic silt	stiff	17.0	15.0	0.0	20.0
EM 1-10	MH	elastic silt with gravel	soft	14.0	15.0	0.0	10.0
EM 1-11	ML	silt w. sand	solid	20.5	22.5	10.0	60.0
EM 1-12	ML	silt w. sand	stiff	19.5	22.5	5.0	25.0

Appendix H: Grain size classifications (1/5).

Name	Textural classes - WRB (IUSS Working Group 2014)	Textural classes (gravel, sand, mud) - Blott and Pye (2012)	Textural classes (sand, silt, clay) - Blott and Pye (2012)
S 1	Silt Loam	sandy mud	slightly clayey sandy silt
S 2	Silt Loam	slightly sandy mud	slightly sandy slightly clayey silt
S 3-1	Silty Clay	very slightly sandy mud	very slightly sandy clayey silt
S 3-2	Clay	mud	silty clay
S 3-3	Silty Clay Loam	very slightly sandy mud	very slightly sandy clayey silt
S 4-1	Silt Loam	slightly sandy mud	slightly sandy slightly clayey silt
S 4-2	Silt Loam	slightly sandy mud	slightly sandy slightly clayey silt
S 4-3	Silt Loam	slightly sandy mud	slightly sandy clayey silt
S 4-4	Silt Loam	very slightly gravelly slightly sandy mud	slightly sandy slightly clayey silt
S 4-5	Silty Clay Loam	mud	clayey silt
S 4-6	Clay	very slightly sandy mud	very slightly sandy silty clay
S 4-7	Clay	very slightly sandy mud	very slightly sandy silty clay
S 4-8	Silty Clay Loam	slightly sandy mud	slightly sandy clayey silt
S 4-9	Silty Clay Loam	slightly sandy mud	slightly sandy clayey silt
S 4-10	Silty Clay Loam	slightly sandy mud	slightly sandy clayey silt
S 4-11	Loam	gravelly sandy mud	slightly clayey sandy silt
S 4-12	Silty Clay	slightly sandy mud	slightly sandy clayey silt
S 4-13	Silty Clay	very slightly sandy mud	very slightly sandy clayey silt
S 4-14	Silty Clay Loam	slightly sandy mud	slightly sandy clayey silt
S 4-15	Silt Loam	slightly sandy mud	slightly sandy clayey silt
S 4-16	Silty Clay Loam	slightly gravelly slightly sandy mud	slightly sandy clayey silt
S 4-17	Silty Clay	slightly sandy mud	slightly sandy clayey silt
S 4-18	Silty Clay	very slightly sandy mud	very slightly sandy silty clay
S 4-19	Silty Clay	slightly sandy mud	slightly sandy clayey silt
FW 1	Loam	sandy mud	slightly clayey sandy silt
FW 2-1	Loam	very slightly gravelly sandy mud	slightly clayey sandy silt
FW 2-2	Silt Loam	sandy mud	slightly clayey sandy silt
FW 2-3	Silt Loam	sandy mud	slightly clayey sandy silt
FW 3-1	Sandy Loam	slightly muddy sandy gravel	slightly clayey silty sand
FW 3-2	Sandy Loam	gravelly muddy sand	slightly clayey silty sand
FW 3-3	Loam	gravelly sandy mud	slightly clayey silty sand
FW 3-4	Sandy Loam	slightly gravelly muddy sand	slightly clayey silty sand
FW 3-5	Loam	slightly gravelly muddy sand	slightly clayey silty sand
FW 3-6	Silt Loam	slightly gravelly sandy mud	slightly clayey sandy silt
FW 3-7	Silty Clay Loam	slightly sandy mud	slightly sandy clayey silt
FW 3-8	Loam	slightly gravelly sandy mud	sandy clayey silt

Appendix H: Grain size classifications (2/5).

Name	Textural classes - WRB (IUSS Working Group 2014)	Textural classes (gravel, sand, mud) - Blott and Pye (2012)	Textural classes (sand, silt, clay) - Blott and Pye (2012)
FW 3-9	Silt Loam	slightly sandy muddy gravel	slightly sandy clayey silt
FW 3-10	Silty Clay Loam	very slightly sandy mud	very slightly sandy clayey silt
FW 3-11	Loam	sandy mud	slightly clayey sandy silt
FW 3-12	Silty Clay Loam	very slightly sandy mud	very slightly sandy clayey silt
FW 3-13	Silt Loam	slightly sandy mud	slightly sandy clayey silt
FW 4-1	Silt Loam	slightly sandy mud	slightly sandy slightly clayey silt
FW 4-2	Silt Loam	very slightly gravelly sandy mud	slightly clayey sandy silt
FW 4-3	Silt Loam	very slightly gravelly sandy mud	slightly clayey sandy silt
FW 4-4	Loam	slightly gravelly sandy mud	slightly clayey silty sand
FW 4-5	Silt Loam	very slightly gravelly sandy mud	slightly clayey sandy silt
FW 4-6	Sandy Loam	muddy sand	slightly clayey silty sand
FW 4-7	Silt Loam	sandy mud	slightly clayey sandy silt
FW 4-8	Loam	slightly gravelly sandy mud	slightly clayey silty sand
FW 4-9	Loam	gravelly muddy sand	slightly clayey silty sand
FW 4-10	Sandy Loam	slightly gravelly muddy sand	slightly clayey silty sand
FW 4-11	Loam	slightly gravelly sandy mud	slightly clayey sandy silt
FW 4-12	Silt Loam	very slightly gravelly slightly sandy mud	slightly sandy slightly clayey silt
FW 4-13	Silt Loam	slightly gravelly sandy mud	slightly clayey sandy silt
FW 5-1	Loam	sandy mud	slightly clayey sandy silt
FW 5-2	Silt Loam	very slightly gravelly sandy mud	slightly clayey sandy silt
FW 5-3	Loam	very slightly gravelly sandy mud	slightly clayey sandy silt
FW 5-4	Loam	slightly gravelly sandy mud	slightly clayey sandy silt
FE 1-1	Loam	gravelly sandy mud	slightly clayey sandy silt
FE 1-2	Loam	gravelly sandy mud	sandy clayey silt
FE 1-3	Loam	slightly sandy muddy gravel	sandy clayey silt
FE 1-4	Silt Loam	slightly gravelly sandy mud	slightly clayey sandy silt
FE 1-5	Silty Clay Loam	very slightly gravelly slightly sandy mud	slightly sandy clayey silt
FE 1-6	Silty Clay Loam	slightly sandy mud	slightly sandy clayey silt
FE 1-7	Silty Clay Loam	slightly sandy mud	slightly sandy clayey silt
FE 1-8	Silty Clay Loam	very slightly sandy mud	very slightly sandy clayey silt
FE 1-9	Silty Clay Loam	slightly sandy mud	slightly sandy clayey silt
FE 1-10	Silty Clay Loam	slightly sandy mud	slightly sandy clayey silt

Appendix H: Grain size classifications (3/5).

Name	Textural classes - WRB (IUSS Working Group 2014)	Textural classes (gravel, sand, mud) - Blott and Pye (2012)	Textural classes (sand, silt, clay) - Blott and Pye (2012)
FE 1-11	Silty Clay Loam	slightly sandy mud	slightly sandy clayey silt
FE 1-12	Silty Clay Loam	slightly gravelly slightly sandy mud	slightly sandy clayey silt
FE 1-13	Silty Clay Loam	slightly sandy mud	slightly sandy clayey silt
FE 2-1	Loam	slightly gravelly sandy mud	slightly clayey sandy silt
FE 2-2	Loam	slightly gravelly muddy sand	slightly clayey silty sand
FE 2-3	Loam	gravelly sandy mud	slightly clayey sandy silt
FE 2-4	Loam	slightly gravelly sandy mud	sandy clayey silt
FE 2-5	Silt Loam	slightly gravelly slightly sandy mud	sandy clayey silt
FE 2-6	Silty Clay Loam	very slightly gravelly slightly sandy mud	slightly sandy clayey silt
FE 2-7	Loam	slightly gravelly sandy mud	slightly clayey sandy silt
FE 2-8	Silty Clay Loam	slightly gravelly slightly sandy mud	slightly sandy clayey silt
FE 2-9	Silt Loam	slightly sandy gravelly mud	sandy clayey silt
FE 2-10	Loam	sandy muddy gravel	slightly clayey silty sand
FE 2-11	Silty Clay	slightly gravelly slightly sandy mud	slightly sandy clayey silt
FE 3	Loam	sandy mud	slightly clayey sandy silt
M 1	Silt Loam	sandy mud	slightly clayey sandy silt
M 2-1	Silty Clay Loam	very slightly sandy mud	very slightly sandy clayey silt
M 2-2	Silt Loam	slightly sandy mud	slightly sandy clayey silt
M 3-1	Silt Loam	slightly gravelly slightly sandy mud	slightly sandy slightly clayey silt
M 3-2	Silt Loam	slightly gravelly sandy mud	sandy clayey silt
M 4-1	Silt Loam	slightly gravelly slightly sandy mud	slightly sandy clayey silt
M 4-2	Silt Loam	slightly sandy mud	slightly sandy slightly clayey silt
M 4-3	Silt Loam	slightly sandy mud	slightly sandy slightly clayey silt
M 4-4	Silt Loam	slightly sandy mud	slightly sandy slightly clayey silt
M 4-5	Silt Loam	slightly sandy mud	slightly sandy slightly clayey silt
M 4-6	Silt Loam	slightly sandy mud	slightly sandy slightly clayey silt
M 4-7	Silt Loam	slightly sandy mud	slightly sandy slightly clayey silt
M5	Sandy Loam	sandy mud	slightly clayey sandy silt
M 6-1	Silt Loam	slightly sandy mud	slightly sandy slightly clayey silt
M 6-2	Silt Loam	slightly sandy mud	slightly sandy slightly clayey silt
M 6-3	Silt Loam	slightly sandy mud	slightly sandy slightly clayey silt
M 6-4	Silt Loam	very slightly sandy mud	very slightly sandy clayey silt
M 6-5	Silty Clay Loam	very slightly sandy mud	very slightly sandy clayey silt
M 6-6	Silt Loam	slightly sandy mud	slightly sandy clayey silt
M 6-7	Silty Clay Loam	slightly sandy mud	slightly sandy clayey silt

Appendix H: Grain size classifications (4/5).

Name	Textural classes - WRB (IUSS Working Group 2014)	Textural classes (gravel, sand, mud) - Blott and Pye (2012)	Textural classes (sand, silt, clay) - Blott and Pye (2012)
M 7-1	Silty Clay Loam	very slightly sandy mud	very slightly sandy clayey silt
M 7-2	Silt Loam	sandy mud	slightly clayey sandy silt
M 8	Silty Clay Loam	slightly sandy mud	slightly sandy clayey silt
SA 1-1	Silty Clay Loam	very slightly sandy mud	very slightly sandy clayey silt
SA 1-2	Silty Clay Loam	slightly gravelly slightly sandy mud	slightly sandy clayey silt
SA 2-1	Silty Clay Loam	slightly sandy mud	slightly sandy clayey silt
SA 2-2	Silt Loam	slightly sandy mud	slightly sandy slightly clayey silt
SA 2-3	Silt Loam	slightly sandy mud	slightly sandy slightly clayey silt
SA 2-4	Silt Loam	slightly sandy mud	slightly sandy slightly clayey silt
SA 2-5	Silt Loam	very slightly sandy mud	very slightly sandy clayey silt
SA 3	Silt Loam	slightly sandy mud	slightly sandy slightly clayey silt
SA 4-1	Silt Loam	slightly sandy mud	slightly sandy slightly clayey silt
SA 4-2	Silty Clay	very slightly sandy mud	very slightly sandy silty clay
SA 4-3	Clay	very slightly sandy mud	very slightly sandy silty clay
SA 5-1	Silt Loam	sandy mud	slightly clayey sandy silt
SA 5-2	Silt Loam	slightly sandy mud	slightly sandy slightly clayey silt
SA 6-1	Silty Clay Loam	mud	clayey silt
SA 6-2	Silt Loam	slightly sandy mud	slightly sandy slightly clayey silt
SA 7	Silty Clay Loam	slightly sandy mud	slightly sandy clayey silt
SA 8	Silt Loam	slightly sandy mud	slightly sandy clayey silt
SA 9-1	Silty Clay Loam	slightly sandy mud	slightly sandy clayey silt
SA 9-2	Silty Clay Loam	slightly sandy mud	slightly sandy clayey silt
SA 9-3	Silty Clay Loam	slightly sandy mud	slightly sandy clayey silt
SA 9-4	Silty Clay Loam	slightly sandy mud	slightly sandy clayey silt
SA 10-1	Silt Loam	slightly gravelly slightly sandy mud	slightly sandy clayey silt
SA 10-2	Silt Loam	slightly sandy mud	slightly sandy slightly clayey silt
EFE 1-1	Silt Loam	slightly gravelly sandy mud	slightly clayey sandy silt
EFE 1-2	Silt Loam	slightly sandy muddy gravel	slightly clayey sandy silt
EFE 1-3	Loam	gravelly sandy mud	slightly clayey silty sand
EFW 1-1	Silty Clay Loam	slightly gravelly slightly sandy mud	slightly sandy clayey silt
EFW 1-2	Silt Loam	slightly gravelly slightly sandy mud	slightly sandy clayey silt
EFW 1-3	Loam	gravelly sandy mud	sandy clayey silt
EFW 1-4	Loam	gravelly sandy mud	slightly clayey silty sand
EFW 1-5	Silty Clay Loam	very slightly gravelly slightly sandy mud	slightly sandy clayey silt
EFW 1-6	Silty Clay Loam	slightly gravelly slightly sandy mud	slightly sandy clayey silt
EFW 1-7	Loam	slightly sandy muddy gravel	sandy clayey silt

Appendix H: Grain size classifications (5/5).

Name	Textural classes - WRB (IUSS Working Group 2014)	Textural classes (gravel, sand, mud) - Blott and Pye (2012)	Textural classes (sand, silt, clay) - Blott and Pye (2012)
EFW 1-8	Silt Loam	slightly sandy muddy gravel	slightly clayey sandy silt
EFW 1-9	Loam	slightly sandy muddy gravel	sandy clayey silt
EFW 1-10	Silt Loam	slightly gravelly sandy mud	slightly clayey sandy silt
EM 1-1	Silt Loam	slightly sandy mud	slightly sandy slightly clayey silt
EM 1-2	Silt Loam	very slightly gravelly slightly sandy mud	slightly sandy slightly clayey silt
EM 1-3	Silt Loam	slightly sandy mud	slightly sandy clayey silt
EM 1-4	Silt Loam	very slightly gravelly slightly sandy mud	slightly sandy clayey silt
EM 1-5	Silt Loam	slightly gravelly slightly sandy mud	sandy clayey silt
EM 1-6	Silt Loam	slightly gravelly sandy mud	slightly clayey sandy silt
EM 1-7	Silt Loam	very slightly gravelly slightly sandy mud	slightly sandy clayey silt
EM 1-8	Silt Loam	very slightly sandy gravelly mud	slightly sandy clayey silt
EM 1-9	Silty Clay Loam	very slightly gravelly slightly sandy mud	slightly sandy clayey silt
EM 1-10	Silty Clay Loam	slightly gravelly slightly sandy mud	slightly sandy clayey silt
EM 1-11	Silt Loam	very slightly gravelly slightly sandy mud	slightly sandy slightly clayey silt
EM 1-12	Silt Loam	slightly gravelly slightly sandy mud	slightly sandy slightly clayey silt

Appendix I: Grain size distribution trigon (gravel, sand, mud) according to Blott and Pye (2012).

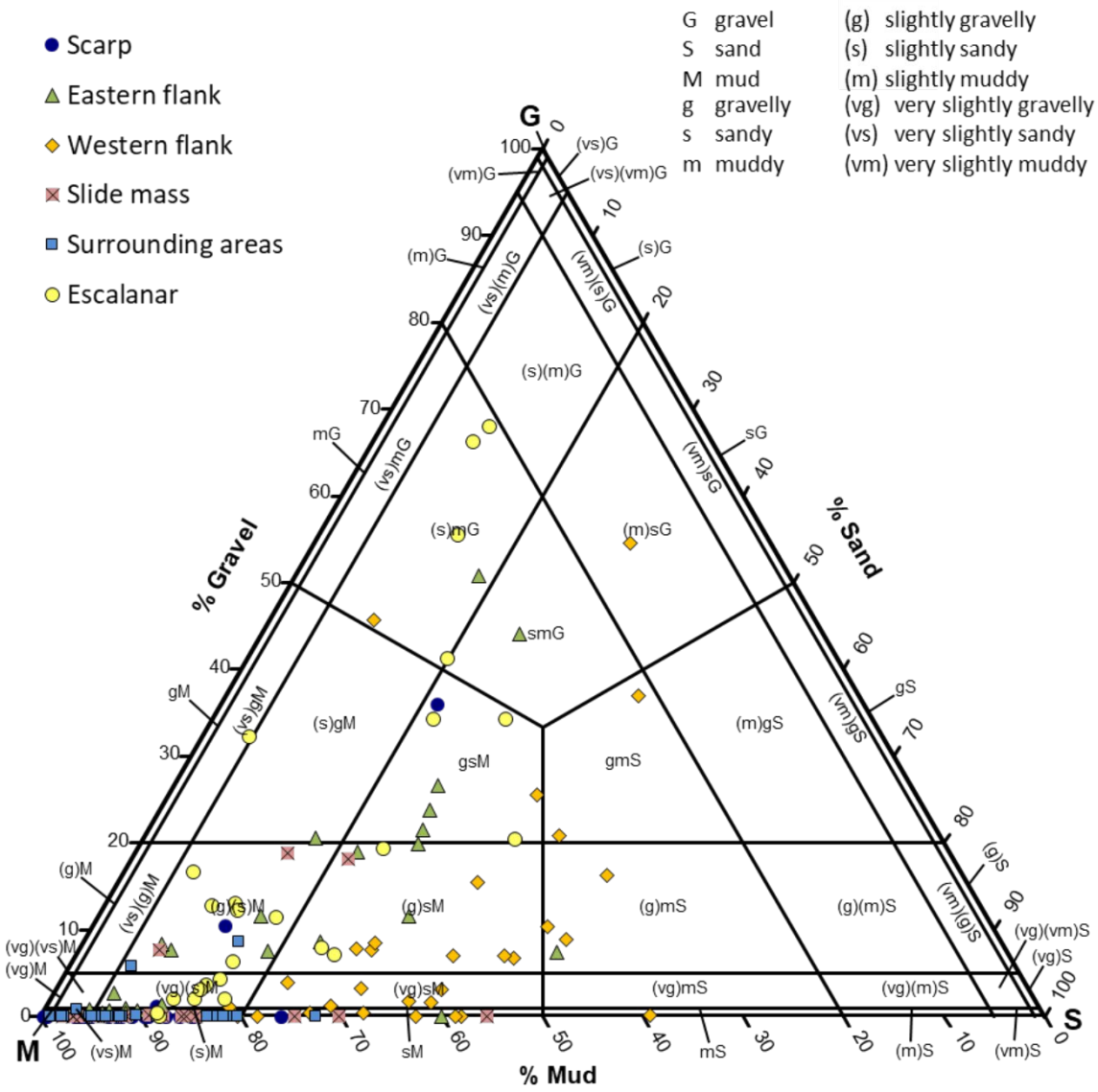

Appendix J: Grain size distribution trigon (sand, silt, clay) according to Blott and Pye (2012).

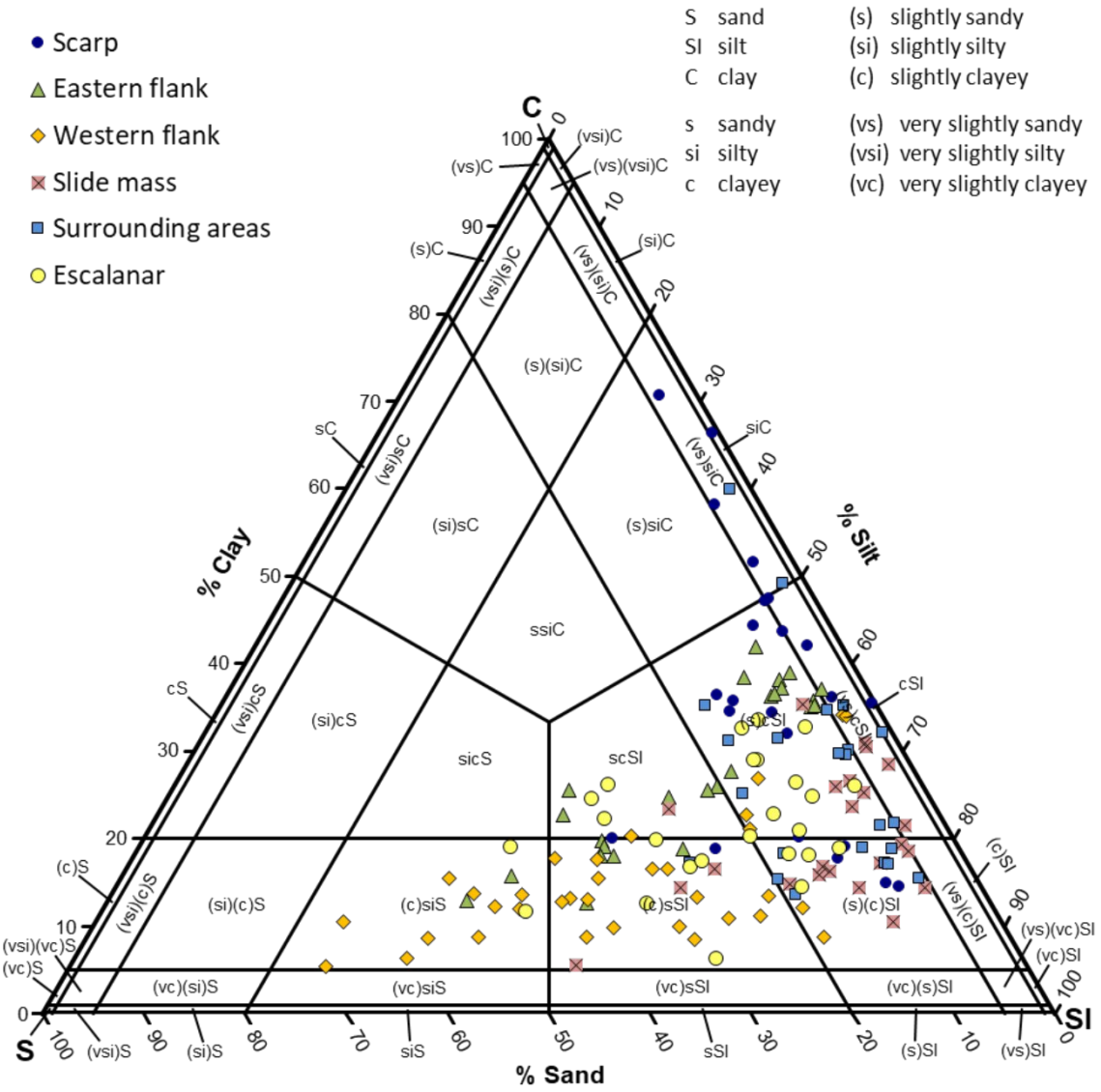

Appendix K: Grain size distribution trigon (sand, silt, clay) according to WRB (IUSS Working Group 2014).